

Om Hari Gupta
S. N. Singh
Om P. Malik *Editors*

Recent advances in Power Systems

Select Proceedings of EPREC 2022

Lecture Notes in Electrical Engineering

Volume 960

Series Editors

Leopoldo Angrisani, Department of Electrical and Information Technologies Engineering, University of Napoli Federico II, Naples, Italy

Marco Arteaga, Departament de Control y Robótica, Universidad Nacional Autónoma de México, Coyoacán, Mexico

Bijaya Ketan Panigrahi, Electrical Engineering, Indian Institute of Technology Delhi, New Delhi, Delhi, India

Samarjit Chakraborty, Fakultät für Elektrotechnik und Informationstechnik, TU München, Munich, Germany

Jiming Chen, Zhejiang University, Hangzhou, Zhejiang, China

Shanben Chen, Materials Science and Engineering, Shanghai Jiao Tong University, Shanghai, China

Tan Kay Chen, Department of Electrical and Computer Engineering, National University of Singapore, Singapore, Singapore

Rüdiger Dillmann, Humanoids and Intelligent Systems Laboratory, Karlsruhe Institute for Technology, Karlsruhe, Germany

Haibin Duan, Beijing University of Aeronautics and Astronautics, Beijing, China

Gianluigi Ferrari, Università di Parma, Parma, Italy

Manuel Ferre, Centre for Automation and Robotics CAR (UPM-CSIC), Universidad Politécnica de Madrid, Madrid, Spain

Sandra Hirche, Department of Electrical Engineering and Information Science, Technische Universität München, Munich, Germany

Faryar Jabbari, Department of Mechanical and Aerospace Engineering, University of California, Irvine, CA, USA

Limin Jia, State Key Laboratory of Rail Traffic Control and Safety, Beijing Jiaotong University, Beijing, China

Janusz Kacprzyk, Systems Research Institute, Polish Academy of Sciences, Warsaw, Poland

Alaa Khamis, German University in Egypt El Tagamoa El Khames, New Cairo City, Egypt

Torsten Kroeger, Stanford University, Stanford, CA, USA

Yong Li, Hunan University, Changsha, Hunan, China

Qilian Liang, Department of Electrical Engineering, University of Texas at Arlington, Arlington, TX, USA

Ferran Martín, Departament d'Enginyeria Electrònica, Universitat Autònoma de Barcelona, Bellaterra, Barcelona, Spain

Tan Cher Ming, College of Engineering, Nanyang Technological University, Singapore, Singapore

Wolfgang Minker, Institute of Information Technology, University of Ulm, Ulm, Germany

Pradeep Misra, Department of Electrical Engineering, Wright State University, Dayton, OH, USA

Sebastian Möller, Quality and Usability Laboratory, TU Berlin, Berlin, Germany

Subhas Mukhopadhyay, School of Engineering and Advanced Technology, Massey University, Palmerston North, Manawatu-Wanganui, New Zealand

Cun-Zheng Ning, Electrical Engineering, Arizona State University, Tempe, AZ, USA

Toyoaki Nishida, Graduate School of Informatics, Kyoto University, Kyoto, Japan

Luca Oneto, Department of Informatics, BioEngineering, Robotics, and Systems Engineering, University of Genova, Genoa, Genova, Italy

Federica Pascucci, Dipartimento di Ingegneria, Università degli Studi "Roma Tre", Rome, Italy

Yong Qin, State Key Laboratory of Rail Traffic Control and Safety, Beijing Jiaotong University, Beijing, China

Gan Woon Seng, School of Electrical and Electronic Engineering, Nanyang Technological University, Singapore, Singapore

Joachim Speidel, Institute of Telecommunications, Universität Stuttgart, Stuttgart, Germany

Germano Veiga, Campus da FEUP, INESC Porto, Porto, Portugal

Haitao Wu, Academy of Opto-electronics, Chinese Academy of Sciences, Beijing, China

Walter Zamboni, DIEM—Università degli studi di Salerno, Fisciano, Salerno, Italy

Junjie James Zhang, Charlotte, NC, USA

The book series *Lecture Notes in Electrical Engineering* (LNEE) publishes the latest developments in Electrical Engineering—quickly, informally and in high quality. While original research reported in proceedings and monographs has traditionally formed the core of LNEE, we also encourage authors to submit books devoted to supporting student education and professional training in the various fields and applications areas of electrical engineering. The series cover classical and emerging topics concerning:

- Communication Engineering, Information Theory and Networks
- Electronics Engineering and Microelectronics
- Signal, Image and Speech Processing
- Wireless and Mobile Communication
- Circuits and Systems
- Energy Systems, Power Electronics and Electrical Machines
- Electro-optical Engineering
- Instrumentation Engineering
- Avionics Engineering
- Control Systems
- Internet-of-Things and Cybersecurity
- Biomedical Devices, MEMS and NEMS

For general information about this book series, comments or suggestions, please contact leontina.dicecco@springer.com.

To submit a proposal or request further information, please contact the Publishing Editor in your country:

China

Jasmine Dou, Editor (jasmine.dou@springer.com)

India, Japan, Rest of Asia

Swati Meherishi, Editorial Director (Swati.Meherishi@springer.com)

Southeast Asia, Australia, New Zealand

Ramesh Nath Premnath, Editor (ramesh.premnath@springernature.com)

USA, Canada

Michael Luby, Senior Editor (michael.luby@springer.com)

All other Countries

Leontina Di Cecco, Senior Editor (leontina.dicecco@springer.com)

**** This series is indexed by EI Compendex and Scopus databases. ****

Om Hari Gupta · S. N. Singh · Om P. Malik
Editors

Recent advances in Power Systems

Select Proceedings of EPREC 2022

 Springer

Editors

Om Hari Gupta
Department of Electrical Engineering
NIT Jamshedpur
Jamshedpur, India

S. N. Singh
Department of Electrical Engineering
Indian Institute of Technology Kanpur
Kanpur, India

Om P. Malik
Department of Electrical and Computer
Engineering
University of Calgary
Calgary, AB, Canada

ISSN 1876-1100

ISSN 1876-1119 (electronic)

Lecture Notes in Electrical Engineering

ISBN 978-981-19-6604-0

ISBN 978-981-19-6605-7 (eBook)

<https://doi.org/10.1007/978-981-19-6605-7>

© The Editor(s) (if applicable) and The Author(s), under exclusive license to Springer Nature Singapore Pte Ltd. 2023

This work is subject to copyright. All rights are solely and exclusively licensed by the Publisher, whether the whole or part of the material is concerned, specifically the rights of translation, reprinting, reuse of illustrations, recitation, broadcasting, reproduction on microfilms or in any other physical way, and transmission or information storage and retrieval, electronic adaptation, computer software, or by similar or dissimilar methodology now known or hereafter developed.

The use of general descriptive names, registered names, trademarks, service marks, etc. in this publication does not imply, even in the absence of a specific statement, that such names are exempt from the relevant protective laws and regulations and therefore free for general use.

The publisher, the authors, and the editors are safe to assume that the advice and information in this book are believed to be true and accurate at the date of publication. Neither the publisher nor the authors or the editors give a warranty, expressed or implied, with respect to the material contained herein or for any errors or omissions that may have been made. The publisher remains neutral with regard to jurisdictional claims in published maps and institutional affiliations.

This Springer imprint is published by the registered company Springer Nature Singapore Pte Ltd. The registered company address is: 152 Beach Road, #21-01/04 Gateway East, Singapore 189721, Singapore

Contents

Sustainable and Optimal Rolling of Electric Vehicle on Roadways with Better Implementation	1
Sarita Samal, Chitralkha Jena, Roshan Kumar Soni, Rahul Verma, Sumeet Sahaya, and Prasanta Kumar Barik	
A Review on Recent Advanced Three-Phase PLLs for Grid-Integrated Distributed Power Generation Systems Under Adverse Grid Conditions	17
Poonam Tripathy, Banishree Misra, and Byamakesh Nayak	
Performance Assessment and Evaluation of a 52-kW Solar PV Plant in India	31
J. Divya Navamani, A. Lavanya, Yash Vardhan Bhargava, Divya Kumar Gupta, and Gaurav Singh	
Green Energy in West Bengal, India: Status, Scope, and Future Challenges	47
Debajit Misra	
Impact of Performance Parameters on the Efficiency of Cu_2SnS_3 (CTS)/Si Tandem Solar Cell by SCAPS-1D	63
Devsmitta Roy, Rajeshwari Garain, Arindam Basak, Subrat Behera, Ranjeeta Patel, and Udai P. Singh	
Expansion of the Burners Structure to Boost up the Ecological Properties of an Average Capacity Boiler “E-270-13.73-560”	77
Uthum Gunasekara and Nilan Jayasinghe	
Rearrangement of the PV Array to Reduce the Effect of Partial Shading Using Meta-Heuristic Techniques	89
Reeva Dhariwal and Bhavnesk Kumar	

Design of Lithium-Ion Battery Thermal Management System for Vehicular Applications	97
Inteti Lakshya Rani, K. Dhananjay Rao, Penmetsa Preetham, and Ghanta Chaitanya	
Wind and Tidal Power as a Dynamic Solution for Sri Lanka's Dependency on Thermal Power Plants	107
Nilan Jayasinghe, Uthum Gunasekara, and Rasika Pothupitiya	
Evaluation of Various Dynamics on Current Transformer Saturation with a Model Study on Power System Protection	121
Dharmesh Patel and Nilesh Chothani	
Cost and Energy Efficiency Study of an ARIMA Forecast Model Using HOMER Pro	137
M. K. Babu, Papia Ray, and A. K. Sahoo	
An Off-MPPT Controller for Standalone PV Systems	153
Piyush Kumar and R. N. Mahanty	
Designing and Simulation of Double Stage Grid-Linked PV System Using MATLAB/Simulink	169
Shamik Kumar Das, M. K. Sinha, and A. K. Prasad	
A Review of Sensor-Based Solar Trackers	197
Ashish Dixit, Suresh Kumar Gawre, and Shailendra Kumar	
Detection and Classification of Faults in VSC-HVDC System Based on Single End Ground and Pole Differential Current Components	217
Ravi Shankar Tiwari, Rahul Kumar, and Om Hari Gupta	
Investigation of Different Types of Bidirectional Charging Operations of Electric Vehicles	229
Sneha Mahobiya, Shailendra Kumar, and Suresh Kumar Gawre	
Intelligent Fault Location Scheme for HVDC System	245
Sunil Kumar Singh	
Energy-Metrics Analysis of 2 kWp Rooftop PV System Located in Gwalior India	255
Saurabh Kumar Rajput, Ankit Kumar Tripathi, and Manjaree Pandit	
The Use of Biogas Energy for Electrical Power Generation in Zimbabwe—A Study	265
Coddell Tanaka Mutate, Artwell Jairo Kanjanda, and Gitanjali Mehta	

Sustainable and Optimal Rolling of Electric Vehicle on Roadways with Better Implementation



Sarita Samal, Chitralekha Jena, Roshan Kumar Soni, Rahul Verma, Sumeet Sahaya, and Prasanta Kumar Barik

1 Introduction

The ceaseless use of fossil fuels is eroding the earth's ability to provide a suitable environment for life. Its takeover of daily life has become so familiar that it is now critical to come up with an idea that is far more convincing than what ancient leaders stated [1, 2]. Electric vehicles are becoming increasingly popular among those who support the transition to a cleaner system of automobiles and avionics. As a result, the development of an electric vehicle plays an important role in avoiding the effects of pollution, climate change, unlikely price hikes and so on, while also putting an end to the use of fossil fuels to power vehicles. The regular spread of carbon dioxide would also be reduced in comparison with what we currently face [3]. Electric vehicles have already taken up slots in the share market with 28.8% in Norway, 6.4% in the Netherlands and China with 1.4%. While Tesla has already recorded a sale of almost 500,000 electric cars with Volkswagen in the second position in the year 2020. It's getting higher with various countries focusing to increase the number of EV

S. Samal (✉) · C. Jena · R. K. Soni
SoEE, KIIT DU, Bhubaneswar, Odisha, India
e-mail: ssamalfel@kiit.ac.in

C. Jena
e-mail: chitralekha.jenafel@kiit.ac.in

R. K. Soni
e-mail: 1803044@kiit.ac.in

R. Verma
ABES Engineering College, Ghaziabad, India

S. Sahaya
Department of EE, IIT (ISM), Dhanbad, Jharkhand, India

P. K. Barik
Department of MEE, CAET, OUAT, Bhubaneswar, Odisha, India

occupancies. If 2020 had been an equally productive year, then a whopping amount of 40 million EVs would have crossed globally. They are powered by renewable energy instead of fossil fuel power plants that are capable of harming the environment. For that, huge number of electric vehicle and charging stations need to be built for a continuous supply of power. And in position, for a vehicle to reach by the time, they run out of charge. It's important to discuss the impact of electric vehicles on the distribution system. It is recorded to leap up with a peak load of 17.9% for 10% access and 35.8% when the access is increased to 20%. Power losses and voltage deviations are generated because of the higher peak load of an electric vehicle. This can also lead to the violation of the thermal limit of transformers and transmission lines. To reduce the distribution system, losses coordinated charging system is brought up. A coordinated charging system also ensures an even voltage range and keeps the distribution system from becoming overloaded. This works in conjunction with a coordinated charging process that generates lower peak loads or stays within limits. A coordinated charging system necessitates customer coordination for serial vehicle charging, which is frequently lacking in practice. As a result, in the majority of cases, refreshing the total area for a non-restricted process has yet to be established. For a rapid increase in the number of electric vehicles, an infrastructure that can provide well-planned facilities must be built [4, 5]. Of which, chargers are categorized into three levels. Level 1 charger or a residential charging option is of low power used for lesser charge consuming vehicles. The level 2 charger is a bit advanced than the previous one and requires protection when inside a residence. Lastly, commercial purposes come with a level 3 charger that is capable of fully charging a vehicle within an hour. It's in huge demand as it's very less time-consuming. But in return, it's costlier and without an appropriate plan, the electric power system can be overloaded. The ability of electric vehicles to provide a power reserve while the batteries are being charged stabilizes the electrical system. Primary supports to the EV system can lead to the control of primary and secondary frequencies and regulation of voltage. In an electrical power system, primary and secondary control reduces the frequency deviation and helps in a balanced supply, respectively. Electric vehicle charger is the major equipment for voltage regulation. Distribution systems follow one-way and outward energy flow while developing voltage safety and regulation plans. For handling daily load consumption, electric vehicles need to go through a regular plan. An unregulated charging process of electric vehicles leads to transmission line crowding that increases transmission line loss and decreases the quality of electric supply. Due to this, both electric vehicle batteries and grid systems are hampered. So, a well-scheduled and managed charging process is necessary to keep smart grids intact. Electric vehicles have a greater scope of making transportation easier and well affecting the electrical power system with the regular and properly planned charging process. They could replace the conventional method to help support the ecosystem.

The following are the primary objectives of this study:

We need to understand the aims and their corresponding objectives when conducting research and presenting a paper on the implementation of an electric vehicle. The aim is simply the abbreviation for targets and objectives, which are the actions we must take in order to achieve our goals.

- Implementation of an electric vehicle as a mode of transportation.
- Reducing the use of traditional fossil fuels.
- Reducing the impact of pollution, particularly, carbon emissions.
- Sustainable development in renewable energy is being implemented.
- The successful implementation of an electrical distribution system for smooth operation.
- Reduced global warming.
- Economic development and technological advancement in society.

If we need to achieve all these aims successfully, then the below objectives should be taken into consideration for a long time because it will not have a short time efficiency.

- People must learn about social responsibilities in order to understand the current situation and gain enthusiasm for using electric vehicles.
- We need to think together to reduce pollutant gases and atmospheric temperature there, so that the overall consumption of fossil fuel through our IC engine-based vehicle can be greatly reduced.
- The entire world is looking for long-term development, particularly in the energy generation sectors. As a result, we must also think about it and contribute to achieving zero-carbon emissions through energy generation from renewable sources. Even for charging our electric vehicles, using renewable energy sources can be a great idea, and this can help a lot in the context of EV implementation.
- If there are so many electric vehicles on the road and there aren't enough charging stations and charging facilities, it won't be a successful strategy. As a result, the installation of a regular charging station within a certain distance must be done correctly.
- As we can see, the process of fossil fuels (Petrol/Diesel) is at its peak, so reducing fossil fuel usage and switching to electric vehicles will also help a lot in avoiding high daily communication costs.

This is how all these possible aims can be achieved after the successful placement of electric vehicles in the distribution system. Later on, in the further parts of the report, we will be discussing methodology and mathematical expressions for better understanding.

2 Problem Statement and Formulation

With the help of lots of researches from different published research papers, it is clear to us that the overall implementation or placement is not that much easier. From the literature review, it is very clear that the distribution system and their placement completely depend on the implementation of charging stations and it is one of the most effective problems for increasing the number of electric vehicles in roadways. The limitation in the implementation of EVs is nothing but its limited range. For

conventional fuel-based vehicles, there is not a limited range due to the presence of fuel pumps and refueling time is very less. But for an electric vehicle since the charging time is long and it is not sufficient in the country, therefore, the problem begins with the implementation of electric vehicles and the distribution network of charging stations throughout the roadways. Following these problem statements, we have to move forward in this paper so that EVs and their charging stations can be implemented [4]. For better understanding, the problem statements are written below in bullet points so that we can proceed with those points step by step.

1. Implementation of an electric vehicle instead of a conventional IC engine-based vehicle.
2. Implementation of charging station on a regular interval in the roadways.
3. Getting advanced technologies for fast charging so that the recharging time can be reduced.
4. Increasing better efficiency for the usage of battery power in terms of better range for a fully charged battery as well as the battery life cycle for economic feasibility within customers.

3 Methodology

For an in-depth understanding of the overall technology few points related to EV are discussed in this part of the paper. The discussion-based on a technological factor will help us to visualize the engineering terminologies and their implementation in the real world. Electric vehicle load modeling, photovoltaic generation modeling and modeling of test systems in open DDS are the basic thing covered here.

Electric vehicle load modeling

The load modeling of an electric vehicle is nothing but the demand of charging in a particular charging station which depends on the overall distribution system. The distribution system has four main factors, and these are arrival time, departure time, number of arrivals and departure and finally traveling distance. Different data based on these parameters will help a lot for its proper implementation/placement. The arrival time of a vehicle is taken as the starting point for a vehicle and the departure time of the vehicle to another charging station is taken as the time of a run. The gap between these times is the time of a run. In between this run time, the traveled distance is the range of the vehicle from a fully charged battery [1]. According to these data, a probability function is prepared for getting their distribution. Estimation of these parameters will help a lot for the charging stations to fulfill the desired demands for a smooth operation. The initial state of charge in an electric vehicle depends on the traveled distance.

This can be expressed as, in (1)

$$\text{SOC}_{\text{initial}} = 1 - \left(\frac{\text{Distance travelled}}{\text{Maximum distance covered}} \right) \forall e \in E \quad (1)$$

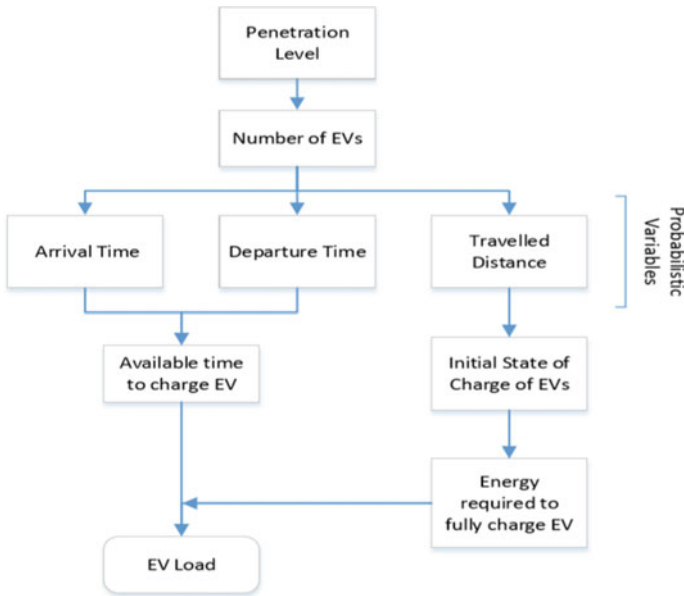


Fig. 1 EV load estimation flowchart

The maximum distance signifies the total distance that can be covered by the vehicle when it is in full charge condition (Fig. 1).

Though the report is based on a review of the electric vehicle placement and its successful rolling in the roadways for upcoming days, but a secondary data is gathered from different research papers which are shown below. The reason behind it is to get a general overview regarding their literature review and data collection [1].

Photovoltaic generation modeling

To enhance the usage of renewable sources of energy along with the implementation in the overall electrical distribution system, the solar/photovoltaic cell implementation is one of the most effective solutions. It can be used just like a solar power grid for the generation of electricity and the generated power can be utilized for charging stations by converting the source current from DC to AC through inverter circuits. There might be some problems during its implementation because of rapid weather changing but as a whole, for a long time, it will have a significant figure in terms of environmental effects (Zero emission) and cost-effectiveness [1]. This type of generation unit can also be implemented in rooftop solutions for small commercial goods carrying vehicles. In some cases, rooftop solar panels proved very efficient for charging electric vehicles within personal property instead of using services from on-road charging stations. In technical point of view for the desired load estimation, the generation from a PV module can be expressed as below (Table 1).

$$P_{PV} = 0.995 \times \eta \times A \times I \times (T_m - T_{ref})$$

where

η Pannel efficiency

A Pannel area

I Irradiance

T_m Measured temperature in °C

T_{ref} Reference temperature 25 °C.

Table 1 Vehicle user and charging station data with probability distribution function researched data [1]

Data	Distribution categories	Different parameters in distribution
<i>Residential feeders (EV)</i>		
Evening arrivals	Extreme value	$\xi = 0.0613$ $\sigma = 0.5129$ $\mu = 18.7393$
Morning departure	Extreme value	$\xi = -0.252$ $\sigma = 1.180$ $\mu = 7.09$
<i>Commercial feeders</i>		
Morning arrivals	Extreme value	$\xi = 0.0629$ $\sigma = 0.546$ $\mu = 8.905$
Evening arrivals	Weibull distribution	$\lambda = 16.038$ $k = 18.022$
Evening departure	Extreme value	$\xi = -0.282$ $\sigma = 1.116$ $\mu = 16.407$
Night departure	Extreme value	$\xi = -0.277$ $\sigma = 0.536$ $\mu = 20.549$
<i>Commercial and residential feeders (EV)</i>		
Traveled distance	Extreme value	$\xi = 0.0474$ $\sigma = 7.901$ $\mu = 12.882$

Modeling of test system in open Data Distribution System (DDS)

In terms of modeling in the test system within the distribution network is not an easy thing to do, but for their testing conventional techniques like Newton Raphson, Gauss Seidal methods will not be appropriate for this particular case study. For these limitations we have seen in different research papers authors are trying to solve them with the help of general theories of Kirchhoff's law maybe it if KCL and KVL [1]. In this case with the help of MATLAB and an open DDS interface, the optimization can be found out if one can successfully implement the below-given flowchart in the interface. All elements are represented by their nodal admittance matrix. In this particular process for optimization, the system builds an admittance matrix and initiates the entire process by selecting any random voltage vector V_o so that the system interface can calculate the current from each of the circuit elements. The new value V_{n+1} is calculated by the below-given equation in the system interface [1]. This particular iterative technique takes place till the convergence criterion takes place in the optimization iteration.

$$V_{n+1} = [Y_{\text{system}}]/I_{\text{PC}} V_n \quad (2)$$

The results in the Open DDS should be imported into MATLAB interface for studying the optimization technique. For getting rid of this complex situation, PSO comes into the role. PSO allows the optimization iteration for its running multiple times. This kind of analysis will help a lot to get estimation about the future scenario and will also help to provide the sizing of charging stations for the optimal placement of the electric vehicle [3].

4 Mathematical Evaluation

The implementation of electric vehicles within the optimal distribution network needs some feasibility for its charging stations. Now one question will be there, that is the main factors to be introduced in the mathematical evaluation for optimal placement of EV in the distribution system. Since there is nothing more technical because the overall feasibility depending on the usage of electricity and their loss makeup. So, the mathematical evaluation focuses on the losses associated with the loss in different sections of the distribution network.

Decision vector

The decision vector is the thing, which represents the actual locations of charging stations within the distribution network. The decision matrix is represented as CSP [5].

$$\text{CSP} = \begin{cases} 1, & \text{if CS is required} \\ 0, & \text{otherwise} \end{cases} \quad i = 1, 2, 3, \dots, n \quad (3)$$

Multi-objective functions

It is a problem-solving phenomenon in which problems related to QCS can be solved. The multi-objective functions consist of two different sub-objectives those are,

1. Transportation energy loss cost
2. Substation energy loss cost.

Transportation energy loss cost

In this process, we can see an EV needs to go a certain distance to reach the nearest charging station. In this process, there might have a loss which is known as transportation energy loss and the cost associated with this is known as TEL cost [5]. Let us consider the EV moves from its j th position to the i th position and in this trajectory, the transportation energy loss will be obtained by a mathematical expression.

$$I_{ij} = \text{diag}(\text{CSP}) \times \left| \text{loc}_{\text{EV}}^j - \text{loc}_{\text{CS}}^i \right|, \quad i = 1, 2, 3, \dots, N_{\text{CS}}$$

where

- N_{CS} Number of charging stations
 loc_{EV}^j Location of EV
 loc_{CS}^i Location of charging station.

$$\text{TEL}_j = P_{\text{E}} \times S_{\text{EC}} \times L_{j \min}$$

where

- P_{E} Electricity price rs/Kwh
 S_{EC} Energy consumption per km
 $L_{j \min}$ Minimum length L_{ij} .

Now the normalized cost associated with TEL can be expressed as,

$$\text{TEL}_{\text{norm}} = \frac{\sum_{j=1}^{N_{\text{EV}}} \text{TEL}_{j \min}}{\text{TEL}_{\text{max}}}, \quad j = 1, 2, 3, \dots, N_{\text{EV}}$$

Substation energy loss cost

Instead of transportation energy losses due to the distribution parameters, there might have some losses too. The EV load within the charging station can be expressed as,

$$L_{\text{EV}}^i = N_{\text{char}}^i \times N_{\text{EV}}^{\text{CS}i} \times P_r$$

where

- N_{EV}^{CSi} Number of EVs utilizing charging station
 N_{char}^i Number of chargers within the charging station
 P_r Required per EV.

There will also be some additional losses in the charging station, those are expressed below.

$$APL_{EV} = TPL_{EV} - TPL_{original}$$

where

- TPL_{EV} Total power loss when CS is connected to the grid with actual load
 $TPL_{original}$ Total power loss when CS is not connected to the grid.

Finally,

$$SEL_m = APL_{EV} \times t_{ef}(m) \times P_E$$

where

- $t_{ef}(m)$ Effective operating hour when CS connected to grid bus(m).

Now the normalized cost due to substation energy loss is,

$$SEL_{norm} = \frac{\sum_{m=1}^{N_{bus}} SEL_m}{SEL_{max}}, \quad m = 1, 2, 3, \dots, N_{bus}$$

where

- N_{bus} Number of busses in the distribution network
 SEL_{max} Maximum SEL cost.

This is how the entire energy loss calculation can be achieved with some simple expression. Though there are so many types of detail mathematical evaluation, which is needed for actual representation, but for optimal placement, since we are using the term optimal; therefore, the losses and their costing are to be optimized in the initial phase. Therefore, it will be sufficient for understanding and for more detailed calculation there, we will need the exact power train solution for individual EVs [5].

5 Result Analysis

According to the mathematical evaluations that have been done in this paper, the entire thing related to the losses is very few for their incorporation. The factors consisting of TEL and SEL costs will not affect the overall distribution system because the charging stations and their charging points will be connected with vehicles all the

time. It is because of the large charging time of EVs. The combination of TEL and SEL represents the optimal solution for the implementation of EV and its distribution system [5]. For reducing the SEL cost, the transmission system of the charging station is to be designed with proper parameters and that can give the best possible optimization.

5.1 Current Scenario and Progress

The entire process for implementation of electric vehicles in the distribution system not only converged to the topic of its charging station sizing and placement. It has so many things to consider when there is a long-time approach to a particular technology. From Asian to European countries, everyone is most capable to achieve their target. 2025 is the target to achieve where most of the countries working so hard to replace 15% of IC engine-based vehicles with electric vehicles. Also, for electric vehicles along with their price, government tax, insurance costing, road tax, and electricity tariff prices are reduced. For these reasons, the electric vehicle selling and their usages for commercial and domestic usages are increasing in nature [6]. As this paper is focused on the optimal placement of electric vehicles, therefore, the charging station and their technology development is also an important thing to be addressed. Now if we can check some secondary Internet source data about the sales of EVs in different countries, then it will be clear to us about the leading country for successful implementation of EV (Fig. 2).

It is very good to see such improvement in the sales of electric vehicles throughout the world which depicts actual sustainable development in terms of getting clean and green energy. Among different countries and subcontinents, China, USA and Europe are leading in its marketing and all other countries are also putting their efforts in its implementation [9]. For a developing country, India is also in the development process in which various small companies are getting the promotion by the government for their EV manufacturing on Make in India context. Also, to increase the level of technology in most of the universities are also applying soft skill development on such type of topics so that students can achieve vast knowledge for the development of

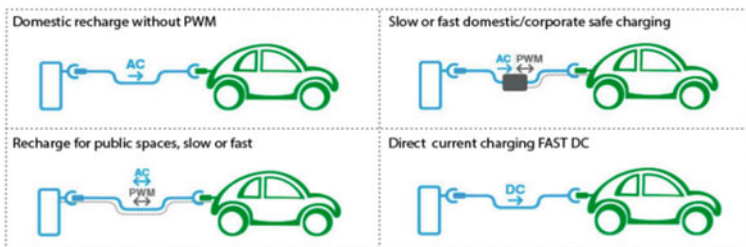


Fig. 2 Different types of charging methods for EVs

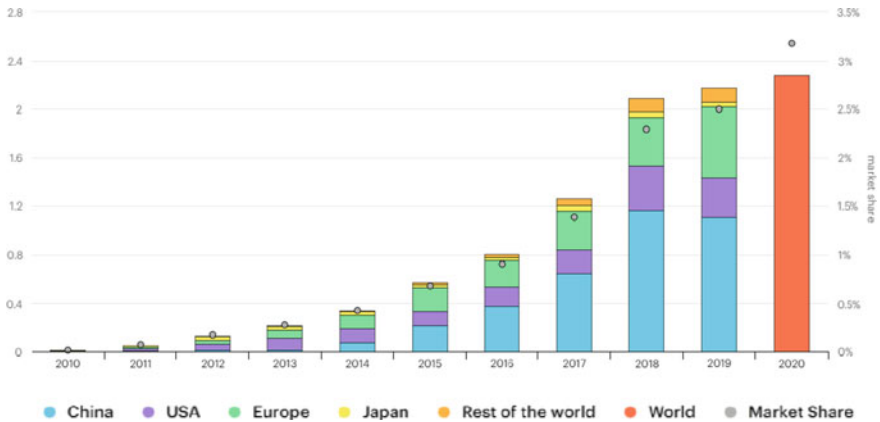


Fig. 3 Global electric vehicles sales from 2010 to 2020 year and country wise data

EV for sustainable development. Society of automotive engineers (SAE) also doing different events in regular years for in-house EV development racing from different college teams. Such kinds of initiatives are giving a hugely positive result and based on it is expected that by 2030 more than 50% of vehicles IC engine-based vehicles will be replaced by electric vehicles [7] (Fig. 3).

5.2 Implementation and Target

Though different countries are achieving their target in EV implementation but some other countries are lagging behind their target. India, Pakistan and Africa continents are not able to match their target. China, US and some European countries are replaced most of their public transport vehicles (Buses and Taxi) with an electric vehicle. In those countries, this is possible just because of adequate charging stations. The countries lagging in the implementation of EV is just because of their branches for charging, their infrastructure is placed only in few metro cities. As per the government announcement, 30% of the vehicles in India will be replaced by EVs within 2030 [8, 9]. Tata, Mahindra, Maruti Suzuki, Nissan and various car manufacturing companies are doing their R&D for a successful implementation, but in a country like India with a very high population, it is not that feasible. So, instead of making a huge change in the public transport medium if we can get some benefit from the implementation of EV in private transport medium will become more feasible. For that reason, companies like Hero Electric, Okinawa and Yo-bikes are getting more exposure from the customer point of view because they are focusing on daily commuting bikes that are not expensive and can be charged in domestic lines also for personal usage. Tesla is one of the leading companies in EV manufacturing field doing great in this field. They are making a greater number of EV charging stations compared to their vehicle

production so that the movement will become flexible. For developing countries to initiate their production plant, they are also working hard on it [10, 11]. Tesla also going to build their production plant in India very soon, which will be a revolutionary decision for Indian EV placement.

5.3 Drawbacks in the Development

Though there are so many good things are available in the optimal placement of electric vehicles in the entire distribution system. But in the actual scenario, there are so many drawbacks. If those limitations or drawbacks cannot be overcome by the meantime, there will not be optimal placement. Therefore, during all these conversations, such type of evaluation is necessary. If there are so many drawbacks, then how it is incorporated in various countries successfully is the main question [12, 13]. So, considering other countries' success factors, we will need to focus on them so that the implementation will achieve sustainability.

All the possible drawbacks are listed below in bullet points,

- Since we are saying about the less usage of fossil fuel by using more numbers of electric vehicles. But the interesting thing is the law of conservation of energy, according to that during charging, we are consuming electricity and for the generation of electrical energy power plants are using fossil fuels like coal [14]. Therefore, how the difference can be achieved is the main problem for a country like India, Pakistan, etc., because these countries are mainly dependent on fossil fuel-based power plants. This type of scenario cannot be changed until or unless the power plants will become renewable.
- Another problem is the placement of charging stations in the whole distribution unit. In this case, we have lots of difficulties. First of all, in conventional petrol pumps, the timing of refueling is very less so the movement of the vehicle is faster and for that reason, there we do not need a large space for vehicle parking [15]. But when it will be a charging station it will take almost 4–5 h for full charging therefore the number of vehicles in the charging station and their movement will become slow. In this situation, the charging station will need a huge space for a parking facility. Also, for a long-time charging, the arrival time will hamper so many urgent activities. Also, in this case, all companies should maintain the same type of design specification for their hardware systems so that all EV brands can use the same charging station just like a fuel pump [16].
- Finally, the last problem can be the non-user-friendly nature of the operation. Basically, electric vehicles are not conventional and their maintenance and operational activities are not conventional. Therefore, the optimal implementation will be achieved only after a long time of usage.

5.4 Environmental Sustainability

The usage of electric vehicles and the optimal placement of charging stations will reduce the usage of fossil fuels like petrol and diesel for daily commutation in cars and bikes. Different pollutant gasses like CO₂, CO, SO₂ and unburned hydrocarbon will affect a lot in the environment [17]. The most effective pollution can be termed as temperature increment/global warming, lesser rain and acid rain. These will harm the healthy life of human beings and plants. For long-term usage of EV, the fossil fuel usage will be reduced and the generation of pollutant gasses will also be reduced. Therefore, the sustainability factors can be achieved in terms of environmental sustainability after long-term usage [12].

5.5 Economical Sustainability

In the context of economical sustainability, the expenditure should be lesser compared to the fossil fuel expenditure. Though there will not be a very high difference for long-term usage, it will have benefits. To describe this thing, a comparative study is explained below for ease of understanding. Here we can see how feasible is the electric vehicle for getting economical sustainability for long-term usage. The general expenditure can be reduced to a great extent for such type of implementation. Even if we can initiate the things like, only using EV for local daily commutation, then also the economical sustainability will become a great factor for our daily expenditure [18] (Table 2).

Table 2 Costing/expenditure analysis for economical sustainable study (as per practical scenario observed)

Conventional ICE vehicle	Electric vehicle
Cost of ICE vehicle: INR 100,000	Cost of electric vehicle: INR 80,000
Daily commute: 50 km	Daily commute: 50 km
Mileage: 50 km/lit of petrol	Mileage: 50 km/charge
Petrol price: INR 100 per lit	Electricity price: INR 30 per charge
Daily expenditure: INR100	Daily expenditure: INR 30
Yearly maintenance cost: INR 10,000 (engine oil change)	Yearly maintenance cost: INR 1000 (only few things to be done)
Total cost for fuel per annum: INR 36,500	Total cost for charging per annum: INR 10,950
Total expenditure per annum for ICEV: 100,000 + 10,000 + 36,500 = INR 146,500	Total expenditure per annum for EVs: 80,000 + 1000 + 10,950 = INR 91,950
Total saving per annum in electric vehicle: 146,500–91,950 = INR 54,550	
If we assume the battery life will be 3 years then also we are saving an amount: $[3 \times 54,550) - \text{Battery price}] = [163650 - 50,000 (\text{approx})] = \text{INR } 113,650$	

Along with this, the charging cost associated with the electric vehicle can be reduced by the implementation of personal rooftop solar panels, which will give zero costing on charging. Hence if one can think properly and can make an initial investment, the overall economical sustainability can be enhanced to a great extent [19–22]. Therefore, in clear terminology, we can see the overall sustainability factors are good enough for the implementation of electric vehicle and their entire distribution unit with effective charging stations for long-distance traveling along with some fast-charging technologies [23].

6 Conclusion

This paper discusses the optimal placement of electric vehicles and their distribution system via charging stations. There are numerous advantages and disadvantages to optimal placement, but the main goal of this paper is to show how they can be successfully placed. As a result, from the beginning to the end of this paper, we covered every possible point, such as introduction, literature review, methodology, mathematical evaluation and many more. All of these points will assist us in obtaining the most accurate information about EV placement. Because the optimal placement of EVs in the distribution network is primarily concerned with the distribution of charging stations, the loss parameters for CS distribution are mathematically explained in the mathematical evaluation. Additionally, sizing is a challenge for optimal placement because during the holiday season, there will be a large number of vehicles on the roads, and charging stations must accommodate all of them, and the electrical parameter with their capacity must be adequate. Even through a comparative analysis, we have demonstrated the economic sustainability factor associated with EVs. Finally, in a nutshell, we can say that the implementation of EV in the distribution network is optimal in some countries, while in others, we must collaborate to make it optimal in all aspects.

References

1. Zeb, M.Z., Imran, K., Khattak, A., Janjua, A.K., Pal, A., Nadeem, M., et al.: Optimal placement of electric vehicle charging stations in the active distribution network. *IEEE Access* **8**, 68124–134 (2020)
2. Jabalameli, N., Su, X., Ghosh, A.: Online centralized charging coordination of PEVs with decentralized var discharging for mitigation of voltage unbalance. *IEEE Power Energy Technol. Syst. J.* **6**(3), 152–161 (2019)
3. Islam, M.M., Shareef, H., Mohamed, A.: A review of techniques for optimal placement and sizing of electric vehicle charging stations. *Elect. Rev.* **91**(8), 122–126 (2015)
4. Osório, G.J., Shafie-khah, M., Coimbra, P.D., Lotfi, M., Catalão, J.P.: Distribution system operation with electric vehicle charging schedules and renewable energy resources. *Energies* **11**(11), 3117 (2018)

5. Vopava, J., Koczwara, C., Traupmann, A., Kienberger, T.: Investigating the impact of E-mobility on the electrical power grid using a simplified grid modelling approach. *Energies* **13**(1), 39 (2019)
6. Reddy, M.S.K., Selvajyothi, K.: Optimal placement of electric vehicle charging station for unbalanced radial distribution systems. In: *Energy Sources, Part A: Recovery, Utilization, and Environmental Effects*, pp. 1–15 (2020)
7. Islam, M., Shareef, H., Mohamed, A.: Optimal quick charging station placement for electric vehicles. *Appl. Mech. Mater.* **785**, 697–701 (2015)
8. Phonrattanasak, P., Leeprechanon, N.: Optimal placement of EV fast charging stations considering the impact on electrical distribution and traffic condition. In: *International Conference and Utility Exhibition on Green Energy for Sustainable Development (ICUE)*, pp. 1–6. IEEE (2014)
9. Qian, K., Zhou, C., Allan, M., Yuan, Y.: Modeling of load demand due to EV battery charging in distribution systems. *IEEE Trans. Power Syst.* **26**(2), 802–810 (2011)
10. Shahidinejad, S., Filizadeh, S., Bibeau, E.: Profile of charging load on the grid due to plug-in vehicles. *IEEE Trans. Smart Grid* **3**(1), 135–141 (2012)
11. Prasomthong, J., Ongsakul, W., Meyer, J.: Optimal placement of vehicle-to-grid charging station in distribution system using particle swarm optimization with time varying acceleration coefficient. In: *International Conference and Utility Exhibition on Green Energy for Sustainable Development (ICUE)*, pp. 1–8. IEEE (2014)
12. Moghaddam, S.Z., Akbari, T.: A mixed-integer linear programming model for the plug-in electric vehicle charging problem in unbalanced low voltage electrical distribution systems considering neutral conductor. *Electr. Power Syst. Res.* **209**, 108049 (2022)
13. Tho, Y.P.: Review of battery charger topologies, charging power levels, and infrastructure for plug-in electric and hybrid vehicles. *IEEE Trans. Power Electron.* **28**(5), 2151–2169 (2013)
14. Sadeghi-Barzani, P., Rajabi-Ghahnavieh, A., Kazemi-Karegar, H.: Optimal fast charging station placing and sizing. *Appl. Energy* **125**, 289–299 (2014)
15. Leou, R.C., Teng, J.H., Su, C.L.: Modelling and verifying the load behaviour of electric vehicle charging stations based on field measurements. *IET Gener. Transm. Distrib.* **9**(11), 1112–1119 (2015)
16. Kamh, M.Z., Irvani, R.: Unbalanced model and power-flow analysis of microgrids and active distribution systems. *IEEE Trans. Power Delivery* **25**(4), 2851–2858 (2010)
17. Rupa, J.M., Ganesh, S.: Power flow analysis for radial distribution system using backward/forward sweep method. *Int. J. Electr. Comput. Electron. Commun. Eng.* **8**(10), 1540–1544 (2014)
18. Qamber, I.S., Alhamad, M.Y.: Smart grid-integrated electric vehicle charging infrastructure: future vision. In: *Developing Charging Infrastructure and Technologies for Electric Vehicles*, pp. 1–24. IGI Global (2022)
19. Tomar, A., Tripathi, S.: Blockchain-assisted authentication and key agreement scheme for fog-based smart grid. *Clust. Comput.* **25**(1), 451–468 (2022)
20. Soares, L., Wang, H.: A study on renewed perspectives of electrified road for wireless power transfer of electric vehicles. *Renew. Sustain. Energy Rev.* **158**, 112110 (2022)
21. Rahman, S., Khan, I.A., Khan, A.A., Mallik, A., Nadeem, M.F.: Comprehensive review and impact analysis of integrating projected electric vehicle charging load to the existing low voltage distribution system. *Renew. Sustain. Energy Rev.* **153**, 111756 (2022)
22. Vempalle, R., Dhal, P.K.: Optimal analysis of time varying load radial distribution system with photovoltaic and wind generating system using novel hybrid optimization technique. *Renew. Energy Focus* **41**, 246–257 (2022)
23. Judge, M.A., Khan, A., Manzoor, A., Khattak, H.A.: Overview of smart grid implementation: frameworks, impact, performance and challenges. *J. Energy Storage* **49**, 104056 (2022)

A Review on Recent Advanced Three-Phase PLLs for Grid-Integrated Distributed Power Generation Systems Under Adverse Grid Conditions



Poonam Tripathy , Banishree Misra , and Byamakesh Nayak 

1 Introduction

The continuously rising grid-integrated distributed power generation systems (DPGS) [1] into the utility grid needs advanced controllers for appropriate operation achieved by the power electronic-based grid side converters (GSC) [2–8]. Therefore, correct designing of the GSC-based controlling system performs an important task for suitable operation during both abnormal and normal grid operating conditions. So, the synchronization method must perform the role of extricating the utility voltage variables information accurately in terms of phase angle, amplitude, and frequency. Generally, phase-locked loop (PLL)-based synchronization methods are utilized for achievement of proper monitoring and control of the utility voltage variables [9–15]. The extracted utility grid voltage variables information leads to the desirable control of the interfaced GSC. Therefore, the accuracy and robustness of the PLL perform a fundamental job in total control operation for the grid-integrated DPGS. The PLL's performance accuracy becomes serious under adverse grid situations like during the utility voltage swells and sags, harmonics, interharmonics, unbalanced and balanced main grid faults, DC offsets, phase jumps, and frequency variations [2, 16–21]. Hence, the PLL structure must be robust enough to handle the adverse grid operating situations with an improved performance, faster dynamic response along with lower computational complexity for an efficient operation and application.

The present work compares and analyzes five numbers of recently developed advanced PLLs based on their performing abilities, design complexity, and dynamic

P. Tripathy (✉) · B. Misra · B. Nayak
School of Electrical Engineering, KIIT Deemed to be University, Bhubaneswar, India
e-mail: poonamtripathy.lali@gmail.com

B. Misra
e-mail: bmisrafel@kiit.ac.in

B. Nayak
e-mail: electricbkn11@gmail.com

response. The discussed PLLs are decoupled dual synchronous reference frame PLL (DDSRF PLL) [22–24], multi-sequence harmonic decoupling cell PLL (MSHDC PLL) [25, 26], decoupling network in $\alpha\beta$ frame PLL (DN $\alpha\beta$ PLL) [2, 9, 26], harmonic interharmonic DC offset PLL (HIHDO PLL) [9, 16], and the less complex disturbance rejection PLL (LCDR PLL) [26, 27]. This review paper aims to provide the detailed idea about the PLLs with their schematic diagrams, detailed description, operating principle, the performance abilities along with their respective merits and demerits. The reason behind selection of these five PLLs is that apart from the DDSRF PLL, rest are the most recently developed accurate synchronization methods for grid-integrated DPGS under abnormal and distorted grid operating conditions. The DDSRF PLL is the commonly used and referred PLL in grid-integrated DPGS under normal and faulty grid conditions. The literature studies on review of different conventional and also advanced PLLs can be found in [9, 28–31]. This paper provides a comparison among these advanced PLLs which are the extended and advanced versions of the DDSRF PLL providing an appropriate selection guide to choose the suitable PLL according to the application considering any specific grid operating conditions. The detailed discussion on each individual PLL is showcased in Sect. 2, whereas Sect. 3 presents the comparative study of the PLLs based on their performance abilities followed by the conclusion in Sect. 4.

2 Detailed Review of the Recently Developed Advanced Three-Phase PLLs

The classical $\alpha\beta$ PLL [32–34] and the SRF or dq PLL [9, 35, 36] operate efficiently in balanced operating grid situations whereas estimate inaccurately under distorted grid conditions like faults, interharmonics, DC offsets, and harmonics. A DDSRF PLL is better than SRF PLL [37] that is an equivalent of DSOGI PLL [38–40] operates properly in unbalanced grid faults leading to accurate extraction of phase angle by rejecting the double-frequency oscillations impact. Still, the DDSRF PLL leads to higher frequency overshoots which makes it prone to the effects of interharmonics, harmonics, and the DC offsets. The hybrid $d\alpha\beta$ PLL [41] decreases the increased overshoot effect in DDSRF PLL though having other similar problems like the DDSRF PLL.

A new multi-sequence harmonic decoupling cell PLL (MSHDC PLL) [25] mitigates the selective lower order harmonics with an improved dynamic response with a higher computational complexity because of larger numbers of the dq transformation modules. To overcome this drawback, the DN $\alpha\beta$ PLL [2] has an equal compensation same as the MSHDC PLL but with lower computational complexity. The DN $\alpha\beta$ PLL still has higher complexity. The foremost disadvantages of the MSHDC PLL and DN $\alpha\beta$ PLL are that in their cases, previous knowledge about the harmonics and interharmonics aimed for compensation is required. Both of these PLLs are also sensitive to the DC offset and interharmonics. So, two recently developed advanced

PLLs based on DDSRF PLL concept used for mitigation of harmonics along with interharmonics and also DC offset have been proposed as HIHDO PLL [16] and LCDR PLL [27].

2.1 Decoupled Dual SRF PLL (DDSRF PLL)

A DDSRF PLL [22] uses two numbers of SRF modules rotating at dissimilar angular speeds which are $+\omega$ speed (fundamental positive sequence SRF module) and $-\omega$ speed (negative sequence SRF module). The DDSRF PLL is represented in Fig. 1 where each SRF module transforms the utility grid voltage $v_{\alpha\beta}$ to the v_{dq}^{+1} positive sequence and negative sequence v_{dq}^{-1} . In the SRF transformations, input signal having more than one fundamental frequency element is converted with a definite angular speed resulting as an undesirable oscillation in the converted components as an impact of residual frequency components [9]. So, after the transformation effect on each SRFs, -2ω and $+2\omega$ oscillations are detected in the v_{dq}^{+1} and v_{dq}^{-1} grid vectors. The -2ω fluctuation of v_{dq}^{+1} is an impact of negative sequence component with $+\omega$ speed transformation and vice versa that is represented by the following equations:

$$v_{dq}^{+1} = [T_{dq}^{+1}] v_{\alpha\beta} = V^+ \begin{bmatrix} 1 \\ 0 \end{bmatrix} + V^- \begin{bmatrix} \cos(-2\omega t) \\ \sin(-2\omega t) \end{bmatrix} \quad (1)$$

$$v_{dq}^{-1} = [T_{dq}^{-1}] v_{\alpha\beta} = V^- \begin{bmatrix} 1 \\ 0 \end{bmatrix} + V^+ \begin{bmatrix} \cos(2\omega t) \\ \sin(2\omega t) \end{bmatrix} \quad (2)$$

$$[T_{dq}^n] = \begin{bmatrix} \cos(n\theta) & \sin(n\theta) \\ -\sin(n\theta) & \cos(n\theta) \end{bmatrix} \quad (3)$$

where $[T_{dq}^n]$ is the dq transformation matrix using PLL estimated angle θ as mentioned in Eq. (3) and $v_{\alpha\beta}$ is also calculated from the three-phase utility grid voltage v_{abc} by using Eq. (4). Accordingly, the transformed grid voltage vectors (v_{dq}^{+1} and v_{dq}^{-1}) are given as an input to the decoupling cells networks (DeCs) for removing oscillations by producing oscillations-free grid voltage vectors as v_{dq}^{+1*} and v_{dq}^{-1*} as shown in Eqs. (5) and (6). The structural presentation of the DeC is portrayed in Fig. 2.

$$v_{\alpha\beta} = \frac{2}{3} \begin{bmatrix} 1 & -\frac{1}{2} & -\frac{1}{2} \\ 0 & \frac{\sqrt{3}}{2} & -\frac{\sqrt{3}}{2} \end{bmatrix} v_{abc} \quad (4)$$

$$v_{dq}^{+1*} = v_{dq}^{+1} - [T_{dq}^{+2}] v_{dq}^{-1} \quad (5)$$

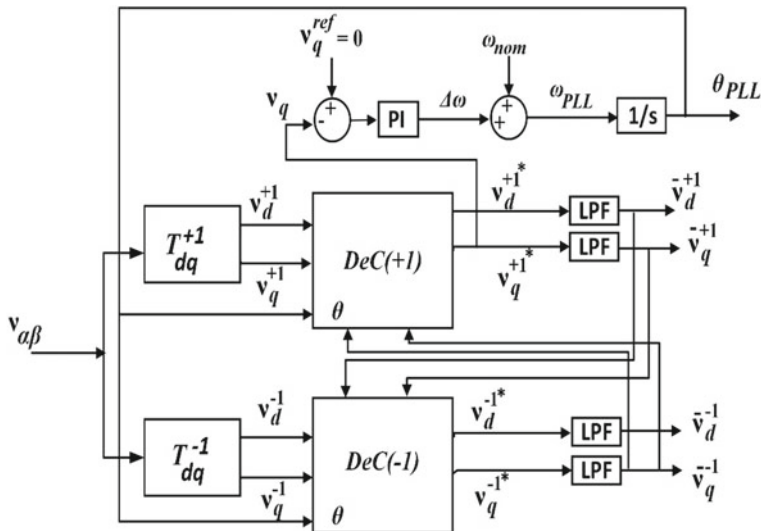


Fig. 1 Structural diagram of DDSRF PLL

$$v_{dq}^{-1*} = v_{dq}^{-1} - \left[T_{dq}^{-2} \right] v_{dq}^{+1*} \quad (6)$$

The oscillations-deprived q component of the resultant positive sequence voltage vector v_{dq}^{+1*} is passed through the phase detector of dq PLL. The DDSRF PLL accurately performs during unbalanced and balanced grid faults, frequency variations, and phase jumps having faster system dynamics still being not immuned to voltage interharmonics, DC offset, and harmonics resulting to higher frequency overshoot during faults.

2.2 Multi-sequence Harmonic Decoupling Cell PLL (MSHDC PLL)

MSHDC PLL [25] is primarily a combination of $\alpha\beta$ PLL and the MSHDC network which offers a better dynamic response by attenuating the undesirable oscillations. MSHDC module mitigates the oscillations present in the fundamental positive sequence grid voltage. MSHDC PLL exhibits an accurate and fast response by improving the quality of power being injected during abnormal grid conditions. It performs appropriately under both the balanced and unbalanced grid fault situations.

Abnormality in the grid conditions represents the rotating grid voltage vectors utilized to decouple for estimating the voltage vectors efficiently and accurately containing the DC and oscillatory terms. MSHDC PLL estimates the desirable DC components by attenuating the oscillations [25]. The MSHDC module basically

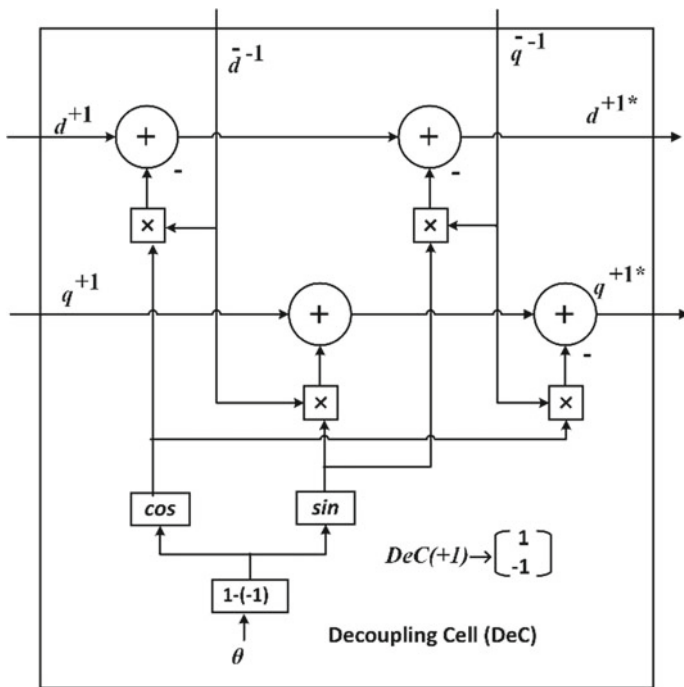


Fig. 2 Internal structure of the single decoupling cell (DeC)

utilizes crossfeedback deduction method making first order-based low pass filter (LPF) to ensure improved stability. The diagram of the MSHDC PLL as illustrated in Fig. 3 detects the positive sequence grid voltage component dynamically and rapidly to produce an oscillation deprived positive sequence v_{dq}^{+1} voltage signal to the $\alpha\beta$ PLL. It cancels out the oscillations and significant harmonics as presented in Fig. 3. The DN $\alpha\beta$ PLL [2] is a reduced version of the original extended version of DDSRF PLL that is the MSHDC PLL in dq frame with a decoupling capability that is mathematically expressed as below where n indicates desirable component, whereas m stands for all values excluding n :

$$v_{dq}^{*n} = [T_{dq}^n]v_{\alpha\beta} - \sum_{m \neq n} \left\{ T_{dq}^{(n-m)} \right\} \bar{v}_{dq}^{*m} \tag{7}$$

2.3 Decoupling Network in A β Frame PLL (DN $\alpha\beta$ PLL)

DN $\alpha\beta$ PLL [2] is the extended version of DDSRF PLL for the elimination of grid harmonics employed in $\alpha\beta$ reference frame and is presented in Fig. 4. The DN $\alpha\beta$

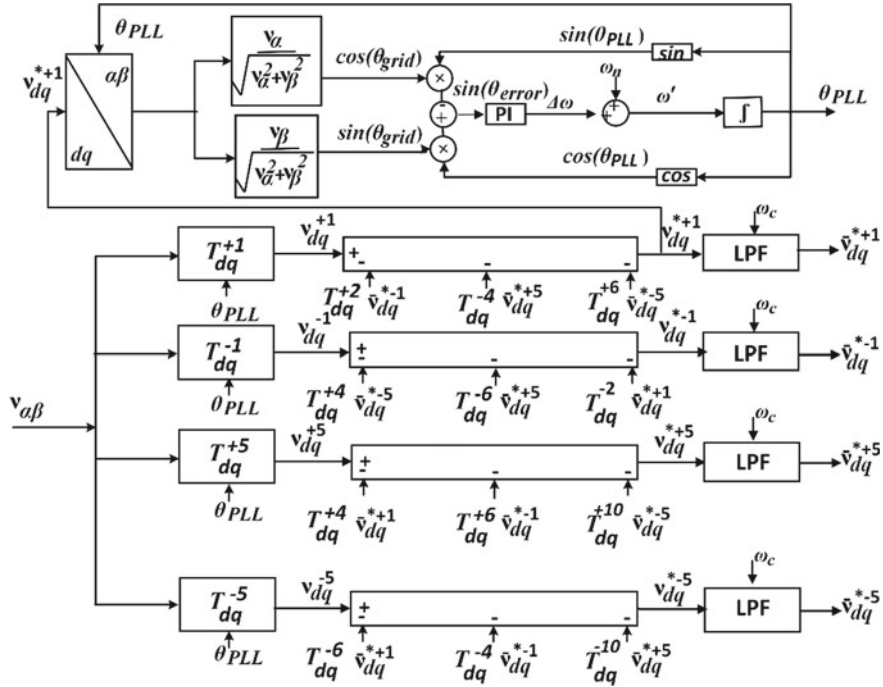


Fig. 3 Structural diagram of MSHDC PLL

PLL exhibits insensitivity to grid unbalanced faults and harmonics. The DN $\alpha\beta$ PLL comprises of the decoupling network (DN) which consists of several decoupling cells (DeCs) which are already pre-defined to specific voltage or harmonic components for extraction and compensation. Contrasting to DDSRF PLL, the utility voltage is transformed by the selective SRFs for obtaining the fluctuations on the specified converted vectors being decoupled by respective DeCs which are attained by the mathematical Eqs. (8) and (9), where n represents the desirable sequence, whereas m indicates all other grid voltage components. As an instance, an unbalanced voltage with the +5th and -7th harmonic distortions, for getting the desirable sequence of +1, $n = +1$, and $m = +5, -7$. $F(s)$ as shown in Eq. (10) signifies the use of LPF for removing the remaining oscillations there by feeding back the resulting filtered decoupled vectors $v_{\alpha\beta}^{*m}$ to the decoupling network as presented in Fig. 2.

$$v_{\alpha\beta}^{*n} = \left[v_{\alpha\beta} - \sum_{m \neq n} [T_{dq}^{-m}] [F(s)] [T_{dq}^m] v_{\alpha\beta}^{*m} \right] \quad (8)$$

$$v_{dq}^{*n} = [T_{dq}^n] v_{\alpha\beta}^{*n} = [T_{dq}^n] \left[v_{\alpha\beta} - \sum_{m \neq n} [T_{dq}^{-m}] [F(s)] [T_{dq}^m] v_{\alpha\beta}^{*m} \right] \quad (9)$$

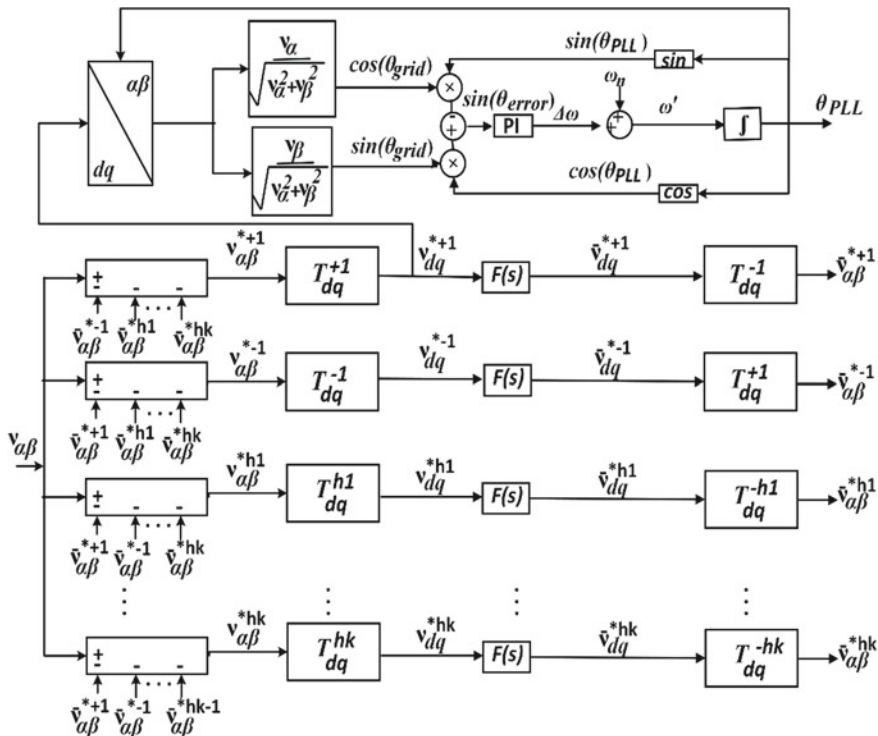


Fig. 4 Structural diagram of DNαβ PLL

$$F(s) = \begin{bmatrix} \frac{\omega_{cf}}{s+\omega_{cf}} & 0 \\ 0 & \frac{\omega_{cf}}{s+\omega_{cf}} \end{bmatrix} \quad (10)$$

The suitable cut-off frequency (ω_c) selection is important to ensure proper subtraction operations. The ideal value of ω_{cf} for negative and positive sequence components DeCs is set as $\omega/\sqrt{2}$ where $\omega = 2\pi 50$ rad/s is the fundamental main grid frequency. The ideal cut-off frequency range of the harmonic block is $0.3\omega \leq \omega_{cf} \leq 0.7\omega$. DNαβ PLL is capable of eliminating selected lower order harmonics by pre-tuning of DeCs on the basis of prior knowledge to target specific harmonics compensation. More harmonics compensation increases complexity as more number of DeCs are needed. DNαβ PLL is also not immunized to the grid voltage DC offset and inter-harmonics. DNαβ PLL is a simplified version of the MSHDC PLL. Both the PLLs have same performance with DNαβ PLL having comparatively low complexity.

2.4 Harmonic Interharmonic DC Offset PLL (HIHDO PLL)

The novel HIHDO PLL [16] as presented in Fig. 5 is capable of compensating grid harmonics, DC offset, grid unbalance, and interharmonics with faster system dynamic response. It uses an innovative mathematically canceling DeC for effectively mitigating the DC offset and also the negative sequence utility voltage. Also, one more simple and effective harmonic interharmonic compensation network is utilized for high-frequency oscillations elimination generated by the grid voltage interharmonics and harmonics. The utility voltage is given as an input to the DeC for the accurate and faster elimination of the negative sequence components and also DC offset as mentioned in Eq. (11).

$$\begin{bmatrix} V_{dq}^{*+1} \\ V_{dq}^{*-1} \\ V_{dq}^{*0} \end{bmatrix} = \begin{bmatrix} v_{dq}^{+1} \\ v_{dq}^{-1} \\ v_{dq}^0 \end{bmatrix} - \begin{bmatrix} [0] \\ T_{dq}^{-1-(+1)} \\ T_{dq}^{0-(+1)} \end{bmatrix} \begin{bmatrix} T_{dq}^{+1-(-1)} \\ [0] \\ T_{dq}^{0-(-1)} \end{bmatrix} \begin{bmatrix} T_{dq}^{+1-(0)} \\ T_{dq}^{+1-(0)} \\ [0] \end{bmatrix} \begin{bmatrix} \bar{V}_{dq}^{*+1} \\ \bar{V}_{dq}^{*-1} \\ \bar{V}_{dq}^{*0} \end{bmatrix} \quad (11)$$

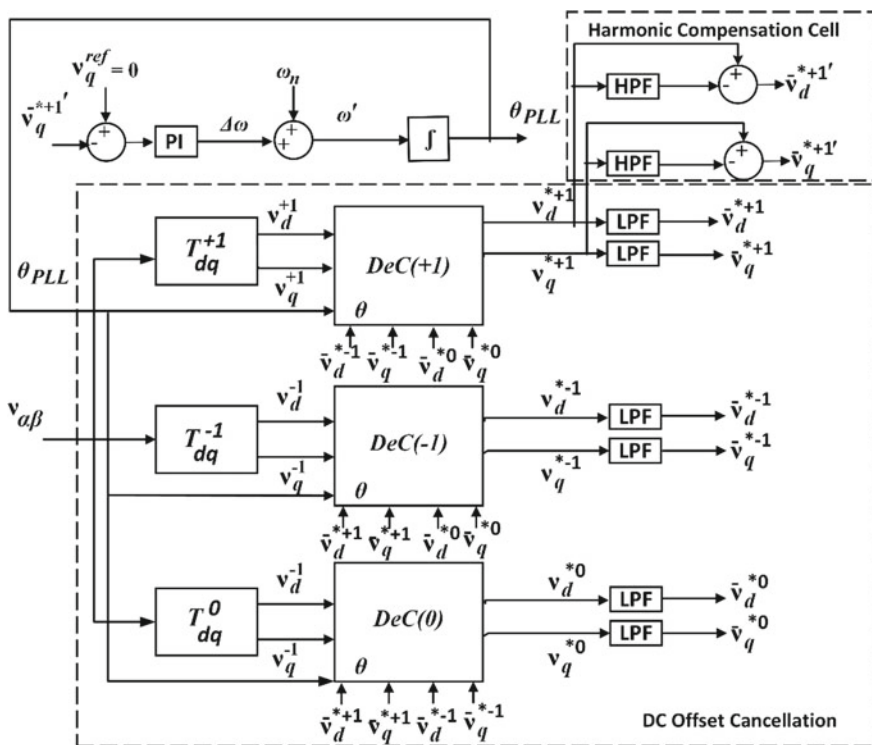


Fig. 5 Structural diagram of HIHDO PLL

Here, $\bar{V}_{dq}^{*n} = F(s)V_{dq}^{*n}$ is the estimated filtered grid voltage, and cut-off frequency selection is not same for each individual component. For the negative and positive sequence components, the optimum cut-off frequency value is $\omega/\sqrt{2}$ with a lower cut-off frequency as $\omega/4.5$ that is needed for the DC component V_{dq}^{*0} extraction [42]. The need for lower cut-off frequency is important to generate the oscillations of DC voltage vectors by the cross-coupled positive sequence and negative sequence components. The extracted positive sequence grid voltage vector V_{dq}^{*+1} for DC offset and unbalance compensation is derived from the DeCs by passing next to the harmonic compensation network making interharmonics and harmonics mitigation effective as stated in Eq. (12). Lastly, the q component of resultant vector \bar{V}_{dq}^{*+1} is then sent to the PLL's phase detector for frequency and phase extraction. The suitable cut-off frequency (ω_H) ranges as $0.2\omega \leq \omega_H \leq 0.45\omega$ for the accurate and speedy dynamic response of high pass filter [16]. The HIHDO PLL needs no prior knowledge of the targeted harmonics and interharmonics for compensation presenting a fast system dynamic response. Any grid harmonics and interharmonics can be compensated by the HIHDO PLL but still as more numbers of Park's transformation modules are used due to its operation in dq frame, the complexity of the controller increases.

$$\bar{V}_{dq}^{*+1} = V_{dq}^{*+1} - \begin{bmatrix} \frac{\omega_{cf}}{s+\omega_H} & 0 \\ 0 & \frac{\omega_{cf}}{s+\omega_H} \end{bmatrix} V_{dq}^{*+1} \quad (12)$$

2.5 Less Complex Disturbance Rejection PLL (LCDR PLL)

Lately, the modification of HIHDO PLL has led to generation of the LCDR PLL [27] which offers superior performance abilities with lower complexity though being same as the HIHDO PLL. The development of the LCDR PLL utilizes a less mathematically complex DC offset mitigating module in dq frame that is depicted in Fig. 6. The governing equation of the developed LCDR PLL is presented as below:

$$\bar{V}_{dq}^{n*} = \begin{bmatrix} T_{dq}^{-n} \end{bmatrix} \left(v_{\alpha\beta} - \sum_{m \neq n} V_{\alpha\beta}^{-m'} \right) \quad (13)$$

The \bar{V}_{dq}^{+1*} found from Eq. (13) is sent to the harmonic compensation module [same as (12)] for oscillations mitigation that are produced by the harmonics and interharmonics disturbances. The output \bar{V}_{q-p}^{+1*} is then fed to the PLL's phase detector to extract the desirable phase angle and grid frequency. Consequently, the LCDR PLL works efficiently under various distorted grid conditions like imbalanced grid faults, interharmonics, DC offset, and grid voltage harmonics with a reduction in the computational complexity with quicker dynamic response. According to the

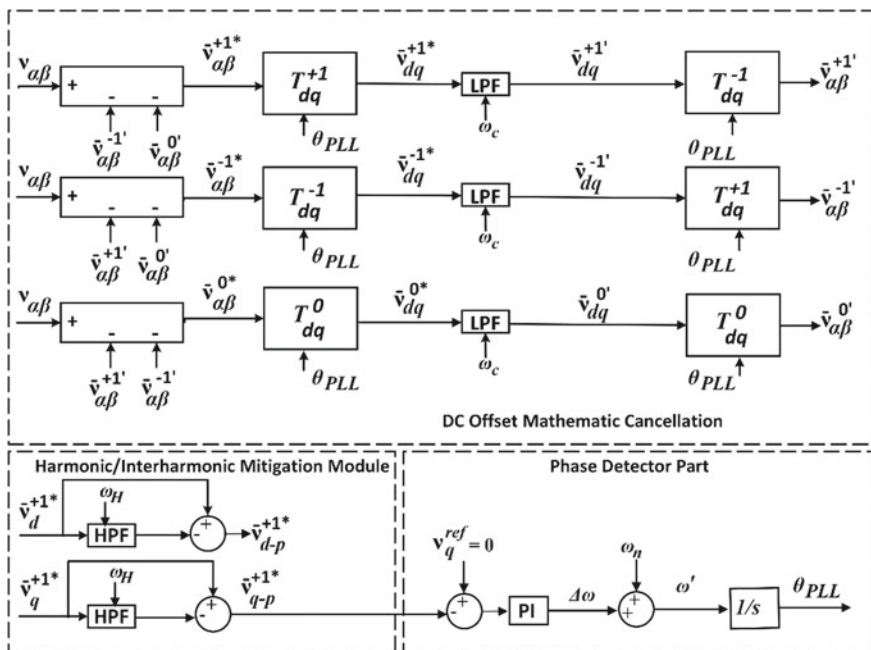


Fig. 6 Structural diagram of LCDR PLL

performing capabilities, lower complexity, and faster dynamic response, LCDR PLL is concluded to be the least complex and most advanced PLL.

3 Performance Comparison of the Three-Phase Advanced PLLs

The performance abilities of various advanced PLLs have been studied, compared, and represented in Table 1. The comparative performance analysis has been done and summarized in terms of PLL's dynamic response, complexity, operation during adverse circumstances, overshoot present in estimated frequency/phase, frequency changes, and three-phase grid blackout or faults. The DDSRF PLL needs least computation among all PLLs though not immuned to the distorted utility grid environments. The MSHDC PLL and $DN\alpha\beta$ PLL exhibit equal performance though the MSHDC PLL has comparatively less complexity. The key demerit of the $DN\alpha\beta$ PLL is that it has still significant complications in comparison to other PLLs as it is only immuned to selective harmonics and has higher overshoot and imprecise response during severe faults. The LCDR PLL still same as HIHDO PLL is found as the simplest, advanced, and fastest PLL with an advantage of compensating any DC offset, interharmonics,

Table 1 Performance comparison among the advanced PLLs

PLL methods		DDSRF PLL [22]	MSHDC PLL [25]	DN $\alpha\beta$ PLL [2]	HIHDO PLL [16]	LCDR PLL [27]
Frequency/phase overshoot		High	High	High	Low	Low
Dynamic response		Low	High	High	Low	Low
Design complexity		Low	High	High	Low	Low
Non-nominal frequency operation		Yes	Yes	Yes	Yes	Yes
Three-phase blackout		Yes	No	No	Yes	Yes
Accurate estimation during	Unbalanced faults	Yes	Yes	Yes	Yes	Yes
	Harmonics	No	Selected	Selected	Yes	Yes
	Interharmonics	No	No	No	Yes	Yes
	DC offset	No	No	No	Yes	Yes

and harmonics existing in grid voltage with a faster system dynamic response without any need of prior knowledge.

4 Conclusion

This paper aims on providing a review of various latest PLLs based on the modification of the DDSRF PLL. Their detailed review has been studied and also compared depending on modification of each PLL’s performance, system dynamic response, and computing complication. Their detailed explanation with operational principle and system performance with the merits and demerits have been showcased. The review provides a conclusion that the LCDR PLL is the superior among all being the best-performing advanced PLL with low complexity. The grid-integrated DPGS control and operation through PLLs must be very accurate and fast (lower settling time) in response to different grid conditions like balanced or unbalanced faults, grid harmonics, DC offset, and interharmonics (Table 1). The DDSRF PLL can be preferred due to its fastest response, but the HIHDO PLL or LCDR PLL was found to be the best choice from the PLL selection guide tackling all kind of grid distortions.

References

1. REN21, P.S.: Renewables 2017 global status report. In: Secretariat Renewable Energy Policy Network for the 21 century (2017)
2. Hadjidemetriou, L., Kyriakides, E., Blaabjerg, F.: A robust synchronization to enhance the power quality of renewable energy systems. *IEEE Trans. Ind. Electron.* **62**(8), 4858–4868 (2015)

3. Teodorescu, R., Liserre, M., Rodriguez, P.: Grid converters for photovoltaic and wind power systems. Wiley (2011)
4. Yang, S., Lei, Q., Peng, F.Z., Qian, Z.: A robust control scheme for grid-connected voltage-source inverters. *IEEE Trans. Industr. Electron.* **58**(1), 202–212 (2010)
5. Blaabjerg, F., Liserre, M., Ma, K.: Power electronics converters for wind turbine systems. *IEEE Trans. Ind. Appl.* **48**(2), 708–719 (2011)
6. Arul, P.G., Ramachandaramurthy, V.K., Rajkumar, R.K.: Control strategies for a hybrid renewable energy system: a review. *Renew. Sustain. Energy Rev.* **42**, 597–608 (2015)
7. Ali, Z., Christofides, N., Hadjidemetriou, L., Kyriakides, E.: Improved transient performance properties of distributed generation grid side converter current controller under grid voltage harmonic distortion and unbalanced faults. In: *IECON 2017–43rd Annual Conference of the IEEE Industrial Electronics Society*, pp. 7783–7788. IEEE (2017)
8. Nejabatkhah, F., Li, Y.W., Wu, B.: Control strategies of three-phase distributed generation inverters for grid unbalanced voltage compensation. *IEEE Trans. Power Electron.* **31**(7), 5228–5241 (2015)
9. Ali, Z., Christofides, N., Hadjidemetriou, L., Kyriakides, E., Yang, Y., Blaabjerg, F.: Three-phase phase-locked loop synchronization algorithms for grid-connected renewable energy systems: a review. *Renew. Sustain. Energy Rev.* **90**, 434–452 (2018)
10. Hassan, F., Kumar, A., Pati, A.: Recent advances in phase locked loops for grid connected systems: a review. In: *IEEE Delhi Section Conference (DELCON)*, pp. 1–6. IEEE (2022)
11. Guo, X.Q., Wu, W.Y., Gu, H.R.: Phase locked loop and synchronization methods for grid-interfaced converters: a review. *Przeł. Elektrotechniczny* **87**(4), 182–187 (2011)
12. Luna, A., Citro, C., Gavriluta, C., Hermoso, J., Candela, I., Rodriguez, P.: Advanced PLL structures for grid synchronization in distributed generation. *Renew. Energy Power Qual. J.* 1747–1756 (2012)
13. Luna, A., Rocabert, J., Candela, I., Rodriguez, P., Teodorescu, R., Blaabjerg, F.: Advanced structures for grid synchronization of power converters in distributed generation applications. In: *IEEE Energy Conversion Congress and Exposition (ECCE)*, pp. 2769–2776. IEEE (2012)
14. Guerrero-Rodríguez, N.F., Rey-Boué, A.B., Rigas, A., Kleftakis, V.: Review of synchronization algorithms used in grid-connected renewable agents. In: *International Conference on Renewable Energies and Power Quality (ICREPQ)*, pp. 1–6 (2014)
15. Guerrero-Rodríguez, N.F., Rey-Boué, A.B., Bueno, E.J., Ortiz, O., Reyes-Archundia, E.: Synchronization algorithms for grid-connected renewable systems: overview, tests and comparative analysis. *Renew. Sustain. Energy Rev.* **75**, 629–643 (2017)
16. Ali, Z., Christofides, N., Hadjidemetriou, L., Kyriakides, E.: Design of an advanced PLL for accurate phase angle extraction under grid voltage HHs and DC offset. *IET Power Electron.* **11**(6), 995–1008 (2018)
17. de Oliveira, F.M., da Silva, S.A.O., Durand, F.R., Sampaio, L.P., Bacon, V.D., Campanhol, L.B.: Grid-tied photovoltaic system based on PSO MPPT technique with active power line conditioning. *IET Power Electron.* **9**(6), 1180–1191 (2016)
18. Wankhede, S.K., Paliwal, P., Kirar, M.K.: Increasing penetration of DERs in smart grid framework: a state-of-the-art review on challenges, mitigation techniques and role of smart inverters. *J. Circ. Syst. Comput.* **29**(16), 2030014 (2020)
19. Karimi-Ghartemani, M., Mojiri, M., Safaei, A., Walseth, J.A., Khajehoddin, S.A., Jain, P., Bakhshai, A.: A new phase-locked loop system for three-phase applications. *IEEE Trans. Power Electron.* **28**(3), 1208–1218 (2012)
20. Luna, A., Rocabert, J., Candela, J.I., Hermoso, J.R., Teodorescu, R., Blaabjerg, F., Rodriguez, P.: Grid voltage synchronization for distributed generation systems under grid fault conditions. *IEEE Trans. Ind. Appl.* **51**(4), 3414–3425 (2015)
21. Wang, X., Taul, M.G., Wu, H., Liao, Y., Blaabjerg, F., Harnefors, L.: Grid-synchronization stability of converter-based resources—an overview. *IEEE Open J. Ind. Appl.* **1**, 115–134 (2020)
22. Rodríguez, P., Pou, J., Bergas, J., Candela, J.I., Burgos, R.P., Boroyevich, D.: Decoupled double synchronous reference frame PLL for power converters control. *IEEE Trans. Power Electron.* **22**(2), 584–592 (2007)

23. Xiao, P., Corzine, K.A., Venayagamoorthy, G.K.: Multiple reference frame-based control of three-phase PWM boost rectifiers under unbalanced and distorted input conditions. *IEEE Trans. Power Electron.* **23**(4), 2006–2017 (2008)
24. Kamil, H.S., Said, D.M., Mustafa, M.W., Miveh, M.R., Ahmad, N.: Recent advances in phase-locked loop based synchronization methods for inverter-based renewable energy sources. *Indonesian J. Electr. Eng. Comput. Sci.* **18**(1), 1–8 (2020)
25. Hadjidemetriou, L., Kyriakides, E., Blaabjerg, F.: Synchronization of grid-connected renewable energy sources under highly distorted voltages and unbalanced grid faults. In: *IECON 2013–39th Annual Conference of the IEEE Industrial Electronics Society*, pp. 1887–1892. IEEE (2013)
26. Ali, Z., Christofides, N., Saleem, K., Polycarpou, A., Mehran, K.: Performance evaluation and benchmarking of PLL algorithms for grid-connected RES applications. *IET Renew. Power Gener.* **14**(1), 52–62 (2020)
27. Ali, Z., Christofides, N., Lestas, M.: A robust and less-complex phase-locked loop algorithm immune to electricity grid disturbances for RES applications. In: *IEEE Conference on Decision and Control (CDC)*, pp. 6711–6716. IEEE (2018)
28. Golestan, S., Guerrero, J.M., Vasquez, J.C.: Three-phase PLLs: a review of recent advances. *IEEE Trans. Power Electron.* **32**(3), 1894–1907 (2016)
29. Jaalam, N., Rahim, N.A., Bakar, A.H.A., Tan, C., Haidar, A.M.: A comprehensive review of synchronization methods for grid-connected converters of renewable energy source. *Renew. Sustain. Energy Rev.* **59**, 1471–1481 (2016)
30. Mohamed Hariri, M.H., Mat Desa, M.K., Masri, S., Mohd Zainuri, M.A.A.: Grid-connected PV generation system—components and challenges: a review. *Energies* **13**(17), 4279 (2020)
31. Gawhade, P., Ojha, A.: Recent advances in synchronization techniques for grid-tied PV system: a review. *Energy Rep.* **7**, 6581–6599 (2021)
32. Teodorescu, R., Blaabjerg, F.: Flexible control of small wind turbines with grid failure detection operating in stand-alone and grid-connected mode. *IEEE Trans. Power Electron.* **19**(5), 1323–1332 (2004)
33. Hu, B., Nian, H., Li, M., Liao, Y., Yang, J., Tong, H.: Impedance characteristic analysis and stability improvement method for DFIG system within PLL bandwidth based on different reference frames. *IEEE Trans. Ind. Electron.* (2022)
34. O'Rourke, C.J., Qasim, M.M., Overlin, M.R., Kirtley, J.L.: A geometric interpretation of reference frames and transformations: dq0, clarke, and park. *IEEE Trans. Energy Convers.* **34**(4), 2070–2083 (2019)
35. Golestan, S., Ebrahimzadeh, E., Wen, B., Guerrero, J.M., Vasquez, J.C.: dq-frame impedance modeling of three-phase grid-tied voltage source converters equipped with advanced PLLs. *IEEE Trans. Power Electron.* **36**(3), 3524–3539 (2020)
36. Babu, Y.N., Padhy, N.P.: Investigation of damping effect of PLL on low-frequency harmonic stability of grid-tied inverter with $\alpha\beta$ and dq current control schemes. *IEEE J. Emerg. Sel. Topics Power Electron.* (2021)
37. Sevilmiş, F., Karaca, H.: Performance analysis of SRF-PLL and DDSRF-PLL algorithms for grid interactive inverters. *Int. Adv. Res. Eng. J.* **3**(2), 116–122 (2019)
38. Reyes, M., Rodriguez, P., Vazquez, S., Luna, A., Teodorescu, R., Carrasco, J.M.: Enhanced decoupled double synchronous reference frame current controller for unbalanced grid-voltage conditions. *IEEE Trans. Power Electron.* **27**(9), 3934–3943 (2012)
39. Sevilmiş, F., Karaca, H.: Performance enhancement of DSOGI-PLL with a simple approach in grid-connected applications. *Energy Rep.* **8**, 9–18 (2022)
40. Xin, Z., Wang, X., Qin, Z., Lu, M., Loh, P.C., Blaabjerg, F.: An improved second-order generalized integrator based quadrature signal generator. *IEEE Trans. Power Electron.* **31**(12), 8068–8073 (2016)
41. Hadjidemetriou, L., Kyriakides, E., Blaabjerg, F.: A new hybrid PLL for interconnecting renewable energy systems to the grid. *IEEE Trans. Ind. Appl.* **49**(6), 2709–2719 (2013)
42. Ali, Z.: Diversifying the role of RES with advanced converter functionalities and performance for improved grid support and operation. PhD dissertation, Electrical Engineering Department, Frederick University, Nicosia, Cyprus (2018)

Performance Assessment and Evaluation of a 52-kW Solar PV Plant in India



J. Divya Navamani, A. Lavanya, Yash Vardhan Bhargava,
Divya Kumar Gupta, and Gaurav Singh

1 First Section

India's electricity consumption was 1381.827 billion units (BU), making it the third most energy consuming nation in the world. The Indian energy scenario is hugely dominated by exhaustible fossil fuels. These sources contribute to about 67% of India's total generation capacity of 383.37 GW [1]. The share of various energy sources in India's generation capacity is shown in Fig. 1. The emissions from these fossil fuels are one of the major causes of air pollution. About 75% of the world's air pollution is caused by these emissions [1]. Therefore, an alternative and greener source of energy, which is sustainable, is the need of the hour. Renewable energy sources (RESs) are the near perfect solution to the above problem. They are sustainable, abundant, and pollution-free sources of energy [2]. Due to these advantages, a lot of notable efforts are being made to utilize RES more effectively and efficiently to cater for the world's energy needs. Significant efforts are made in this direction in India. These include formulation of policies that encourage the use of RES, development of necessary infrastructure and technology. By 2030, India aims to amass its generation from RES to 175 GW [1].

The country has a promising potential in RES. About 22.5% of its generation capacity is dedicated to RES. The major RE sources are solar, wind, hydro and biomass, etc. [3]. Solar photovoltaic (PV) is currently leading the renewable energy (RE) market. The boom in solar PV technology can be attributed to the decrease in cost of mass production and more importantly the increased efficiencies of the PV modules [4]. India has a great solar potential, due to its tropical location. It receives an annual solar radiation of 4.7 kWh/m². Almost, 45% of the country receives 3000 h of sunlight. So, it is a great source of decarbonized energy. It has a solar PV

J. Divya Navamani (✉) · A. Lavanya · Y. V. Bhargava · D. K. Gupta · G. Singh
Department of Electrical and Electronics Engineering, SRM Institute of Science and Technology,
Kattankulathur, India
e-mail: divyanaj@srmist.edu.in

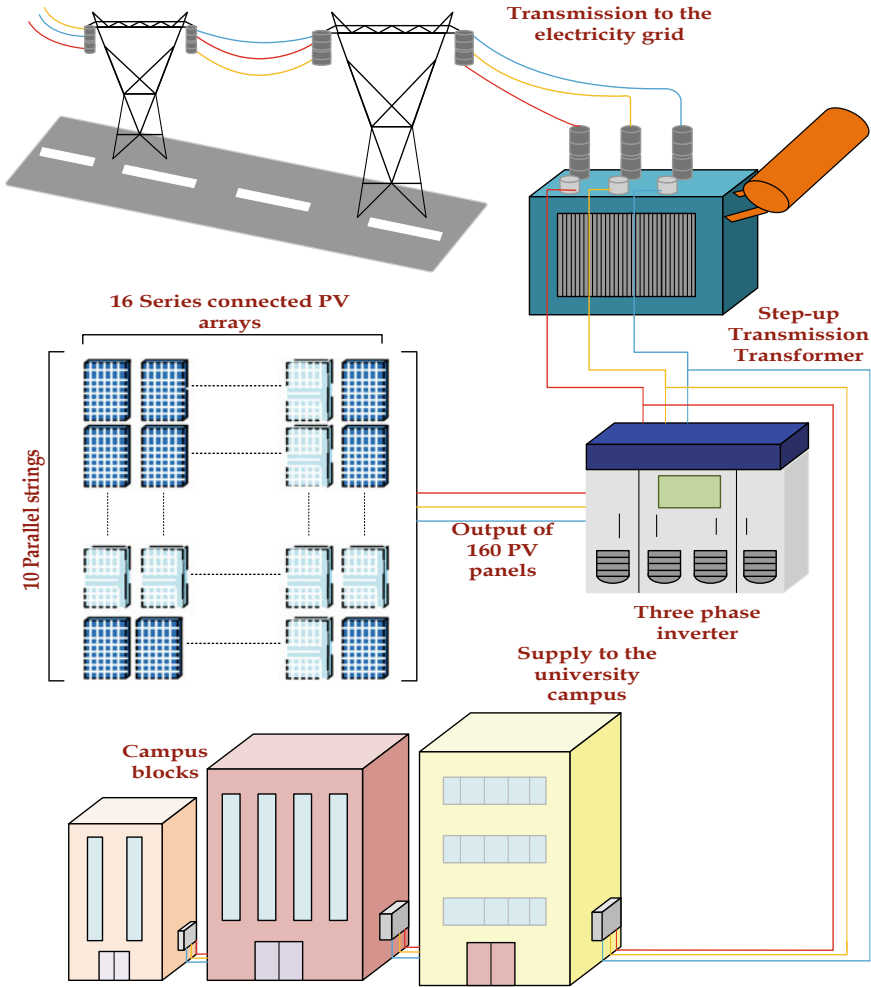


Fig. 1 Layout of the 52 kW PV plant

installed capacity of 39,083 MW as of 2021. India ranks third among the countries producing maximum solar energy, dominating 9% of the global solar market [5, 6]. This study aims to analyze and evaluate an ultra-high-power PV plant using simulation and compare the results with the specifications mentioned in IEC 61724 standards. For this case study, a 52 kW plant situated in the SRMIST campus is considered. Now, in order to extract electricity form sunlight, solar panels are used. When a large number of such PV panels are collected and connected to produce electrical energy, they form a PV plant [4]. PV plants have several merits such as easy and noiseless operation, inexhaustible fuel and pollution-less generation [5]. However, the performance and efficiency of PV plants are deeply affected by

many parameters and ambient conditions. Parameters such as availability factor (AF), capacity factor (CF), yield factor (YF), final yield (FY), and performance ratio (PR) are the most crucial in evaluating and analyzing the plant's utility and robustness. Various ambient conditions such as surrounding temperature, solar irradiance, and wind speed have a great impact on a PV plant's performance. Apart from these, the module technology used, their associated efficiencies and the tilt of the panel are also essential [4, 7]. In this regard, this study has the following objectives: (1) To assess and evaluate an ultra-high-power solar PV plant, on various parameters such as AF, CF, PR, YF, and module technology used, tilt, etc. (2) To estimate the efficiency and robustness of the plant, by software simulation and IEC 61724 standards [8]. The rest of the paper is structured as follows. Section 1.1 contains the literature survey, followed by Sect. 2, which discusses the plant description and its geographical overview along with the proposed methodology. Section 3 covers the performance evaluation of the plant which is followed by Sect. 4 which discusses the obtained results and its subsequent analysis. Section 5 concludes the paper and contains conclusion and summary of the work presented.

1.1 Literature Survey

The recent boom in the PV technology and the popularity of RES, the number of PV plants has increased rapidly. This has triggered a new field in the academic community as well. Several researchers and academicians have attempted to study, assess, and evaluate PV plants of various sizes. Some of them are discussed in this section. Martin-Martínez et al. [4] attempted a study of six large PV plants located in Spain. The authors discussed various factors that affect the performance of a PV plant significantly. The performance parameters were calculated according to the accumulated data, and the plant performance was thus evaluated. Parameters such as plant degradation rate (DR) and PR were considered for the study. Along with these, the effect of panel technology used; mounting techniques used, and the location of the plant was taken into account to estimate the plant's performance. A performance comparison among various cell technologies was presented. Moreover, ambient conditions such as temperature and wind speed were incorporated in the analysis. The authors concluded that PR and wind speed along with module technology and cell types are crucial in determining the plant's performance.

A 1 MWp solar PV plant was considered in [5]. In the study, the AF of the plant was found out to have an integral impact of the plant performance and its utility. It was found that AF keeps on varying and gives an indication about the plant's robustness and reliability. AF is a measure of the interruption of power generation in a plant's operation. The inverter start-time and end-time were analyzed to calculate the AF. The results obtained suggested that the plant did not produce any power for 4.3–8% of its operational time. Researchers in [2] studied three PV plants situated in Morocco, each of 2 kWp capacity to analyze and assess their performance.

A similar attempt was made by Satsangi et al. [7] where a 40 kWp grid-interactive PV plant located in Agra, India was assessed and evaluated. Parameters such as AY, FY, CF, and PR were taken as performance indicators. The methodology used was the calculation of efficiencies of the individual plant components to estimate the plant utility and efficiency. A comprehensive study of a grid-integrated 1 MWp PV plant located in Andhra Pradesh, India was presented in [6]. In this case study, the real-time monitoring of the plant data was done. Plant's energy output, SI, YF, CF, and PR were the concerned performance parameters. The period for data collection was an entire year of operation. The plant was modeled and simulated using three software, namely PV Watts, PV syst, and PVGIS, and the generated results were compared. The error deviation in the three software was also treated. Apart from that, the PV technology employed in the modules, their mounting techniques, tilt and azimuth were also considered in the plant evaluation. Another notable attempt was made by authors in [9], where a 5 MWp grid-connected PV plant located in Tamil Nadu, India, was assessed and evaluated. An estimation of the concerned plant's efficiency was done by surveying the individual efficiencies of the plant components such as inverters and module strings. The parameters examined were AY, reference yield (RY), PR, CF, and capture loss. In addition to these, module technology and inverter efficiencies were also considered. RET Screen software was used to simulate and validate the calculated efficiencies. Study suggested that the incorporation of MPPT-based inverter would boost the plant output. Kumar and Sudhakar [10] studied a 10 MW plant located in India. The plant was connected to the 33 kV grid. The accumulated plant data were employed in calculating specifications such as AY, RY, PR, CF, FY, and inverter efficiency. The effect of conditions such as SI and temperature on the plant's peak power output was also analyzed. PV syst and PVGIS software were used to model the plant and validate the outcomes. In the study, the authors found that the peak output of the plant was 10.3 MW, and minimum output came out to be 40.8 kW. The plant had an ability of 99%, indicating that the plant had a sturdy operation. A study similar to [4, 6] is presented in [11], in which an airport-based 281 kWp PV plant situated in Lesotho was evaluated. The considered parameters were AY, PR, inverter efficiency, CF, FY, capture losses, and array efficiency. For further analysis, tilt and positioning of the PV modules was also studied. PR was taken to be the chief performance indicator in this case study. A 960 kWp PV plant located in Italy was studied by Malvoni et al. [12].

2 Plant Description and Proposed Methodology

2.1 Plant Description

The plant considered for this case study is located in the southern Indian state of Tamil Nadu. It is situated in SRM Institute of Science and Technology, Kattankulathur. The plant is installed in the Science and Humanities block of the "green" campus. It was

commissioned and integrated with the southern grid on 20th November 2019. It has total installed capacity of 52 kWp, spread over an area of 304 m². The geographical coordinates are (12.4912° N, 80.0466° E). Due to the climatic nature of its location, the plant is exposed to temperatures ranging from 38 to 21 °C. The weather is generally hot and humid due to coastal proximity. A fair amount of sunshine is received, with an average of 12.12 h daily. The place also experiences sufficient amount of rainfall ranging from a maximum of 360 cm in November to the minimum of about 10 cm in March. Multi-crystalline-type PV panels with an individual wattage of 325 W are used. There are 10 strings of PV panels, each string having 16 panels connected in series to form an array. The tilt of the panels is made optimum, by setting it equal to the latitude, which is 13°. The panels have an efficiency of 16.7%. A 50 kW/55 kVA three-phase inverter is employed for the DC–AC conversion. The peak inverter efficiency is 98.6%. It has a DC–AC ratio of 1.2. The inverter also has an MPP tracker.

2.2 Proposed Methodology

The proposed methodology for this study is shown in Fig. 2. The initiation is done by the collection of the relevant plant data and particulars. These include the global irradiance (GI), diffused irradiance (DI), yield of the plant, and module parameters for the year 2020. The next step is the mathematical calculation of performance specifications from the accumulated data. For this step, parameters such as CF, PR, AF, and RY are considered. The effect of the ambient conditions such as wind speed and temperature on the plant performance is studied. This is followed by the calculation and verification of the performance parameters by using PV Watt's simulation. Next step is the study of the MPPT techniques employed in the plant or the inverter. The last step is the comparison and analysis of the obtained and simulated results to estimate the plant's performance and robustness and compare it with the guidelines in the IEC 61724 standards. The plant specification is presented in Table 1.

3 Plant Performance Evaluation

In this section, the plant's performance is evaluated by calculating various performance parameters, namely PR, CF, RY, and AF. This is carried out in two ways.

Firstly, the plant data are collected by PV Watt's software using the plant; PV panel specification is listed in Table 1. The data are for an entire year. This data are utilized for the calculation of the aforementioned parameters using their mathematical definitions, on both monthly and annual basis. After this, a model of the plant with the listed specifications is simulated using PV syst software.

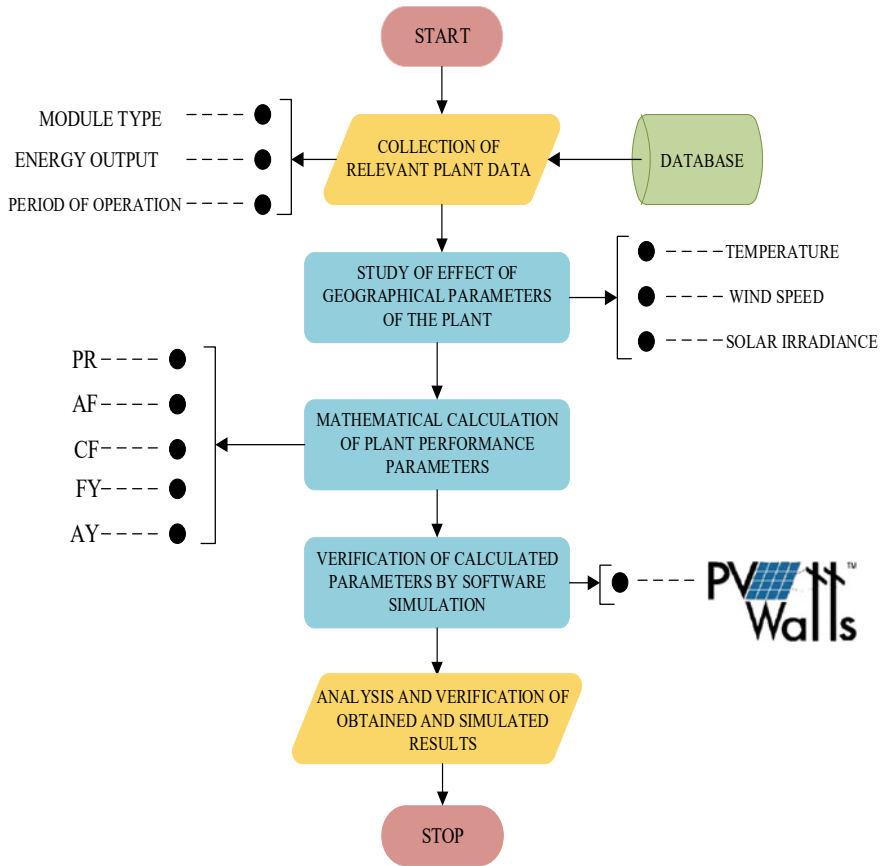


Fig. 2 Proposed methodology

Table 1 Plant specifications

Plant power	52 kWp	Panel type	Multi-crystalline
Plant area	304 m ²	Panel wattage	325 W
Commissioning date	November 20, 2019	No. of panels	160
Location	Potheri, Kattankulathur, TN	Panel tilt	13°
Latitude	12.4912°	Module efficiency	16.7%
Longitude	80.0466°	No. of series/parallel connected panels	16/10

3.1 Final Yield (FY)

FY is defined as the ratio of the total real AC power supplied by the plant to the nameplate installed capacity of the plant [2].

Therefore,

$$FY = \frac{\text{Total real AC power supplied}}{\text{Total Installed Capacity}} \quad (1)$$

From the expression, it is evident that FY incorporates the losses associated in the panels and inverter.

3.2 Reference Yield (RY)

RY can be expressed as the ratio of total incident solar radiation to the reference solar irradiance [4]. The reference solar irradiance is 1 kW/m².

Therefore,

$$RY = \frac{\text{Total incident irradiance}}{\text{Reference irradiance}} \quad (2)$$

RY includes all the losses pertaining to the variation in incident irradiance, shading of the panel, and the effect of dust on the panel performance.

3.3 Performance Ratio (PR)

PR is defined as the ratio of the plant's final active energy output in kWh to the product of the plant's installed capacity in kWp and GI in kWh/m² [4]. PR signifies the effect of various losses on the performance of the plant. The losses considered are the panel losses, losses due to the ambient conditions such as temperature and wind speed, shading losses, and wiring losses. It also accounts for the losses occurring in the inverter [2]. Mathematically, PR can be expressed as:

$$PR = \frac{FY}{RY} \quad (3)$$

Firstly, PR is calculated on a monthly basis, using the daily plant data collected from PV Watts. The procedure for the month of January is shown below. The total inverter output for the month of January is 7383.666 kWh, and the total installed capacity is 52 kWp.

So,

$$FY_{Jan} = \frac{7383.666}{52} = 141.993$$

The total incident irradiance on the panel area for January is 184.740 kW/m².

So,

$$RY_{Jan} = 184.740$$

Therefore,

$$PR_{Jan} = \frac{FY_{Jan}}{RY_{Jan}} = \frac{141.993}{184.740} = 0.768 \text{ or } 76.8\%$$

Table 2 shows the FY, RY, PR, CF, AY, ACL, temperature, wind, and CL calculation on the monthly basis for the entire year.

Now, the annual PR for the plant is calculated using the above expressions. The total FY for the plant is 1623.196, and total RY is 2146.293. Therefore, the total PR = $\frac{1623.196}{2146.293} = 0.756$ or 75.6%.

3.4 Capacity Factor (CF)

CF is defined as the ratio of the total actual energy generated by the plant to the total energy that that plant could produce over a specified period of time. It indicates the capacity of the plant that is not being utilized in generating active energy. If the plant's entire generation is equal to its total capacity, then CF will be unity. It also is an estimation of how much increase in the demand, the PV plant can handle in the future.

So,

$$CF = \frac{\text{Total real AC power supplied}}{\text{Total rated capacity} \times \text{Time Period}} \quad (4)$$

The CF calculation for the month of done as follows using the PV Watts data.

The total inverter output for the month of January is 7383.666 kWh, and the total plant capacity is 52 kW. The plant's total possible operating period is 744 h.

Therefore, $CF_{Jan} = \frac{7383.666}{52 \times 744} = 0.1908$ or 19.08%. Now, the total annual AC power supplied by the plant is 84406.219 kWh, and the total operating hours are 8760, and the rated capacity is 52 kW. So, the annual plant CF is,

Table 2 Monthly PV plant parameter measurement and calculation

Month	FY (kWh)	RY (kWh)	PR (%)	CF (%)	AY (kWh)	ACL (kWh)	Temp (°C)	Wind speed (m/s)	CL (kWh)
January	141.993	184.740	76.8	19.08	144.295	40.445	25.85	2.39	2.302
Feb	138.429	184.211	75.1	20.59	140.624	43.587	27.77	2.25	2.195
March	160.065	217.528	73.6	21.51	162.682	54.846	30.47	2.06	2.617
April	150.32	201.647	74.5	20.87	152.803	48.844	30.03	2.00	2.477
May	139.76	186.5	74.9	18.78	142.119	44.438	31.51	2.77	2.35
June	132.6	174.7	75.9	18.42	139.373	35.403	29.79	3.21	6.746
July	124.1	164.1	75.6	16.68	126.412	37.732	30.28	2.88	2.262
Aug	133.10	175.2	75.9	17.89	135.414	39.791	29.23	2.46	2.306
Sep	134.56	177.0	76.0	18.69	136.898	40.121	28.29	2.29	2.329
Oct	125.91	165.5	76.0	16.92	132.229	43.365	28.07	1.59	6.313
Nov	115.46	148.8	77.6	16.03	117.569	31.25	26.85	2.73	2.109
Dec	126.77	164.6	77.0	17.03	128.952	35.682	26.50	2.86	2.179

Table 3 Plant performance comparison

S. No.	Plant study	Year	Period	Size	Location	PR %	CF	AY kWh	RY kWh	FY kWh	Losses kWh
1	Present study	2021	1 year	52 kW	Tamil Nadu	75	18.52	1659.37	2146.293	1623.1	495.50
2	Berwal et al.	2017	7 month	50 kW	Haryana	85	-	-	-	7198.4	-
3	Omkar et al.	2015	1 year	50 kW	Andhra Pradesh	85	10.7	-	-	230	-
4	Singh et al.	2014	3 years	58 kW	Rajasthan	16-98	-	-	-	-	-

$$CF = \frac{84406.219}{52 \times 8760} = 0.1852 \text{ or } 18.52\%.$$

3.5 Array Yield (AY)

AY is defined as the ratio of the total DC output of the PV panel array to the total installed capacity of the plant. It accounts for the losses occurring in the PV panel and before the power is fed to the inverter [7]. Therefore, it can be defined mathematically as follows.

$$AY = \frac{\text{Total DC output of the PV panel}}{\text{Total rated capacity of the plant}} \quad (5)$$

Table 8 presents the monthly AY for the plant.

3.6 Array Capture Losses (ACL)

These losses are comprised of losses that occur due the array conversion losses, shading, soiling, mismatching, and losses due to the ambient temperature. These are mathematically calculated by considering the difference between the RY and the AY, which provides the estimation of the losses occurring in the panel [10, 12].

Therefore,

$$ACL = RY - AY \quad (6)$$

3.7 Conversion Losses (CL)

These are the losses that occur in the inverter, while DC–AC conversion. These are mathematically defined as the difference between AY and FY [9, 11].

Therefore,

$$CL = AY - FY \quad (7)$$

4 Analysis and Comparison of Obtained Results

In this section, the values and the trends of various performance parameters mentioned in the IEC 61724 standards, obtained in the previous section for the present plant, are compared with the parameters of other PV plants located in India. Also, the analysis of the performance evaluation results obtained for the present plant is done.

4.1 Analysis of the Present Plant

In the following text, the variation of the plant parameters such as PR, CF, AY, and RY with temperature, wind and over time for an entire year is presented.

1. **PR:** The monthly variation of PR is shown by the chart in Fig. 3a.

The PR for the plant lies between 73.6 and 77% over the entire year. The maximum PR is recorded in the month of December (77%), whereas the minimum is obtained in March (73.6%). An interesting feature is that in March, monthly FY and RY reach their respective maximum values, but the PR reaches its lowest value. The annual PR is 75.6%

2. **RY:** The monthly RY variation is depicted in Fig. 3b.

The RY for the plant falls in the range of 148.819–217.528 kWh. The maximum RY is obtained in the month of March (217.528 kWh), and the minimum is recorded in the month of November (148.819 kWh). The net annual RY is 2146.293 kWh.

3. **FY:** FY for the plant lies in between 115.46 and 160.065 kWh. The maximum FY is obtained in the month of March, whereas the minimum FY is observed in November. The monthly variation in FY is shown in Fig. 4a. The total annual FY is 1623.196 kWh.
4. **CF:** The monthly CF values for an entire year for the plant are shown in Fig. 4b. The CF values range from 16.03 to 21.51%. The maximum CF was observed in

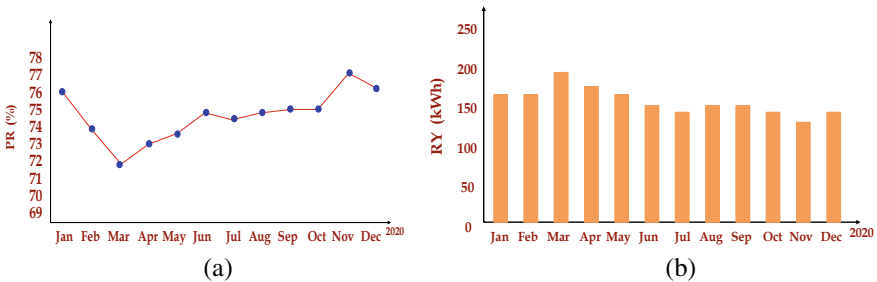


Fig. 3 a Monthly PR values. b Monthly RY values

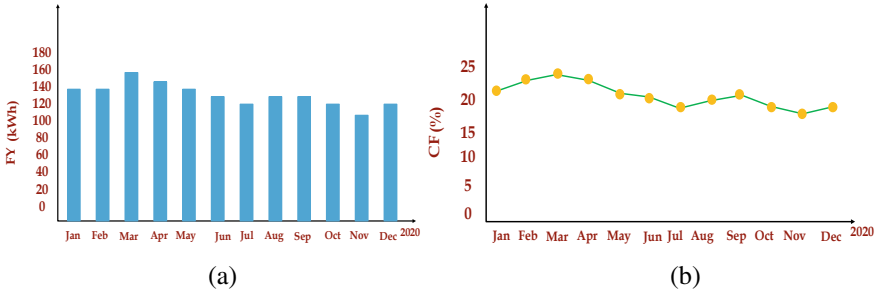


Fig. 4 **a** Monthly FY values. **b** Monthly CF values

March, and CF reached its lowest point in the month of November. The annual CF for the plant is 18.52%.

5. **AY**: The monthly variation of AY for the plant is portrayed by Fig. 5a. The maximum and minimum values were observed at 162.682 and 117.569 kWh. The highest AY was obtained in the month of March and the lowest in November. The total annual AY for the plant is 1659.37 kWh.
6. **ACL**: The monthly variation of ACL for the plant is portrayed in Fig. 5b. The maximum losses were observed in the month of March, 54.846 kWh, and the minimum losses occurred in the month of November, during which the losses were 31.25 kWh. From the trend, it can be concluded that the maximum losses occur, while the plant delivers the maximum yield and minimum when the yield is the lowest.
7. **CL**: CL for the plant for the entire annual operation fell in the range of 2.109–6.746 kWh. In terms of DC–AC conversion, November was the most efficient month, whereas June was the least efficient. Figure 6a depicts the monthly CL variation for the plant.

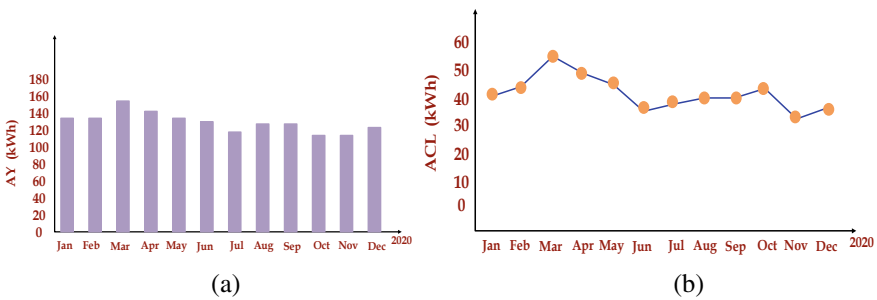


Fig. 5 **a** Monthly AY values. **b** Monthly ACL values

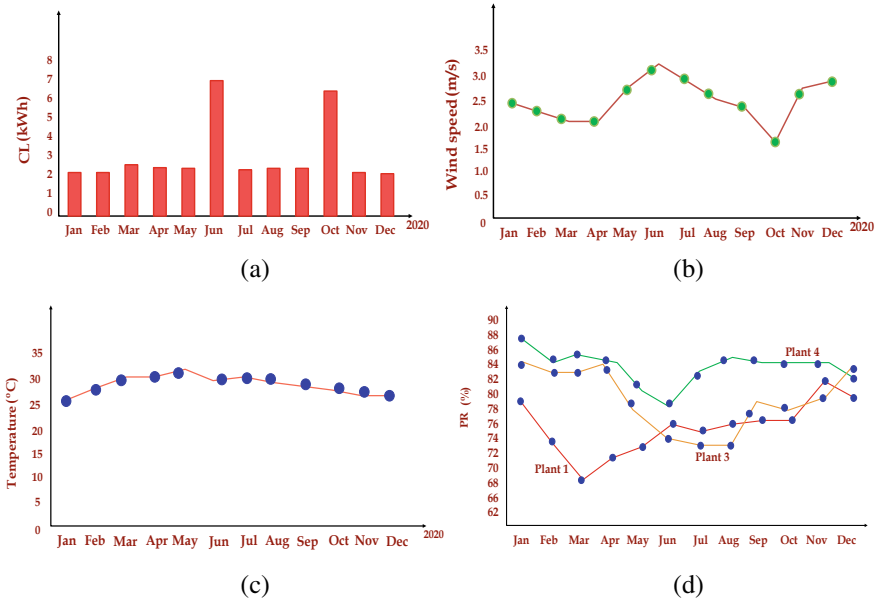


Fig. 6 a Monthly CL values. b Monthly average wind speeds. c Monthly average temperatures. d Comparison of monthly PR of different PV plants

4.2 Effect of Wind Speed and Ambient Temperature on Plant's Performance

Figure 6b and c shows the variation of wind speeds and ambient temperature. In this text, an attempt is made to analyze the effect of ambient temperature and wind speed on the plant performance and output. It is seen that the wind speed and temperature have pronounced effects on the losses subduced in the system.

An indication of the same is that the CL is maximum when there is maximum wind speed, in the month of June. Also, it is inferred that lower wind speed and ambient temperature prove to be the optimum conditions for the plant yield.

4.3 Comparison with Other Plants

Table 3 shows the comparison of the plant's performance with other plants situated across India.

Figure 6d presents a comparison of the PR values for the present study along with PV plants that have been previously assessed and analyzed. The PR values on a monthly basis are plotted for plant no. 1, 3, and 4 from Table 2. Figure 6d clearly indicates the variation in performance and output of different plants. Although the

plants have similar capacities, yet their output and PR differ considerably due to the geographical location and native ambient conditions of the plant.

5 Conclusion

In this article, the performance of 52 kW solar PV plant in SRMIST is studied, and the results are presented. Average performance ratio of the plant studied is 75% which is observed to be less compared to the plant taken for comparison. It is also observed that the plants performance ratio depends on the geographical location and its potential in solar radiation. This study will pay the way to researchers to perform the study on the existing PV plant and its capacity utilization factor. This will help to improve the performance of the commissioned plant. Moreover, it also guides to do the solar forecasting in the location before planning for the PV plant.

References

1. Rajvikram, M., Leonpraj, S., Ramakumar, S.: Experimental investigation on the abasement of operating temperature in solar photovoltaic panel using PCM and aluminum. **188**, 327–338 (2019)
2. Adar, M., Youssef, N., Mohamed, G.: Three PV plants performance analysis using the principal component analysis method. **207**, 118315 (2020)
3. Gxasheka, A., Van Dyk, E., Meyer, E.L.: Evaluation of performance parameters of PV modules deployed outdoors. **30**(4), 611–620 (2005)
4. Martín-Martínez, S., et al.: Performance evaluation of large solar photovoltaic power plants in Spain. **183**, 515–528 (2019)
5. Kumar, N.M., Dasari, S., Reddy, J.B.: Availability factor of a PV power plant: evaluation based on generation and inverter running periods. **147**, 71–77 (2018)
6. Thotakura, S., et al.: Operational performance of megawatt-scale grid integrated rooftop solar PV system in tropical wet and dry climates of India. **18**, 100602 (2020)
7. Satsangi, P., Bhagwan Das, D., Sailesh Babu, G.S., Saxena, A.K.: Performance analysis of grid interactive solar photovoltaic plant in India. **47**, 9–16 (2018)
8. https://webstore.iec.ch/preview/info_iec61724%7Bbed1.0%7Den.pdf
9. Sundaram, S., Babu, J.S.C.: Performance evaluation and validation of 5 MWp grid connected solar photovoltaic plant in South India. **100**, 429–439 (2015)
10. Kumar, B.S., Sudhakar, K.: Performance evaluation of 10 MW grid connected solar photovoltaic power plant in India. **1**, 184–192 (2015)
11. Mpholo, M., Nchaba, T., Monese, M.: Yield and performance analysis of the first grid-connected solar farm at Moshoeshoe I International Airport, Lesotho. **81**, 845–852 (2015)
12. Malvoni, M., et al.: Long term performance, losses and efficiency analysis of a 960 kWp photovoltaic system in the Mediterranean climate. **145**, 169–181 (2017)

Green Energy in West Bengal, India: Status, Scope, and Future Challenges



Debajit Misra

1 Introduction

Green energy is associated with renewable energy and clean energy as it is derived from natural resources. Renewable energy also comes from natural resources that are constantly being replenished, and clean energy means it emits no or very low greenhouse gases into the environment [1]. Although in most cases, renewable energy is considered as a major alternative energy option, and it comes from almost the same sources as green energy; the latter is broader in terms of source and applications. Green energy is an important and environmentally friendly alternative to the replacement of fossil fuel. If we consider its full life cycle, it will release very low greenhouse gases compared to fossil fuels. It is more acceptable due to the availability of resources like solar, wind, hydroelectric, geothermal, and tidal. However, these resources are available in some specific geographic locations. Other resources, like biogas and biomass, can be generated at any place. Thus, green energy is becoming a viable, sustainable solution to a greater extent to reduce the dependency of traditional power plants.

West Bengal comprises of immense green energy resources; it is located in eastern India and consists of fertile agricultural land and reserve forests capable of producing a large amount of biomass. The state is economically prosperous with its natural resources, and it holds a notable position in the context of the Indian economy. Again, it is one of the highest power-consuming states in India due to its high population density. Presently, the state depends mainly on traditional energy sources like thermal power and hydroelectric power. Most of the natural energy resources are still unrevealed compared to other Indian states. West Bengal often faces power crises, and the rural areas remain without electricity for certain times of the day. But, due to the huge population density, land acquisition in West Bengal for the establishment of

D. Misra (✉)

Department of Mechanical Engineering, Techno India Group, Kolkata 700091, India
e-mail: dmbesu@gmail.com

power plants is a problem. To overcome such a shortcoming, new sustainable solutions should have to be considered. The major natural resources in West Bengal are solar, wind, biogas, biomass, and hydropower. Solar radiation, sunshine hours, and the number of clear sunshine days in a year are the key parameters for establishing a solar plant [2–4]. In this context, the southern and western parts of the state are suitable for developing more solar plants. The northern part of the state is less suitable for solar power generation as average solar radiation and the number of clear sunny days are low. However, the reserve forests in the northern part and the mangrove forests of the Sundarbans in the southern part of the state flourish with biomass potential, which could play a vital role in the development of socioeconomic conditions if these resources could be utilized to generate useful energy. The state could also largely utilize wind energy as it has 158 km of coastline surrounded by the Bay of Bengal [5]. West Bengal should be concerned about carbon emissions due to environmental constraints and finite fossil fuel depletion, in addition to energy generation. Presently, the state is launching numerous small-scale green energy projects to minimize grid power dependency. Rooftop solar projects have rapidly progressed in the state in the last two years. Recently, West Bengal Green Energy Development Corporation Limited (WBGEDCL) has been set up to promote renewable energy-based projects in the state.

2 Traditional Power Scenarios

West Bengal has been a pioneer state in India in the generation and utilization of electricity. At first, electric power was demonstrated in Calcutta, West Bengal on July 24, 1879, through lighting some bulbs [6]. On November 10, 1897, India's first hydroelectric power station was built with 2×65 kW capacity at Sidrapong tea state, which was in Darjeeling district [7]. A few years later, in 1899, India's first thermal power plant was set up by The Calcutta Electric Supply Corporation Ltd. (CESC), a pioneer of electricity supply agency in India. Since then, CESC has been continuing power generation and distribution in Kolkata. There has been dynamism in the power sector in West Bengal. To harness the potential growth, several state-owned and privately owned companies have been working together. Apart from CESC, other major developers to establish power plants in West Bengal are West Bengal State Electricity and Distribution Company Ltd. (WBSEDCL), Durgapur Projects Ltd. (DPL), Haldia Energy Ltd. (HEL), National Thermal Power Corporation and Steel Authority of India Limited (NSPCL), Damodar Valley Corporation (DVC), and National Thermal Power Corporation Limited (NTPC).

In 2010, total installed power plant capacity in West Bengal was 8149.5 MW, including traditional and renewable energy generation [8]. The installation growth is almost uniform through the years. In the last ten year, installed capacity has been increased with a compound annual growth rate (CAGR) of 3.07%. In 2020, installation capacity is 11026.5 MW (Fig. 1).

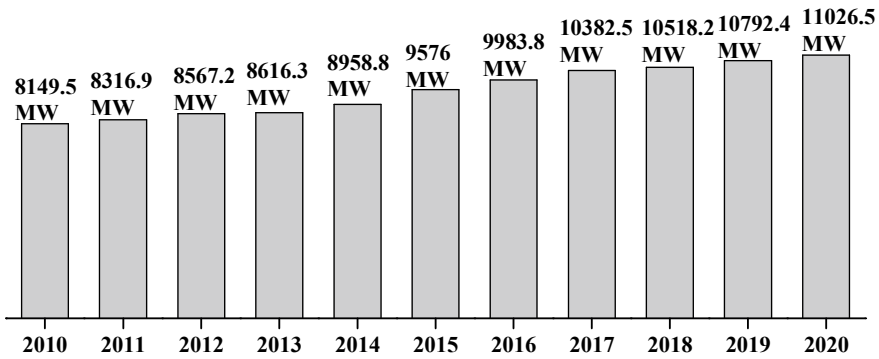


Fig. 1 Yearwise power plant capacity in West Bengal [8]

Figure 2 shows the energy consumption in million unit (MU). It is clearly seen that energy consumption steadily increases up to 2014, and then, it sharply increases. In 2010, energy consumption is 31,455 MU, and in 2020, it reaches to 52,948 MU. Consumption is growing at a CAGR of 5.34% over the years. Thus, it is clear that power generation should be increased with the proportional consumption rate.

In the year 2020, energy supplied to the consumer was 52,824 MU, and there was an energy deficit of 124 MU. However, the state also imported 1822 MW power from the outside state [10]. In view of generating a sustainable power, the state could shift its focus toward green energy or renewable energy.

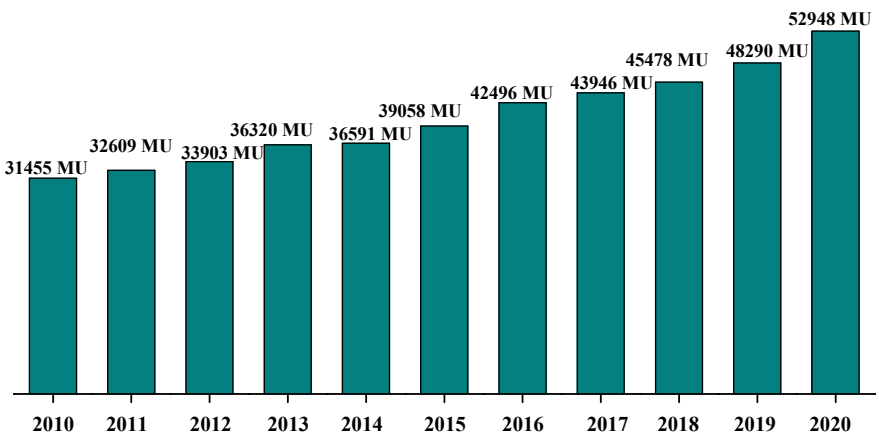


Fig. 2 Yearly power consumption in West Bengal [9]

3 Present Status of Green Energy

The green energy in Indian states has been taken momentum taking considerable support from the Indian government policy. India is already on the way to reach its target of 175 GW renewable power installation by 2022 as government made a commitment in Paris Agreement to provide sovereign nations by reduction of greenhouse gases emission. At present, India crossed 100 GW renewable power generations, and the country is in fourth position in the world in it, fourth position in wind power development and fifth position in solar power development. Indian government has initiated lots of solar policies and program for the states toward supporting solar energy deployment. A separate ministry has been formed named as “Ministry of New and Renewable Energy” (MNRE) with a separate annual budget has been declared for each year. Recently, central government has proposed some rules naming “Draft Electricity Rules, 2021” [11]. These rules are proposed for the purchase and use of green energy, including energy from waste. It is designed to address the various concerns related to the green energy sector for the rapid use of renewable energy.

At present, renewable or green energy is growing at snail speed in West Bengal compared to the other states. West Bengal depends mainly on thermal power plant to supply energy throughout the state. Here, installed renewable power capacity is just 532.88 MW excluding hydroelectric sources [12]. In this total renewable energy development, major growth has been occurred in biomass power generation. The state is unable to compete in solar and wind power development with other Indian states. Presently, the state government has been initiated lots of projects to enhance the green power sector, particularly solar and biomass power projects.

Figure 3 shows major Indian states and their biomass power generation capacities. Maharashtra, Uttar Pradesh, and Karnataka are the major states positioning first, second, and third, respectively whereas West Bengal stands in seventh position.

3.1 Solar Energy

At present, 162.68 MW solar projects are present in West Bengal [12]. The journey was primarily started from Sundarbans in 1994 [13]. Recent times, deployment of solar PV in Sundarbans is more progressive than other zone. Each village has 200,000 rooftop panels though the locations are islands and remote. Now, around 4000 people are benefitted by using solar microgrids. In West Bengal, first large-scale solar power generation of 1.1 MW capacity was done in 2009 at Jamuria, Asansol, and later in 2011, it was augmented to 2 MW [14]. It was first grid-connected solar PV plant in India. Recently, 1 MW ground-mounted solar plant has been established at the Haldia Dock Complex. OCL has installed 5.5 MW solar PV plant for powering their existing cement grinding plant at Salboni, Midnapore [15]. It was first large solar plant in the state (Fig. 4).

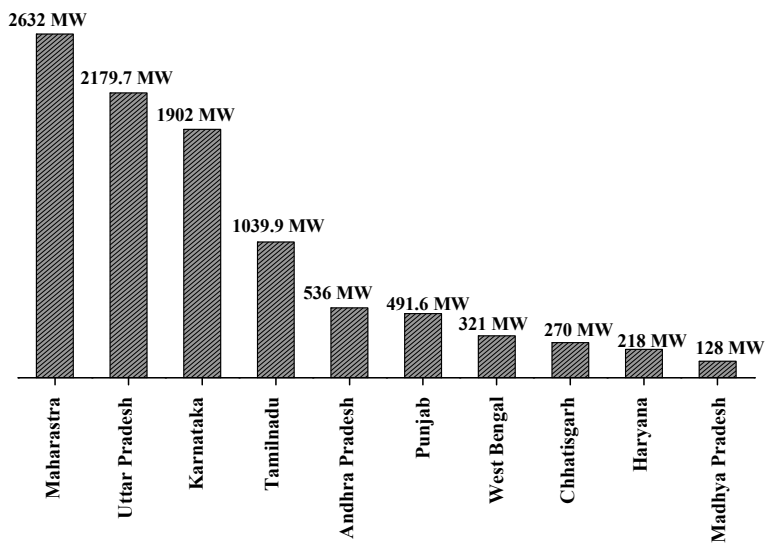


Fig. 3 Major biomass power generation states in India and their capacities [12]



Fig. 4 5.5 MWp power plant at Salboni in West Bengal [15]



Fig. 5 Floating solar PV of 10 KWp capacity in Kolkata [16]

In 2014, India's first floating solar plant of 10 KW capacity was set up at Newtown, Kolkata which is a joint venture project of Vikram Solar and Arka Renewable Energy College [16] (Fig. 5).

West Bengal is now in remarkable position as world's largest solar tree is developed here. The solar tree has been made of metallic structure, which was formed like a tree to hold solar panels. Central Mechanical Engineering Research Institute (CMERI) has established it with 35 PV panels; each of the panel's capacity is 330 W [17]. The solar tree has been built at Durgapur, CMERI residential area. The total power generation capacity of the solar tree is 11.5 kW, which generates 12,000–14,000 units of green power in a year (Fig. 6).

West Bengal government now gives more attention toward rooftop solar PV, and lots of small-scale projects have been implemented recently. Total 1.8 MW small-scale rooftop solar projects are in running condition in different institutes in West Bengal. The major projects are developed in administrative buildings, schools, and colleges. Total 240 schools have been electrified by using rooftop solar PV, with 10 KW of each [18]. WBSEDCL has implemented some large-scale solar power projects in the areas of thermal and hydroelectric power plants. Table 1 shows the different places where they are in operation.



Fig. 6 11.5 KWp solar tree at CSIR-CMERI, Durgapur [17]

Table 1 Current solar projects at different traditional power plants [18, 19]

Location	Description	Capacity (MW)
(i) Sagardighi Thermal Power Project (SgTPP)	Grid-connected ground-mounted solar PV project	13.511
(ii) Bakreswar Thermal Power Station (BKTPS)	Rooftop solar PV project	2.866
(iii) Kolaghat Thermal Power Station (KTPS)	Rooftop-mounted solar PV project	2.27
(iv) Bandel Thermal Power Station (BTPS)	Rooftop-mounted solar PV project	1.08
(v) Santaldih Thermal Power Station (STPS)	Rooftop-mounted solar PV project	0.807
(vi) Teesta Canal Fall Hydro Electric Power Plant, Stage-II	The canal bank solar	10

The state also utilizes decentralized solar application, particularly for rural electrification in Sunderban, Bankura Mednapore, and Purulia. Solar PV plant was installed with 26 kW capacity at Kamalpur village at Sagardweep [20]. Later, 25 and 110 kW plants were set up in two different locations in Sundarbans. Again, first solar power village in Purulia district was Pandri, which is a village at the base of Ayodhya hill with 1.2 KW capacity. A 5 HP water pump is fitted nearby to it for irrigation. Presently, there are 8726 street lighting system, 145,332 home lighting system, 17,662 solar lanterns, and 653 numbers of solar pumps are in operation in the state [21].

3.2 Wind Energy

West Bengal has set up wind farm at Fasergunj, South 24 Parganas which is located at the coast of Bay of Bengal. Since 2001, West Bengal Renewable Energy Development Agency (WBREDA) has been operating this wind farm. The project was started with four 250 KW wind electric generators, and later in 2016, the project capacity has been augmented to 2 MW capacity. A 1 MW hybrid production facility combining solar and wind diesel has been developed, which could distribute power about 2000 households. WBREDA is also operating a Wind-Diesel-Gasifier Hybrid Power Project having 200 KW capacity at Sundarbans [19]. Besides wind farm, the state has some small wind aero generators of cumulative capacity of 74 KW at Sundarbans (Fig. 7).



Fig. 7 2 MWp wind farm at Frasergunj in West Bengal [19]

3.3 *Hydroelectric Energy*

Currently, the state is generating 1434 MW hydropower, of which conventional hydro power is 539.15 MW and pumped storage type hydropower is 900 MW [22]. In 2008, Turga Pumped Storage Project was commissioned at Ajudhya hill in Purulia district. It has a capacity to generate 900 MW power at a time when water is discharged from upper reservoir to lower reservoir. Reversible pump-turbine and generator motor has been used to run the project where the upper dam covers an area of 8.29 km² across Turga Nala and the lower dam covers an area of 12.66 km². Table 2 shows the current hydroelectric projects, their capacities, numbers, and locations.

3.4 *Biogas and Biomass Energy*

According to West Bengal Renewable Energy Development Agency (WBREDA), there are already 11,000 numbers of small capacity (10–40 m³) biogas plants in the state [19]. Recently, a large-scale biogas plant of 600 m³ has been built by New Town Kolkata Development Authority (NKDA) in Kolkata [24]. It covers 1.5 acre area to process biodegradable waste which is gathered from the city. Nearly, one month time is required when wet biodegradable waste is filled into a tank to produce biogas. Again, the state has now three biomass gasifier plants in the coastal region of South 24 Parganas district, which are operated and managed by WBREDA. These are located at Gosaba with 500 KW capacity, Chotto Mollakhali with 500 KW capacity, and Herembo Gopalpur with 400 KW capacity. All plants are operating for rural electrification purpose. Again, total 199 numbers of rice husk-based gasifiers have been installed under MNRE program with total power capacity of 66.5 MW [12, 25].

Table 2 Hydroelectric projects in operational phase in West Bengal [23]

Project name	Site	Capacity (MW)	River
(i) Jaldhaka Stage-I	Kalimpong	36 (4 nos.)	Jaldhaka
(ii) Jaldhaka Stage-II	Kalimpong	8 (2 nos.)	Jaldhaka
(iii) Rammam Stage-II	Lodhma, Darjeeling	51 (4 nos.)	Rammam
(iv) Teesta Canal Fall Hydel Project (PS-I, PS-II, and PS-III)	Phansidewa, Darjeeling	67.5 (9 nos.)	Teesta
(v) Teesta Low Dam Project IV HEP	Teesta Bazar village, Darjeeling	160 (4 nos.)	Teesta
(vi) Teesta Low Dam Project III HEP	Reang, Kalimpong	132 (4 nos.)	Teesta
(vii) Mungpoo Kalikhola Hydel Project	Mungpoo, Kalimpong	3 (3 nos.)	Teesta
(viii) Rinchington Hydel Project	Kurseong, Darjeeling	2 (2 nos.)	Rangit
(ix) Little Rangit Hydel Project	Bijonbari, Darjeeling	2 (2 nos.)	Rangit
(x) Fazi Hydel Project	Kurseong, Darjeeling	1.2	Teesta
(xi) Sidrapong Hydel Project	Darjeeling	0.4 (2 nos.)	Jhora
(xii) Massanjore Hydel Project	Near Suri, Birbhum	4 (2 nos.)	Mayurakshi
(xiii) Maithon DVC HEP	Asansol, Burdaman	60 (3 nos.)	Damodar
(xiv) Lodhama Small Hydro Project	Darjeeling	3 (2 nos.)	Lodhama
(xv) Neora Small Hydro Project	Darjeeling	3 (2 nos.)	Neora
(xvi) Moondakotee-R.C. Micro Hydroelectric Project	Moondakothi, Darjiling	0.375 (3 nos.)	Balason
(xvii) Bandukey Khola Micro Hydroelectric Project	Darjiling	0.20 (2 nos.)	Simphok
(xvii) Margaret's Hope Micro Hydroelectric Project	Kurseong, Darjeeling	0.10	Beltra

The electricity generation of the plants is primarily used to supply the captive needs of rice mills (Fig. 8).

3.5 Green Transportation

West Bengal Transport Corporation (WBTC) has introduced green mobility by launching electric buses. Initially, 80 electric buses have been started in Kolkata. Presently, it is in third position among six Indian megacities in adoption of electric mobility [26]. It is found that conventional vehicles create major pollution in the city and the state government thus targeting to bring more electric buses. Apart from Kolkata, electric buses are running in other cities like Siliguri and Durgapur. At



Fig. 8 500 KWp Chhoto Mollakhali biomass gasifier power plant [19]

present, total 100 numbers of electric buses is running around different cities in West Bengal [27]. In 2018, Eicher Skyline Pro has launched three e-buses in collaboration with West Bengal Housing Infrastructure Development Corporation [28]. Phoenix India Research and Development Group in association with Ashok Leyland have begun the biogas operated bus in Kolkata. It was first biogas-based bus service in India. A fully fuel-filled bus can carry 80 kg of compressed biogas (CBG) and can run up to 1600 km. The biogas production cost found to be Rs. 20/kg, and a bus can run 5 km per kg of gas [29, 30]. The biogas is mainly generated from cow dung, and a biogas plant has been set up at Ultadanga, Kolkata. The state soon starts their large-scale biogas plant at Dubrajpur in Birbhum district as it has already got permission to set up 100 biogas fuel pumps. State Transport Corporation also launched three dual-fuel engine buses which can be operated by diesel as well as CNG to reduce carbon emission [31].

4 Resource Potential

India has set a goal related to sustainable energy solutions and is consistently reaching close to it by adopting green and renewable energy technology in different states. West Bengal is a state which is slowly adopting this technology compared to the other Indian states though it has lots of potential which has to be revealed. The state has an average of 300–330 sunny days and receives 5–5.5 KW/m²/day of solar insolation level [32]. West Bengal must understand the need for this solar energy in order to

emerge as a major hub for the solar industry. In 1994, government-owned Websol Energy System Limited was one of the first manufacturers of solar energy panels in West Bengal. Other renowned companies that have marked their footprints in the state are as follows: Reliance Industries, Suntechnics Energy Systems, Geetanjali Solar Enterprises, Synergy Renewable Energy, Environ Energy Tech Services, Vikram Solar, etc. The state introduces different solar energy development programs and utilizes its potential, which is 6260 MW.

West Bengal has a 158 km coastal area. A 2 MW wind farm has already been built on the coastal bank, and various studies have been conducted to extract more wind power. The evaluation of available wind power is based on a term which is called wind power density (WPD) in W/m^2 . It determines the amount of energy available at a particular site that can be converted into electrical energy. To exploit the wind potential, the Nodal Agency initially undertakes a comprehensive wind resource assessment and offers identified potential sites for development. In the future, government-owned waste land areas with a minimum annual mean wind power density (WPD) of $200 W/m^2$ at a hub height of 50 m will be used for wind power generation [33]. The Nodal Agency undertook an assessment of the 450 MW wind potential in West Bengal.

Hydropower is another key to fulfill West Bengal's renewable energy deployment. The upstream of Teesta river basin, which is in hilly areas, has potential to generate electricity. Already, there are some hydroelectric projects under running condition, but still, some projects could be developed in future. Other river basin like Rangeet, Damodar, Mayurakshi, Kangsabati, and Rupnarayan could be utilized for small hydropower projects. West Bengal has a hydroelectric potential of 6300 MW of which 4800 MW could be generated by pumped storage and 1500 MW by canal falls [34].

Another green energy source is biomass, which comes from waste materials produced by agriculture, forest operations, etc. Some examples of biomass sources produced as a byproduct of processing operation of agricultural materials are stalks, straws, husks, shells, de-oiled cakes, etc. Rice husk is a main raw material or feedstock in biomass energy project in West Bengal. However, other form of agriculture waste like wood, straw, and maze are being considered for generating biomass power in the state. Feedstock availability and piercing are the critical determinants of success for biomass plants. Reserve forest of North Bengal and Sagar Islands is the main locations for forest residue or biomass. Moreover, the availability of land and cultivation-related extract material along with human and cattle waste materials also show huge potential for generation of biomass. In order to ensure smooth availability of feedstock, WBGEDCL has classified the rice-producing areas based on the quantity of production of rice. Based on the clustering study conducted by Nodal Agency, they would allocate projects in the predefined command area. Such allocation shall be periodically reviewed by the Nodal Agency and obtained a potential of 6663 MW [35].

5 Current Policy and Projects

In 1993, the state government formed a Nodal Agency named the West Bengal Renewable Energy Development Agency (WBREDA) for the promotion and development of renewable energy. Initially, the primary goal of this Nodal Agency was to promote and raise awareness about the use of renewable energy. It also provides facilities to private sector investors in the development of energy. The state government has decided to provide available vested land on lease for 30 years for the installation of renewable power plants. West Bengal declared its solar policy in 2012. It has launched a net-metering rooftop PV policy to increase energy consumption for 2–100 KW users to reach a target of 16 MW by 2017. Net metering is also allowed for individual household rooftop solar power generation (Table 3).

Recently, the state government has set up a new solar policy as per central government's aims to develop 4500 MW solar project in 2022 within the state [37]. A new mandatory rule has been introduced by West Bengal government for large buildings—in order to meet the energy demand of a large building, 1.5% of total electric energy must be supplied from their own solar panels. Subsidies for solar PV installation are provided as per Solar Energy Corporation of India Limited (SECI) guidelines.

Presently, various renewable energy development programs and schemes have been implemented by the state, which is listed below:

- (i) Solar photovoltaic
- (ii) Rooftop and small solar PV installations
- (iii) Solar thermal program
- (iv) Wind farm
- (v) Battery-operated vehicle
- (vi) Small, mini, and micro-hydel projects
- (vii) Bio-energy program
- (viii) Biomass projects
- (ix) Co-generation plant
- (x) Waste to energy
- (xi) Evacuation infrastructure.

Following are the major project proposals [18, 19, 38, 39].

- (i) 1200 MW (3×300 MW) solar PV-powered pumping projects have been conceived in Purulia district.

Table 3 West Bengal's target of green energy by 2022 [36]

Resources	Cumulative target (MW)
Solar energy	4500
Biomass cogeneration	600
Biomass energy	662
Waste to energy	100
Wind energy	4

- (ii) 500 MW solar park is being developed in Purba & Paschim Medinipur and Bankura district.
- (iii) A 10 MW ground-mounted solar PV project has sanctioned at Bhajanghat, Nadia.
- (iv) 5 MW rooftop solar projects have also been initiated for implementation at different sub-stations and offices.
- (v) WBREDA has initiated a land-based 1 MW solar PV plant at Ganga Sagar, South 24 Parganas.
- (vi) A project has been conceived to set up grid-connected rooftop PV system at 18 colleges with 340 KW capacity and four universities with 350 KW capacity.
- (vii) 200 KW ground-mounted grid-connected solar PV project has been initiated at DPL, Durgapur.
- (viii) 190 KW grid-connected rooftop solar PV projects have been launched for powering some state-owned buildings.
- (ix) 100 KW grid-connected solar PV plant with net metering system has been commissioned in Santoshpur hospital in Kolkata.
- (x) 140 solar PV power projects, each with 5 KW capacity (grid connected with net metering, Phase-III), have been sanctioned in various schools in West Bengal.
- (xi) Installation of 75 grid-interacted PV projects, each with 10 KW capacity, has been initiated in various schools in Purulia and Jhargram.
- (xii) A 5.4 MW floating solar PV project has been inaugurated at Sagardighi thermal power plant in Murshidabad.
- (xiii) Howrah Municipal Corporation's (HMC) has floated a tender to develop 7.5 MW solid waste power plant.

6 Challenges

The state's slow progress in green energy development is due to the different barriers. Lack of understanding between investors and financial intermediaries is the main challenge that often arises in the implementation of renewable energy projects. West Bengal has little vested land, and some lands are occupied by the government. Due to higher population density in the state, there is very limited land for establishing large-scale solar projects. Again, the intensity of solar radiation is low in the state compared to the southern and western states in India. The state has coal mines and easy availability of thermal power plants. In most cases in West Bengal, only, rich people are interested in installing solar PV for power generation. As a result, the government subsidized up to 5 kWp for solar PV installation. However, people are reluctant to install solar systems because they think that they will be more expensive than the traditional grid power system. Also, if individuals are allowed to generate energy through rooftop PV installations of up to 5 kWp, the increased supply will disrupt the power distribution system's tariff structure. Distribution companies under the cross-subsidy model aim to save electricity for small users by charging more per

customer than those who spend more. In most cases, when urban people utilize rooftop solar power, they consume less power from the distribution firms.

Biomass projects are installed in West Bengal only for regional power demand. Biomass power can be used to generate electrical energy by burning biomass, and the burned biomass's heat can run gas turbines or steam turbines. It has some limitations, like its low energy concentration and its transmission difficulty. Its energy utilization is rather low. To store biomass gas, a large storage volume is required, and preventive measures should be taken carefully; otherwise, moisture may be absorbed. The main challenge of biomass gasification is its environmental impact. Sagar Island's biomass application may not be viable due to its sensitive ecology. In this context, hydrogen production from biomass could be reduced by such challenges. However, this technology in West Bengal has still not been adopted.

7 Conclusions and Remarks

The present study shows the current green energy status of West Bengal state. It presents a clear idea of how the state is involved with green energy for future energy security. Though the state's present green energy generation is low, it could be enormous in the future as the state has taken an aggressive policy to ramp up energy generation capacity. Presently, large numbers of projects have been granted for biogas energy, rooftop solar, and green building with solar rooftops all around the state. The government's strong policies related to greater investment indicate that the green energy generation in West Bengal is likely to be in a good position in the near future with low dependency on traditional power plants.

References

1. What is green energy? (Definition, types and Examples). <https://www.twi-global.com/technical-knowledge/faqs/what-is-greenenergy#WhyGreenEnergyIsImportant>
2. Misra, D.: Floating photovoltaic plant in India: current status and future prospect. In: International Conference on Thermal Engineering and Management Advances 2020, LNME, pp. 219–232. Springer, Singapore (2020)
3. Misra, D.: Design of a stand-alone rooftop PV system for electrification of an academic building. *Int. J. Eng. Adv. Technol.* **9**(2), 3955–3964 (2019)
4. Ganguly, A., Misra, D., Ghosh, S.: Modeling and analysis of solar photovoltaic-electrolyzer-fuel cell hybrid power system integrated with a floriculture greenhouse. *Energy Build.* **42**(11), 2036–2043 (2010)
5. Centre for Coastal Zone Management and Coastal Shelter Belt. <http://iomenvi.nic.in/index3.aspx?ssid=876&subsublinkid=106&langid=1&mid=1>
6. CESC Ltd. https://www.cesc.co.in/?page_id=223
7. Biswas, P., Mandal, S.: Indian electricity sector under regulatory regime. White Falcon Publishing, Chandigarh, 160047 (2019)
8. Installed power capacity in West Bengal. <https://www.statista.com/statistics/1077931/india-west-bengal-installed-power-capacity/>

9. Electricity consumption utilities: West Bengal. <https://www.ceicdata.com/en/india/electricity-consumption-utilities/electricity-consumption-utilities-west-bengal>
10. Energy Statistics 2020. <https://www.niua.org/csc/assets/pdf/key-documents/phase-2/Energy-Green-Building/Energy-Statistics-2020.pdf>
11. Electricity (promoting renewable energy through Green Energy Open Access) Rules (2021). <https://static.pib.gov.in/WriteReadData/specificdocs/documents/2021/aug/doc202181611.pdf>
12. State wise installed capacity of renewable power. <https://mnre.gov.in/the-ministry/physical-progress>
13. Mondal, M., Mandal, S.: Remote village electrification through renewable solar energy: a case study of Sagar Island, West Bengal, India. *Int. J. Eng. Sci.* **2**(01), 201–205 (2013)
14. Basak, S.: Solar electrification scenario in India: technological development and challenges. *Int. Adv. Res. J. Sci. Eng. Technol.* **6**(10), 14–23 (2019)
15. OCL India inaugurates West Bengal's first and largest 5.5 MW solar PV Power Plant. <https://www.saurenergy.com/solar-energy-news/ocl-india-inaugurates-west-bengals-first-largest-5-5-mw-solar-pv-power-plant>
16. Floating solar power plant in West Bengal, India. www.vikramsolar.com/case-studies/floating-solar-power-plant-in-west-bengal-india/
17. Council of Scientific and Industrial Research. <https://www.csir.res.in/slider/csir-cmeri-has-developed-world%E2%80%99s-largest-solar-tree-which-installed-csir-cmeri-residential>
18. Department of Power Government of West Bengal. <https://wbpower.gov.in/solar-projects/>
19. West Bengal Renewable Energy Development Agency. <http://www.wbreda.org/>
20. Chakrabarti, S., Chakrabarti, S.: Rural electrification programme with solar energy in remote region—a case study in an island. *Energy Policy* **30**(1), 33–42 (2002)
21. Energy Statistics 2019. http://mospi.nic.in/sites/default/files/publication_reports/Energy%20Statistics%202019-final.pdf
22. West Bengal Green Energy Development Corporation Limited. <https://www.wbgedcl.in/>
23. West Bengal State Electricity Distribution Company Limited. https://www.wbsedcl.in/irj/go/km/docs/internet/new_website/Home.html
24. Waste powered electricity to light up New Town streets. <https://www.telegraphindia.com/west-bengal/calcutta/waste-powered-electricity-to-light-up-new-town-streets/cid/1806718>
25. Solar Energy, Ministry of New and Renewable Energy. <https://mnre.gov.in/solar/currentstatus/#:-:text=India%20is%20endowed%20with%20vast,providing%20huge%20scalability%20in%20India>
26. Tata Motors to supply 80 Electric buses to West Bengal Transport Corporation. <https://www.tatamotors.com/press/tata-motors-to-supply-80-electric-buses-to-west-bengal-transport-corporation/>
27. Outlook traveler. <https://www.outlookindia.com/outlooktraveller/travelnews/story/71275/kolkata-wins-the-electric-vehicle-race-against-london>
28. Eicher electric buses completes one year of successful operations in Kolkata. <https://www.vecv.in/press-releases/eicher-electric-buses-completes-one-year-of-successful-operations-in-kolkata>
29. West Bengal Begins Biogas for Buses. <https://www.ngvglobal.com/blog/west-bengal-begins-biogas-for-buses-0110>
30. India's First Biogas-Fuelled Bus Launched in Kolkata. <https://thelogicalindian.com/news/first-biogas-fuelled-bus/>
31. West Bengal kick starts CNG buses to reduce fare during diesel price rise. <https://www.getbenegal.com/details/west-bengal-kick-starts-cng-buses-to-reduce-fare-during-diesel-price-rise>
32. Solar Map of India. <http://map.sunrator.com/>
33. Dawn, S., Tiwari, P.K., Goswami, A.K., Singh, A.K., Panda, R.: Wind power: existing status, achievements and government's initiative towards renewable power dominating India. *Energy Strat. Rev.* **23**, 178–199 (2019)
34. Power and Energy Industry. <https://wb.gov.in/business-power-energy-industry.aspx>
35. Biomass Power. https://cag.gov.in/uploads/download_audit_report/2015/Union_Civil_Performance_Renewable_Energy_Report_34_2015_chap_6.pdf

36. Power for all West Bengal. https://powermin.gov.in/sites/default/files/uploads/joint_initiative_of_govt_of_india_and_West_Bengol.pdf
37. Saur Energy. <https://www.saurenergy.com/solar-energy-news/west-bengal-working-on-a-new-solar-policy-to-meet-its-target-of-4500mw>
38. Solar Energy Corporation of India Limited. https://www.seci.co.in/archives/data_archives
39. Solar Projects. https://www.wbsedcl.in/irj/go/km/docs/internet/new_website/solar.html

Impact of Performance Parameters on the Efficiency of Cu_2SnS_3 (CTS)/Si Tandem Solar Cell by SCAPS-1D



Devsmita Roy, Rajeshwari Garain, Arindam Basak, Subrat Behera, Ranjeeta Patel, and Udai P. Singh

1 Introduction

Solar cells are a form of photoelectric cell that serve as the foundation for photovoltaic modules. A solar cell's fundamental components are a p -type absorber layer, an n -type window layer, a front contact, and a rear contact. Because solar energy is a renewable resource, it is a superior alternative for replacing fossil fuels, which are the primary source of energy. Scientists have been working to build high-efficiency, low-cost solar cells in response to the growing demand for sustainable and renewable energy [1].

Thin film solar cells are gaining popularity among researchers because they use less material during the depositing process, lowering the manufacturing cost. In addition, many commercially feasible deposition processes for depositing thin films are available.

Copper tin sulfide (CTS) is a ternary compound and one of the most noteworthy secondary phases that results from the intermixing of binary CuS and SnS compounds during the manufacture of the CZTS absorber layer. CTS has attractive optoelectronic features, including p -type conductivity and a high absorption coefficient (105 cm^{-1}) as well as a wide band gap range (0.9–1.6 eV) [2]. However, transparent CTS cells with a standard n -doped TCO as the back contact already had an efficiency of more than 2.92% [3].

D. Roy · R. Garain · A. Basak · U. P. Singh (✉)
Thin Film Photovoltaic Lab, School of Electronics Engineering, KIIT (Deemed to be University),
Bhubaneswar, Odisha, India
e-mail: singhup@kiit.ac.in

S. Behera · R. Patel
School of Electrical Engineering, KIIT (Deemed to be University), Bhubaneswar, Odisha, India
e-mail: sbeherafel@kiit.ac.in

R. Patel
e-mail: ranjeeta.patelfel@kiit.ac.in

The aim of this paper was to study the performance of tandem solar cell to achieve higher efficiency with least material usage. We have used Cu_2SnS_3 on the top of p -Si to make a tandem structure. The incoming photon will be totally absorbed by the two layer tandem structure which in turn will enhance the efficiency. The output characteristics of a CTS thin film solar cell were simulated using the SCAPS program version 3.3.0.7, which allows users to enter parameters to determine the solar cell's materials and interfaces.

2 Device Structure and Simulation Methodology

Although there is a variety of software available for modeling solar cells and computing photovoltaic parameters, SCAPS-1D was used for this study since it is specifically designed for thin film solar cells. SCAPS-1D is a one-dimensional solar cell simulator created at the University of Gent's Department of Electronics and Information Systems (ELIS) [4]. The PV research association has free and open access to the program (universities and research institutes).

We studied the construction of a CTS/ p -Si/ n -Si tandem solar cell in this simulation work, where thin film CTS is employed as the top layer and silicon is used as the bottom layer. Optimizing the layer thickness of CTS, n -Si, p -Si, and CTS carrier concentration resulted in improved photovoltaic effects. The material characteristics for CTS, p -Si, and n -Si, as illustrated in Fig. 1, were derived from various research groups [2, 5, 6] and are included in Table 1. In presence of light, the current–voltage characteristics (I – V) curve was obtained for different CTS, p -Si, and n -Si absorber layer thicknesses.

Firstly, the n -Si layer thickness was changed from $0.01\ \mu\text{m}$ to $0.1\ \mu\text{m}$ with constant CTS and p -Si layer thickness at $5\ \mu\text{m}$ and $140\ \mu\text{m}$, respectively, to notice the thickness dependence on the efficiency of solar cells. And then thickness of p -Si layer was varied from $130\ \mu\text{m}$ to $200\ \mu\text{m}$ with fixed CTS and n -Si layer thickness of $5\ \mu\text{m}$ and $0.03\ \mu\text{m}$, respectively.

There after that thickness of CTS layer was varied from $1\ \mu\text{m}$ to $5\ \mu\text{m}$ keeping the thickness of p -Si and n -Si at $140\ \mu\text{m}$ and $0.03\ \mu\text{m}$, respectively. Different parameters related to solar cell performance were derived from the obtained current–voltage (J – V) characteristics curve, and efficiency was calculated hence the optimum absorber layer thickness was found from the observed data.

Secondly, the carrier concentration of CTS was changed from 1×10^{14} to $1 \times 10^{23}\ \text{cm}^{-3}$ and the corresponding efficiency was observed with the variation of carrier concentration. As a result, the collected data were used to estimate the appropriate carrier concentration. To investigate the influence of carrier concentration on solar cell performance, many factors connected with solar cell performance were evaluated using the resulting current–voltage (J – V) characteristics curve.

Lastly, the effect of ambient operating temperature on the performance of tandem solar cell has been calculated for different optimum layer thickness of Al/CTS/ p -Si/ n -Si/Al (5 , 140 and $0.03\ \mu\text{m}$) keeping the carrier concentration constant ($2.3 \times$

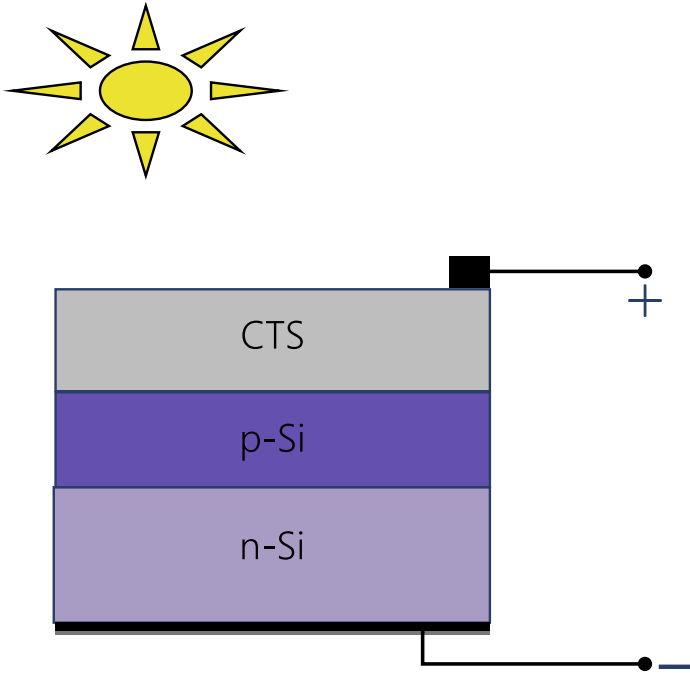


Fig. 1 Schematic structure of CTS/p-Si/n-Si tandem solar cell

Table 1 Material properties for Al/p-CTS/p-Si/n-Si/Al tandem solar cell

Parameters	p-CTS	p-Si	n-Si
Thickness, (μm)	1–5 μm	130–200 μm	0.01–0.1 μm
Dielectric ratio (ϵ/ϵ_0)	10.000	11.900	11.900
Electron mobility, μ_N (cm^2/Vs)	5	1.35×10^3	1.35×10^3
Hole mobility, μ_P (cm^2/Vs)	9	4.5×10^2	4.5×10^2
Acceptor concentration, (cm^{-3})	2.3×10^{17} , 1×10^{14} , -1×10^{23}	1.0×10^{16}	0
Donor-concentration, (cm^{-3})	1	0	1.0×10^{16}
Bandgap, (eV)	0.870	1.120	1.120
Density of states, N_C (cm^{-3})	2×10^{18}	2.8×10^{19}	2.8×10^{19}
Density of states, N_V (cm^{-3})	1.8×10^{18}	1.04×10^{19}	1.04×10^{19}
Electron affinity, X (eV)	4.500	4.050	4.050

10^{17} cm^{-3}). The ambient temperature used for the simulation was 300, 350, 400, and 425 K. The efficiency and fill factor was studied for all the ambient temperatures.

3 Results and Discussion

The thickness of the n -Si, p -Si, and p -CTS layers was varied to find the optimal CTS/Si solar cell values in a multi-junction technique. CTS layer thickness and carrier concentration have been modified while maintaining Si layer thickness constant after observing the optimal values of n -Si and p -Si layer thickness. Finally, the influence of operating ambient temperature on tandem solar cell efficiency was investigated.

3.1 Effect of n -Si Layer Thickness

The thickness of the n -Si layer was varied from 0.01 to 0.10 μm while the other parameters remained fixed. By adjusting the thickness of the n -Si layer, the cell's output parameters are illustrated in Fig. 2.

From the simulation, it is visible that the variation of n -Si layer thickness did not affect the solar cell output parameters [1]. At a layer thickness of 0.03 μm , the efficiency is found to be little higher than other thickness parameters which is negligible. Here, Si is behaving as an n -type, so after absorption of higher than 90% from the top cell CTS, it is used to move the longer wavelength photons to the p -type Si and a proper p - n junction between silicon was obtained. Therefore, the highest efficiency of 18.58% has been attained with $\text{FF} = 80.71\%$ by using 0.03 μm of n -Si layer thickness. After tunneling into top and bottom cells, the initial n -type Si layer should be thicker to allow maximal photons to reach the next layers, both experimentally and physically.

J_{sc} reduces significantly as layer thickness increases for regions more than 0.03 μm , but V_{oc} increases significantly as layer thickness increases for regions greater than 0.02 μm . Increases in layer thickness, on the other hand, have a greater

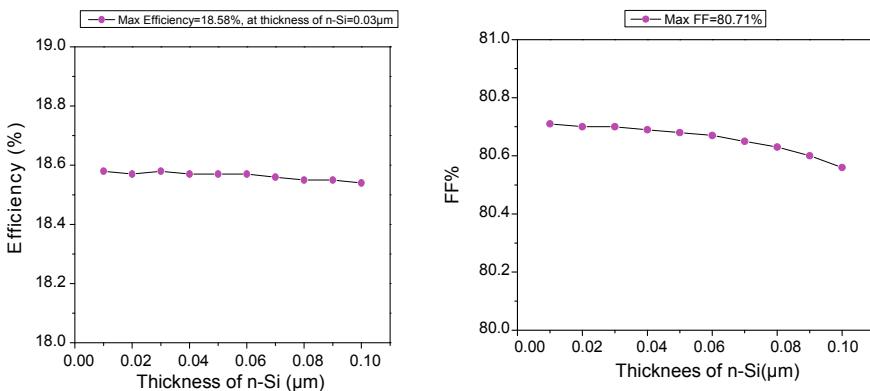


Fig. 2 Effect of the thickness of n -Si on efficiency and fill factor

Table 2 Parameter values for *n*-Si layer

Thickness of <i>n</i> -Si (μm)	V_{oc} (V)	J_{sc} (mA/cm^2)	FF %	Efficiency %
0.01	0.522	44.093	80.71	18.58
0.02	0.521	44.091	80.70	18.57
0.03	0.521	44.101	80.71	18.58
0.04	0.521	44.095	80.69	18.57
0.05	0.522	44.091	80.68	18.57
0.06	0.522	44.084	80.67	18.57
0.07	0.522	44.078	80.65	18.56
0.08	0.522	44.071	80.63	18.55
0.09	0.522	44.064	80.60	18.55
0.10	0.522	44.056	80.56	18.54

impact on FF and efficiency. Table 2 shows that as the layer thickness increases, the FF and efficiency decreases for regions greater than 0.03 μm [7].

3.2 Effect of *p*-Si Layer Thickness

The thickness of the *p*-Si layer is varied between 140 and 200 μm depending on the availability of *p*-type Si wafers. As can be seen in Fig. 3, the effect of changing the *p*-Si thickness is not as strong, although the efficiencies do increase. However, increasing the *p*-Si layer thickness has little influence on the cell's performance characteristics such as efficiency and FF [7, 8]. The refractive index increases when the thickness of the *p*-Si layer, which has a longer wavelength, is raised. The short wavelength photons were completely absorbed by the top cell.

In order to get more photons from the longer wavelength, more thickness of the *p*-Si layer will be necessary. By keeping 140 μm thickness of *p*-Si layer, the efficiency which we achieved was 18.58% with FF = 80.71%. For area higher than 150 μm , with the increase in layer thickness, the J_{sc} decreases. While V_{oc} is significantly constant with the rise in the layer thickness for all values greater than 140 μm . However, increase in the layer thickness has more prime effect on the FF and efficiency. From Table 3, we can see that with increase in the layer thickness, FF and efficiency gradually falls for region higher than 140 μm .

3.3 Effect of CTS Layer Thickness

The most reliable absorber among the thin film solar cells is CTS. The direct band gap available in the CTS has the ability to absorb more than 90% of the incoming photons

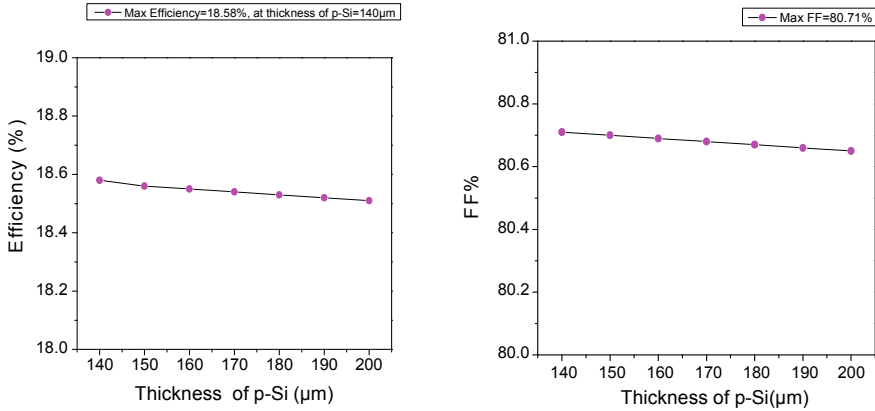


Fig. 3 Impact of the thickness of *p*-Si layer on efficiency and fill factor

Table 3 Parameter values for *p*-Si layer

Thickness of <i>p</i> -Si (μm)	V_{oc} (V)	J_{sc} (mA/cm ²)	FF %	Efficiency %
140	0.521	44.101	80.71	18.58
150	0.521	44.076	80.70	18.56
160	0.521	44.048	80.69	18.55
170	0.521	44.026	80.68	18.54
180	0.521	44.007	80.67	18.53
190	0.521	43.982	80.66	18.52
200	0.521	43.965	80.65	18.51

considering around 1.0 μm thickness. For experimental and numerical survey, the ideal thickness is 2.0 μm. Here, the efficiency is rising proportionally with the increasing thickness of layer. However, the rate at which the efficiency increases is less for every parameter in SCAPS-1D which has a thickness of more than 1.0 μm. Due to possible recombination of the electrons in the bulk, the efficiency will decrease if electrons take some amount of time to traverse from the absorber layer to the back contact. For shorter wavelength photon absorption purposes, CTS is a better option while compared with other alternatives solar cell material. A measure of 18.58% was achieved as the conversion efficiency and FF = 80.71% has been attained at the final time for CTS cell of 5.0 μm thickness (Fig. 4).

As we go on increasing the thickness of the layer for area more than 1 μm, J_{sc} also increases, while with the increase in the layer thickness there is a significant decrease in FF for region higher than 2 μm. However, increase in the layer thickness has more prime effect on the V_{oc} and efficiency. From Table 4, we can observe that with increase in the layer thickness, V_{oc} and efficiency gradually rises for region higher than 2 μm.

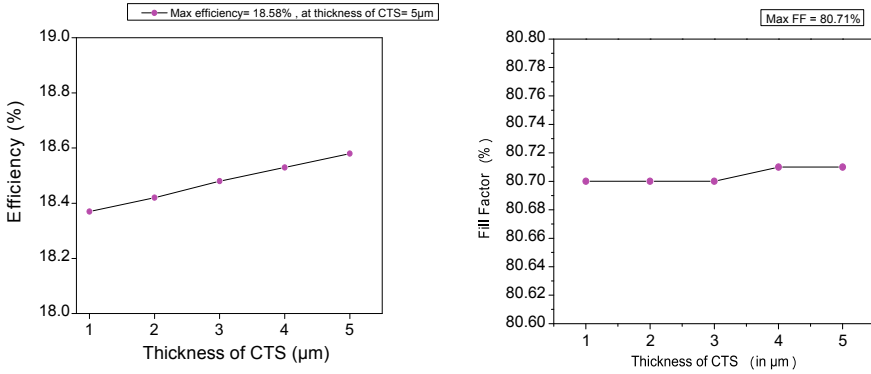


Fig. 4 Effect of CTS layer thickness on efficiency and fill factor

Table 4 Parameter values for CTS layer thickness

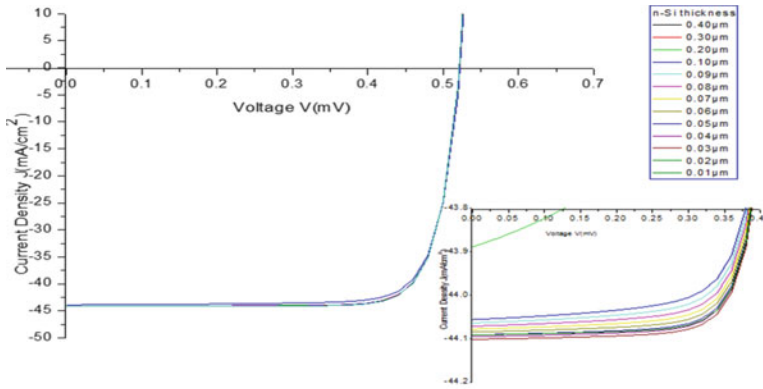
Thickness of CTS (μm)	V_{oc} (V)	J_{sc} (mA/cm ²)	FF %	Efficiency %
1	0.521	43.629	80.71	18.37
2	0.521	43.753	80.71	18.42
3	0.521	43.873	80.70	18.47
4	0.521	43.939	80.70	18.53
5	0.521	44.101	80.71	18.58

3.4 I–V Characteristics

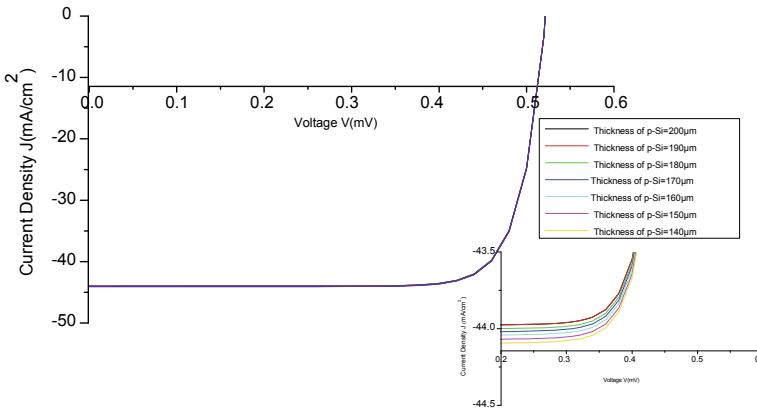
From the graph, Fig. 5 it is clear that the performance of *p*-CTS/*p*-Si/*n*-Si tandem solar cell is better than other CTS baseline cells in terms of efficiency. All the curves in the *I–V* plot are accurate for solar cells. It is clear that the effect is visible from the graph plotted for the spectral response for the solar cell which has the modifications.

3.5 Effect of CTS Carrier Concentration

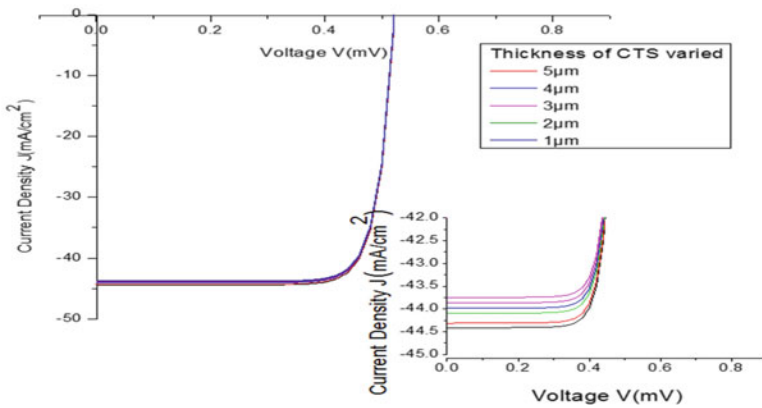
The features of the influence of CTS carrier concentration on tandem solar cells of *p*-CTS/*p*-Si/*n*-Si are shown in Fig. 6. The efficiency of the cell is shown to alter dramatically when the CTS carrier concentration is changed. It has been discovered that when concentration increases, efficiency declines. The fundamental cause is that the semiconductor turns metallic when the acceptor concentration exceeds 1.0×10^{18} . In fact, the CTS semiconductor’s range carrier concentration is 1.0×10^{14} or 1.0×10^{23} . As a result, we may deduce that $2.3 \times 10^{17} \text{ cm}^{-3}$ is optimized carrier concentration. With the rise in the carrier concentration higher than 10^{15} cm^{-3} , J_{sc} increases, while with the increase in the carrier concentration for region higher than



(a)



(b)



(c)

Fig. 5 $I-V$ Characteristics of p -CTS/ p -Si/ n -Si tandem solar cell by varying **a** n -Si, **b** p -Si, and **c** CTS thickness

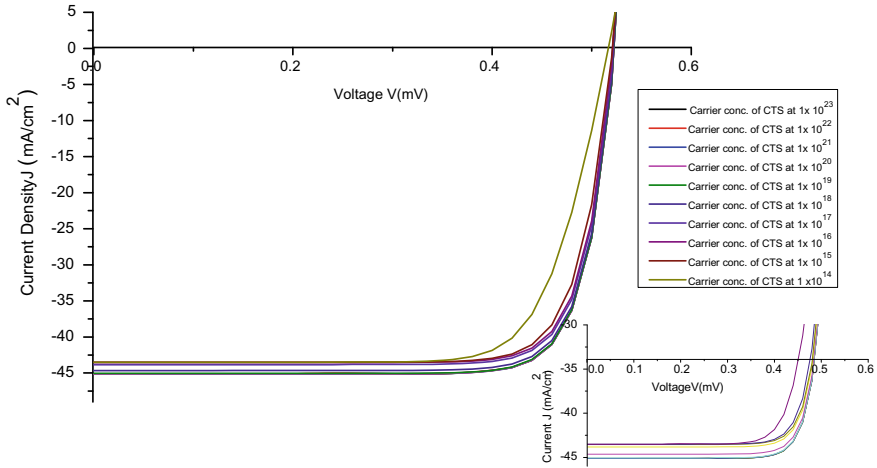


Fig. 6 Effect of CTS carrier concentration on *p*-CTS/*p*-Si/*n*-Si tandem solar cell

Table 5 Parameter values for CTS layer carrier concentration

Carrier concentration of CTS (cm ⁻³)	V _{oc} (V)	J _{sc} (mA/cm ²)	FF %	Efficiency %
1 × 10 ¹⁴	0.516	43.513	75.06	16.88
1 × 10 ¹⁵	0.520	43.518	79.71	18.07
1 × 10 ¹⁶	0.521	43.553	80.50	18.30
1 × 10 ¹⁷	0.521	43.836	80.69	18.45
1 × 10 ¹⁸	0.522	44.653	80.73	18.83
1 × 10 ¹⁹	0.522	45.059	80.75	19.02
1 × 10 ²⁰	0.522	45.123	80.75	19.05
1 × 10 ²¹	0.522	45.123	80.75	19.06
1 × 10 ²²	0.522	45.128	80.75	19.06
1 × 10 ²³	0.522	45.130	80.75	19.06

10¹⁵ cm⁻³, V_{oc} significantly increases and then remains constant. Increased carrier concentration, on the other hand, has a greater impact on FF and efficiency. Table 5 shows that for regions larger than 10¹⁵ cm⁻³, the FF and efficiency steadily improve as the carrier concentration increases.

3.6 Effect of Operating Temperature

The simulation involved varying the temperature from 300 to 425 K. The fact that the efficiency of the solar cell decreases with the rise in temperature has been shown

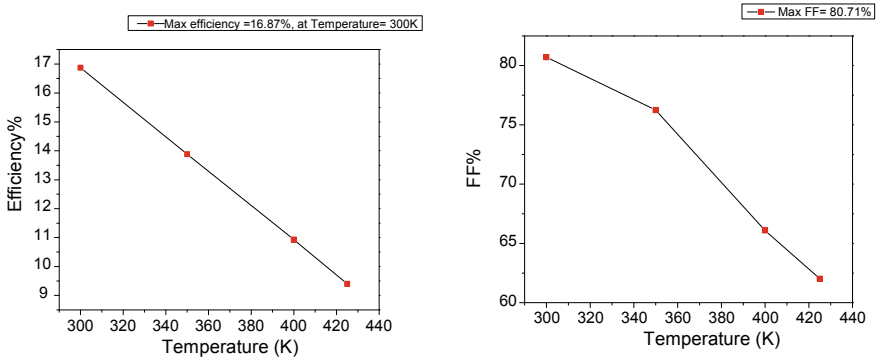


Fig. 7 Effect of temperature of *p*-CTS/*p*-Si/*n*-Si tandem solar cell on efficiency and fill factor

Table 6 Parameter values for varying temperature on *p*-CTS/*p*-Si/*n*-Si tandem solar cell

Temperature (K)	V_{oc} (V)	J_{sc} (mA/cm ²)	FF %	Efficiency %
300	0.521	44.101	80.71	16.87
350	0.448	45.457	76.25	13.88
400	0.374	47.382	66.08	10.93
425	0.335	48.290	62.02	9.40

in Fig. 7. Fill factor has been contrived by the rising temperature. Extreme heat leads to damaged cells and reduced life time. The maximum efficiency of 16.87% is achieved for the *p*-CTS/*p*-Si/*n*-Si tandem solar cell. When the temperature increases, the tendency in the energy band gap of the semiconductor shows a downward trend as well. This kind of behavior has been elaborated by Varshini equation, if one considers the space between the atoms rises when the atoms vibrate with greater amplitude due to the increase in thermal energy. Linear expansion coefficient of a material describes this effect.

With the rise in temperature above 300 K, the J_{sc} increases markedly, while there is a significant decrease in V_{oc} with the increase in the temperature for region higher than 300 K. However, increase in the temperature has more prime effect on the FF and efficiency. From Table 6, we can see that with rise in the temperature, FF and efficiency gradually falls for region higher 300 K.

3.7 Simulation Results

To connect the load combination and battery with the PV array, a boost converter was utilized instead of a series and shunt type of controller since it allows for optimal usage and smooth control of the PV source. The boost converter regulates the output

of the PV array in order to feed the load. Figure 8 shows an example of a simple arrangement. To check or decrease harmonic distortions, the traditional inverter can be replaced by a multilayer inverter (Table 7).

In Figs. 9 and 10, the load voltage and load currents have been shown, respectively, with the parameters considered during simulation.

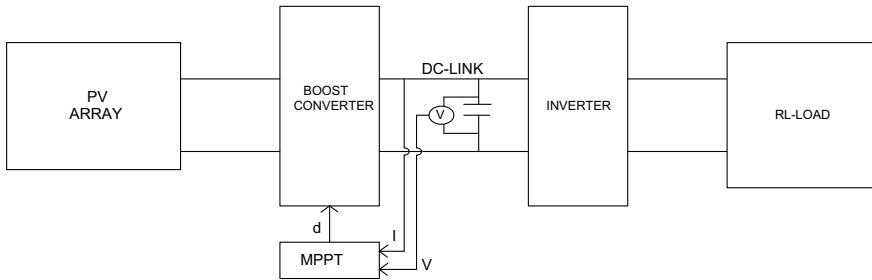


Fig. 8 Circuit diagram of PV cell

Table 7 Parameters of different components used in simulation

Name of components	Ratings
Inductance	1.15 mH
Capacitance	4.03 mF
Load resistance	100 Ω
K_C	0.044 A/cm ²
Q	1.69e ⁻¹⁹ C
K	1.38e ⁻²³ JK ⁻¹
N	1.3
E_{go}	0.87 eV
R_s	3 Ω
R_{sh}	500 Ω
T_n	298 °C
V_{oc}	0.5219 V
I_{sc}	1 A
N_s	20
T	Operating temperature

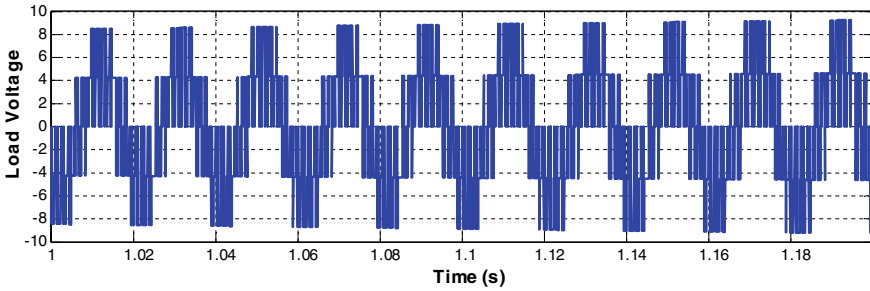


Fig. 9 Load voltage with RL load

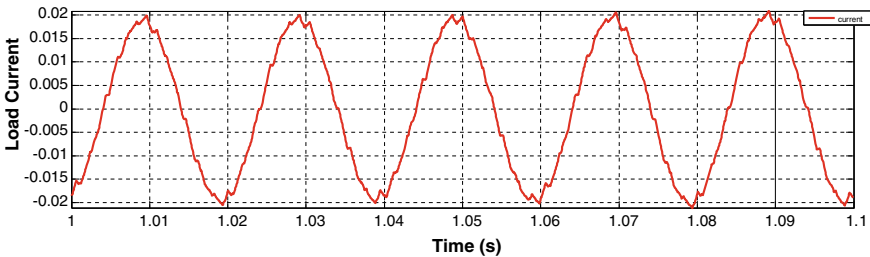


Fig. 10 Load current with RL load

4 Conclusion

The numerical investigation which was conducted on this work explored the regular CT-based solar cells with slight modifications in the silicon tandem structure. In this SCAPS-1D simulation, the n -Si, p -Si and the p -CTS layers' thicknesses were varied and the ideal output parameters of the cell were found. The observed result from the simulation which showed that the tandem structure helps in increasing the efficiency. The parameters which were finally obtained from the output were $V_{oc} = 0.5219$ V, $J_{sc} = 44.1016$ mA/cm², and FF = 80.71%, and the achieved conversion efficiency was increased to 18.58%. On the other hand, a basic CTS solar cell has a significantly lower efficiency of 3.7637%. Moreover, the conversion efficiency and the temperature rise are inversely proportional which depicts the better stability of the cell at 300 K.

Therefore, it can be expected that with the given modifications in the CTS structure, an efficient and economical p -CTS/ p -Si/ n -Si tandem thin film solar cell is possible to develop using rudimentary fabrication methods for real-life purposes in the upcoming days.

Simulation results have been observed with the load current having minimal THD which proves to be better for various load applications.

References

1. Silvi, C.: 2004 Survey of Energy Resources, 20th edn., pp. 295–334 (2004)
2. Chierchia, R., Pigna, F., Valentini, M., Malerba, C., Salza, E., Mangiapane, P., Polichetti, T., Mittiga, A.: Cu_2SnS_3 based solar cell with 3% efficiency. *Phys. Status Solidi C* **13**, 35–39 (2016)
3. Bal, S.S., Basak, A., Singh, U.P.: Numerical modeling and performance analysis of Sb-based tandem solar cell structure using SCAPS–1D. *Opt. Mater.* **127**, 112282 (2022)
4. Heriche, H., Rouabah, Z., Bouarissa, N.: New ultra-thin CIGS structure solar cells using SCAPS simulation program. *Int. J. Hydrogen Energy* **42**(15), 9524–9532 (2017)
5. Lokhande, A.C., Chalapathy, R.B.V., He, M., Jo, E., Gang, M., Pawar, S.A., Lokhande, C.D., Kim, J.H.: Development of Cu_2SnS_3 (CTS) thin film solar cells by physical techniques: a status review. *Solar Energy Mater. Solar Cells* **153**, 84–107 (2016)
6. Saha, A., Banerjee, P., Basak, A., Singh, U.P.: Effect of annealing on the thin $\text{Cu}_2\text{Sn}(\text{S}_x, \text{Se}_{1-x})_3$ films deposited by chemical route. In: International Conference on Applied Electromagnetics, Signal Processing and Communication (AESPC), pp. 1–4 (2018)
7. Basak, A., Deka, H., Mondal, A., Singh, U.P.: Effect of Substrate on the structural, optical and electrical properties of CuSnS thin films prepared by doctor blade method. *Mater. Today: Proc.* **4**(14), 12529–12535 (2017)
8. Sha, R., Basak, A., Maity, P.C., Badhulika, S.: ZnO nano-structured based devices for chemical and optical sensing applications. *Sens. Actuators Rep.* **4**, 100098 (2022)

Expansion of the Burners Structure to Boost up the Ecological Properties of an Average Capacity Boiler “E-270-13.73-560”



Uthum Gunasekara  and Nilan Jayasinghe 

1 Introduction

Industrial high-temperature super-heating processes require significant amounts of energy, usually generated by the combustion of hydrocarbon fuels such as coal, natural gases, or fuel oil. Fossil fuel burning gives the bulkiest capacity of energy for humans in electricity power generation, transportation, central heating, industrial heating, and so on. Nevertheless, the by-product of pollutants such as carbon monoxide (CO), carbon dioxide (CO₂), nitrogen oxides (NO_x), sulfur dioxide (SO₂) gases, and combustions are a serious threat to the global environment and the existence of the human beings [1]. With the increasingly stringent regulations globally for pollutant gases emission from combustion process, and modern hi tech technologies with high efficiency, high effectively, and low pollutant gases emission are needed. Thermal power engineering is the leading branch of the global energy sector. It plays a significant role in the development of industry in many countries of the world. Still, it exceeds all other sectors in emissions of pollutants into the atmosphere (ash particles, sulfur dioxide, nitrogen, and carbon oxides). Since the coal fuel and energy cycle is one of the most environmentally hazardous, developed countries refuse to use it, choosing a more environmentally friendly fuel—natural gas [2]. For developing countries, the impact on the environment remains a secondary factor, and traditional coal-fired energy is successfully developing due to its low cost. The development of the energy sector is leading in creating technologies to reduce the negative impact on the environment. Currently, various methods are used to minimize harmful dust

U. Gunasekara (✉)

Higher School of Nuclear and Thermal Power Engineering, Peter the Great St. Petersburg Polytechnic University, Saint-Petersburg, Russia
e-mail: uthumgunasekara@gmail.com

N. Jayasinghe

Higher School of High Voltage Energy, Peter the Great St. Petersburg Polytechnic University, Saint-Petersburg, Russia

and gas emissions at coal-fired TPPs: changing combustion technology and cleaning gases after combustion [3]. Changes in combustion technology include the use of modified burners, recirculation of exhaust gases, staged fuel combustion, plasma preparation of low-grade coals for combustion, radiation technologies, and combustion of fuel in fluidized bed furnaces. This research paper discusses changing the direction of the burners' rotation since its implementation at operating TPPs requires low investment and contributes to a significant reduction in NO_x emissions. In addition, when this technology is combined with other measures to control and reduce NO_x formation, it is possible to achieve the maximum reduction in their emissions. Using numerical simulation methods, research has been carried out to determine the effect of introducing the technology of combustion coal process on the main characteristics of heat, NO_x emission, and mass transfer processes in the furnace of the E-270-13.73-560 steam boiler.

The main purpose of this research paper is to develop and increase the environmentally friendly performance and the efficiency of the superheated-steam generation boiler by boosting the design direction of rotation of the burners.

2 Methods and Characteristics of Research

The object of this research paper, steam boiler "E-270-13.73-560" is considered. U-shaped designed layout with natural circulation and solid slag removal, and drum boiler [4–6]. The steam boiler furnace is finished gas-tight with dimensions in the proposal of $12,000 \times 8000$ mm (screen pipes along the axes length and width). According to the calculation, the supposed fuel for the superheated-steam generation boiler is hard coal of grade name D of the INTHINSKOE field. The design essentials of the steam boiler are given in Table 1.

The physical and technical characteristics of hard coal operated for computation are given in Table 2.

Table 1 Describe characteristics of the steam boiler E-270-13.73-560

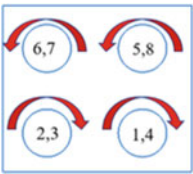
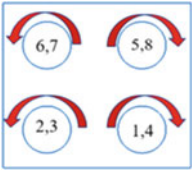
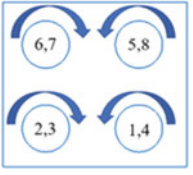
Title	Dimension	Designation	Value
Temperature of steam	°C	$T_{t.o.s}$	560
Steam capacity	kg/s; (t/h)	D	75 (270)
Pressure of overheated steam	MPa; (kg/cm ²)	$P_{p.o.s}$	13.73 (140)
Pressure of feedwater	MPa; (kg/cm ²)	$P_{p.o.f}$	15.7 (160)
Temperature of feed water	°C	$T_{t.f.w}$	210
Estimated coefficient of efficiency (gross)	%	$K_{e.c.e}$	93.21
Total fuel rate	kg/s; (t/h)	$B_{t.o.t}$	11.77 (42.375)
Temperature of flue gases	°C	$T_{t.f.g}$	140
Temperature of hot air	°C	$T_{t.h.a}$	350

Table 2 Technical characteristics of hard coal of grade named of the INTHINSKOE field

Character	Dimension	Designation	Value
Devolatilization (dry ash free)	%	V^c	40
Lower heating value	MJ/kg	Q_H^p	17.69
Carbon content	%	C^c	46.5
Oxygen content	%	O^c	8.50
Nitrogen content	%	N^c	1.25
Hydrogen content	%	H^c	3.09
Sulfur content	%	S^c	2.51
Ash content	%	Ash ^c	24.15
Humidity	%	W^c	14

Table 3 is given the arrangements of burners which were performed for three modifications of change the direction of rotation of the burners in the boiler when the hub-trip ration $m = 0.3$; swirl factor $n_1 = 1.5$; and $n_2 = 3.0$ parameters are constant.

Table 3 Compromises of burners

Variant No.	Quantity of burners	Position of burners in the furnace	Direction of rotation of the burners
1	8	Opposite	
2	8	Opposite	
3	8	Opposite	

3 Designing Steam Boiler Model E-270-13.73-560 by Using the SigmaFlame Software Package Research Analysis Appliance

The SigmaFlame SigmaFlow software package is a primary research tool which was developed by universal CFD software package SigmaFlow VTI (Moscow), SFU (Krasnoyarsk), IT SO RAN (Novosibirsk), and SibENTC (Krasnoyarsk), which has a better matching experimental data of calculated results. The SigmaFlame software regulates the concentrations of NO_x brought about by three mechanism structures: fuel NO_x , thermal, and “fast” [7–9].

To demonstrate the perimeters of the replicated operational area, applying the combustion chamber furnace constructor application, relative to the parameters under deliberation (Table 3), a three-dimensional model (3D model) of the steam boiler furnace “E-270-13.73-560” it was built Fig. 1a, afterward which, to carried out the definite volume design, the furnace area was separated into grid-cells Fig. 1b.

The numerical simulation of the combustion chamber processes through the SigmaFlame is carried out applying an affiliation of physical models representing the

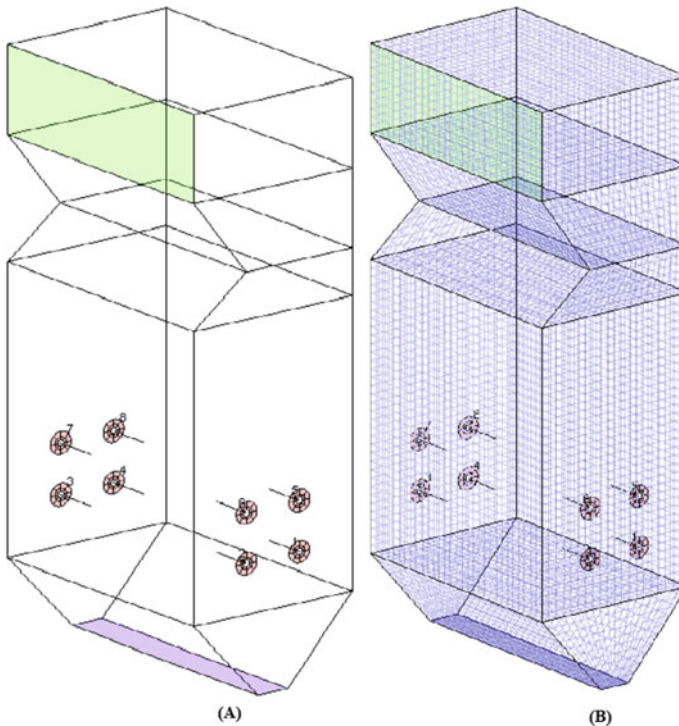


Fig. 1 Steam boiler model E-270-13.73-560 with burners **a** boiler view; **b** boiler view with grid-cells

aerodynamics of the furnace, radiation and convective heat exchange, combustion of coal particles, slagging processes on the walls, and the formation of NO_x .

A mathematical model of a non-isothermal incompressible multi-dimensional gas is applied to describe the flow in the furnace. Gas flow model includes continuity equations, momentum equations, transfer equations, and energy transfer equations [10].

In accordance with this model, boiler has calculated the chemical under burning (q_3) is determined by the formula [11].

$$q_3 = \frac{Q_{\text{chem.ub.}}}{Q_T}; \quad (1)$$

where $Q_{\text{chem.ub.}}$ —total chemical under burning (MW) and Q_T —heat output of the furnace.

The mechanical under burning q_4 calculated in SigmaFlame turned out to be higher than the standard in the thermal calculation of the boiler (the total residue on the sieve is $90 \mu\text{m } R90 = 33\%$; the polydispersity coefficient $n = 1.3$. Mass second flow of NO_x at the outlet of the furnace (G_{NO_x})

$$G_{\text{NO}_x} = \mu_{\text{NO}_x} \cdot \sum G_r \quad (2)$$

where μ_{NO_x} —average NO_x concentration in the selected furnace cross-section, (kg/kg); $\sum G_r$ —mass second flue gas flow rate. Concentration of nitrogen oxides in exhaust flue gases, mg/m^3

$$M_{\text{NO}_x} = \frac{G_{\text{NO}_x}}{V_G} \quad (3)$$

where V_G —specific volume of flue gases at $\alpha = 1, 4$. Mass NO_x emission (kg/Ton of fuel equivalent)

$$m_{\text{NO}_x}^{\text{F.E.}} = \frac{G_{\text{NO}_x} \cdot 3600}{B_{\text{H.N.F.C}}} \quad (4)$$

where $B_{\text{H.N.F.C}}$ —hourly nominal fuel consumption (T/h.): According to the upper formulas and the numerical calculation have calculated for three variants and below shown results wherein Table 4.

4 The Analysis and Discussion of Numerical Results of the Designing Furnace Process

According to the analysis in the given variants, did not change other conditions, but only changed the direction of rotation (wherein Table 3).

Table 4 Calculated results for three variants of boiler

Variant No.	The average NO _x concentration	Chemical under burning	Mechanical under burning	Concentration of nitrogen oxides in exhaust flue gases
	(kg/kg); (10 ⁻⁴)	<i>q</i> ₃ : %	<i>q</i> ₄ : %	<i>M</i> _{NO_x} ; mg/M ³
1	4.233	0.01	0.0968	327.44
2	4.530	0.05	0.659	377.20
3	4.249	0.05	0.0965	343.12

And upper are given Fig. 2 shows the vector field of gas velocities, the aerodynamics of the furnace; a boiler installation is installed in the furnace chamber. The gas flow pattern generally corresponds to what is given in the sources in [12, 13]. There are three different circulation zones in the furnace. The lower vortex occupies the cold funnel, and the gas velocity is about 20–25% of the initial one. On the front wall, the vortex velocity is slightly lower [14, 15]. The formation of the third vortex (on top of the aerodynamic projection) is influenced by the features of the software—the restrictions that are imposed when creating three-dimensional models of the furnace, and the small maximum number of grid-cells in the demo version in the SigmaFlame software package (50,000 pieces).

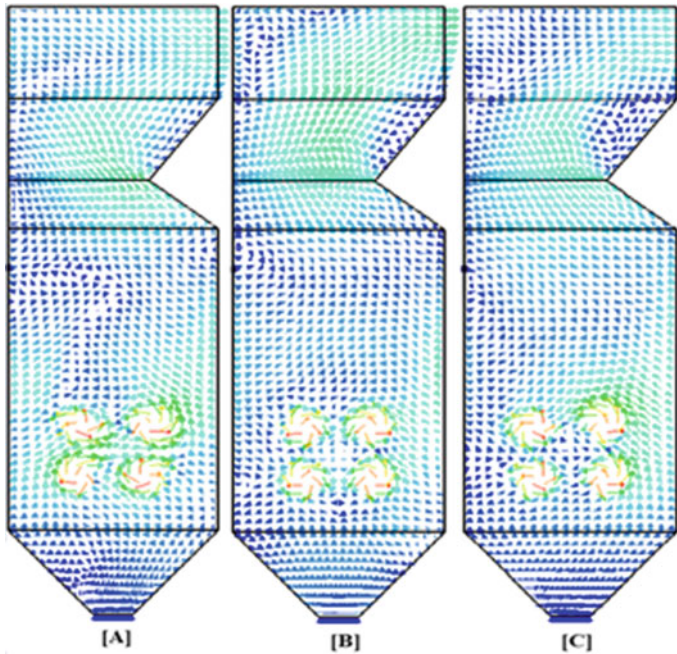


Fig. 2 Vector field of gas velocities, the aerodynamics of the furnace. Numerical simulation results for the variants; a 1; b 2; c 3

The numerical simulation of the hard-coal combustion chamber process in the steam boiler furnace E-270-13.73-560 focused for coal with the consecutive granulometric typical features: total sieve residue with cell size $90 \mu\text{m}$ when $R90 = 33\%$ [16], where the polydispersity index $n = 1.3$. The size of the bulkiest particle decided alike to the propositions $\beta = 650 \mu\text{m}$ [17]. The research analysis results are given for the longitudinal dimensional view of the steam boiler furnace penetrating the edge of the burners.

Trajectories of burning hard-coal dust particles (sprinkle tiny particles) in the superheated-steam generation boiler E-270-13.73-560 for the given numerical simulation options are given in Fig. 3. The color of the flow line correlates to the particle velocity: gold color for high speed ($V_{(p, \max)} \approx 30 \text{ m/s}$) and blue color for low speed ($V_{(p, \min)} \approx 6 \text{ m/s}$). Consequently, the flow is ejected onto the rear screens of the furnace, and the slopes of the inclined lower side (bottom) are given in Fig. 3a, which essentially increases the likelihood of slag formation on these surfaces. In the first simulation, Fig. 3b and c is shown the particle velocity decreases, which fall off the dynamic impact of the flame on the screens and the erosive wear of the convective heating surfaces of the screen.

The gas temperature circulation in the central longitudinal zone of the furnace is given in Fig. 4. In the version, Fig. 4a shows the climax highest temperature of the flame core probably deviated close to the rear end screens of the furnace. The distribution of coal sprinkle tiny particles on them boosts the likelihood of slag formation.

When the burners are positioned in such a way that a different direction of rotation is set from above (Fig. 4b and c), the flame core is concentrated in the center of the boiler furnace, but the temperature in the lower part increases.

The location of the burner designs in the boiler furnace has a considerable reaction on the number of NO_x formed, as given in Fig. 5. When building the concentration fields of NO_x , the total concentration of fuel, thermal, and fast NO_x was contemplated. The formation of NO_x fuel depends mainly on the aerodynamic scheme of the gas flow in the chamber is determined by the value of the maximum temperature in the boiler furnace and the combustion rate in the section under deliberation. The maximum temperature value determines the formation of thermal NO_x in the steam boiler's furnace and the combustion chamber's speed in the research study area.

The total amount of nitrogen oxides generated relies on which factors (furnace speed or residence time) will have the most effective effect on the process in the combustion chamber. Based on the numerical simulation analysis results, the upper is given in Fig. 5 reduces nitrogen oxide emissions.

According to the variants of Fig. 5a, the NO_x concentration in the combustion furnace decreases, and the variants (b and c) increase and according to the analysis can be recommended that the considered option (a) (the first option) is the best in terms of efficiency and environmental friendliness.

The concentrations of NO_x (mg/nm^3)—under the general conditions when $\alpha = 1.4$ in the flue gases at the furnace outlet for versions 1–3 are given in Fig. 6.

The values of mechanical under burning calculated by the program for all variants were less than the calculated value of $q_4 = 1\%$. In the second variant, there is

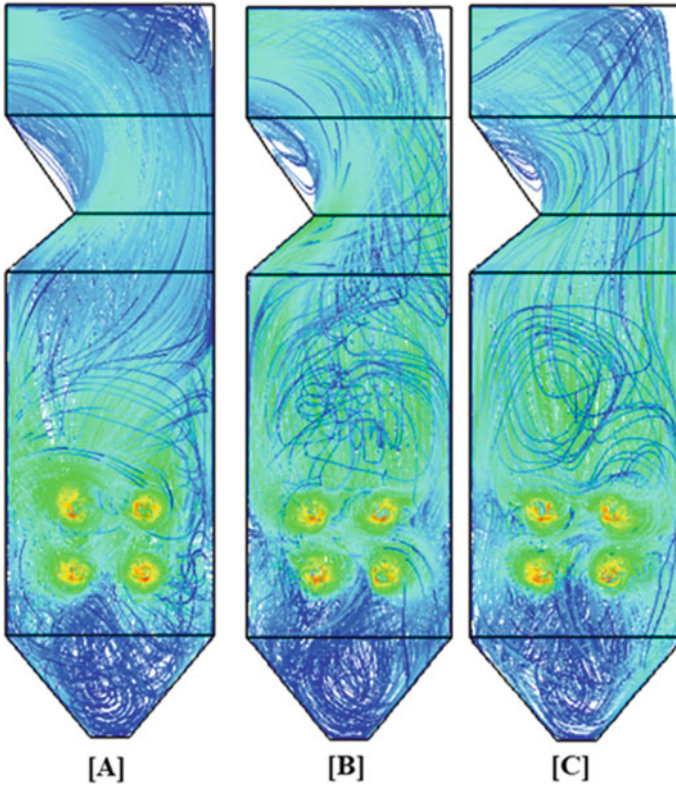


Fig. 3 Trajectories of burning coal particles in the central longitudinal zone of the furnace for versions: **a** 1; **b** 2; **c** 3

a high probability of slagging the rear screens of the furnace and, in addition, a high concentration of nitrogen oxides in the exhaust gases. From the first and third variants, the NO_x concentration in the furnace decreases compared to the second option. According to the totality of the considered characteristics and parameters, it shows that the first option under consideration is the best in terms of efficiency, the most environmentally friendly, and safe choice of each option: the value of mechanical under burning was approximately a tiny part of the calculated value, chemical under burning was insignificant (moreover, it should bear in mind that the calculation of q_3 was performed by the program in the calculated section at the level of the end of the aerodynamic projection), increased dynamic impact of the burner on screens, and particle contours are not observed; the NO_x concentration is the lowest of all the options considered and is almost equal to the permissible value according to GOST R 50831-95 [18]. A more visual representation of the decrease in the concentrations of nitrogen oxides in the flue gases are given in Fig. 6.

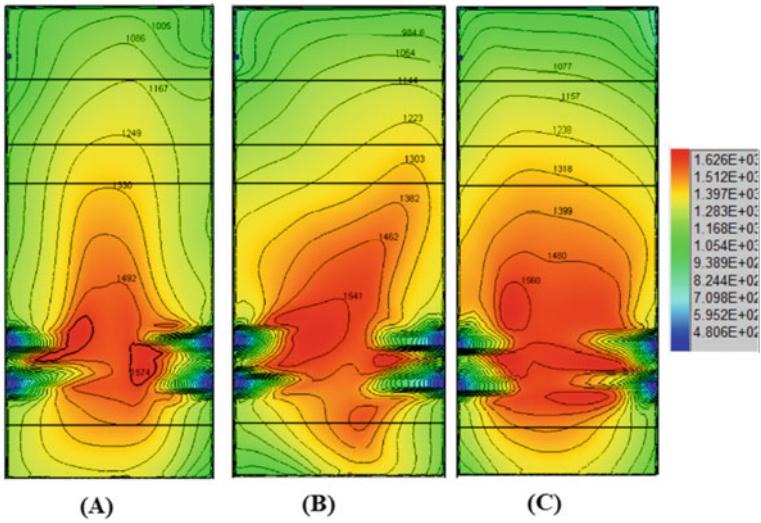


Fig. 4 Circulation of gas temperature in the central longitudinal zone of the furnace passing through the central burners for versions: a 1; b 2; c 3

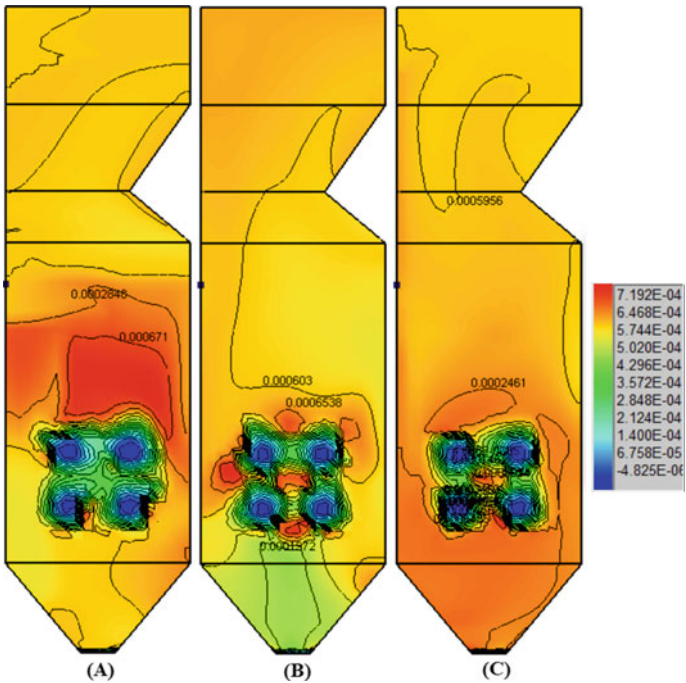


Fig. 5 Circulation of concentration of nitrogen oxides in the central longitudinal zone of the furnace for versions: a 1; b 2; c 3

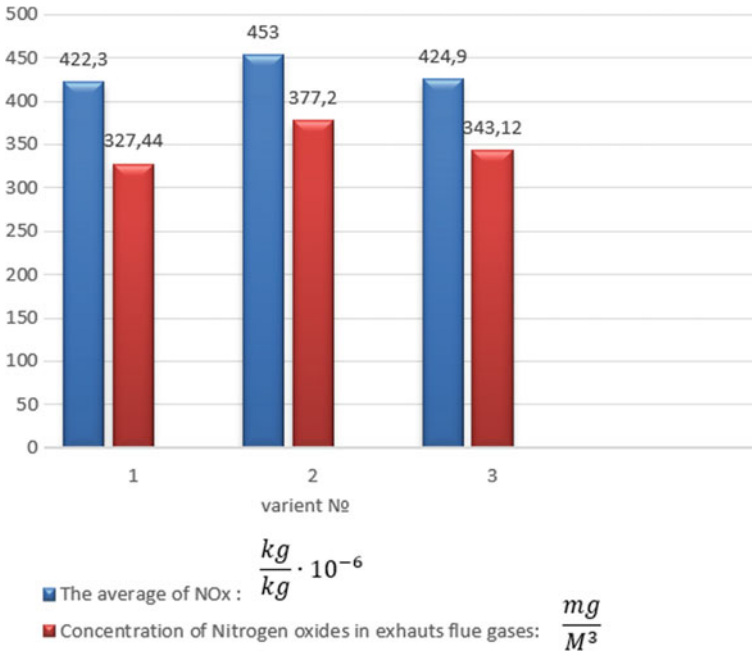


Fig. 6 Concentrations of NO_x in flue gases at the outlet of the furnace for calculated versions

According to the research analysis, the first variant of the rotation direction of burners in the combustion furnace and their design characteristics is the most recommendable and efficient because it provides the lowest concentrations of NO_x and satisfies the administrative exigencies for the level of NO_x emissions during combustion chamber process. The first variant is the environmental friendliness option for reducing greenhouse gas emissions.

5 Conclusion

According to the calculated results of the analysis of each variant of numerical simulation, an analysis of devices for all selected variants of burner devices was carried out. In all cases, fuel combustion efficiency was increased (mechanical under burning index q_4 does not exceed the calculated values according to standards, and the chemical under burning index q_3 is close to 0%). In the third variant, there is a high probability of slagging the rear screens of the furnace and, in addition, a high concentration of nitrogen oxides in the exhaust gases. From the first to the third and fifth variants, the NO_x concentration in the furnace decreases. Per the characteristics considered in general, it is possible to discuss and decide that the best efficiency, environmental friendliness, and safety are the first option under consideration. There

is no such drawback; in addition, the NO_x concentration in the flue gases is lower. Of all the options, the first option was chosen as the best in terms of characteristics. (Eight burners in the opposite arrangement, the sleeve coefficient $m = 0.3$; the twist coefficient of the dust-air mixture $n_1 = 1.5$; the twist coefficient of the secondary air $n_2 = 3.0$). The decrease in the NO_x concentration at the outlet was reduced in this version by 15.2% compared to the third version.

References

1. Gaber, C., Schluckner, C., Wachter, P., Demuth, M., Hochenauer, C.: Experimental study on the influence of the nitrogen concentration in the oxidizer on NO_x and CO emissions during the oxy-fuel combustion of natural gas. *Energy* **214**, 118905 (2021). <https://doi.org/10.1016/j.energy.2020.118905>
2. Tu, Y., Xu, S., Xie, M., Wang, Z., Liu, H.: Numerical simulation of propane MILD combustion in a lab-scale cylindrical furnace. *Fuel*, **290**(November 2020), 119858 (2021). <https://doi.org/10.1016/j.fuel.2020.119858>
3. Askarova, A., Bolegenova, S., Maximov, V., Bolegenova, S., Askarov, N., Nugymanova, A.: Computer technologies of 3D modeling by combustion processes to create effective methods of burning solid fuel and reduce harmful dust and gas emissions into the atmosphere. *Energies* **14**(5), 1236 (2021). <https://doi.org/10.3390/en14051236>
4. Access, O.: Development of engineering and technical environmental measures for technogenic atmospheric pollution by thermal power facilities Development of engineering and technical environmental measures for technogenic atmospheric pollution by thermal power facilities (n.d.). <https://doi.org/10.1088/1757-899X/962/4/042067>
5. Maryandyshv, P.A., Chernov, A.A.: Numerical simulation of the furnace process of a low-emission vortex boiler. *Int. J. Exp. Educ.* **7**, 59–66 (2015). <http://expeducation.ru/ru/article/view?id=7728>
6. Kiselgof, M.L., Sokolov, N.V.: Calculation and design of dust preparation installations of boiler units (Normative materials). Guidelines. Leningrad: CCTI 316p (1971) (In Russian)
7. Chernetsky, M.Y.: Improvement of heat transfer modeling in coal-dust combustion chambers with solid slag removal. In: Abstract of the Dissertation for the Degree of Candidate of Technical, Sciences, Novosibirsk, IT SB RAS (2012) (In Russian)
8. Chernetsky, M.J., Degtyarev, A.A.: Experience using the package SigmaFlame programs for optimizing the operation of coal-dust power boilers. In: Mat. of the IX All-Russian Conference with International Participation “Fuel Combustion: Theory, Experiment, Applications”. Institute of Thermophysics SB RAS (2015) (In Russian)
9. Experience of using the Sigmaflame software package to optimize the operation of pulverized coal power boilers—pdf download for free.pdf (n.d.) (In Russian)
10. Dvoinishnikov, V.A., Deev, L.V., Izyumov, M.A.: Design and calculation of boilers and boiler installations. In: Textbook for Technical Schools in the Specialty “Boiler Building” , 264p (1988) (In Russian)
11. Kotler, V.R.: Nitrogen oxides in flue gases of boilers. *Energoatomizdat* (1987) (141, p: ill.; 22 cm. Nitrogen, oxides—Formation Atmosphere—Pollution Waste gases of thermal power plants—Cleaning FB 2 87-46/346 FB 2 87-46/345)
12. Chernov, A.A., Maryandyshv, P.A., Pankratov, E.V., Lyubov, V.K.: CFD simulation of the combustion process of the low-emission vortex boiler. *J. Phys.: Conf. Ser.* (2017). <https://doi.org/10.1088/1742-6596/891/1/012216>
13. Izyumov M.A., Roslyakov P.V. /Ed. Vilensky T.V. Design and calculation of burners. M.: Publishing House of MEI, 1990 - 115 p. (in Russian)

14. Khzmalyan, D.M.: Gorenje theory and furnace devices. In: Kagan, Y.A. (ed.) Textbook for Heat and Power Engineering Specialties of Universities. Technical Sciences, 487p. Energia, Moscow (1976). FB B 76-13/150 FB B 76-13/151
15. Vortex pulverized coal burners, dust and gas burners and their arrangement with furnaces. Methods of calculation and design of OST 108.030.26-78. Editorial and publishing department of the NGO TSKTI named after I.I. Polzunov. Leningrad, 64p (1979) (in Russian)
16. Thermal Calculation of Boiler Units (Normative Method). "Energia" Publishing House, Moscow (1973) (In Russian)
17. V.V. Pomerantsev, K.M. Aref'ev, and D.B. Akhmedov, "Fundamentals of practical combustion theory", Leningrad: "Energoatomizdat", 1986. (In Russian)
18. GOST R 50831-95 Boiler installations. Thermal mechanical equipment. General technical requirements (In Russian)

Rearrangement of the PV Array to Reduce the Effect of Partial Shading Using Meta-Heuristic Techniques



Reeva Dhariwal and Bhavnesh Kumar

1 Introduction

Non-renewable resources have begun to deplete at an alarming rate, and the world is now searching for other safer options. As a result, the increasing use of renewable energy sources is the most obvious solution to this problem. Solar energy is gaining momentum in the field of power generation. Photovoltaic panels are used in this case whose output is affected by the illumination received by the PV modules. The PV modules are connected in different interconnection patterns namely series–parallel (SP), bridged-link (BL), honey-comb (HC), and total cross-tied (TCT) to improve the output [1]. Further, improvement in the shade dispersion can be achieved with the reconfiguration of PV panels based on Su Do Ku [2], puzzle shade [3], magic square [4], zig-zag [5], and odd–even [6] technique. Another method is the electrical array reconfiguration (EAR) scheme, which uses a high-speed processor, low-cost switching devices, and data acquisition system to disperse the shade. Researchers in [7] discussed another EAR method by inserting a controlled switch matrix between the PV array and the inverter. Although EAR shows good output, but they were not practical for the large PV system. Apart from the standard EAR system, the researchers in [8] presented fast switching matrix (FSM) for shade dispersion. Similarly, dynamic electrical scheme (DES) reorganization had also been proposed, but the use of two independent algorithms limits the flexibility of this scheme [9].

R. Dhariwal (✉)

Electrical Engineering Department, Netaji Subhas University of Technology, Delhi, India
e-mail: reevad.ee20@nsut.ac.in

B. Kumar

Instrumentation and Control Engineering Department, Netaji Subhas University of Technology, Delhi, India
e-mail: Kumar_bhavnesh@nsut.ac.in

The previous attempts to mitigate the negative effects due to shading in the PV system have several drawbacks such as skilled workers, complex switching combinations, and rewiring. Therefore, one of the possible ways to solve the above problem is to use meta-heuristic optimization, since they provide suitable switching combination that shows better results. This paper discusses two meta-heuristic optimization algorithms namely particle swarm optimization (PSO) and genetic algorithm (GA). Genetic algorithm (GA) was demonstrated in [10], which showed that this technique gives the better result as compared to the TCT and Su Do Ku arrangement. This method has the drawback of poor convergence and large computational steps. Hence, particle swarm optimization (PSO) was proposed in [11]. PSO can deal with large solution space which makes this method more suitable for EAR problems. In this paper, a comparison is done between reconfigured PV array based on GA and PSO taking into consideration BL-TCT, HC-TCT, and TCT interconnections.

2 System Description

2.1 Model of the PV Cell

The electrical equivalent circuit of the PV cell is shown in Fig. 1. The PV cell can be connected in a variety of configurations to form the PV array. The current of the PV array is given by

$$I_a = N_{PP} \left(I_{ph} - I_0 \left[\exp \left(\frac{V + I R_S}{V_T N_{SS}} \right) - 1 \right] \right) - \frac{V + I R_S}{R_P} \tag{1}$$

where I_a is the PV array current, N_{SS} and N_{PP} are the number of modules connected in series and parallel, respectively, I_{ph} is photon current, R_S is series resistance, R_P is parallel resistance, I_0 is the reverse saturation current, I is current of PV cell, and $V_T = \frac{N_s K T}{q}$ is the thermal voltage.

For experimentation, PV module BP Solar BP3170N with specification at standard test conditions (STC) of 1000 W/m², 25 °C is used and given in Table 1.

Fig. 1 Equivalent circuit of PV cell

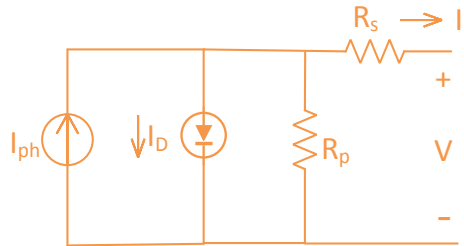


Table 1 Specifications for PV module BP solar BP3170N

Parameter	Value
Maximum power	170.88 W
Open circuit voltage	44.3 V
Short circuit current	5.2 A
Nominal voltage	35.6 V
Nominal current	4.8 A

2.2 PV Array Configurations

The conventional configurations of the PV array are series–parallel (SP), bridged-link (BL), honey-comb (HC), and total cross tied (TCT). The BL-TCT configuration is formed using BL and TCT scheme, similarly, HC-TCT configuration is formed using HC and TCT scheme. In this paper, TCT, BL-TCT, and HC-TCT configurations are considered to perform the optimization techniques during partial shading condition and the results are compared before and after the reconfiguration. Figure 2 represents the above mentioned PV array reconfiguration schemes.

3 Reconfiguration Using Meta-Heuristic Optimization Algorithm

3.1 Genetic Algorithm (GA)

Genetic algorithm is one of the meta-heuristic techniques formulated on Darwin’s principle-based stating “survival of the fittest”. This method focuses on increasing the output power of the PV array by minimizing the current difference of each row. The GA optimization depends mainly on two factors, i.e., generating the population and fitness function. The fitness function in the reconfiguration of the PV array is defined as follows:

$$\text{Max}(f(i)) = \text{sum}(P) + \left(\frac{W_e}{E_e}\right) + (W_p * P_a) \quad (2)$$

where $f(i)$ denotes fitness corresponding to i th element, $\text{sum}(P)$ is the total power, E_e is the sum of the error difference between maximum row current, i.e., $E_e = \sum_{k=1}^6 |I_m - I_k|$, I_m is the maximum value of current when bypassing is considered, P_a is the output power without bypassing, and W_e and W_p are the weights having value 10.

The rate of convergence about the global optimum point depends on the parameters of the genetic algorithm. Hence, selecting a parameter is a problem in case of GA. Therefore, for the algorithm to converge at the global optimum point, some

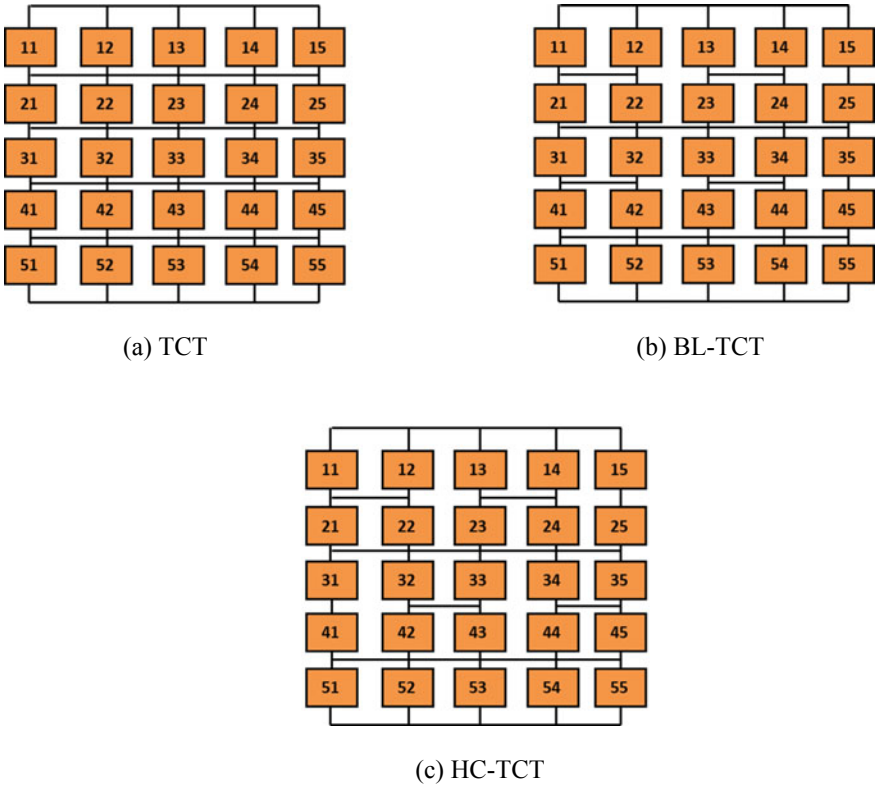


Fig. 2 Various configurations of PV array. **a** TCT, **b** BL-TCT, **c** HC-TCT

parameters such as population size and the number of iterations are fixed and some parameters such as the mutation and crossover probability, and point of crossover can be randomly chosen.

3.2 Particle Swarm Optimization (PSO)

PSO is an optimization algorithm used to solve any nonlinear stochastic problem. This technique is based on the behavior of the flock of organisms, such as a swarm of birds and fishes. In this optimization, the particles in the group keep the local best solution known as p_{best} as well as the global best solution known as g_{best} for a given problem with each successive sequence so that the algorithm can achieve the optimum solution. The steps followed in this algorithm for reconfiguration are as shown below:

Step 1 Initialization: Firstly, initialization of parameters such as social constant (C_c), cognitive constant (C_g), and weight (W) is done having values 1.20, 1.80, and 0.90, respectively. The initial velocity of each particle can be calculated using the following equation

$$\text{vel}(k) = 1 + \text{round}(\text{rand}() * 8) \quad (3)$$

where k is particle number.

Step 2 Irradiance Evaluation: The irradiance received by the PV module can be evaluated through sensor system. Otherwise, the irradiance is calculated the as follows:

$$G_{ij} = \alpha \left[I_{ij} + I_o \left(e^{\frac{V_{ij}}{nV_T} - 1} \right) \right] \quad (4)$$

where I_{ij} and V_{ij} are the current and voltage of i th row and j th column, the values of the parameters such as ' α ', I_o , and nV_T ' are taken from the manufacturer datasheet.

Step 3 Solution Evaluation: Based on the current and voltage value of the PV module, the fitness of each solution is assessed. The fitness function used in this case is same as Eq. (2).

Step 4 Updation of Velocity: The following equation is used to update the particle velocity during the next iteration:

$$V_i^{t+1} = w * V_i^t + \text{rand} * C_c * (P_{\text{best}} - X_i^t) + \text{rand} * C_g * (G_{\text{best}} - X_i^t) \quad (5)$$

where ' i ' denotes the optimization vector variable, ' t ' is iteration number, and X_i^t and V_i^t are the position and velocity of t th iteration.

Step 5 Termination Phase: The termination conditions are reached after getting the appropriate switching pattern, and there is no further change. In the event of a change in illumination, the algorithm should be initialized again.

4 Results and Discussion

To demonstrate the result of the meta-heuristic techniques, three 5×5 conventional PV array configurations are considered namely TCT, BL-TCT, and HC-TCT. The shading pattern chosen for the analysis is shown in Fig. 3a, whereas Fig. 3b and c shows the shade dispersion after applying PSO and GA, respectively.

It is evident that the PSO gives the best result in the case of TCT configuration with a maximum power of 3860 W, and the voltage at which GP occurs is nearest to the nominal voltage in the case of PSO as compared to the shade dispersion obtained from GA technique. Moreover, Fig. 4 shows the PV characteristics that support the

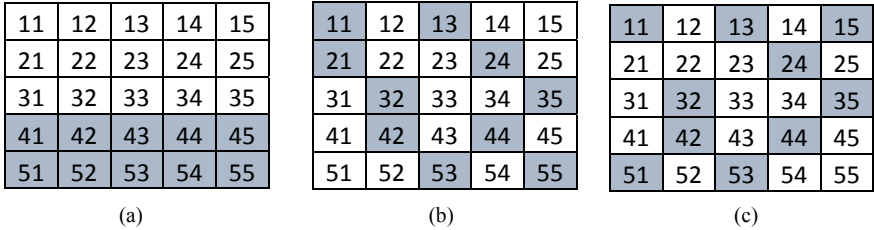
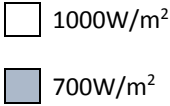


Fig. 3 Shading pattern **a** before shade dispersion, **b** after shade dispersion using PSO, and **c** after shade dispersion using GA

above statement. Finally, the power enhancement and fill factor are evaluated for all the configurations and are shown in Table 2. They can be calculated from the equations given below:

$$\% \text{Power enhancement} = \left(\frac{GP^O - GP^W}{GP^W} \right) \times 100 \tag{6}$$

$$\text{Fill Factor(FF)} = \frac{(V_{mpp} I_{mpp})_{PSC}}{V_{OC} I_{SC}} \tag{7}$$

where GP^O is the optimally generated PV array power, GP^W is the power generated without any reconfiguration, V_{mpp} and I_{mpp} are the voltage and current at maximum power during partial shading condition, V_{OC} is the open circuit voltage, and I_{SC} is the short circuit current.

5 Conclusion

This paper discusses GA and PSO techniques for the reconfiguration of PV modules in the PV array. The objective of the optimization technique is to maximize the output power by equalizing the current in each row during partial shading conditions. The above techniques disperse the shade by providing optimal position of the modules in the PV array and accordingly, the reconfiguration of the array takes place by changing the electrical connection without changing the physical position of the modules. The performance is analyzed for three conventional configurations namely TCT, BL-TCT, and HC-TCT. The results shows that TCT performs better as compared to other configuration followed by HC-TCT, and the power enhancement percentage in

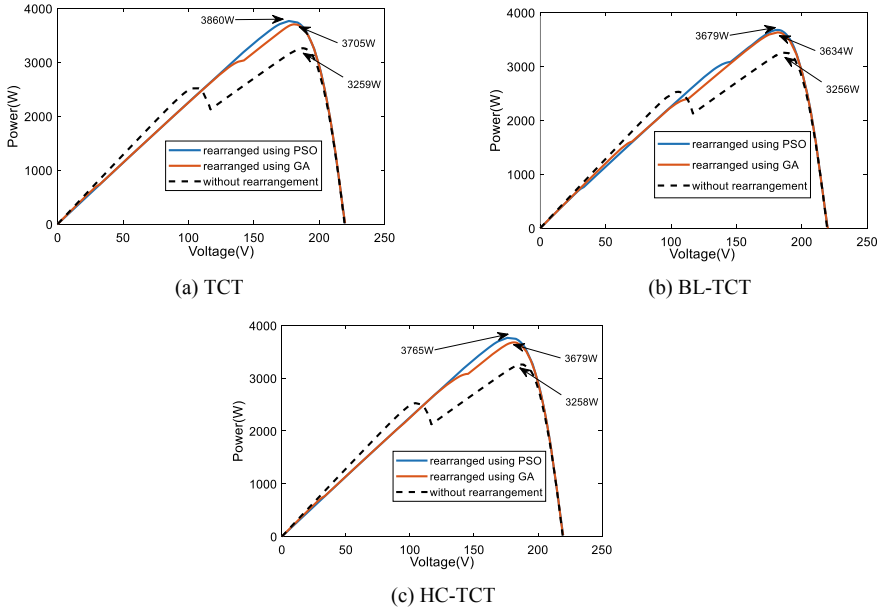


Fig. 4 PV characteristic after applying PSO and GA for various configurations. **a** TCT, **b** BL-TCT, **c** HC-TCT

Table 2 Power enhancement percentage and fill factor for various configurations

Configuration	Maximum power (W)		Power enhancement (%)		Fill factor (FF)	
	PSO	GA	PSO	GA	PSO	GA
TCT	3860	3705	18.44	13.68	0.77	0.69
BL-TCT	3679	3634	12.99	11.61	0.68	0.67
HC-TCT	3765	3679	15.56	12.92	0.74	0.68

the case of PSO is more as compared to the reconfiguration obtained through GA in all the cases with a maximum of 18.44% in the case of TCT configuration followed by 15.56% for HC-TCT and 12.99% for BL-TCT. And the fill factor is highest in the case of PSO configured TCT having a value 0.77.

References

1. La Manna, D., Vigni, V.L., Sanseverino, E.R., Di Dio, V., Romano, P.: Reconfigurable electrical interconnection strategies for photovoltaic arrays: a review. *Renew. Sustain. Energy Rev.* **33**, 412–426 (2014)
2. Rani, B.I., Ilango, G.S., Nagamani, C.: Enhanced power generation from PV array under partial shading conditions by shade dispersion using su do ku configuration. *IEEE Trans. Sustain. Energy* **4**(3), 594–601 (2013)

3. Yadav, A.S., Pachauri, R.K., Chauhan, Y.K.: Comprehensive investigation of PV arrays with puzzle shade dispersion for improved performance. *Sol. Energy* **31**(129), 256–285 (2016)
4. Yadav, A.S., Pachauri, R.K., Chauhan, Y.K., Choudhury, S., Singh, R.: Performance enhancement of partially shaded PV array using novel shade dispersion effect on magic-square puzzle configuration. *Sol. Energy* **1**(144), 780–797 (2017)
5. Vijayalekshmy, S., Bindu, G.R., Iyer, S.R.: A novel Zig-Zag scheme for power enhancement of partially shaded solar arrays. *Sol. Energy* **31**(135), 92–102 (2016)
6. Yadav, K., Kumar, B., Swaroop, D.: Mitigation of mismatch power losses of PV array under partial shading condition using novel odd even configuration. *Energy Reports* **6**, 427–437 (2020)
7. Ajmal, A.M., Babu, T.S., Ramachandaramurthy, V.K., Yousri, D., Ekanayake, J.B.: Static and dynamic reconfiguration approaches for mitigation of partial shading influence in photovoltaic arrays. *Sustain. Energy Technol. Assess.* **40**, 100738 (2020)
8. Alahmad, M., Chaaban, M.A., Kit Lau, S., Shi, J., Neal, J.: An adaptive utility interactive photovoltaic system based on a flexible switch matrix to optimize performance in real-time. *Solar Energy* **86**, 951–963 (2012)
9. Romano, P., Candela, R., Cardinale, M., Li Vigni, V., Musso, D., Riva Sanseverino, E.: Optimization of photovoltaic energy production through an efficient switching matrix. *J. Sustain. Dev. Energy Water Environ. Syst.* **1**(3), 227–236 (2013)
10. Deshkar, S.N., Dhale, S.B., Mukherjee, J.S., Babu, T.S., Rajasekar, N.: Solar PV array reconfiguration under partial shading conditions for maximum power extraction using genetic algorithm. *Renew. Sustain. Energy Rev.* **43**, 102–110 (2015)
11. Babu, T.S., Ram, J.P., Dragičević, T., Miyatake, M., Blaabjerg, F., Rajasekar, N.: Particle swarm optimization based solar pv array reconfiguration of the maximum power extraction under partial shading conditions. *IEEE Trans. Sustain. Energy* **9**, 74–85 (2017)

Design of Lithium-Ion Battery Thermal Management System for Vehicular Applications



Inteti Lakshya Rani, K. Dhananjay Rao, Penmetsa Preetham,
and Ghanta Chaitanya

1 Introduction

Over the past decade, electric vehicle technology has seen an enormous breakthrough in the history of mankind. Lithium-ion batteries which have a very high energy density have found their place in electric vehicles. But these batteries have their pros and cons. Though it is said to be the safest battery source, yet it can still cause fire accidents if not dealt with properly. Therefore, these batteries should never be overcharged or be allowed to be over-discharged or it will result in thermal runaway. Thermal Runaway is a condition where the current flowing through the battery on charging or overcharging causes the cell temperature to rise. Thus, it is essential to consider these parameters while designing a proper thermal management system for the battery [1, 2]. These systems need to be designed properly such that battery temperature can be controlled with ease. Although lithium batteries are considered to be the safest cells, there is always a need to monitor it [3].

As and when lithium batteries are manufactured, the batteries undergo an aging phenomenon due to the various physical and chemical reactions in the cell. Even when they are in use, they have a lot of internal chemical reactions taking place when the cell is being charged and discharged constantly. The cells are not charged equally either. This is called charge imbalance. A charge imbalance leads to the improper utilization of the cells. Some could be overcharged and some may be undercharged. This causes overheating in cells and results in a thermal imbalance. Both cell imbalance and temperature are interdependent on each other [4].

The heat due to imbalance might spread from one cell to another cell. Thus it is important to ensure that temperature is distributed evenly across cells. Thus we require a proper thermal management system to cool down the cells. There are various battery thermal issues that need to be considered before designing a battery thermal

I. L. Rani · K. Dhananjay Rao (✉) · P. Preetham · G. Chaitanya
Velagapudi Ramakrishna Siddhartha Engineering College, Vijayawada, AP 520004, India
e-mail: kdhananjayrao@gmail.com

management system. This includes the various heat generation phenomenon that needs to be considered and managed correctly. The chemical reactions occurring in the battery are the main reason for thermal runaway. It can also be due to the materials by which the cells are made. The battery storage temperature might also be one of the reasons for the rise in temperature [5, 6].

These temperature variations greatly impact the state of health of the battery. The battery aging phenomenon depends on the temperature of the batteries. As the temperature increases or decreases the battery health also decreases [7]. Both excess voltage and under voltage affect the cell temperature. The battery voltage should not exceed its optimum value or else it causes a heavy inrush of currents. These currents increase the temperature and increase the breakdown of electrode materials. Thus, overcurrents and voltage cause thermal runaway [8–10]. Overheating causes a higher reaction rate. As the chemical reactions are linearly related to the temperature, the battery capacity to carry current decreases. As a result heat dissipation increases and finally results in thermal runaway conditions [11, 12]. The battery thermal management system requires a microcontroller to monitor the parameters of voltage, current, and temperature [13].

The battery thermal management system is necessary to control the temperature variations that occur on the battery due to the movements of EVs [14]. The system needs to monitor the required parameters and suitably apply the necessary control system. Here, to control temperature, a cooling system using a coolant is applied to control it. Choice of coolant is very important while designing a cooling system as some could be corrosive [15, 16]. The current trend involves the use of the Internet of Things (IOT) through which the ESP8266 node MCU has occurred as a majorly flexible microcontroller [17]. The above literature lacks the smart BMS techniques involving IOT and machine learning techniques. In this regard, a smart BMS technique has been proposed to control the battery parameters such as voltage, current, temperature and SOC by using various sensors and IOT technology. Further, each of these parameters is monitored and controlled effectively using the designed BMS mechanism.

1.1 Battery Thermal Management System

For the design of a battery thermal management system, several parameters need to be taken into consideration. It should be light in weight, flexible, easy to install and simple in design aspects. For these reasons, the design of a battery thermal management system should be carefully done. This paper proposes an effective, simple and cost-efficient battery thermal management system for electric vehicles. Often, the values of voltage and current keep changing continuously. Overvoltages and overcurrents need to be monitored properly, the cooling system will operate to take care of the excess heat obtained.

At present, the battery management systems that are in use today are less efficient and tend to fail easily. Even if all the requirements are met, the system will not

be economical. The proposed BMS uses state of the art techniques to monitor the cell parameters. The BMS is able to protect the battery from high temperatures and measures the state of charge (SOC) using the lookup table method. The temperature of the battery increases as the battery gets charged and discharged continuously. Just like how the discharge cycles vary when an electric vehicle moves on the road, the temperature of the battery varies accordingly. Thus, there is a need to monitor the temperature continuously. The battery pack of an EV consists of several cells connected in series or parallel. This project makes use of a simple battery pack consisting of 4 cells connected in series. The battery pack needs to be monitored for the analog parameters of temperature, voltage, and current. In order to perform this measurement, the battery pack is connected to a temperature sensor, voltage sensor and current sensor. In practice, monitoring for the individual parameters is required and so a temperature sensor is mounted on the surface of the battery pack. From this, the surface temperature of the battery can be monitored effectively. The voltage sensor and current sensors are placed to obtain individual cell voltage and pack current. The readings from the voltage sensor are in turn used to measure the state of charge (SOC) of the battery. The microcontroller continuously monitors the battery for changes in voltage and current. The lookup table algorithm is used to calculate the SOC of the battery. The block diagram depicted in Fig. 1 demonstrates the sensors are connected with a microcontroller (ESP8266 node MCU) unit for measuring SOC and monitoring the voltage, current and temperature. It continuously compares with the set values and if the temperature is found to be out of range, immediately performs the corrective actions through the control circuit. It turns on the coolant or the fan as per our cost requirements for controlling temperature. It operates a relay for protecting the battery pack if the battery is found to be under overvoltage or overcurrent conditions.

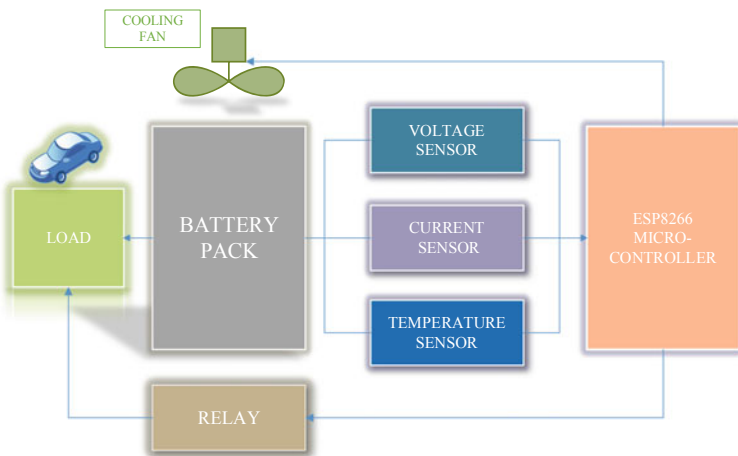


Fig. 1 Block diagram of proposed BTMS

2 Experimental Setup

The battery management system that is proposed has experimented on a battery pack consisting of 4 cells connected in series. The lithium iron phosphate battery voltage and capacity are 12.8 V and 3.5 Ah, respectively. For simplicity purposes, ESP8266 node MCU unit. This system mainly consists of a microcontroller ESP8266 board which continuously monitors the parameters of voltage, current, temperature, and state of charge. A temperature sensor that is used to measure the pack temperature is connected to the battery pack when the battery is continuously charged and discharged. The DHT11 temperature sensor is able to measure temperatures ranging from 0 to 50 °C. The operating voltage of this sensor is from 3.5 to 5.5 V whereas its resolution is 16 bit. The output data is serial data which is well-compatible with the Arduino UNO board. This makes the overall system operation effective. An algorithm for measuring the temperature through the DHT 11 sensor has been written in Arduino software and executed. A set value of the temperature is set in the microcontroller and if the temperature exceeds this set value then the microcontroller directs the control system. A dc fan is placed for cooling the pack temperature if it exceeds the set value. A motor driver L298N 2A module is used for varying speeds of the fan for different temperatures as required.

For the measurement of SOC, the same ESP8266 node MCU is used to monitor the charge and discharge cycles. The SOC varies continuously as the load is being applied while discharging. The load used here is a lamp load rated 12 V. The charge and discharge are measured using an algorithm called the lookup table method. The Li battery has a nominal voltage of 12.8 V. The maximum operating voltage is 14.4 V. The following mathematical formulation has been used to measure battery SOC.

$$\%SOC \text{ of battery} = \frac{V_t - V_n}{V_m - V_n} * 100 \quad (1)$$

In the above equation, V_t represents the terminal voltage of the battery and V_n is the nominal voltage of the battery whereas V_m represents the maximum operating voltage of the battery. Here, the terminal voltage is measured from the voltage sensor. This reading is given to the microcontroller for SOC measurement.

The voltage sensor used in the proposed system is the 25 V (maximum) voltage sensor module. Its input range is 0–25 V DC, whereas the voltage detection range is from 0.02445 to 25 V DC. The resolution of this sensor is 0.00489 V. The current sensor used is the INA219 I2C bidirectional current sensor module. This sensor is able to measure upto ± 3.2 mA with a resolution of 0.8 mA. Its operating voltage is 3.3–5 V. The accuracy may vary by $\pm 0.5\%$. Due to these features, the aforementioned two sensors are apt for the proposed BTMS.

The measured voltage and currents are received by a microcontroller and operate the respective control systems accordingly. Further, a relay is placed for the control of overvoltage and overcurrents. The well-known fact is that the battery overcharging increases the overvoltage and similarly the over-discharging causes overcurrent.

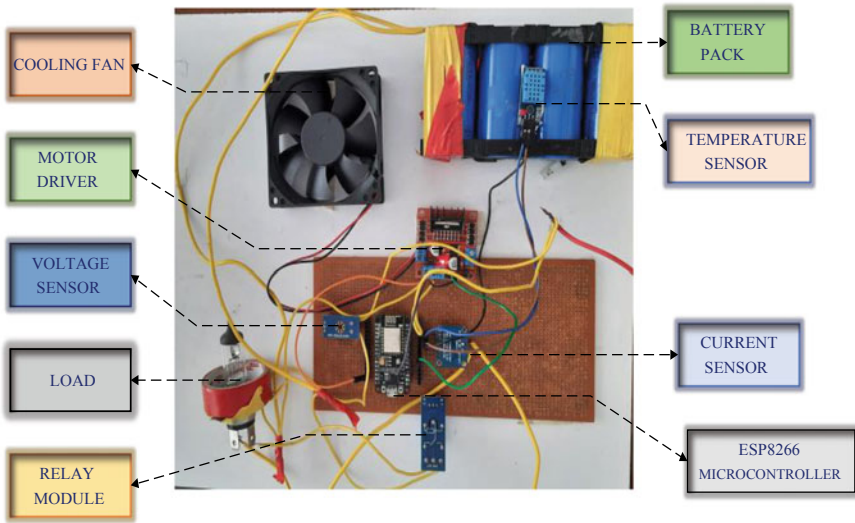


Fig. 2 Experimental prototype setup

Therefore, if the battery is overcharged or if it is under an overvoltage condition, then the relay operates to switch off the supply. Similarly, for overcurrent protection, a relay operation takes place. The experimental setup for the system proposed is depicted in Fig. 2.

3 Experimental Results and Analysis

Various charge–discharge tests were conducted on the battery at different operating conditions. At different operating temperatures, the tests were conducted on the battery. Also, during discharge of the battery SOC is measured and the relevant tests are conducted. The battery pack was charged and discharged continuously. During discharge cycles, it was observed that the battery temperature was around 25–30 °C. A set temperature range was given in the algorithm for the operation of a DC fan. When the temperature increased beyond the value of 30°, then the cooling fan was automatically operated through the control system provided. The current sensor is placed in series with the battery pack to obtain the battery pack current. These current values are collected by the microcontroller. The microcontroller continuously monitors for any overcurrent values. In this experiment, different loads were applied to discharge the battery and reciprocate it like in real-time applications. Figure 3 depicts the discharging current of the battery. It is observed that during discharge, the current increases continuously. When the applied load is increased, the current drawn by the battery increases. If the battery current is drawn for a long duration, it

causes an overcurrent. The rise in battery current magnitude will increase the battery temperature and thermal runaway may take place. For the safe and secure operation of EVs, overcurrents need to be controlled properly. Hence, whenever an overcurrent occurs, the operation of the relay takes place. Thereby, the load is disconnected from the battery using a relay and the battery pack is protected. Therefore, the experiment is conducted on the battery pack for different loads while discharging.

The voltage of the battery pack was measured by placing a voltage sensor across the battery pack. The pack voltage is measured by the sensor and it is sent to the microcontroller. Using Arduino programming, the program was executed for monitoring the voltage. Figure 4 depicts the battery terminal voltage measurement during discharging for a load applied. It is observed that the voltage is decreasing while discharging the battery. The voltage is continuously measured so that the battery will not be in overvoltage conditions.

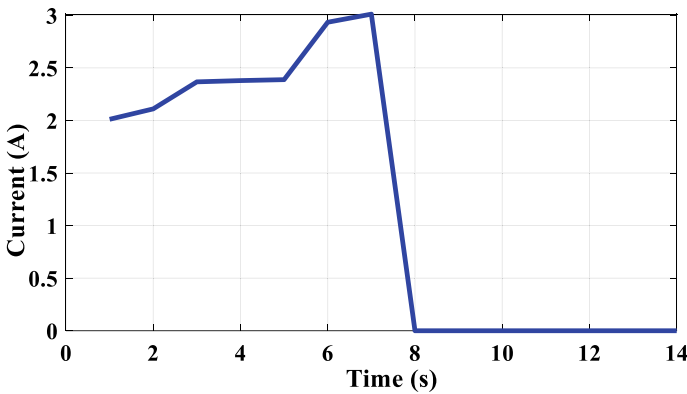


Fig. 3 Battery discharging current

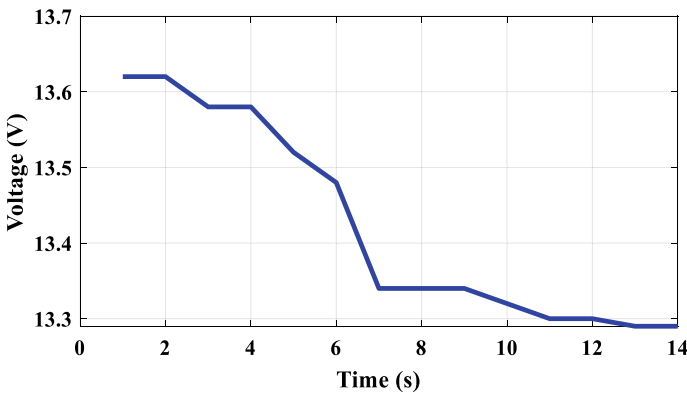


Fig. 4 Battery terminal voltage

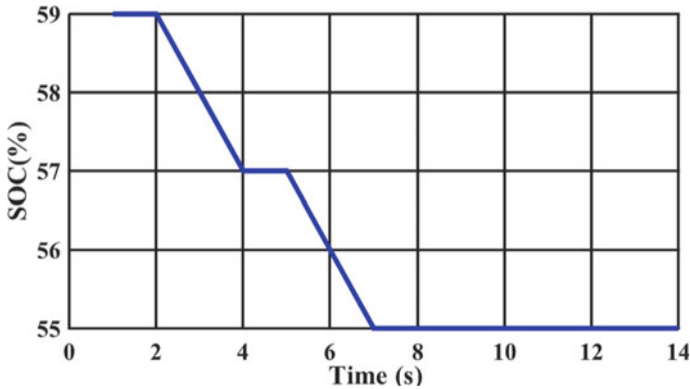


Fig. 5 Battery state of charge measurement from 59%

The state of charge was measured using the lookup table method. The related program was written in Arduino programming language and is fed to the microcontroller. The SOC was measured as the battery is discharged continuously. Figure 5 provides the measurement of SOC, as the battery was discharged through the application of a load (12 V DC Bulb). Also, the SOC value was obtained during the discharging of the battery and their relevant results were obtained. Just like how the electric vehicle will be subjected to different loads ranging from bumpy roads to smooth roads, a similar profile has been replicated by applying different loads to the battery.

Figure 6 depicts the temperature variation of the battery during the discharging condition. It is observed that the temperature increases continuously. As it is difficult to operate the battery at higher temperatures, the battery was operated within a safe range. It is observed that when the battery surface temperature increases beyond the set value (i.e. 28°), then the operation of the cooling fan takes place and so the temperature starts decreasing accordingly. The set value can be given to the microcontroller through Arduino programming. Similarly, even while charging the temperature increases and when it is beyond the set value, the cooling fan starts to operate and so the temperature is brought down accordingly.

Further, SOC estimation for the battery has been carried out using (1) for different SOC levels such as 50% SOC and 75% SOC. The measured 50% SOC and 75% SOC are depicted in Figs. 7 and 8. These estimated value depicts the efficacy of the proposed SOC estimation technique. Similarly, SOC estimation of the battery can be carried out for any level SOC.

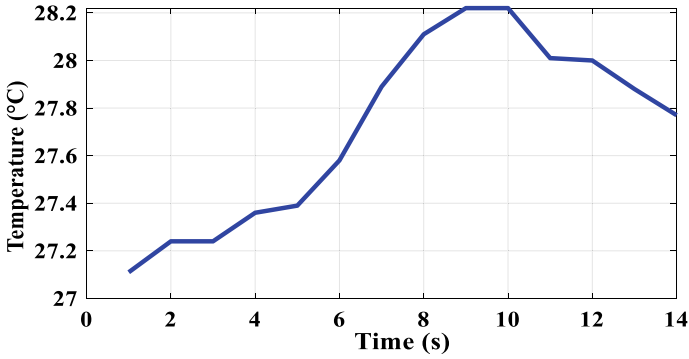


Fig. 6 Battery pack temperature variation

Fig. 7 Battery state of charge measurement from 50%

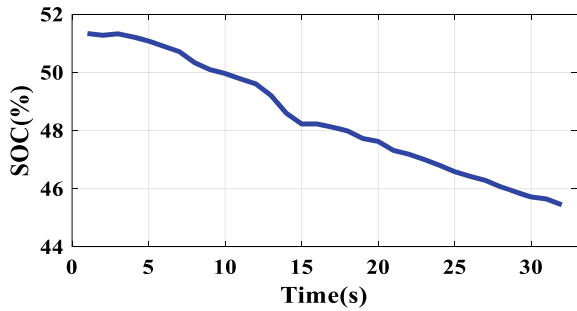
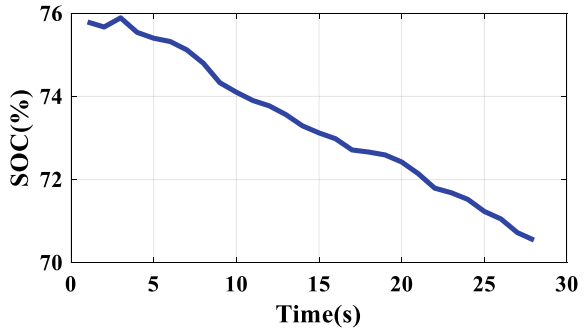


Fig. 8 Battery state of charge measurement from 75%



4 Conclusion

This paper is focused on the design of a simple and economic battery thermal management system by using simple components. This proposed system makes use of various sensors for obtaining battery parameters. These parameters are voltage, current, temperature and state of charge (SOC). They are measured and monitored using sensors and a microcontroller connected to the battery pack. They are controlled

using a control system provided for each. Whenever there is an overvoltage or overcurrent, the relay has been operated successfully by tripping the circuit and providing safety to the battery. The battery temperature changes as the load is applied and due to the high and safe operating characteristic of a lithium iron phosphate battery, the temperature could not be increased more than safe limits. The state of charge of the battery was monitored and measured by using the terminal voltages and operating voltage range. Thus, the proposed system showed effective results and therefore, a simple and economic battery thermal management system can be obtained.

References

1. Vishnu Murthy, K., et al.: Overview of Battery Management Systems in Electric Vehicles. *E-Mobility*, pp. 137–147. Springer, Cham (2022)
2. Rao, K.D., Ghosh, S., Keshri, R.: A resilient temperature suppressed optimal charging strategy for ultracapacitors to attain desired state of charge. *IEEE Trans. Energy Convers.* <https://doi.org/10.1109/TEC.2022.3144478>
3. Han, W., Wik, T., Kersten, A., Dong, G., Zou, C.: next generation battery management systems, dynamic reconfiguration. In: *IEEE Industrial Electronics Magazine*, pp. 1932–4539 (2020)
4. Tang, H., et al.: Design of power lithium battery management system based on digital twin. *J. Energy Storage* **47**, 103679 (2022)
5. Tomin, N., et al.: Design and optimal energy management of community microgrids with flexible renewable energy sources. *Renewable Energy* **183**, 903–921 (2022)
6. Cheng, K.W.E., Divakar, B.P., Wu, H., Ding, K., Ho, H.F.: Battery-management system (BMS) and SOC development for electrical vehicles. *IEEE Trans. Veh. Technol.* **60**, 1175–9884 (2011)
7. Li, J., Zhu, Z.: *Battery Thermal Management Systems of Electric Vehicles*. Chalmers University of Technology—Department of Applied Mechanics, Sweden (2014)
8. Ma, S., Jiang, M., Tao, P., Song, C., Wu, J., Wang, J., Deng, T., Shang, W.: Temperature effect and thermal impact in lithium-ion batteries: a review. *Prog. Nat. Sci.: Mater. Int.* **28**, 653–666 (2018)
9. Imre, T., Buidin, C., Mariasiu, F.: Battery thermal management systems: current status and design approach of cooling technologies. *Energies* **14**(16), 4879 (2021)
10. Rao, K.D., Chander, A.H., Ghosh, S.: Robust observer design for mitigating the impact of unknown disturbances on state of charge estimation of lithium iron phosphate batteries using fractional calculus. *IEEE Trans. Veh. Technol.* **70**(4), 3218–3231 (2021)
11. Naik, I., Nandgaonkar, M.: Review of the approaches and modeling methodology for lithium-ion battery thermal management systems for electric vehicles. In: *Select Proceedings of ICFTMME, Advances in Materials and Mechanical Engineering*, pp. 75–109 (2020)
12. Wei, T., Xu, X., Ding, H., Guo, Y., Liu, J., Wang, H.: Sensitivity analysis of the battery thermal management system with a reciprocating cooling strategy combined with a flat heat pipe. *ACS Omega* **5**(14), 8258–8267 (2020)
13. Abdelkareem, M.A., et al.: Thermal management systems based on heat pipes for batteries in EVs/HEVs. *J. Energy Storage* **51**, 104384 (2022)
14. Luo, J., et al.: Battery thermal management systems (BTMs) based on phase change material (PCM): a comprehensive review. *Chem. Eng. J.* **430**, 132741 (2022)
15. Wu, W., Wang, S., Wu, W., Chen, K., Hong, S., Lai, Y.: A critical review of battery thermal performance and liquid-based battery thermal management. *Energy Convers. Manage.* **182**, 262–281 (2019)

16. Lin, J., Liu, X., Li, S., Zhang, C., Yang, S.: A review on recent progress, challenges and perspective of battery thermal management system. *Int. J. Heat Mass Transf.* **167**, 120834 (2021)
17. Mesquita, J., Guimarães, D., Pereira, C., Santos, F., Almeida, L.: Assessing the ESP8266 WiFi module for the Internet of Things. In: *IEEE 23rd International Conference on Emerging Technologies and Factory Automation (ETFA)*, pp 1946–0759 (2018)

Wind and Tidal Power as a Dynamic Solution for Sri Lanka's Dependency on Thermal Power Plants



Nilan Jayasinghe , Uthum Gunasekara , and Rasika Pothupitiya 

1 Introduction

According to the last ten years, climate change has been a growing concern that has led nations worldwide to rethink the use of fossil fuels [1]. This applies to every country, including the developing nations. In our case, Sri Lanka, the island nation, occupies an almost total area of 65,610 km², with 62,705 km² of land and 2905 km² of territorial water [2], and 1680 km of coastline in the Indian Ocean [3] until recent time's country's electricity generation depended mainly on renewables like hydropower. Up until the mid-90s, hydropower plants were the primary mode of electricity generation in Sri Lanka. But with the rapid increase in electricity demand, authorities had to seek alternatives. Unfortunately, those alternatives were old-fashioned thermal power plants powered mainly by burning coal and fossil fuels. According to the Ceylon Electricity Board (CEB) data from 2020, about 9936 GWh were generated by thermal coal and thermal oil. Compared with the total generation that year, this was about 37%—thermal coal and 27% thermal oil. In 2020, about 64% of the total electricity generation was produced through thermal power plants [4]. However, in the specific case of Sri Lanka, this trend was accelerated from the 2020s due to the malfunctioning of thermal plants and bad economic situation in

N. Jayasinghe

Higher School of High Voltage Energy, Peter the Great St. Petersburg Polytechnic University, Saint-Petersburg, Russia

U. Gunasekara (✉)

Higher School of Nuclear and Heat Power Engineering, Peter the Great St. Petersburg Polytechnic University Saint-Petersburg, Saint Petersburg, Russia

e-mail: uthumgunasekara@gmail.com

R. Pothupitiya

Department of Electrical Technology and Converter Engineering, St. Petersburg State Electrotechnical University, Saint Petersburg, Russia

the country. After the pandemic situation with COVID-19, there are crises with the growing up of the country economy [5].

Moreover, Sri Lanka joined the 2016 Paris Accord Agreement; an agreement with the United Nations Framework Convention on Climate Change (UNFCCC) dealing with greenhouse gas emissions. The island should go to the zero-carbon emitting while increasing the generational power [6]. The use of thermal power plants has two main inconveniences. First, the high costs of the electric power generation system are mainly due to the purchase and transportation of explosives. For these reasons, the efforts of Sri Lankan authorities are currently being focused on the design and development of renewable energy-based plans to replace the existing systems. According to the CEB, these efforts will lead to a renewable target between 22 and 24% of the power supply in 2036.

2 Research Study and Methods

Sri Lanka is a relatively large island situated south of India, extending offshore into the Indian Ocean. This allow the island to interact with the seasonally changing monsoon. Monsoonal patterns around Sri Lanka throughout the year are given in Fig. 1.

The southwest (SW) monsoon generally operates between June and October, and the northeast (NE) monsoon operates from December through April. During the SW monsoon, the southwest monsoon current flows from west to east, while during the NE monsoon, the currents reverse in direction [7, 8].

As an island country that lacks the necessary land to install large amounts of onshore wind or solar power, work is being focused on exploiting marine renewable

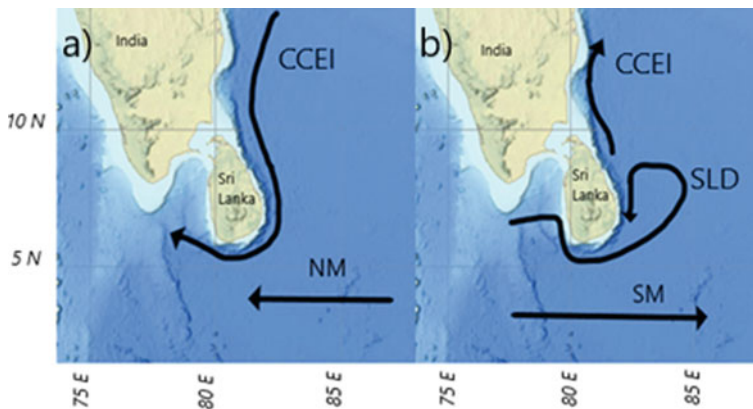


Fig. 1 Monsoonal patterns around Sri Lanka during **a** Northeast monsoon and **b** Southwest monsoon. NM—North monsoonal currents; CCEI—Coastal current from east India; SM—South monsoonal currents; SLD—Sri Lankan Dome

energy sources. In this regard, tidal current energy appears as a very promising alternative, especially for isolated areas, since it requires less grid capacity and reduces costs in energy storage. Wind farms at seas generate the majority of the marine renewable energy, and it is economically beneficial for the small communities in coastal areas [9, 10]. So far, tidal stream energy cannot compete in absolute numbers of power production and cost with solar photovoltaics (PV) or wind energy. Therefore, the use of hybrid wind and tidal platform solutions will be an excellent option to achieve the carbon zero policy for developing nations with access to oceans.

The main purpose of this research study is to propose suitable sites for the installation of combined wind and tidal power plants in Sri Lanka and their usage as an alternative to the excess use of fuel oil and coal-powered thermal plants. In the given figure, they are considering massive maritime traffic around Sri Lanka [11]. Hybrid farms must be installed close to land with less interference to maritime routes and abundant wind in seas and due to the onshore limitations [12]. This research study discusses two sea patch areas close to Mannar and Hambantota to Kalmunai is given in Fig. 2.

Hybrid farms should not disturb the existing marine traffic around the island and as well as local fishing community. However, further, research has to be done on the consequences of man-made structures on existing marine environment and sea bed [14].

2.1 Proposed Sites for Turbine Installation

According to this research paper, locations along the southwest and northeast coastlines of Sri Lanka were considered by available energy density in the Indian ocean [15] (monsoonal wind streams) and other marine economic agents such as fishery marine traffic lines. The proposed locations in the waters around Sri Lanka are given in Fig. 3.

Site a—Northwest of the island including Mannar region considered. Sea patch area for hybrid turbine installation represented below with their respective longitudinal and latitudinal coordinates.

Latitudes: 8.01–8.78;
Longitudes: 79.41–79.84;
Ocean depth range (m): 12–2000.

Site b—Offshore region to the southwest of Sri Lanka which includes sea area from Hambantota to Kalmunai.

Latitudes: 6.18–7.36;
Longitudes: 81.48–82.32;
Ocean depth range (m): 30–2500.

Considering the vast area of selected sea patch sectors, there is more likelihood to launch many hybrid units in near future. The proposed sites have a favorable

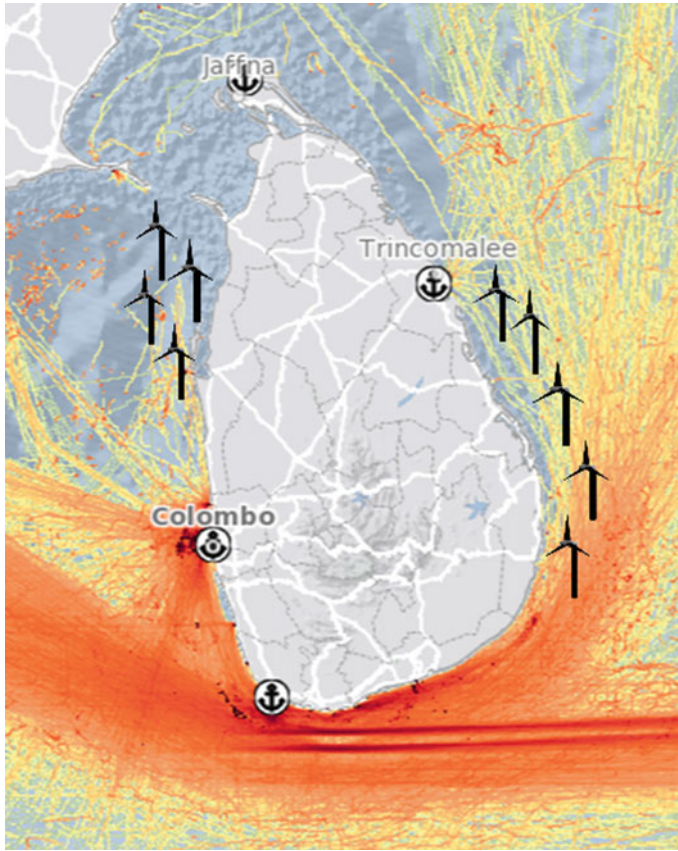


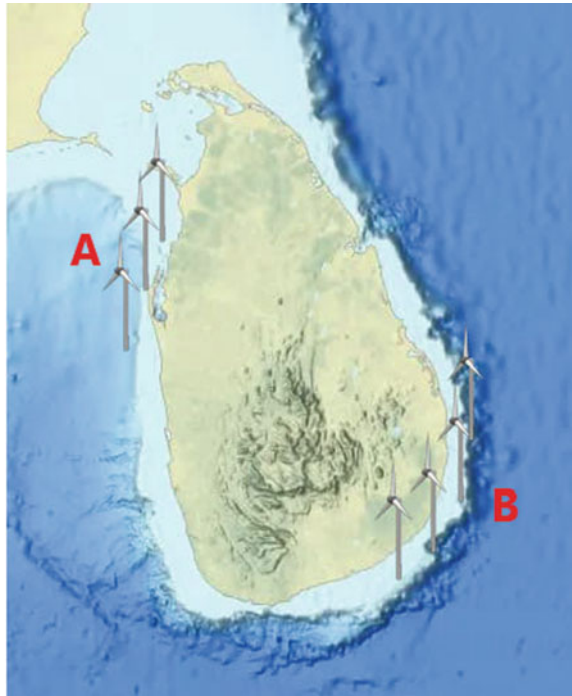
Fig. 2 Major maritime routes along the western and southern coasts of Sri Lanka frequently used routes are marked with bright red, orange, and yellow. Sourced from global maritime traffic [13]

wind throughout the year. Weather changes rapidly in South Asia due to the pressure depression over Bay of Bengal Winds from northeast monsoon and southwest monsoon sweeping the area. The sea becomes rough due to the powerful waves created by abundant winds [16, 17].

2.2 Wind Patterns for Selected Areas Around the Island

Wind speed for ten consecutive days for the three selected locations is given in Fig. 4. It is shown that in the selected sectors, wind speeds are varying within a range of 4–8 m/s making it an appropriate location for wind turbine operation. Winds forcing from the Bay of Bengal and equatorial Indian Ocean affects the wind patterns in the selected offshore sites [19].

Fig. 3 Area of interest around the island **a** Northwestern coast and **b** Southeastern coast of Sri Lanka



2.3 Tidal Turbines

A crucial element needed for electricity generation is Turbine. Many factors should be considered when it comes to offshore installation. Materials should withstand harsh marine conditions with time [20, 21]. Tidal stream turbines extract kinetic energy from water flow. Except for the medium in which the tidal Turbine operates, its operational behavior is like that of a wind turbine. Tidal stream turbines function according to the principles of aerodynamic lift, and it is more efficient than aerodynamic drag [22]. The density of the medium in which turbine blades operate conclude the more efficient way.

Tidal currents are usually much slower than the wind; however, the dense sea water matches this output power, allowing tidal turbines to generate the same power output. Tidal turbines must withstand harsh conditions under the sea [23].

Tidal turbines can be classified mainly into two groups regarding the design: cross flow turbine and axial-flow turbine. According to this research paper, a hybrid tower is proposed with horizontal axis flow turbines. The principle of working axial-flow turbine with a horizontal axis of rotation is illustrated in Fig. 5. This type of tidal turbine sweeps a large circular area of seawater that flows parallel to the axis of rotation [24]. Mathematically, the amount of power of a turbine can be described by actuator disc theory [25]

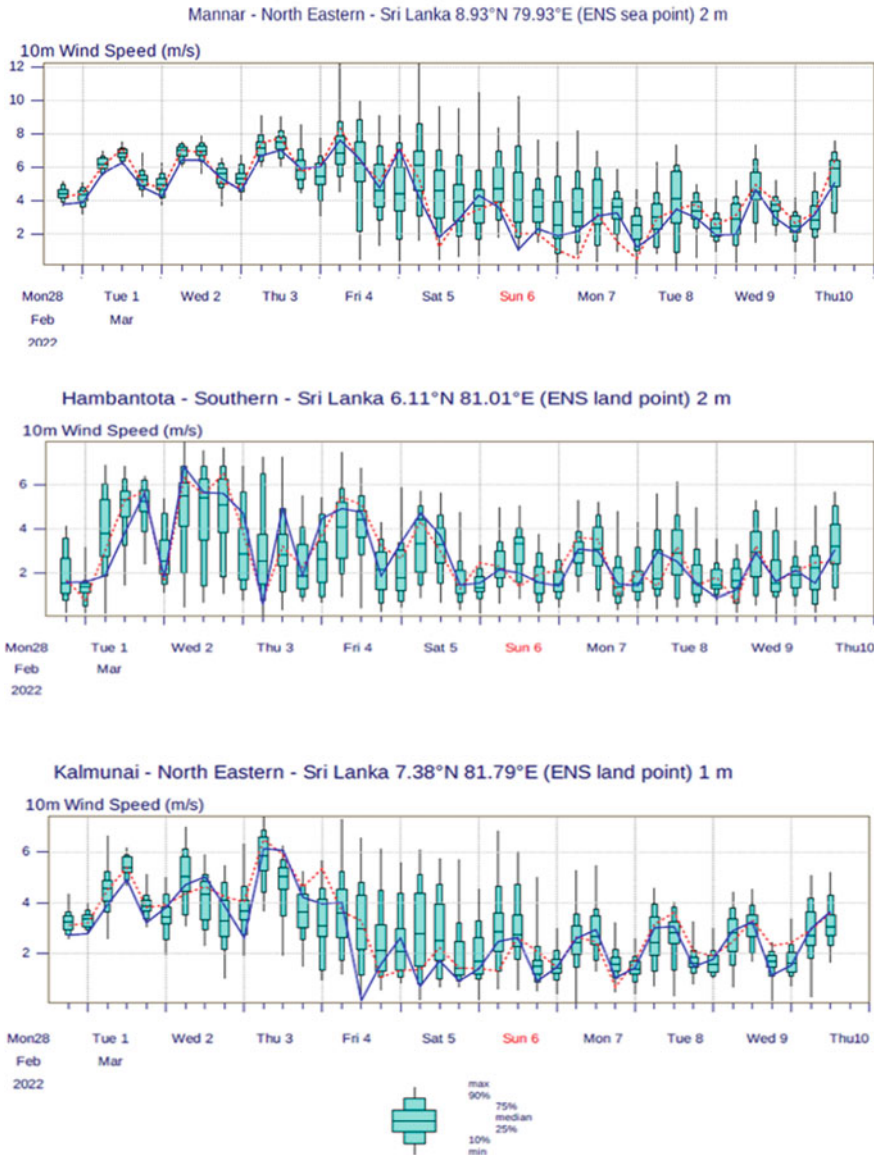
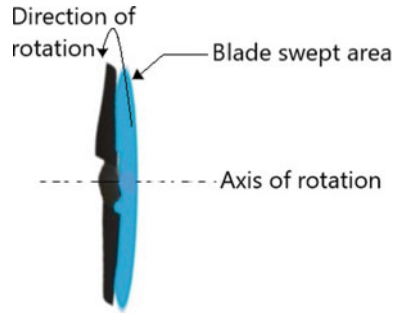


Fig. 4 Wind speed changes during 10 days for proposed sites Mannar, Hambantota, and Kalmunai. Sourced from European Centre for Medium-Range Weather Forecasts (ECMWF) [18]

Fig. 5 Tidal turbine blade with axial-flow configuration



$$P_{\text{tidal}} = \frac{1}{2} \rho A_{B.S} C_P v^3 \tag{1}$$

P_{tidal} —Power (W) generated by the tidal turbine, ρ —Density of liquid (water, kg/m^3), $A_{B.S}$ —Blade swept area (m^2), C_P —Power coefficient of tidal turbine, and v —Water flow speed (m/s).

Power generated per m^2 of blade swept area (power density) of tidal turbine can be calculated as below

$$P_{d.\text{tidal}} = \frac{P_{\text{tidal}}}{A_{B.S}} = \frac{1}{2} \rho C_P v^3 \tag{2}$$

$P_{d.\text{tidal}}$ —Power density of tidal turbine (W/m^2).

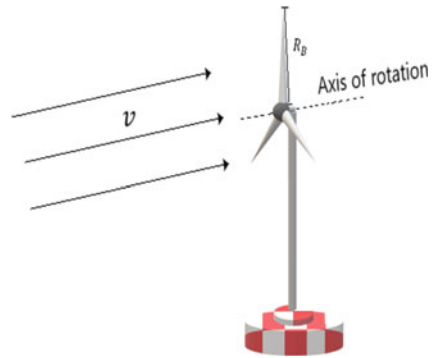
2.4 Wind Turbines

Wind turbines work by converting kinetic energy into rotational kinetic energy. The turbine then converts into electric energy that generates electricity. Wind turbines can extract almost 59.3% of the accessible wind power in the area [26]. Generally, the power is limited by the Betz limit [27]. The amount of energy that wind turbines can extract from wind can be given mathematically shown below [28].

$$P_{\text{wind}} = \frac{1}{2} \rho \pi R_B^2 \cdot C_P(\lambda, \beta) v^3 \tag{3}$$

P_{wind} —Power (W) generated by the wind turbine, ρ —Density of air (kg/m^3), R_B —Rotor blade radius (m), $C_P(\lambda, \beta)$ —Wind turbine power coefficient with tip speed ratio λ and pitch angle β , and v —Airflow speed (m/s). Operation of a wind turbine is given in Fig. 6.

Fig. 6 Principle of wind turbine operation, v —wind speed before reaching the blades, R_B —rotor blade radius

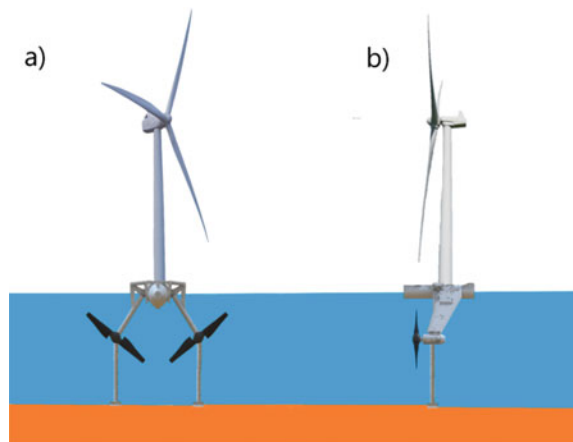


2.5 Hybrid Tower Model with Triple Turbine Complex

The combination of two accessible offshore renewable energy sources, wind + tidal, avoid the hazardous effects of using thermal oil power plants and gives the prospect for future developments in the marine renewable sector [29]. A hybrid tower with both wind and tidal turbines will enhance the ability to extract wind energy and tidal energy simultaneously with less cost compared with separate installations [30]. Model hybrid tower constructed with two tidal turbines and separate wind turbines are given below in Fig. 7.

Hybrid tower shown in Fig. 7 consists a pair of 2 MW underwater tidal turbine which has a total generating capacity of four megawatts. Upper segment which is above the surface of water contains wind turbine unit. Wind turbine has a generating capacity of 6 MW, thus from a single hybrid unit it is possible to extract an estimated value of 10 MW.

Fig. 7 a Model hybrid tower including one wind and two tidal turbines each in one complex and **b** profile-view of hybrid tower



Ease of transmission of electricity from offshore generating platform is also an important factor that is to be considered. The marine renewables currently in operation typically use high voltage alternative current (HVAC) transmission systems due to the relatively small distance to electrical substations, cutting off the excess transmission costs. If the turbine sites are farther away from the coast, using a high voltage direct current system for transmission would be beneficial [31, 32].

The total CO₂ emissions between installed capacities by year for Sri Lanka from 1998 till 2044 are given in Fig. 8.

According to this research paper, a hybrid wind-tidal turbine tower is introduced, and it is expected to reduce CO₂ emissions by 5% at the end of 2031. 7.5% for the year 2036, 10% reduction by the year 2041, and at the end of 2044, it is expected to cut off total CO₂ emissions by 15% using hybrid renewables.

In accordance with Table 1, if the project initiated the total number of 10 MW hybrid units that can be installed by year 2031 will be 24 units. For next five years that number will be almost twice the value achieving a generation target of 460 MW. By year 2044, a total of 140 hybrid units will be operational around the island, hence this reduces the carbon emissions to a considerable extent.

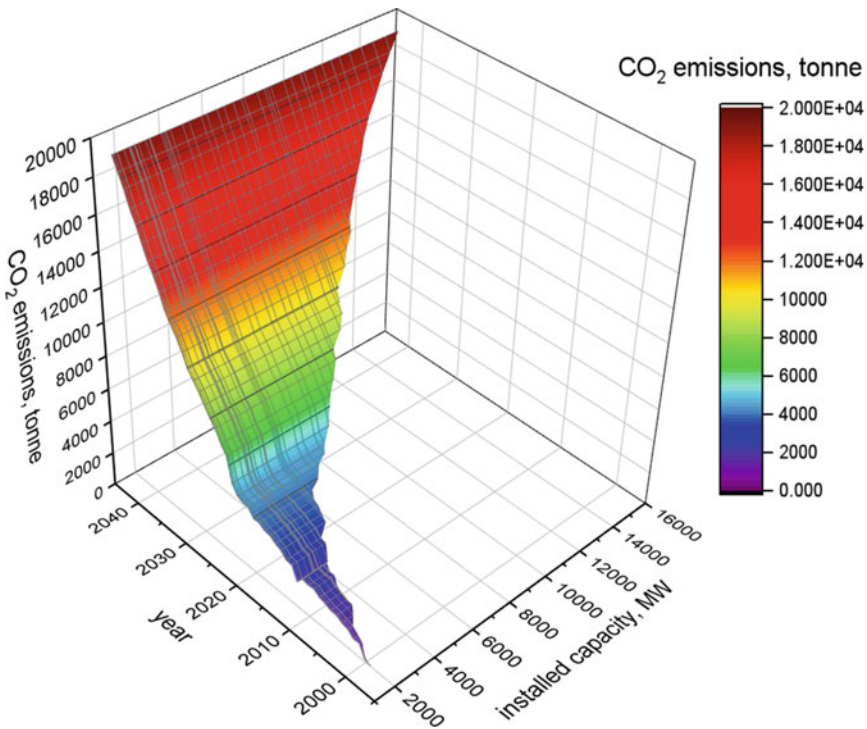


Fig. 8 Total CO₂ emission and prediction according to the installed capacity by year for Sri Lanka from 1998 till 2044

Table 1 Demand, net generation forecast, and required hybrid complexes for 2031–2046

Year until	Demand (GWh)	Net generation (GWh)	Peak demand	Number of 10 MW hybrid towers need to be install at the proposed sites
2031	27.438	29.647	4.755	24
2036	35.100	37.844	6.078	46
2041	43.859	47.288	7.602	76
2044	53.703	57.901	9.317	140

Based on the chart is given in Fig. 9, by realization of the hybrid wind and tidal farm project, it is observed that total CO₂ emissions has reduced according to the predicted values. This shows a good startup to achieve clean energy with the utilization of renewable energy sources.

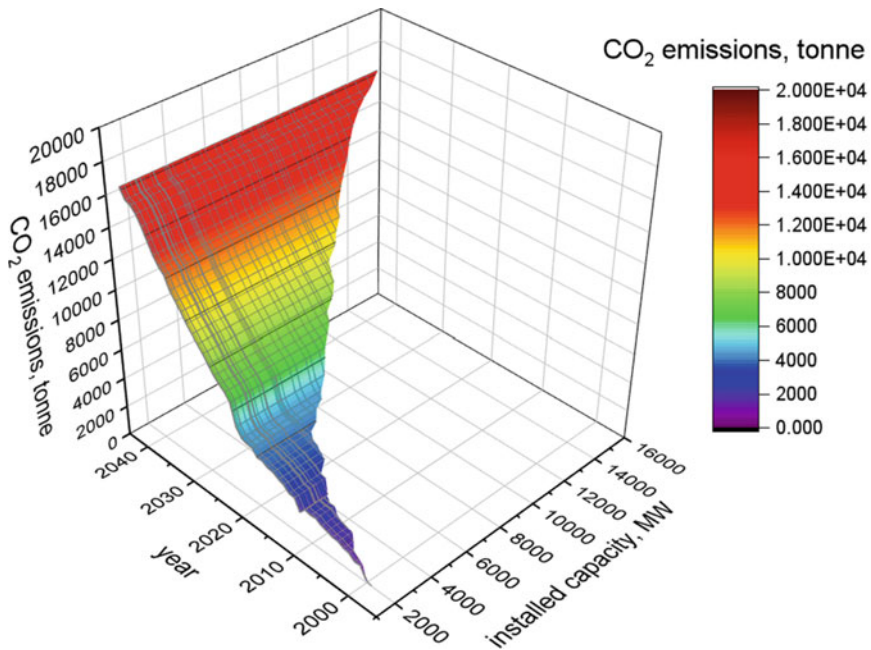


Fig. 9 CO₂ emission and calculation of installed capacity by year for Sri Lanka from 1998 till 2044 during 2030 to 2044 with hybrid power plant as 100% clean energies without producing greenhouse gases

3 Conclusion

This research study has suggested combining tidal and wind current energy to provide continuous electric power by optimizing the operation of 24 hybrid turbines, 10 MW of installed capacity each, considering 12 hybrid turbines for each site by 2031. By 2044, 140 hybrid complexes will be operational around the island, cutting off the CO₂ emissions by 15%. According to this research paper, the hybrid turbines reviewed represent the latest achievements in the MW level offshore renewable technologies in present times. These hybrid turbine technologies will be installed in the proposed wind-tidal hybrid farms. In addition to these industrialized significant hybrid turbine technologies (with sea-bottom supporting structures), research has been carried out to achieve more efficient megawatt-level power capacities. This study accommodates several turbines (one wind and two tidal) on a single platform structure to minimize system installation value and achieve high power generation capacity. To further influence, it is possible to install vertical axial turbines in lagoons such as Puttalam, Negombo, and Batticaloa. Sri Lanka energy sector is heavily dependent on imports. With oil price increasing each year, the government has not been able to pay for thermal power plant fuel. Total availability of power is very high in the country with suitable conditions since island surrounded by Indian Ocean and as shown above more sites are available for the hybrid renewable.

References

1. York, R., Bell, S.E.: Energy transitions or additions? Why a transition from fossil fuels requires more than the growth of renewable energy. *Energy Res. Soc. Sci.* **51**, 40–43 (2019). <https://doi.org/10.1016/j.erss.2019.01.008>
2. Rathnayake, C.W.M., Jones, S., Soto-Berelov, M.: Mapping land cover change over a 25-year period (1993–2018) in Sri Lanka using landsat time-series. *Land* **9**(1) (2020). <https://doi.org/10.3390/land9010027>
3. Dastgheib, A., Jongejan, R., Wickramanayake, M., Ranasinghe, R.: Regional scale risk-informed land-use planning using Probabilistic Coastline Recession modelling and economical optimisation: East Coast of Sri Lanka. *J. Mar. Sci. Eng.* **6**(4) (2018). <https://doi.org/10.3390/jmse6040120>
4. Ceylon Electricity Board: Sri Lanka Statistical Digest 2020 (2019). https://ceb.lk/front_img/img_reports/1626946210CEB-Statistical_Digest-Form-2020-Web_Version.pdf
5. Economic and Poverty Impact of COVID-19 Sri Lanka Development (2021). www.worldbank.org/en/country/srilanka
6. Jayasinghe, B.M.D.N.S., Sulakna Gunasekara, U.J.: Nuclear power as a possible direction of developing the energy sector of Sri Lanka. In: *IEEE Conference of Russian Young Researchers in Electrical and Electronic Engineering (ElConRus)*, pp. 1435–1440 (2021). <https://doi.org/10.1109/ElConRus51938.2021.9396457>
7. de Vos, A., Pattiaratchi, C.B., Wijeratne, E.M.S.: Surface circulation and upwelling patterns around Sri Lanka. *Biogeosciences* **11**(20), 5909–5930 (2014). <https://doi.org/10.5194/bg-11-5909-2014>
8. Jayasinghe, N., Gunasekara, U.: Floating nuclear power plants for energy supply of the Maldives. In: Gupta, O.H., Sood, V.K., Malik, O.P. (eds) *Recent Advances in Power Systems*.

- Lecture Notes in Electrical Engineering, vol 812. Springer, Singapore. https://doi.org/10.1007/978-981-16-6970-5_44
9. Dannheim, J., Bergström, L., Birchenough, S.N.R., Brzana, R., Boon, A.R., Coolen, J.W.P., Dauvin, J.C., de Mesel, I., Derweduwén, J., Gill, A.B., Hutchison, Z.L., Jackson, A.C., Janas, U., Martin, G., Raoux, A., Reubens, J., Rostin, L., Vanaverbeke, J., Wilding, T.A., et al.: Benthic effects of offshore renewables: identification of knowledge gaps and urgently needed research. *ICES J. Mar. Sci.* **77**(3), 1092–1108 (2020). <https://doi.org/10.1093/icesjms/fsz018>
 10. Hirth, L., Müller, S.: System-friendly wind power. How advanced wind turbine design can increase the economic value of electricity generated through wind power. *Energy Econ.* **56**, 51–63 (2016). <https://doi.org/10.1016/j.eneco.2016.02.016>
 11. Karl, D.J.: Sri Lanka, the maritime silk road, and Sino-Indian relations. In: *China's Maritime Silk Road Initiative and South Asia*, pp. 137–172. Springer, Singapore. https://doi.org/10.1007/978-981-10-5239-2_6
 12. Weiss, C.V.C., Guanche, R., Ondiviela, B., Castellanos, O.F., Juanes, J.: Marine renewable energy potential: a global perspective for offshore wind and wave exploitation. *Energy Convers. Manage.* **177**, 43–54 (2018). <https://doi.org/10.1016/j.enconman.2018.09.059>
 13. Global Maritime traffic. <https://globalmaritimetraffic.org/gmtds.html>
 14. Caine, C.A.: The race to the water for offshore renewable energy: assessing cumulative and in-combination impacts for offshore renewable energy developments. *J. Environ. Law* **32**(1), 83–109 (2020). <https://doi.org/10.1093/jel/eqz031>
 15. Karunarathna, H., Maduwantha, P., Kamranzad, B., Rathnasooriya, H., de Silva, K.: Impacts of global climate change on the future ocean wave power potential: a case study from the Indian Ocean. *Energies* **13**(11) (2020). <https://doi.org/10.3390/en13113028>
 16. Rath, S., Vinayachandran, P.N., Behara, A., Neema, C.P.: Dynamics of summer monsoon current around Sri Lanka. *Ocean Dyn.* **69**(10), 1133–1154 (2019). <https://doi.org/10.1007/s10236-019-01295-x>
 17. Webber, B.G.M., Matthews, A.J., Vinayachandran, P.N., Neema, C.P., Sanchez-Franks, A., Vijith, V., Amol, P., Baranowski, D.B.: The dynamics of the southwest monsoon current in 2016 from high-resolution in situ observations and models. *J. Phys. Oceanogr.* **48**(10), 2259–2282 (2018). <https://doi.org/10.1175/JPO-D-17-0215.1>
 18. European Centre for Medium-Range Weather Forecasts (ECMWF). https://apps.ecmwf.int/webapps/opencharts/products/opencharts_metogram?base_time=202203140000&epsgram=classical_10d&lat=51.43&lon=-1&station_name=Reading
 19. Suresh, I., Vialard, J., Izumo, T., Lengaigne, M., Han, W., McCreary, J., Muraleedharan, P.M.: Dominant role of winds near Sri Lanka in driving seasonal sea level variations along the west coast of India. *Geophys. Res. Lett.* **43**(13), 7028–7035 (2016). <https://doi.org/10.1002/2016GL069976>
 20. Payne, G.S., Stallard, T., Martinez, R.: Design and manufacture of a bed supported tidal turbine model for blade and shaft load measurement in turbulent flow and waves. *Renewable Energy* **107**, 312–326 (2017). <https://doi.org/10.1016/j.renene.2017.01.068>
 21. Nachtane, M., Tarfaoui, M., Goda, I., Rouway, M.: A review on the technologies, design considerations and numerical models of tidal current turbines. *Renewable Energy* **157**, 1274–1288 (2020). <https://doi.org/10.1016/j.renene.2020.04.155>
 22. Rouway, M., Nachtane, M., Tarfaoui, M., Chakhchaoui, N., El, L., Omari, H., Fraija, F., Cherkaoui, O.: 3D printing: rapid manufacturing of a new small-scale tidal turbine blade (n.d.). <https://doi.org/10.1007/s00170-021-07163-7/Published>
 23. Kennedy, C.R., Jaksic, V., Leen, S.B., Brádaigh, C.M.Ó.: Fatigue life of pitch- and stall-regulated composite tidal turbine blades. *Renewable Energy* **121**, 688–699 (2018). <https://doi.org/10.1016/j.renene.2018.01.085>
 24. Roberts, A., Thomas, B., Sewell, P., Khan, Z., Balmain, S., Gillman, J.: Current tidal power technologies and their suitability for applications in coastal and marine areas. *J. Ocean Eng. Mar. Energy* **2**(2), 227–245 (2016). <https://doi.org/10.1007/s40722-016-0044-8>
 25. Ramos, V., Carballo, R., Ringwood, J.V.: Application of the actuator disc theory of Delft3D-FLOW to model far-field hydrodynamic impacts of tidal turbines. *Renewable Energy* **139**, 1320–1335 (2019). <https://doi.org/10.1016/j.renene.2019.02.094>

26. Njiri, J.G., Söffker, D.: State-of-the-art in wind turbine control: trends and challenges. In: *Renewable Sustain. Energy Rev.* **60**, 377–393 (2016). <https://doi.org/10.1016/j.rser.2016.01.110>
27. Betz, A.: *Introduction to the Theory of Flow Machines*. Elsevier (2014)
28. Uddin, M.S., Kumar, S.: Energy, emissions and environmental impact analysis of wind turbine using life cycle assessment technique. *J. Clean. Prod.* **69**, 153–164 (2014). <https://doi.org/10.1016/j.jclepro.2014.01.073>
29. Nasab, N.M., Kilby, J., Bakhtiaryfard, L.: Case study of a hybrid wind and tidal turbines system with a microgrid for power supply to a remote off-grid community in New Zealand. *Energies* **14**(12) (2021). <https://doi.org/10.3390/en14123636>
30. Coles, D., Angeloudis, A., Goss, Z., Miles, J.: Tidal stream versus wind energy: the value of cyclic power when combined with short-term storage in hybrid systems. *Energies* **14**(4) (2021). <https://doi.org/10.3390/en14041106>
31. Korompili, A., Wu, Q., Zhao, H.: Review of VSC HVDC connection for offshore wind power integration. *Renewable Sustain. Energy Rev.* **59**, 1405–1414 (2016). <https://doi.org/10.1016/j.rser.2016.01.064>
32. Wang, L., Lin, C.Y., Wu, H.Y., Prokhorov, A.V.: Stability analysis of a microgrid system with a hybrid offshore wind and ocean energy farm fed to a power grid through an HVDC link. *IEEE Trans. Ind. Appl.* **54**(3), 2012–2022 (2018). <https://doi.org/10.1109/TIA.2017.2787126>

Evaluation of Various Dynamics on Current Transformer Saturation with a Model Study on Power System Protection



Dharmesh Patel and Nilesh Chothani

1 Introduction

Practically electrical power system network works smoothly by measuring current and voltage signals and decisions for relaying purposes are derived from these measurements. The relaying system works with a lower range of current (in amperes, not kA) and voltage (volts, not kV). So, currents and voltages magnitudes must be scaled to lower the levels and then fed to the meters and relays. This work can be done by Current Transformers (CTs) and Voltage Transformers (VTs). These measuring transformers are also electrically isolating the relaying system from the high range of power apparatus, which also provides safety for both human beings and the equipment. Considering this reason into account we can say that CTs and VTs are the measuring sensors for the relay. Based on the sensed quantity by these instruments, the decision-making block (relay) processes these signals and generates decision commands to circuit breakers, alarms, etc. The working quality of the current-based relaying scheme depends upon the authentic reproduction of the signal on the secondary side of the CT.

The CTs can be classified into measurement CTs and protection CTs [1]. Two types of CTs are classified as per ANSI/IEEE standards: Class T and Class C. Same as auxiliary CTs are used for circuit isolation to permit independent grounding and change in ratio to match current requirements.

Hooshyar et al. [2] proposed current differential function to detect the saturation of CT from the properties of the current signal wave shape. They have also considered

D. Patel

Electrical Department, Government Engineering College, Old N.H., College Road, Bholav, Bharuch, Gujarat 392002, India

N. Chothani (✉)

Electrical Department, Pandit Deendayal Energy University, Knowledge Corridor, Raisan Village, PDPD Rd, Gandhinagar, Gujarat 382007, India

e-mail: chothani_nilesh@rediffmail.com

mathematical morphological solutions based on wave shape properties of current derivatives, but practical implementation is remained left. After that, Hooshyar and Sanaye-Pasand [3] elaborated precise measurement of fault currents breached with decaying dc offset and CT saturation result confirmation throughout the system is perfect, even simulation results are also validated. Hooshyar and Sanaye-Pasand [4] involved CT saturation identification based on waveform analysis with the use of a variable-length window. Solak et al. [5] suggested transmission line differential relay immune to CT saturation based on a fuzzy adaptive concept. Results are highly validated with 5000 test data with 0% error in simulation on ATP software. Bertrand et al. [6] presented CT saturation calculations: IEC standards and nonconventional instrument transformers which give a general idea regarding the effect of CT saturation. dos Santos et al. [7] proposed the detection of CT saturation with the use of the distance between consecutive points in the plans formed by the secondary current samples and their different functions on EMTP software-based simulation with mathematical explanations. Moreover, THD-based CT saturation detection techniques are also adopted under transformer protection under various test conditions [8]. Various CT saturation effects are incorporated in transformer protection with adaptively shifting percentage biased characteristics under linear and non-linear load conditions [9–11].

Kuzhekov et al. [12] proposed a technique to compute the coefficient of the transient regime and the time-to-saturation of CT. However, the method depends only on the characteristics of CT and not on the external parameters of the 500 kV power system network. Vakhnina et al. [13] have presented a system of non-linear differential equations considering the non-linearity of the inductive resistances of the magnetization curve. The developed model considers the effect of DC offset on the saturation of the transformer core. However, other effects like over fluxing and remnant flux are not considered in the analysis. A novel scheme has suggested a technique using the dynamic current saturation with phasor estimation [14]. An index is calculated to compute the difference between the estimated current samples regenerated from the dynamic phasor and the actual current samples value. However, the noise and harmonics must be taken into consideration while estimating the phasor values of CT secondary signals.

A controlled voltage source (CVS)-based device is introduced in series with a relay to compensate for Current transformer (CT) saturation [15]. The suggested CVS produces a voltage change with time to cancel out the voltage induced across the CT burden. Therefore, the CT core flux remains undistorted and virtually constant during the power system faults. On the other hand, the asymmetry in the original waveform and the presence of DC decaying components may affect the operation of protective devices. Detection and resolution of CT saturation are important to eliminate the maloperation of the current-based protective relays. Haghjoo and Pak [16] have demonstrated least square error and artificial neural network-based compensation and reconstruction of the distorted secondary current waveform of CT. The suggested method can work for minor variations in system parameters and noisy environments.

Davarpanah et al. [17, 18] elaborated a saturation suppression approach for the CT as a fundamental concept with flux condition flag (FCF). Schettino et al. [19] offered a new method of CT saturation detection in the presence of noise, and signal-to-noise

ratio (SNR). Smith and Hunt [20] elucidated CT saturation effects on coordinating time intervals based on partial differential loss of coordination. Hooshyar et al. [21] carried out several simulations on PSCAD software on a current derivative-based algorithm to detect saturation phenomenon in CT. Hooshyar and Sanaye-Pasand [22] detailed wave shape recognition technology to detect CT saturation. Esmail et al. [23] presented the detection of partial saturation and waveform compensation of CTs using the Kalman filtering technique. Also, three state Kalman filtering-based technique [24] provides better results than DFT based algorithm. Even under real-time monitoring of transformer special effects of CT saturations are also given distinctive consideration [25, 26].

Ajaei et al. [27] explicated compensation of the CT saturation. They are using Least Estimation Square (LES) filtering technology for the current waveform and make validation through PSCAD™ software, and they introduce Minimum Estimation Error Tracking (MEET). Now a day, artificial intelligence is incorporated to improve the accuracy of any system protection section of the power systems. Many classifiers [28–31] and regression techniques are adopted to discriminate CT saturation conditions under various parameter considerations and variations. Even in transmission line protection various abnormalities and advance protection systems are elaborate nicely [32, 33] to avoid power system stress and unwanted blackout.

CT saturation is affected by various parameters and comprehensive knowledge is required to analyze or discriminate those conditions. Otherwise, the power system protective scheme may malfunction under unwanted power system abnormalities.

2 Saturation Problem in Current Transformer (CT)

CT is a specially designed transformer for the higher rating of fault current capturing. So, in CT, there are special designs for core manufacturing. Core saturation normally occurs due to the core characteristics and material used for manufacturing. Saturation is a basic physical phenomenon of CT under excessive current or burden. This singularity occurs when the combined magnetic flux is so powerful that all magnetic domains of core material are allied in one direction and thus do not allow for any further intensification in the flux. The electromechanical conversion principle states that the secondary output of CT is closely related to the changing coupled magnetic flux. That's why the conventional transformer and regular CT do not operate on DC supply. Along with fundamental AC, a small transient DC is applied to the primary of the CT, however, this DC does not replicate on the secondary side of CT. This DC transient current merely produces unidirectional flux and thus contributes to core saturation.

Saturation of the CT is caused by the non-linear nature of the electromagnetic core. Thus, the output signal of CT will be severely distorted whenever the core flux density enters the region of saturation. During this situation, two components of flux are set up in the core: (1) Alternating flux Φ_{AC} which is propositional to the fundamental frequency component of the fault current and (2) Transient flux Φ_{DC}

which is induced by the DC decaying component of the fault current. The second component Φ_{DC} is a function of CT primary and secondary circuit time constants. Primary CT is connected to the power system network and hence primary constant. The time constant of the secondary circuit is defined by the burden impedance and leakage impedance on the secondary side.

The factors affecting CT saturation are: (a) Secondary burden, (b) Primary current, (c) Asymmetry in the primary current, and (d) Remnant flux in the core of the CT.

For simplicity, let us accept that initially at $t = 0$ the magnitude of flux in core of CT is zero. Then using the Faraday's law, one can find the flux setup in the core of transformer as per below equation:

$$V_2 = N_2 \frac{d\phi}{dt} \quad (1)$$

$$\begin{aligned} \phi(t) - \phi(0) &= \frac{1}{N_2} \int_0^t v_2 dt \\ &= \frac{RI_0}{N_2} \tau (1 - e^{-\frac{t}{\tau}}) \\ &= \frac{LI_0}{N_2} (1 - e^{-\frac{t}{\tau}}) \\ \phi(t) &= \phi(0) + \frac{LI_0}{N_2} (1 - e^{-\frac{t}{\tau}}) \\ &= \frac{LI_0}{N_2} (1 - e^{-\frac{t}{\tau}}) \end{aligned} \quad (2)$$

The peak value of flux in the core which exponentially increases to

$$\phi_{dc}^{\max} = \frac{LI_0}{N_2}$$

as

$$t \rightarrow \infty = \frac{L}{N} \frac{V_m}{|Z|} = \frac{V_m}{|Z|} = \phi_{dc}^{\max} \quad (3)$$

Here, the flux as derived in Eq. (3) is unidirectional, unlike flux induced by sinusoidal ac voltage. The flux set up in a practical CT core during transient conditions is the addition of AC flux and DC flux.

The ac flux induced in core can be derived by replacing operator $\frac{d}{dt}$ by $j\omega$.

Hence phasor relationship between phase \bar{V}_2 and $\bar{\phi}_{ac}$ is given by

$$\bar{\phi} = \frac{\bar{V}_2}{j\omega N_2} \quad (4)$$

If, $V_2(t) = V_m \sin(\omega t + \phi)$, then

$$\phi_{ac} = \frac{V_m}{\omega N_2} \sin(\omega t + \phi - \frac{\pi}{2}) \tag{5}$$

The maximum value of ac flux is given by

$$\phi_{ac}^{max} = \frac{V_m}{\omega N_2}$$

However, $V_m = R_2 I_0^{max}$ Hence,

$$\phi_{ac}^{max} = \frac{R_2 I_0^{max}}{\omega N_2}$$

And peak value of the total flux is given by

$$\phi_{ac}^{max} + \phi_{dc}^{max} = \frac{V_m}{\omega N_2} + \frac{L I_0^{max}}{N_2} \tag{6}$$

In practice, if this flux crosses the knee point flux in the core, then the CT core will saturate as shown in Fig. 1.

While CT is operating in a saturation region, the primary current would not reliably be transformed into a secondary current. It has been observed that the secondary current is trimmed and may lead to the relay maloperation and under the worst

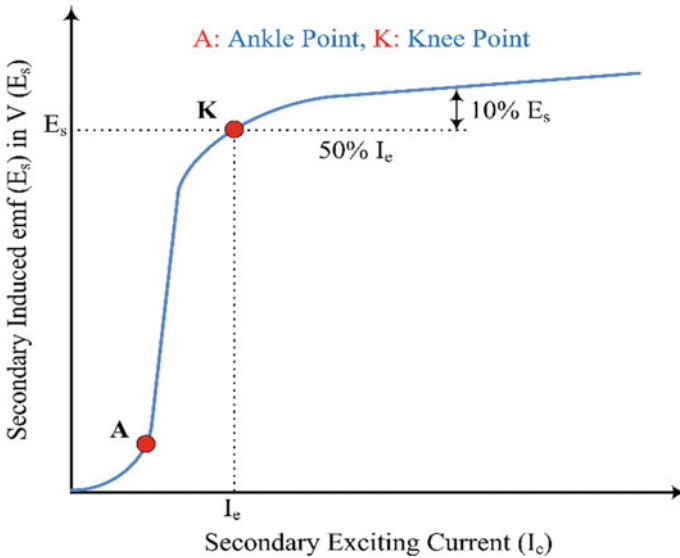


Fig. 1 CT saturation curve

condition relay fail to operate. It has been proved that the core saturation does not start instantly after the inception of the fault. Thus, the fast operating relay can decide to detect the fault at that particular time before CT saturation. Else, a slow-acting relay generates a wrong decision and creates a glitch in the operation of the power system network. Thus, it is necessary to evaluate the parameters of CT and its saturation effect under varying power system scenarios.

2.1 CT Oversizing Factors

Characteristically, the cross-section of the CT core would be selected so that ϕ_m^{ac} on B-H curve should be near the knee point (Fig. 1). Oversizing the core is the understandable way to avoid the saturation of CT by dc flux so that, for the given flux ($\phi_{ac}^{max} + \phi_{dc}^{max}$) the equivalent flux density B remains below the knee point. Hence, the factor

$$\frac{(\phi_{ac}^{max} + \phi_{dc}^{max})}{\phi_{ac}^{max}}$$

is known as the core-over sizing factor.

$$\begin{aligned} \text{Core - over sizing factor} &= 1 + \frac{\phi_{dc}^{max}}{\phi_{ac}^{max}} \\ &= 1 + \frac{LI_0/N_2}{RI_0/\omega N_2} \\ &= 1 + \frac{\omega L}{R} \\ &= 1 + \frac{X}{R} \end{aligned} \quad (7)$$

Here, X/R is the reactance to resistance ratio of the power system network line parameter X/R ratio. This X/R ratio is approximately 10 for a 220 kV transmission line. Thus, the core size of the instrument transformer should be a factor of 11. Similarly, for a 400 kV line typical value of this ratio will be 20. This suggests that the necessity of core oversizing is around 21 times the actual core design. This amount of oversizing of the core is practically not possible. Thus, the important decision is such that, protection engineers should bare the saturation problem and find an alternative solution to mitigate it.

2.2 *Minimizing the Effects of CT Saturation*

Generally, the performance specification for protective relays only covers operation at fundamental frequency sinusoidal currents. A rule of thumb frequently used in relating to minimizing the CT saturation effects is to select a CT with a C voltage rating at least twice that required for the maximum steady-state symmetrical fault current [34].

2.3 *Time-to-Saturation*

It can be observed that the distortion in the secondary signal begins a certain amount of time after the fault inception. Time-to-saturation is a measure of time just after the inception of fault in the power system by which the secondary current accurately reproduces the primary current as per the CT ratio. Time-to-saturation can be determined systematically based on the given power system parameters and saturation factor of CT. Time-to-saturation is important in the design and application of protective CTs. The time-to-saturation of a CT is determined by the following parameters:

- Asymmetry in fault current
- Severity of fault current
- Remnant flux in the CT core
- Burden of the secondary circuit
- Knee point (Saturation) voltage
- Turns ratio of CT.

2.4 *Carefulness in CT Selection*

Proper selection of a CT is required for a good protection scheme operation.

- Maximum load current and the rating of CT must be perfectly matched. As an example, if the max continuous load current is 900 A, a 1000:5 A CT may be suitable but a 500:5 A CT is not acceptable.
- Magnitude of fault current (maximum) should be less than 20 times the rated current of CT. For example, 1000:5 A CT can be used, so long as the burden on the CT and maximum primary fault current are below 20,000 A.
- The voltage rating of CT should be compatible with knee point in saturation characteristic. For example, 1000:5 C100 would give a linear response, up to 20 times rated current provided CT burden is kept below $(100/20 * 5 = 1 \Omega)$. With higher burdens than 1Ω , this CT can only be used if the maximum current is limited to 20 times the rated current.

3 Consequences of CT Saturation on Protective Relays

3.1 Impact of CT Saturation on Electromechanical Relays

The operation of an electromechanical relay cannot be projected for non-sinusoidal currents without detailed knowledge of the operating principles of the relay. The operation of electromechanical relays is related to the RMS value of current applied to the relay coil. However, during saturation, distorted current other than fundamental frequency components produce phase-shifted fluxes which may perform differently and produce unwanted torque in the relay.

3.2 Impact of CT Saturation on Static/Digital Relays

These types of relays either receive an analog current signal directly as an input or analog to digital converters is used. Depending on the construction, analog-type static relay reacts to an average value of current after applying filters. The digital relays response mainly depends on the technique used for current estimation and the software used for the same.

3.3 Impact of CT Saturation on Differential Relays

In a power system, a differential relay is the most sensitive and important protective scheme for the unit protection medium to large equipment. Differential relay's basic purpose is to operate under internal fault only whether it is severe or else. And it remains inoperative under any type of external affairs, abnormalities, or severe external faults. In the differential relay, the CT saturation effect depends on the burden offered by different types of relays and on the intensity of the fault. The design and settings of differential relay should be such that it successfully operates during internal fault even in presence of distorted waveforms. The more dominant suffering is the possible maloperation of differential relays for external faults due to CT saturation. Moreover, percentage differential characteristic-based differential relays have some immunity to mis-operation on severe external faults because their operating characteristic needs a substantial ratio of operating current to restraining current. Furthermore, advanced techniques based on artificial intelligence may aid significant contributions to early and severe CT saturation detection incorporated in existing percentage differential relays.

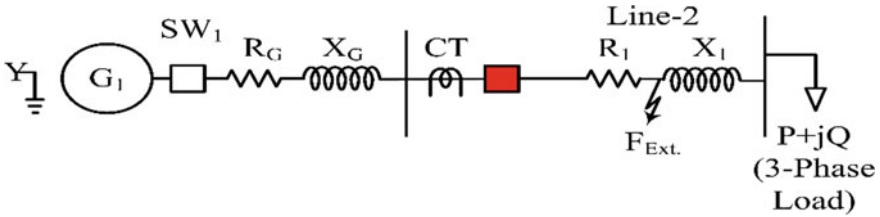


Fig. 2 Single line diagram of a portion of power system

4 System Diagram and Parameters

Where R_G and X_G are the Resistance and reactance of the generator, respectively, the generator is further connected to the bus and a CT with the relay is shown in the diagram, R_1 and X_1 are the line parameters, and the line is again connected to the load side bus and the supply is given through that bus to the load.

Figure 2 shows a one-line diagram of a typical power system for simulation modeling. In which a star grounded generator supplies power to a 3-phase load through a medium-length transmission system. CT observes the whole system continuously and gives a signal to the relaying system to make decisions and generate trip signals under faulty conditions. In case of fault occur in the system breaker must operate via the tripping signal of the relay.

The detailed parameters of the system are given in Appendix.

5 Results Related to CT

A wide range of parameters is considered for testing and confirming analysis. Results show that due to the CT saturation effect and CT ratio mismatch, a current difference is generated between primary and secondary protective CTs. FIA generate decaying DC component.

5.1 Result for the Various Condition of CT (Normal and Saturation Condition)

$$\begin{aligned}
 \text{Core – over sizing factor} &= 1 + \frac{\phi_{dc}^{max}}{\phi_{ac}^{max}} \\
 &= 1 + \frac{LI_0/N_2}{RI_0/\omega N_2} \\
 &= 1 + \frac{X}{R}
 \end{aligned}$$

$$= 1 + \frac{\omega L}{R}$$

Figure 3a–c shows the effect of the variation of X and R , with the fault inception angle is 0.515 (second) consider so $\phi_{ac}^{max} = \phi_{dc}^{max}$. Due to this there is no offsetting effect is seen. But, due to an increase in inductance and resistance, the current effect and DC offset effect is also appearing in Fig. 3a–c.

Now at inception angle at 0.5 (second) and $R = 1 \Omega$ and $L = 0.1$ H. DC offset current is clearly shown in Fig. 4.

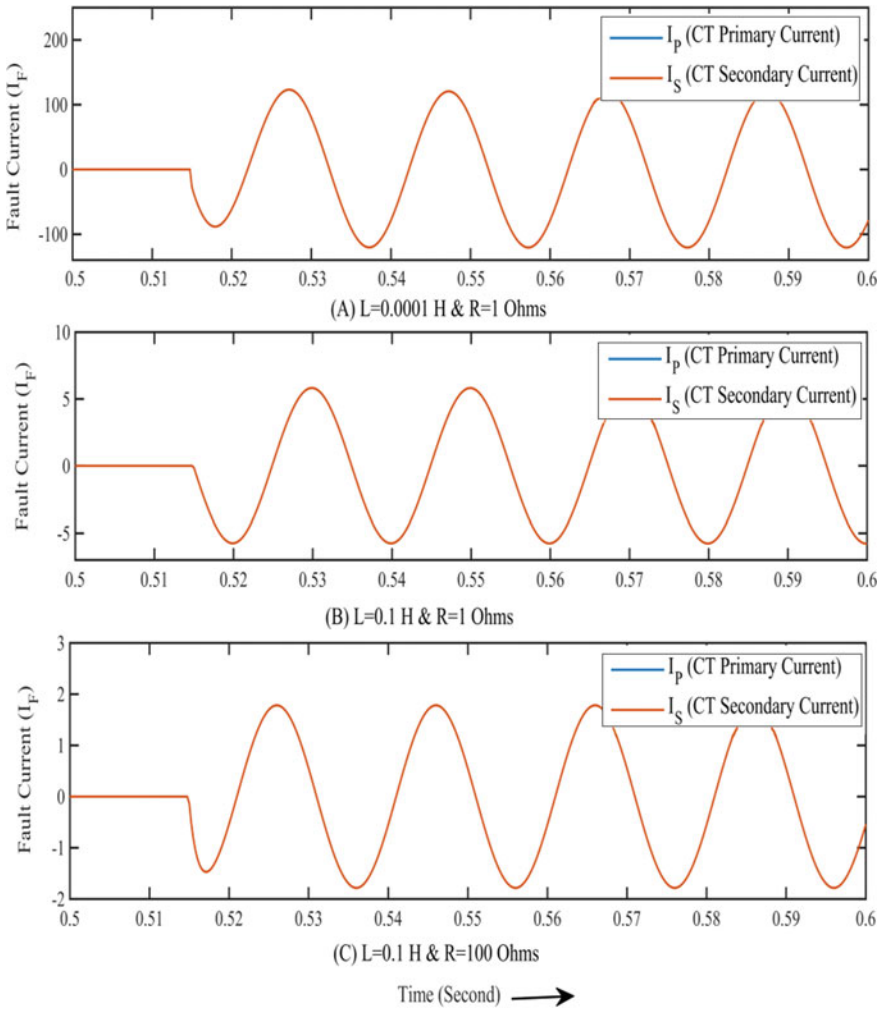


Fig. 3 Fault current versus time under change in inductance at inception angle 0.515 in second

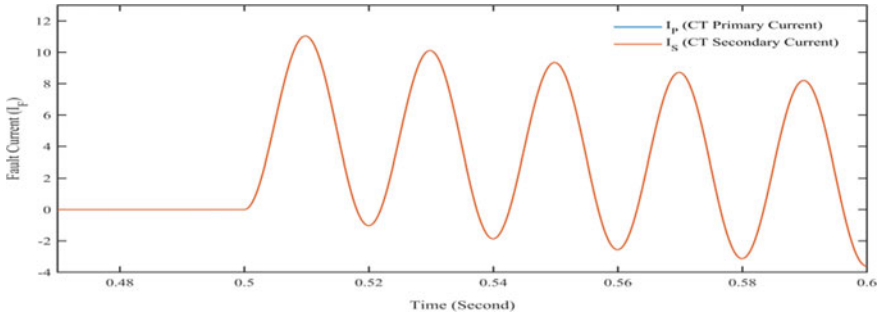


Fig. 4 Fault current versus time at fault inception angle at 0.5 s and $R = 1 \Omega$ and $L = 0.1 \text{ H}$

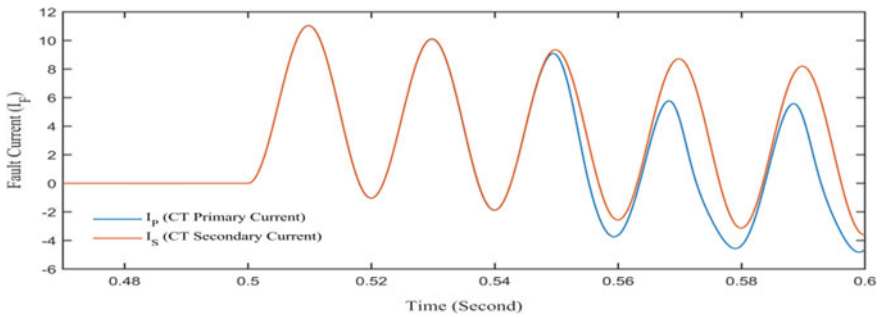


Fig. 5 Fault current versus time at fault inception angle at 0.5 (second) and $R = 10 \Omega$ and $L = 0.1 \text{ H}$ (with the high burden of CT)

5.2 Effect of a High Burden on CT Saturation

Figure 5 clearly shows an effect of CT saturation after 1.5 cycles at a fault inception angle of 0.5 (second) when we apply a high burden on CT secondary.

5.3 Effect of Remnant Flux

Figure 6a–d shows an effect of remnant flux on CT saturation, if remnant flux is lesser, then saturation of CT is occurred after a lesser time and it will reduce if remnant flux increases.

We can easily see that at remnant flux 0.5 T at that time CT gets saturation after 0.75 cycles, at remnant flux 0.9 T at that time CT gets saturation after 0.60 cycles, at remnant flux 1 T at that time CT gets saturation after 0.35 cycle, and at remnant flux, 2 T at that time CT get saturation after 0.05 cycle.

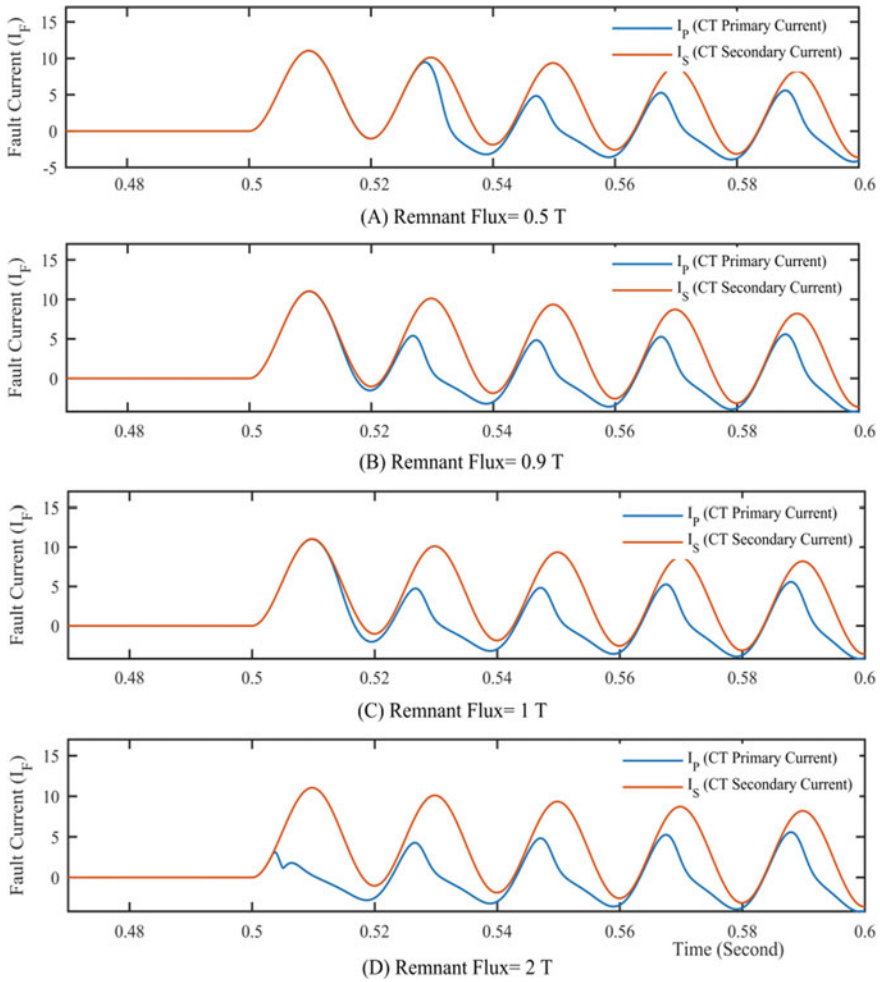


Fig. 6 Effect of remnant flux on CT saturation, fault inception angle 0.5 (second), line $R = 1 \Omega$ and $L = 0.1 \text{ H}$ with burden 0.5Ω

5.4 Variation of Fault Inception Angle

Mostly it is seen that DC offset is not offered to change in waveform after its five-time of the time constants. The value of I_0 can be formulated by setting the current to zero value $t = t_0$. This infers that

$$I_0 = -\frac{V_m}{|Z|} \sin(\omega t_0 + \varphi - \theta)$$

$$i(t) = \frac{V_m}{|Z|} \sin(\omega t + \phi - \theta) - \frac{V_m}{|Z|} \sin(\omega t + \phi - \theta) e^{-\left(\frac{t-t_0}{\tau}\right)}$$

Noticeably, the maximum amplitude of DC decaying current be subject to,

- Fault inception time
- The phase angle ϕ of applied AC voltage
- $|Z|$ and θ of power system/transmission line.

In the above analysis (Fig. 7) of fault inception at different times, a single-phase fault is considered. Looking to the waveform of Fig. 7 for different fault inception angles, it is concluded that

1. DC offset current may be absent, e.g., If $\varphi = \theta, t_0 = 0$ (see Fig. 7a)
2. The DC offset current can be positive or negative (see Fig. 7b-c).

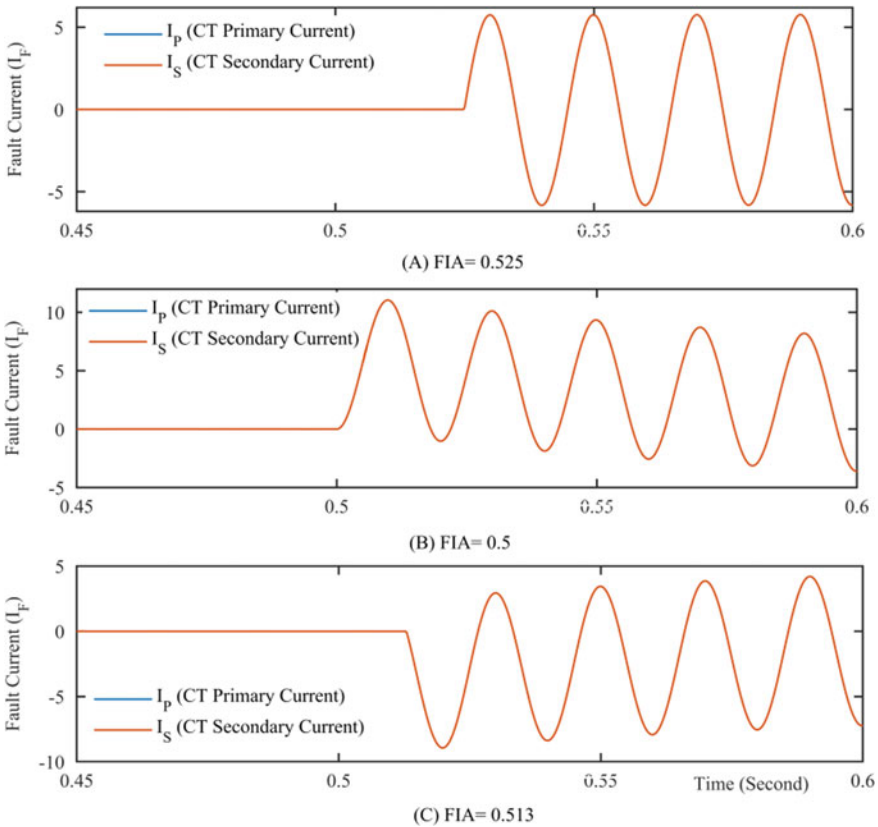


Fig. 7 Effect fault inception angle

6 Conclusion

Due to CT saturation, many protective schemes are malfunctioning in the existing power system. So, protective relays must be equipped with suitable CT saturation discrimination techniques to notice CT saturation (Based on the criteria that the CT can deliver 20 times rated secondary current without exceeding a 10% ratio error). Every protective CT must fruitfully transform the primary current into the secondary side without any distortion. However, considering the size of the core, secondary burden, and DC offset in primary current and external network parameters, saturation is likely to occur in the worst condition of the fault scenario. These parameters variation results in distortion of the waveform, current magnitudes dramatically drop, and secondary current contains harmonics. In absence of I_m , CT works in ideal mode, and $I_s = NI_p$. However, the actual CT secondary current (I_s) is subject to an error due to the presence of a high magnetization current (I_m) during a severe fault condition. There are so many schemes available like Zero-Crossing Detection, Kalman filtering method, symmetric assessment window base system, signal to noise ratio, etc. to make $I_m = 0$. In this article, the system is simulated in PSCAD™ for obtaining CT saturation and various typical waveform results are obtained during the variation in burden, different fault inception angles, the effect of remnant flux, and DC offset. It has been observed from the simulation results and waveform how CT behave during the different operating condition of the power system. The future objective is to determine the proper method or any mathematical morphology to detect saturation or reduce the CT saturation effect and implement it in real practice.

Appendix

System Modelling (Simulation Parameters for CT saturation)

Sr	Particulars	Value (Range)
CT data		
1	Primary turns	1
2	Secondary turns	1000
3	Secondary resistance	0.5 Ω
4	Secondary inductance	0.8e-3 (H)
5	Area path length	2.601e-3 (m*m)
6	Remnant flux	0-2 T
Line data		
1	Resistance	1 Ω (-100 Ω)
2	Inductance	0.1 H (0.1-0.0001 H)
Source data		

(continued)

(continued)

Sr	Particulars	Value (Range)
1	Type	AC
2	Voltage	110 kV
3	Frequency	50 Hz

References

1. Committee, P.S.R.: ANSI/IEEE C57.13.1-198X guide for field testing of relaying current transformers. *IEEE Trans. Power Appar. Syst.* (1981). <https://doi.org/10.1109/TPAS.1981.316949>
2. Hooshyar, A., Sanaye-Pasand, M., El-Saadany, E.F.: CT saturation detection based on wave-shape properties of current difference functions. *IEEE Trans. Power Deliv.* **28**, 2254–2263 (2013)
3. Hooshyar, A., Sanaye-Pasand, M.: Accurate measurement of fault currents contaminated with decaying DC offset and CT saturation. *IEEE Trans. Power Deliv.* **27**, 773–783 (2012)
4. Hooshyar, A., Sanaye-Pasand, M.: CT saturation detection based on waveform analysis using a variable-length window. *IEEE Trans. Power Deliv.* **26**, 2040–2050 (2011)
5. Solak, K., Rebizant, W., Klimek, A.: Fuzzy adaptive transmission-line differential relay immune to CT saturation. *IEEE Trans. Power Deliv.* **27**, 766–772 (2012)
6. Bertrand, P., Mendik, M., Hazel, T., Tantin, P.: CT saturation calculations: IEC standards and nonconventional instrument transformers. *IEEE Ind. Appl. Mag.* **18**, 12–20 (2012)
7. dos Santos, E.M., Cardoso, G., Farias, P.E., de Moraes, A.P.: CT saturation detection based on the distance between consecutive points in the plans formed by the secondary current samples and their difference-functions. *IEEE Trans. Power Deliv.* **28**, 29–37 (2013)
8. Raichura, M., Chothani, N., Patel, D., Mistry, K.: Total harmonic distortion (THD) based discrimination of normal, inrush and fault conditions in power transformer. *Renew. Energy Focus* **36**, 43–55 (2021)
9. Patel, D.D., Chothani, N., Mistry, K.D., Tailor, D.: Adaptive algorithm for distribution transformer protection to improve smart grid stability. *Int. J. Emerg. Electr. Power Syst.* **19**, 1–14 (2018)
10. Raichura, M., Chothani, N., Patel, D.: Development of an adaptive differential protection scheme for transformer during current transformer saturation and over-fluxing condition. *Int. Trans. Electr. Energy Syst.* **31**, 1–19 (2020)
11. Patel, D., Chothani, N.: Adaptive digital differential protection of power transformer. In: *Digital Protective Schemes for Power Transformer*, pp. 83–106. Springer, Singapore (2020). https://doi.org/10.1007/978-981-15-6763-6_4
12. Kuzhekov, S.L., Degtyarev, A.A., Vorob’ev, V.S., Moskalenko, V.V.: Determination of the time-to-saturation of current transformers in short-circuit transient regimes. *Power Technol. Eng.* **51**, 234–239 (2017)
13. Vakhnina, V.V., Kuznetsov, V.N., Shapovalov, V.A., Samolina, O.V.: Modeling the saturation processes of a power-transformer core under simultaneous direct and alternating current passing through the winding. *Russ. Electr. Eng.* **88**, 223–228 (2017)
14. Biswal, S., Biswal, M.: Algorithm for CT saturation detection with the presence of noise. In: *4th International Conference on Electrical Energy Systems (ICEES)*, pp. 248–251 (2018). <https://doi.org/10.1109/ICEES.2018.8443196>
15. Hajipour, E., Vakilian, M., Sanaye-Pasand, M.: Current-transformer saturation prevention using a controlled voltage-source compensator. *IEEE Trans. Power Deliv.* **32**, 1039–1048 (2017)

16. Haghjoo, F., Pak, M.H.: Compensation of CT distorted secondary current waveform in online conditions. *IEEE Trans. Power Deliv.* **31**, 711–720 (2016)
17. Davarpanah, M., Sanaye-Pasand, M., Iravani, R.: A saturation suppression approach for the current transformer-Part I: fundamental concepts and design. *IEEE Trans. Power Deliv.* **28**, 1928–1935 (2013)
18. Davarpanah, M., Sanaye-Pasand, M., Iravani, R.: A saturation suppression approach for the current transformer—Part II: performance evaluation. *IEEE Trans. Power Deliv.* **28**, 1936–1943 (2013)
19. Schettino, B.M., Duque, C.A., Silveira, P.M., Ribeiro, P.F., Cerqueira, A.S.: A new method of current-transformer saturation detection in the presence of noise. *IEEE Trans. Power Deliv.* **29**, 1760–1767 (2014)
20. Smith, T., Hunt, R.: Current transformer saturation effects on coordinating time interval. *IEEE Trans. Ind. Appl.* **49**, 825–831 (2013)
21. Hooshyar, A., Sanaye-Pasand, M., Davarpanah, M.: Development of a new derivative-based algorithm to detect current transformer saturation. *IET Gener. Transm. Distrib.* **6**, 207–217 (2012)
22. Hooshyar, A., Sanaye-Pasand, M.: Waveshape recognition technique to detect current transformer saturation. *IET Gener. Transm. Distrib.* **9**, 1430–1438 (2015)
23. Esmail, E.M., Elkalashy, N.I., Kawady, T.A., Taalab, A.I., Lehtonen, M.: Detection of partial saturation and waveform compensation of current transformers. *IEEE Trans. Power Deliv.* **30**, 1620–1622 (2015)
24. Patel, D.D., Mistry, K., Raichura, M.B., Chothani, N.: Three state kalman filter based directional protection of power transformer. In: 20th National Power Systems Conference (NPSC), pp. 1–6. IEEE (2018). <https://doi.org/10.1109/NPSC.2018.8771716>
25. Chothani, N.G., Raichura, M.B., Patel, D.D., Mistry, K.D.: Real-time monitoring protection of power transformer to enhance smart grid reliability. In: IEEE Electrical Power and Energy Conference (EPEC), pp. 1–6. IEEE (2018). <https://doi.org/10.1109/EPEC.2018.8598427>
26. Chothani, N.G., Raichura, M.B., Patel, D.D., Mistry, K.D.: Real-time monitoring protection of power transformer to enhance smart grid reliability. *Electr. Control Commun. Eng.* **15**, 104–112 (2019)
27. Ajaei, F.B., Sanaye-Pasand, M., Davarpanah, M., Rezaei-Zare, A., Iravani, R.: Compensation of the current-transformer saturation effects for digital relays. *IEEE Trans. Power Deliv.* **26**, 2531–2540 (2011)
28. Patel, D., Chothani, N.: Relevance vector machine based transformer protection. In: *Digital Protective Schemes for Power Transformer*, pp. 107–131. Springer, Singapore (2020). https://doi.org/10.1007/978-981-15-6763-6_5
29. Patel, D., Chothani, N.G., Mistry, K.D., Raichura, M.: Design and development of fault classification algorithm based on relevance vector machine for power transformer. *IET Electr. Power Appl.* **12**, 557–565 (2018)
30. Raichura, M.B., Chothani, N.G., Patel, D.D.: Identification of internal fault against external abnormalities in power transformer using hierarchical ensemble extreme learning machine technique. *IET Sci. Meas. Technol.* **14** (2020)
31. Raichura, M., Chothani, N., Patel, D.: Efficient CNN-XGBoost technique for classification of power transformer internal faults against various abnormal conditions. *IET Gener. Transm. Distrib.* **15**, 972–985 (2021)
32. Venkatanagaraju, K., Jose, T., Biswal, M., Malik, O.P.: Third zone protection to discriminate symmetrical fault and stressed system conditions. *Int. Trans. Electr. Energy Syst.* **29**, e12121 (2019)
33. Venkatanagaraju, K., Biswal, M.: A time-frequency based backup protection scheme for enhancing grid security against power system blackout. *Int. J. Electr. Power Energy Syst.* **137**, 107780 (2022)
34. Guide for the application of current transformers used for protective relaying purposes, Sponsor. IEEE/ANSI C, IEEE Stand. C37.110-2007, IEEE Power Syst. Relaying Comm. **37**, 110–2000 (2008)

Cost and Energy Efficiency Study of an ARIMA Forecast Model Using HOMER Pro



M. K. Babu, Papia Ray, and A. K. Sahoo

Nomenclature

HOMER	Hybrid optimization model for electrical renewables
O&M	Operation and maintenance
HRES	Hybrid renewable energy system
CNG	Compressed natural gas generator
PV	Photovoltaic
WT	Wind turbine
BT	Battery
KW	Killo watt
DG	Diesel generator
AR	Auto regressive
INR	Indian rupees
NPC	Net present cost
COE	Cost of energy
MA	Moving average

1 Introduction

Nations around the globe have increased the focus on renewable energy growth over the years in order to counteract climate change and achieve security of energy. Wind power is becoming one of the most widely used substitute energies, making up for 432,883 MW of total global energy consumption [1]. The Indian government planned

M. K. Babu · P. Ray (✉) · A. K. Sahoo
Department of Electrical Engineering, Veer Surendra Sai University of Technology, Burla, India
e-mail: papiaray_ee@vssut.ac.in

to increase renewable energy capacity to nearly 175 GW by the end of 2022. Wind power is expected to contribute 60 GW to this total. Implementation of Wind turbine (WT) as a true self-regulating source of electrical energy, the most significant barrier is WT intermittency. Bulky wind energy providers must comply with several issues concerning wind energy production, the green energy market, energy planning and norms, power grid reliability and quality, turbine servicing, etc. [2].

In this research the authors contribution is mentioned below in bullet points.

- Selection of historical data of the Jafrabad location
- Forecasting the wind speed using ARIMA
- Execution of the forecasted data into 2 cases considered in this research in HOMER pro to find the COE and NPC of the two cases
- Then study of two cases on the basis of COE and energy efficiency.

1.1 Literature Review

Wind power is directly proportional to wind speed's cube. A simple variation in wind velocity consequences in a huge modification in wind power. As a result, wind speed forecasting is critical in energy planning and allocating. A consolidated wind speed prediction model, on the other hand, cannot be used. The model should be changed based on the regions and environmental changes [3]. A wind speed estimate is an evaluation of what the wind speed will be in the coming days. This aids in determining the wind output power of the turbine. Power available in the wind,

$$P_{\text{wind}} = \frac{1}{2} \rho v^3 A \quad (1)$$

$$P_E = \frac{1}{2} \rho v^3 A C_p \quad (2)$$

where P_E = Extracted wind power (W/m^2), ρ = Density of air (Kg/m^3), i.e., 1.225 kg/m^3 at 15°C and 1 atm , v = Wind speed (m/s), A = Swept area of the blade (m^2), C_p = Coefficient of Power. According to Eq. (1), there is a directly proportional relationship between wind power and air density, rotor swept area, C_p (59.26% Betz limit) and wind speed cube. The classification of wind speed forecasting includes several categories, including time horizons, techniques and precepts, forecast object, inputs, prediction data [4]. This categorization of wind speed forecasting which is based on precepts and techniques is crucial [5]. Wind speed forecasting is divided into four-time scales: long term, medium term, ultra-short-term and short-term [6]. Given the unstable nature of wind speed, the variational mode decomposition technique is used in [7] to breakdown historical wind speed data into a sequence of stable components with varying frequencies. A unique ensemble prediction model was developed in [8] that includes data pre-processing, feature selection, parameter optimization, three intelligent prediction models, and an ensemble approach.

In the paper, the wind speed forecasting is carried out using ARIMA. The performance of the methodology is evaluated using the numerical error measures such as MAE, MAPE and MSE. The value of MAE, MAPE and MSE can be determined using error Eq. (3) [9].

$$\text{Error } E_t = A_t - F_t \tag{3}$$

Here, A_t is considered as the true value, F_t as the predicted value and n as the number of time periods.

$$\text{MAE(m/s)} = \frac{1}{n} \sum_{t=1}^n |e_t| \tag{4}$$

$$\text{MSE(m/s)} = \frac{1}{n} \sum_{t=1}^n e_t^2 \tag{5}$$

$$\text{MAPE(\%)} = \frac{100}{n} \sum_{t=1}^n \left| \frac{e_t}{F_t} \right| \tag{6}$$

On the other hand, the large number of technology options, optimization and sensitivity analysis set of rules make it easy-to assess the several probable system configurations [10]. To input an hourly energy usage profile, the user can use HOMER and match renewable generation to the load demand [11, 12]. It enables users to assess microgrid potential, renewables-to-total-energy ratio, peak renewable penetration, and stability of grid, especially for medium and large projects [13, 14]. In addition to this, HOMER has a significant optimizing task which is playing a key role to determine the value of different energy project situations [15–17]. At this point, the tool allows cost reduction and scenario optimization depending on a various factor [18–20]. Different published studies have conducted sufficient wind forecasting studies to deliver consistent estimations or a controller for evaluating alternative estimation methodologies in recent years. But execution of estimated data into some tool or software has not been done to study the COE and NPC of a microgrid. In this work after wind prediction has been done, the wind data has been fed to two cases as inputs of wind turbine in HOMER which find the COE and NPC of the two cases.

1.2 Description of Paper

In different sections the paper is described below. The next sub section describes about the data taken for forecasting and daily variation of wind speed of that location. In the next section discussion about ARIMA has been done and Auto correlation and partial autocorrelation of wind speed have been described. Section 3 indicates the investigation of the effects of different load profiles, considering two cases and shows

how to use homer to improve sustainable energy system depending on their NPC from a list of possible combinations. Simulation Results and analysis have been described in Sect. 4. In the last section conclusion and future scope of the paper have been displayed.

1.3 Data Measurement

2 years of Jafrabad, (Gujurat, India) from 2018 January to 2019 December. To model the system the initial 18 months of time series data are used and the subsequent 6 months of data are used to evaluate the model. After forecasting, forecasted data was fed to the two different cases in HOMER and it gives us the better cost and energy efficient model for the specified location.

2 Auto Regressive Integrated Moving Average (ARIMA)

The fall back of differenced series including the lags of the prediction errors are displayed by AR and MA constraints, respectively. In order to become stationary, the time series data which is non-stationary need to be differentiated. In ARIMA p , d , and q are denoted as the number of AR terms, non-seasonal deviations, and lagged prediction errors, respectively showing the model to be ARIMA. Obviously, if d is considered as zero, then the ARIMA model converted into an ARMA (p , q) model. At this point, if both d and q are considered to be zero, then ARIMA model is converted into an AR (p) model. However, for the case of both d and p to be zero, the ARIMA model is changed into an MA (q) model.

A particular ARIMA model, characterize as ARIMA (p , d , q), can be represented as:

$$Y_t = c + f_i Y_{t-1} + \dots + f_p Y_{t-p} + \theta_j \varepsilon_{t-1} + \dots + \theta_q \varepsilon_{t-q} + \varepsilon_t \quad (7)$$

where c is expressed as a constant value (i.e., means of the underlying stochastic process), ϕ_i is the i th AR parameter, θ_j is known as the j th MA parameter, E_t is expressed as the error term at time t , and Y_t is parameter of the wind speed at the time t [10].

The ARIMA model consists of different procedures are represented as a block diagram in Fig. 1. The steps are: (i) Identification of an appropriate model for the wind speed predictions at that site. (ii) Determine the model parameters. Validation of the model (iii). (iv) Using the verified model, calculate the expected wind speed [10].

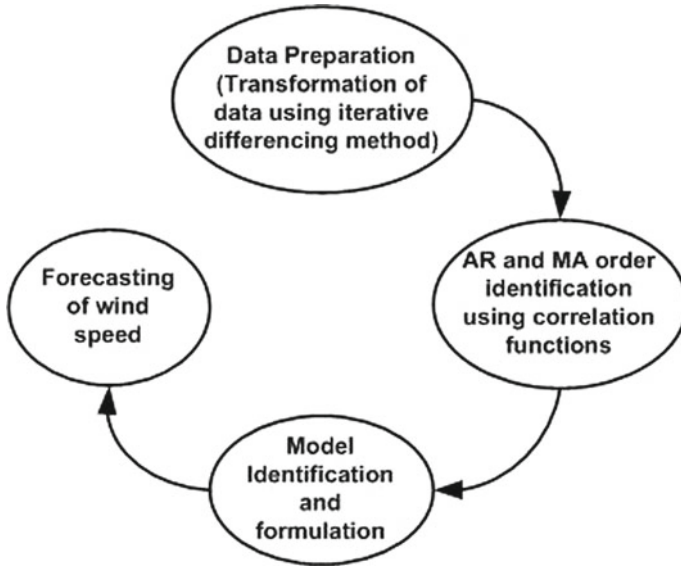


Fig. 1 Block diagram of ARIMA model

2.1 ARIMA Results and Analysis

Figure 2a and b represents Autocorrelation coefficient (ACF) and Partial autocorrelation coefficient (PACF) of Jafrabad wind speed, respectively, and it is clear from the figure that that data is non-stationary and must be integrated.

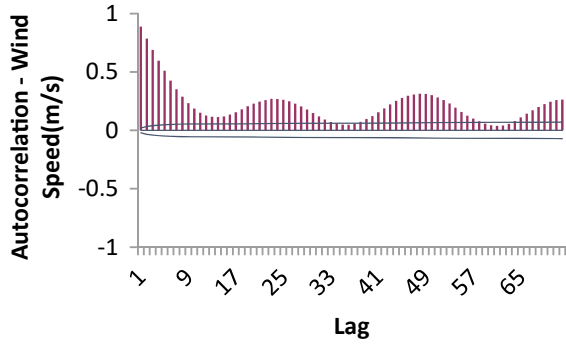
Figure 3a and b show the corresponding ACF and PACF of the same site after integration. Here we did take the integration value as 1. So, the value of d is 1. Using ACF and PACF, the value of p , and q are computed. As a result, the value of p and q equals 3 for this site.

Table 1 shows the results of ARIMA model for different steps ahead forecast accuracy results of Wind speed of Jafrabad site. The findings of the ARIMA model show that forecasting wind speed one hour ahead of time provides the Jafrabad location less error. It can be seen from above table that or short-term forecasting ARIMA gives improved results.

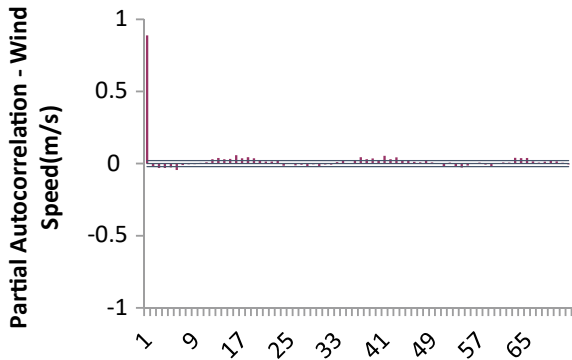
3 Load Profile and System Model

In Fig. 4 initial system model investigated in this research in Case 1 is depicted which is having a PV system and a 1 kwh lithium battery is linked to the dc bus. A 30 kw natural gas generator and a 1.5 kW wind turbine whose input is the forecasted wind speed and linked to the ac bus of the system. 1 kw converter is bridged among ac

Fig. 2 a ACF of Jafrabad site. b PACF of Jafrabad site



(a)



(b)

and dc bus. A load of 355.00 kwh/d whose peak is 34.17 kW is connected between ac and dc bus.

Case 2 is the second model of the system shown in Fig. 5 which is having a PV system and a 1 kwh lithium battery is linked to the dc bus. A 30 kw Diesel generator and a 1.5 kW wind turbine whose input is the forecasted wind speed that are linked to the ac bus of the system. 1 kw converter is bridged among ac and dc bus. A load of 355.00 kwh/d whose peak is 34.17 kW is connected between ac and dc bus.

Figure 6 represents the load data that are used in two different cases. For a particular set of energy sources HOMER estimates the system and utilization expenses throughout the stated period as well as the annual performance of all of the system combination options in the system model. HOMER simulates the load profiles and system performance by doing the calculation for energy balance of each and every one of the 8760 h in a year.

Fig. 3 **a** ACF of integrated wind speed. **b** PACF of integrated wind speed

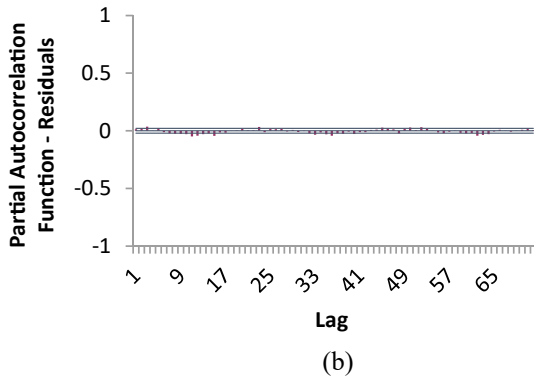
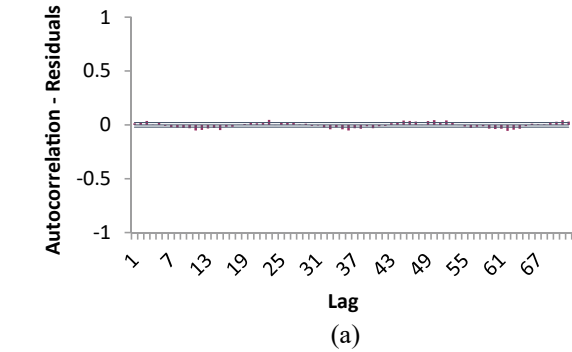


Table 1 ARIMA results for Jafraabad site

	MAE (m/s)	MSE (m/s)	MAPE (%)
One hour ahead	0.49	0.72	15.9
Eight hours ahead	1.48	1.03	25.35
Twenty-four hours ahead	0.91	1.28	26.54

The significance of bold is that one hour ahead short term forecasting gives better accuracy than eight hours and twenty-four hours ahead forecasting

4 Simulation Results and Analysis

The figures below demonstrate some of the simulation findings for the 2 cases covered in this study. Figures 7 and 8 illustrate the power output of wind in graphical form. Here the maximum output power range of the wind turbine in case 2 is 2.5 kw. In case 1, it is 80 kw.

Figures 9 and 10 illustrate the state of charge of the battery for first and second case. Here battery performance varies hourly throughout the year in both cases.

Fig. 4 System model case 1 with gas generator

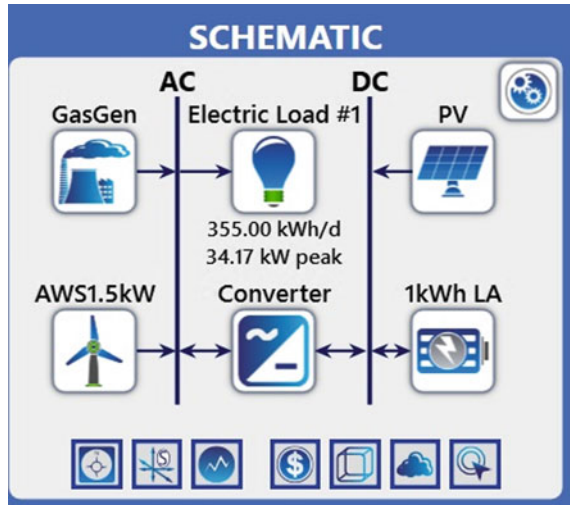
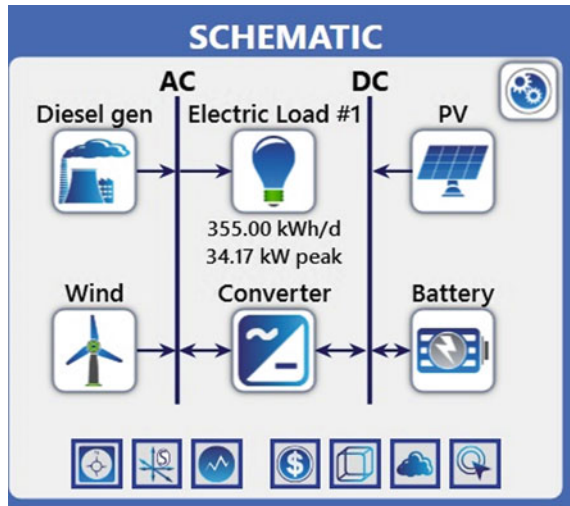


Fig. 5 System model case 2 with diesel generator



Figures 11 and 12 show that PV power output in both cases. In case 1 its maximum power is 64 kW whereas in case 2 its maximum power is 112 kW.

Table 2 shows the result of the cost of every single piece of equipment and its contribution. It is clear that Generic 30 kw Gas Microturbine cost is more than other equipment. On the other hand, Table 3 displays the result of the cost of every single piece of equipment and its contribution. It is clear from the Table 3 that the Generic 1 kw lead acid battery cost is more than other equipment used in case 2. From Table 3 total cost of the Generic 1 kwh lead acid battery cost is the highest that is 10,366,325.45 INR among other equipment.

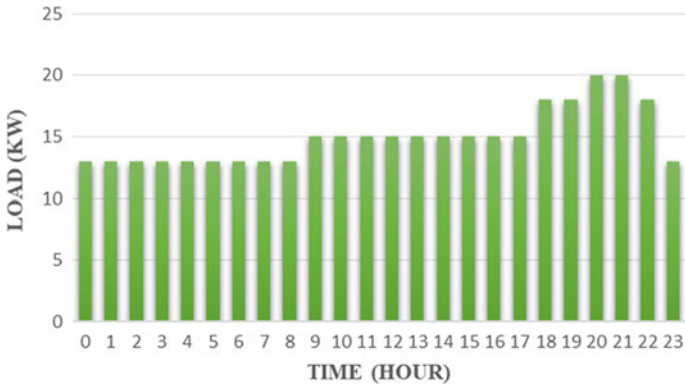


Fig. 6 Load flow data

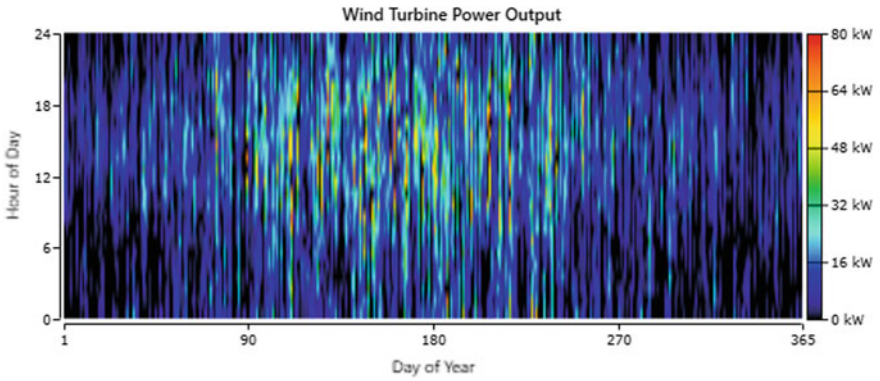


Fig. 7 Wind turbine power output for case 1

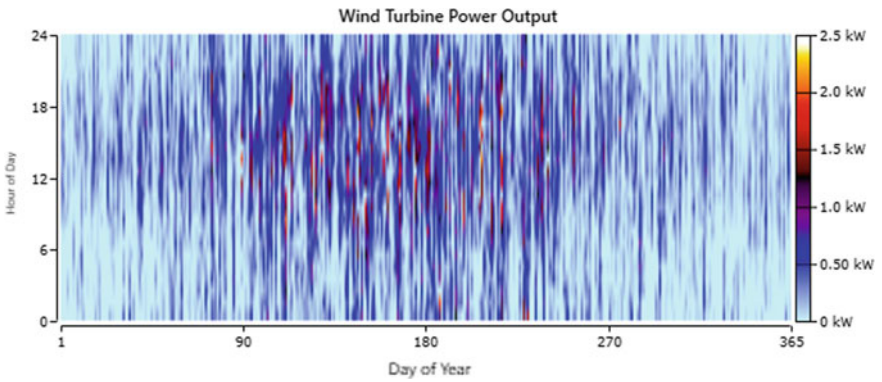


Fig. 8 Wind turbine power output for case 2

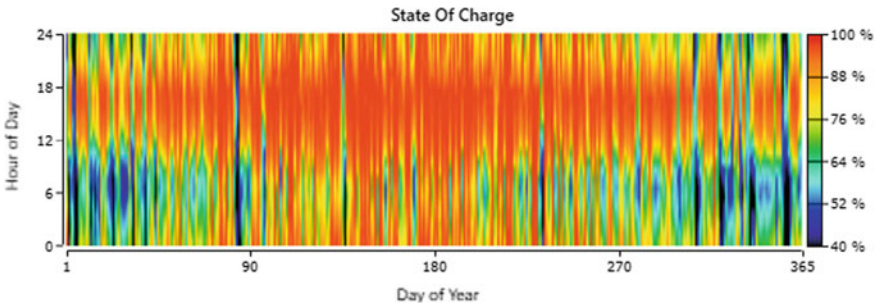


Fig. 9 State of charge of a battery for case 1

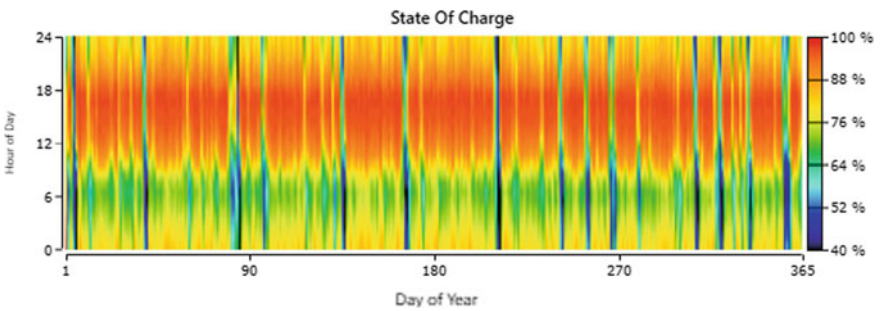


Fig. 10 State of charge of a battery for case 2

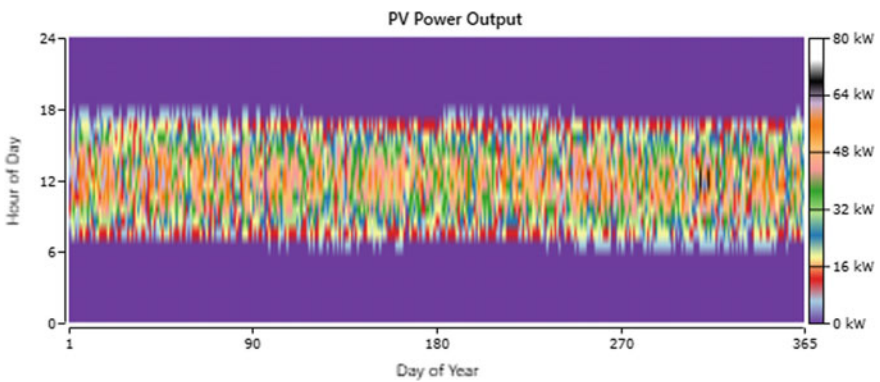


Fig. 11 PV power output for case 1

Table 4 shows the result of all possible combinations of case 2. It shows that PV/WT/CNG/BT is the best proposed HRES. The NPC of case 1 is 7.63 rs as the cost of CNG fuel is less compared to diesel. Whereas Table 5 shows the result of all possible combinations of case 2. It shows that PV/WT/DG/BT is the best proposed

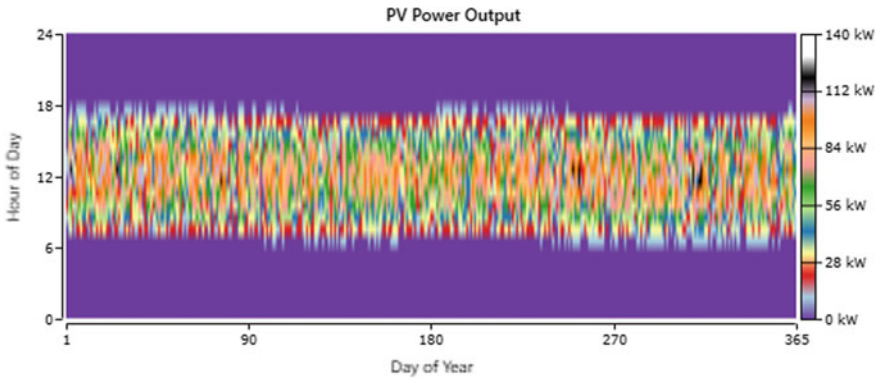


Fig. 12 PV power output for case 2

HRES. The NPC of case 1 is 9.20 rs as the diesel price is too high. Case A from both Tables 4 and 5 is the suitable system combination. Power contribution of PV, WT, CNG, DG and converters are also displayed in both the tables.

5 Conclusion

The application of the ARIMA forecasting model for building renewable systems using HOMER with energy efficiency was reported in this article. ARIMA model was used for wind speed forecasting of Jafrabad (Gujarat, India). As to make the data stationary the number of integrations required is 1, so the value of d is 1. Using ACF and PACF, the value of p , d , and q are computed. As a result, the value of p and q equals 3 for this site. The optimum ARIMA structure (p, d, q) for forecasting wind speed in the Jafrabad area, according to this study, is $(3, 1, 3)$. From this study it is found that the One hour ahead that is short-term ahead forecast performs better in ARIMA giving higher accuracy. The predicting accuracy of the model is determined by the MSE, MAPE and MAE. In the first case system, natural gas generator is taken whereas in second case diesel generator is considered. Then forecasted wind speed data is fed to HOMER pro for cost and energy efficient calculation in both the cases. The working capital summary results indicate that the DG increases the project’s capital, scrap value for the wind turbine, fuel, operating, replacement, and diesel, battery and PV, systems. Among the two cases the CNG gas generator system shows less COE that is 7.63 rs, and for diesel generator the COE is 9.20 rs.

In future to increase the forecasting accuracy hybrid models (ARIMA along with other techniques) should be addressed and using HOMER pro the sensitivity analysis of the two cases should be done.

Table 2 Lifecycle cost distribution of every component for case 1

Component	Capital (INR)	Replacement (INR)	O&M (INR)	Fuel (INR)	Salvage (INR)	Total (INR)
AWS HC 1.5 KW WindTurbine	2,520,000.00	803,394.52	46,539.60	0.00	-452,764.34	2,917,169.25
Generic 1 kwh lead acid	2,976,000.00	373,723.13	64,120.48	0.00	-691,658.98	6,087,184.63
Generic 30 kw gas micro turbine	300,000.00	0.00	67,998.74	759,003.46	-60,054.16	1,066,948.04
Generic flat plate PV	1,923,345.77	0.00	9945.63	0.00	0.00	1,933,291.40
System converter	550,698.11	233,646.80	35,595.79	0.00	-43,974.69	775,966.02
System	8,270,043.88	4,775,764.45	224,199.71	759,003.46	-1,248,452.16	12,780,559.34

Table 3 Lifecycle cost distribution of every component for case 2

Component	Capital (INR)	Replacement (INR)	O&M (INR)	Fuel (INR)	Salvage (INR)	Total (INR)
AWS HC 1.5 KW WindTurbine	70,000.00	22,316.51	1292.75	0.00	-12,576.79	81,032.48
Generic 1 kwh lead acid	5,100,000.00	6,369,079.73	109,883.89	0.00	-1,212,638.17	10,366,325.45
Generic 30 kw Protector	250,000.00	0.00	21,718.0.23	401,987.42	-51,504.94	622,200.71
Generic flat plate PV	3,440,431.52	0.00	17,790.49	0.00	0.00	3,458,222.01
System converter	631,675.65	268,003.45	40,829.99	0.00	-50,440.95	890,068.13
System	9,492,107.17	6,659,399.69	191,515.35	401,987.42	-1,327,160.85	15,417,848.78

Table 4 System architecture of all possible scenarios for case 1

System	Scenarios	PV (KW)	Wind (KW)	CNG (KW)	Battery (no)	Converter (KW)	NPC (INR)	COE (INR)
PV/WT/CNG/BT (proposed HRES)	Case-A	76.9	36	30	496	27.5	12.8 M	7.63
PV/WT/CNG/BT	Case-B	75.3	35	30	509	27.6	12.8 M	7.68
PV/WT/CNG/BT	Case-C	79.6	36	30	502	27.4	12.8 M	7.8
PV/WT/CNG/BT	Case-D	76.0	36	30	500	27.2	12.8 M	7.91
PV/WT/CNG/BT	Case-E	78.9	34	30	506	27.6	12.8 M	8.1
PV/WT/CNG/BT	Case-F	73.7	37	30	498	27.4	12.8 M	8.23

The significance of bold is optimal configuration i.e. proposed HRES

Table 5 System architecture of all possible scenarios for case 2

System	Scenarios	PV (KW)	Wind (KW)	DG (KW)	Battery (no)	Converter (KW)	NPC (INR)	COE (INR)
PV/WT/DG/BT (proposed HRES)	Case-A	138	1	30	850	31.6	15.4 M	9.20
PV/WT/DG/BT	Case-B	136	1	30	856	32.6	15.4 M	9.25
PV/WT/DG/BT	Case-C	138	1	30	856	32.1	15.4 M	9.28
PV/WT/DG/BT	Case-D	136	1	30	845	32.0	15.4 M	9.41
PV/WT/DG/BT	Case-E	139	1	30	841	32.2	15.4 M	9.58
PV/WT/DG/BT	Case-F	134	1	30	841	31.7	15.4 M	9.73

The significance of bold is optimal configuration i.e. proposed HRES

References

1. John, K.K., Zafirakis, D.: The wind energy revolution: a short review of a long history. *Renewable Energy* 1887–1901 (2011)
2. Wang, X., Guo, P., Huang, X.: A review of wind power forecasting models. *Energy Procedia* 770–778 (2011)
3. Chang, W.-Y.: A literature review of wind forecasting methods. *J. Power Energy Eng.* **2**, 161–168 (2014)
4. Lange, M., Focken, U.: New developments in wind energy forecasting. In: *IEEE Power and Energy Society General Meeting—Conversion and Delivery of Electrical Energy in the 21st Century*, pp. 1–8 (2008)
5. Zhao, X., Wang, S., Li, T.: Review of evaluation criteria and main methods of wind power forecasting. *Energy Procedia* **12**, 761–769 (2011)
6. National Renewable Energy Laboratory: *Energy efficiency and renewable energy*, USA (2008)
7. Tian, Z., Li, H., Li, F.: A combination forecasting model of wind speed based on decomposition. *Energy Rep.* **7**, 1217–1233 (2021). <https://doi.org/10.1016/j.egy.2021.02.002>
8. Quan, J., Shang, L.: An ensemble model of wind speed forecasting based on variational mode decomposition and bare-bones fireworks algorithm. *Math. Probl. Eng.* **2021**, 1–16 (2021). <https://doi.org/10.1155/2021/6632390>

9. ECOWAS Center for Renewable Energy and Energy Efficiency (ECREEE): HOMER Software for Renewable Energy Design (2013)
10. HOMER Energy: Getting Started Guide for HOMER Legacy (Version 2.68), Homer Energy and National Renewable Energy Laboratory, Colorado
11. Report IEA-PVPS T11- 01:2011 World-wide overview of design and simulation tools for hybrid PV systems
12. ESMAP Technical Paper 121/07 Technical and Economic Assessment of Off-grid, Mini-grid and Grid Electrification Technologies, The World Bank, Washington (2007)
13. Givler, T., Lilienthal, P.: Using HOMER Software, NREL's Micro Power Optimization Model, to Explore the Role of Gen-sets in Small Solar Power Systems; Case Study: Sri Lanka Technical Report. National Renewable Energy Laboratory, USA (2005)
14. Kassam, A.: HOMER Software Training Guide for Renewable Energy Station Base Design. Green Power for Mobile (2010)
15. Alabdul Salam, M. et al.: Optimal sizing of photovoltaic systems using HOMER for Sohar, Oman. *Int. J. Renewable Energy Res.* **3**(2), 301–307 (2013)
16. Al-Karaghoul, A., Kazmerski, L.L.: Optimization and life-cycle cost of health clinic PV system for a rural area in Southern Iraq using HOMER software. *Sol. Energy* **84**, 710–714 (2010)
17. Ajao, K.R., Oladosu, O.A., Popoola, O.T.: Using HOMER power optimization software for cost benefit analysis of hybrid-solar power generation relative to utility cost in Nigeria. *IJRRAS* **7**(1), 96–102 (2011)
18. Ahmed, S., Othman, H., Anis, S.: Optimal Sizing of a Hybrid System of Renewable Energy for a Reliable Load Supply without Interruption". *Eur. J. Sci. Res.* **45**(4), 620–629 (2010)
19. Fraunhofer Institute for Solar Energy System (ISE): Levelized Cost of Electricity Renewable Energy Technologies (2013)
20. Ueckerdt, F., Hirth, L., Luderer, G., Edenhofer, O.: System LCOE: What are the Costs of Variable Renewables. Institute for Climate Impact Research, Potsdam, Germany (2013)

An Off-MPPT Controller for Standalone PV Systems



Piyush Kumar and R. N. Mahanty

1 Introduction

PV systems have seen extensive usage around the world, due to the fact that fossil fuels are depleting as well as polluting, and that solar energy is available in abundance on the earth's surface [1]. PV systems come in various forms, but all of them are reduced to two most general forms, which are standalone systems and grid-connected systems [2]. Grid-connected PV systems operate in synchronism with main grid, whereas standalone PV systems operate isolated from the grid.

It is crucial that standalone PV systems utilize energy storage systems [3]. PV system is plagued by intermittency [4], due to unpredictably varying solar irradiance on earth's surface. Energy storage systems like batteries solve the plaguing issue of intermittency in PV systems. However, use of energy storage systems creates its own issues. One major issue is that charging of energy storage system may become incompatible with use of MPPT controllers. MPPT or maximum power point tracking is a technique in which power electronic interfaces like DC–DC controllers are utilized to extract maximum power from PV arrays under any meteorological conditions.

Constant use of MPPT may cause overcharging of batteries [5, 6]. MPPT controller will continuously pump power into the DC bus of the system; if injected power is greater than load demand, then excess energy goes into battery. Once batteries achieve their maximum charge, the excess energy still present in system would further charge the batteries. It was found that typical battery, like valve-regulated lead–acid batteries, life span decreases drastically when used in a PV system [1].

P. Kumar (✉) · R. N. Mahanty
Department of Electrical Engineering, National Institute of Technology Jamshedpur, Jamshedpur,
India
e-mail: piyushk097@live.com

R. N. Mahanty
e-mail: rmmahanty@nitjsr.ac.in

Kim and Bae proposed a control technique which switches the PV operation between maximum power point (MPP) operation and power regulation (PR) operation [7]. Initially, the PV arrays operate in MPP mode, and if the load requirement is less than the power generation, the excess energy is absorbed by the battery system. The control switches the PV operation mode from MPP to PR if the load suddenly drops, causing battery charging current to exceed a threshold value.

An active PV power control method, integrated within the MPPT algorithm, has been suggested in [5] which reduces the PV power generation to protect batteries from overcharging. In a nutshell, the battery charging voltage and currents are limited, based on three-stage battery charging algorithm, which hence acts as active power control. In [6], a modified MPPT controller was presented in with the DC–DC converter interfacing PV arrays to DC bus shifts from MPPT control to DC voltage control when battery is full to prevent overcharge.

An intelligent energy management system was proposed in [8] which could shift PV system operating mode from MPPT to voltage regulation resulting in reduction of power generation under light loading and excess power generation conditions. This mode shift is necessary under these conditions to prevent power generation in exceeding the combined maximum charging power to battery and load demand.

Intermittency itself may also cause the overcharging of batteries, as sudden increase in irradiance may cause high-power input in the DC bus, which may cause sudden increase in battery charging current. A novel battery charger has been proposed in [9] which monitors the state of charge of batteries and adjusts the battery charge and discharge rates so that in the event of a rapid fluctuations in the PV power, it doesn't over charge or deep discharges the batteries. Ramp rate control refers to limiting the rate of change of PV power during severe weather changes. Several ramp controls have been discussed in [9–12].

Overall, it is seen that change in irradiance and constant use of MPPT controller can cause battery overcharging or deep discharge, which will severely reduce the battery life span. This paper discusses a modified overall MPPT controller, which can reduce the power under several circumstances to avoid battery overcharging as well as deep discharge, under falling irradiance. This reduced power generation mode can be termed as Off-MPPT mode, whereas when the controller inputs maximum power, the operation mode can be termed as MPPT mode. The controller works based on the battery SOC state, incident irradiance, and battery current.

2 Design of a Generic DC Standalone PV System

A generic DC standalone PV system with constant loading is designed and simulated in MATLAB/SIMULINK. The system contains PV arrays, connected to a DC bus via boost converter-based MPPT controller. To the same DC bus, a battery system is connected via a bidirectional DC–DC converter, which enables proper control for battery charging as well as DC bus voltage regulation. A constant DC load is also

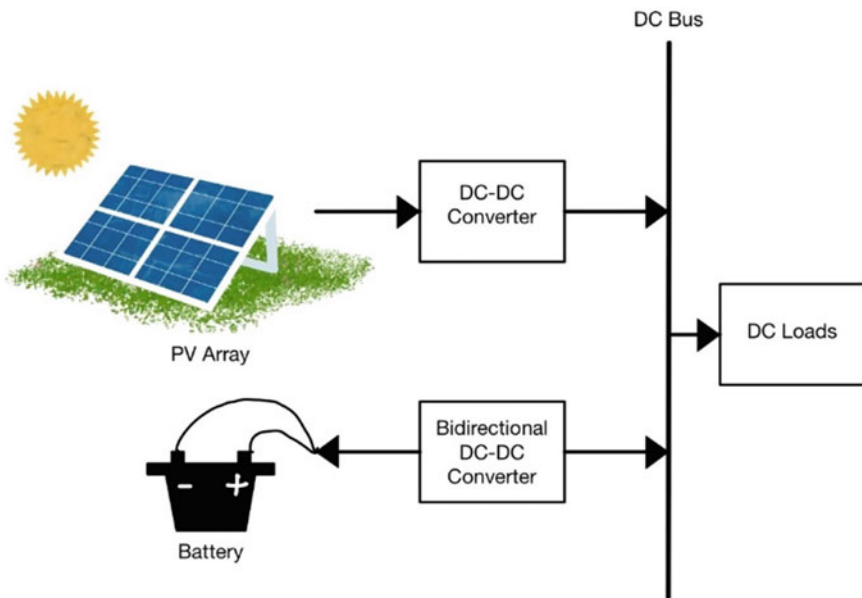


Fig. 1 DC-coupled PV system (PV array image obtained from Notability app)

connected to the bus. A DC-coupled PV system is discussed in [13]. Figure 1 shows such a system.

2.1 Model of PV Arrays and MPPT Controller

PV arrays are a series—parallel connection of several individual PV panels. These PV panels are themselves a series—parallel connection of PV cells. A PV cell can be termed as a current source connected anti-parallel to a diode. A series resistance R_s with low resistive value is present which represents PV cell’s internal resistance. A shunt resistance R_{sh} with high resistive value is also present which shows PV cell’s leakage resistance. Figure 2 shows the equivalent circuit diagram of a typical single-diode model of PV cell. The current source supplies current I_1 when a load is connected across its terminal and a potential V is developed. It is seen that the diode is forward biased; hence, a current I_d flows through it. The cell leakage and internal resistance is represented by resistors R_{sh} and R_s . From this, using KVL, the I_{sc} can be given as,

$$I = I_1 - I_0 \left[\exp\left(\frac{e(V + I.R_s)}{mkT}\right) - 1 \right] - \frac{V + I.R_s}{R_{sh}} \tag{1}$$

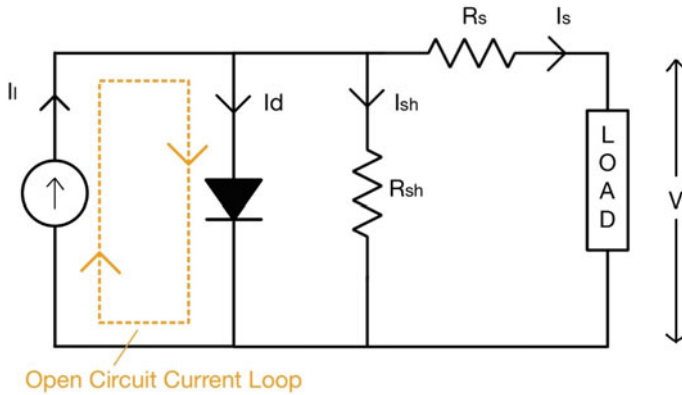


Fig. 2 Single-diode PV model

And,

$$I_d = I_0 \left[\exp\left(\frac{e(V + I.R_s)}{mkT}\right) - 1 \right] \quad (2)$$

where I_1 is light-generated current, I_0 is reverse saturation current, e is charge of electron, m is ideality factor, k is Boltzmann constant, and T is temperature.

The maximum power that can be obtained in a given solar irradiance and temperature is

$$P_m = \left(\frac{eV_m^2/kT}{1 + eV_m/kT} \right) \cdot (I_{sc} + I_0) \quad (3)$$

For a given PV module shown in Fig. 3 in which the cells are connected first in series and then in parallel, let N_s be cells connected in series and N_p be cells in parallel; then, the current from the PV modules can be given as [14].

$$I = N_p I_1 - N_p I_0 \left[\exp\left(e \left(\frac{V}{N_s} + \frac{I.R_s}{N_p} \right) / mkT \right) - 1 \right] - \frac{N_p}{R_{sh}} \left(\frac{V}{N_s} + \frac{I.R_s}{N_p} \right) \quad (4)$$

For PV array, whose Norton equivalent is shown in Fig. 4, consider M_s modules are connected in series, and then, M_p module series strings are connected in parallel to form the array; then, the PV array current is determined from Norton equivalent of Fig. 4, which gives [15]

$$I_{array} = M_p I_i \left(\frac{R_p}{R_p + R_s} \right) \quad (5)$$

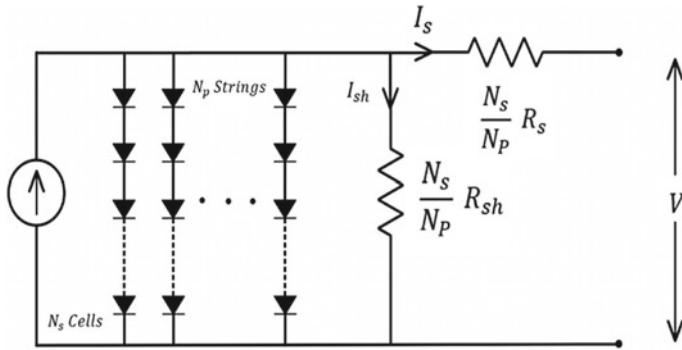


Fig. 3 Equivalent circuit for PV module

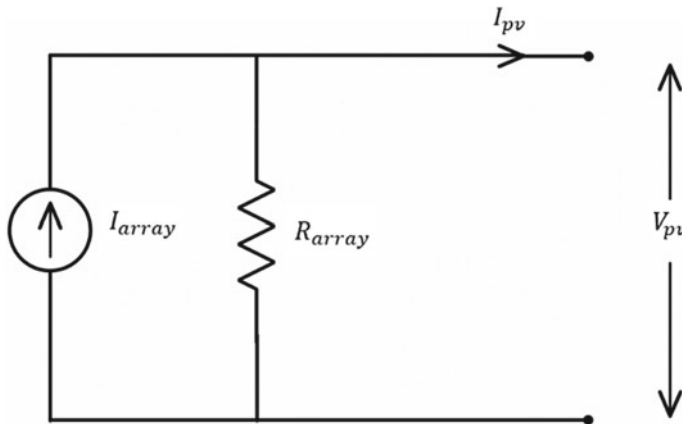


Fig. 4 Norton equivalent circuit of PV array

And,

$$R_{array} = \frac{M_s}{M_p} \times \frac{N_s}{N_p} (R_p + R_s) \tag{6}$$

The MPPT technique used for extracting maximum power from PV cell is incremental conductance [16]. The technique only requires measurement of PV voltage and current and outputs a suitable duty ratio for the DC–DC boost converter. Incremental conductance is based on the fact that slope of power curve is null at MPP, positive to the right side of the MPP, and negative to the left side of MPP. The control algorithm is explained in Figs. 5 and 6.

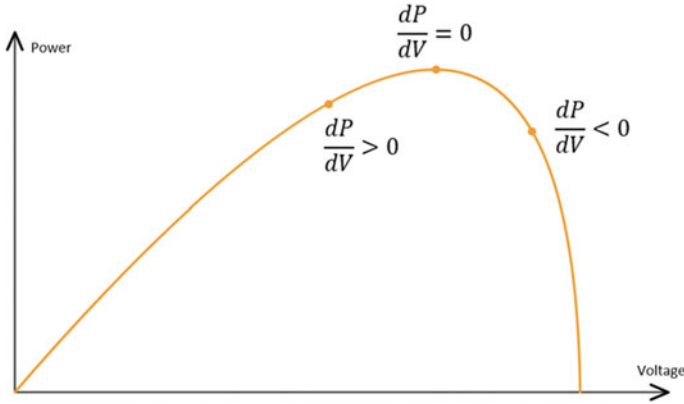


Fig. 5 Working concept of incremental conductance algorithm

2.2 Battery System

Due to indeterministic nature of chemical energy in batteries and nonlinear operation of battery under load, it has become a challenge to present a mathematical model which properly describes battery characteristics. There are several battery characteristics [13, 15] yet the general battery model was provided in [17] which avoids excessive complexity, while still considering the dynamic behavior of the battery. The equivalent battery circuit is shown in Fig. 7. Using KVL, the internal voltage is related to the terminal voltage as,

$$V_{\text{bat}} = E_b - i_b \times r_b \quad (10)$$

The internal voltage E_b is a function of the charge, the chemical energy stored in the battery, which is represented as the state of charge of the battery. State of charge or SOC is the measure of charge remaining in the battery; mathematically, SOC is given as,

$$\text{SOC} = \frac{Q - \int i_b dt}{Q} \quad (11)$$

where Q is the overall charge and the integral term is charge used up from the battery. The internal voltage E_b , as a function of SOC, is given by the equation,

$$E_B = E_{B0} - K \frac{Q}{Q - \int i_b dt} + A \cdot \exp(-B \cdot \int i_b dt) \quad (12)$$

Equation 12 can be plotted as shown in Fig. 8.

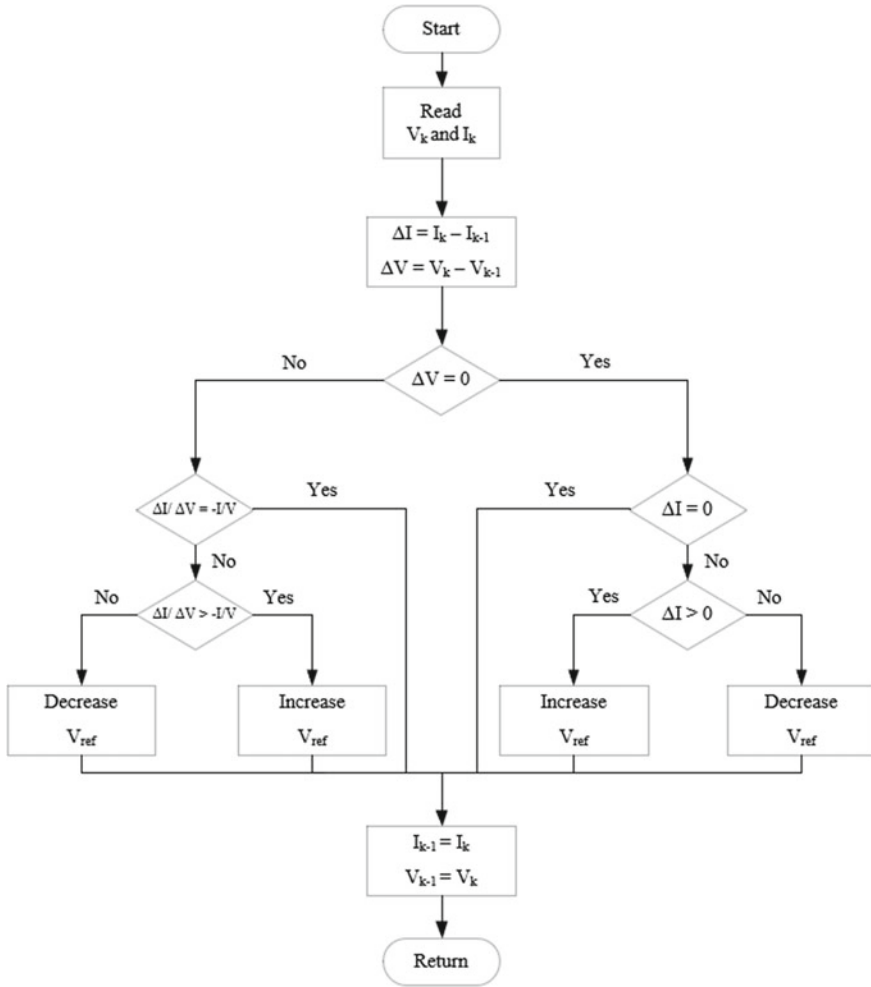
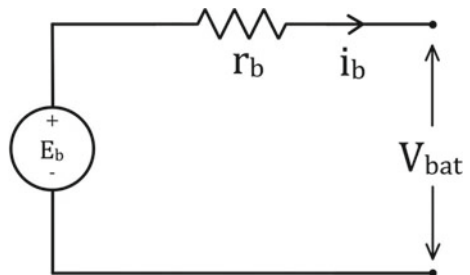


Fig. 6 Flowchart of incremental conductance algorithm

Fig. 7 Battery model



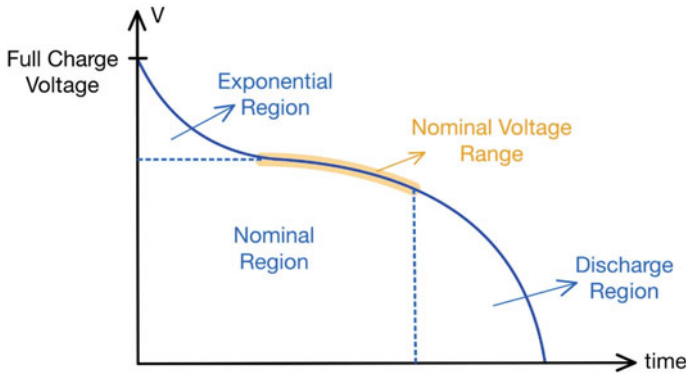


Fig. 8 Battery characteristics

Battery charger and voltage controller

The battery charges and discharges while maintaining constant DC bus voltage by using a bidirectional converter as shown in Fig. 9. The control strategy utilizes two-loop control [2, 14]. A reference voltage is set, and the error between the reference voltage and actual DC bus voltage is calculated; the reference voltage for the modeled system is 100 V. The error is fed to a PI controller, and the output of this PI controller is reference for the battery charging or discharging current I_{bat_ref} ; this is the first loop. In the second loop, the error between this reference and actual battery current is determined and fed to a PI controller, which outputs the required duty cycle for bidirectional converter to keep this error zero.

For example, assume that the V_{dc} is less than V_{ref} , then the PI controller needs to output a positive current reference, which is the discharging current for the battery.

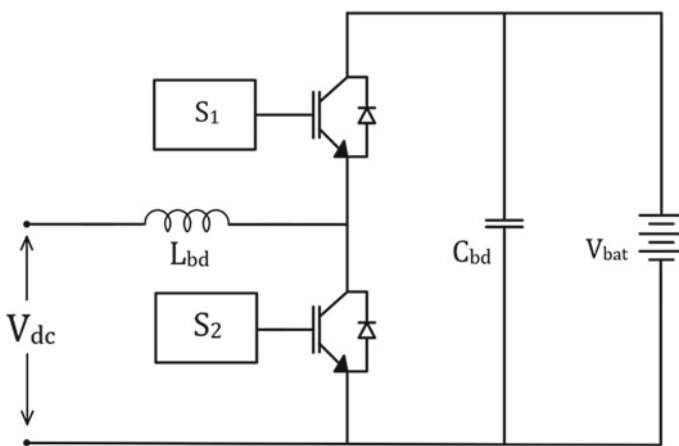


Fig. 9 DC-DC bidirectional battery charger

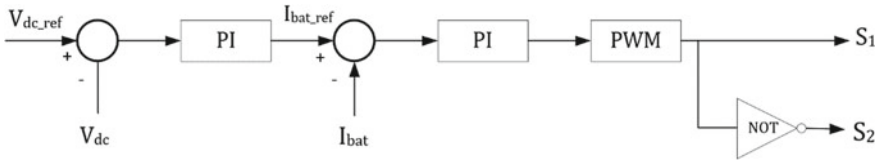


Fig. 10 Two-loop battery charging control

The inner current loop then has to adjust the duty cycle for the converter such that battery discharges with the determined current reference. This way the DC bus voltage is maintained. The two-loop control is shown in Fig. 10.

3 Proposed MPPT Controller

As batteries can charge to a finite capacity, PV arrays operating at MPPT at all times pose a problematic scenario. If the batteries reach their defined full capacity, the charge control should stop charging the battery to prevent overcharge and hence battery degradation. But, since batteries no long charge, they top absorbing the excess energy from the PV arrays. Loads only take what they require, and hence, this excess energy starts accumulating in the bus which results in increase in DC bus voltage and overcharging of batteries [2, 5, 6].

To prevent this, the PV array should generate power which is equal to requirement of power by the load, once the battery reaches it rated full capacity. This prevents the generation of excess power and accumulation of energy in the DC bus, and hence, DC bus voltage is maintained. Figure 11 shows a control logic of what is called an Off-MPPT controller. This controller measures the SOC of battery, when SOC is between the full charge and discharged conditions, the controller forces the PV array to operate at maximum power point by implementing incremental conductance algorithm. When the SOC exceeds the predetermined value, which represents the full charge condition of the battery; the controller switches to Off-MPPT mode, in which the power generated from the arrays matches with the load requirement.

When load increases such that battery discharge rate is high, or when battery SOC falls below a certain value, the controller switches back to MPPT mode, to prevent battery from depleting faster than its nominal discharge rate, while also preventing the battery to discharge completely while the PV arrays are capable of providing power. Keeping the battery charge rate in mind, the controller also switches from MPPT to Off-MPPT when battery charge rate (battery charging current) exceeds a reference value [7]. This occurs when there is a sudden disconnection of load, resulting in battery charging current exceeding the nominal charge rate of the battery.

Another control logic also needs to be implemented which takes into account the changing irradiance. In simulating the controller in Simulink, when the controller is in Off-MPPT mode, it was seen that once irradiance falls below the load requirement,

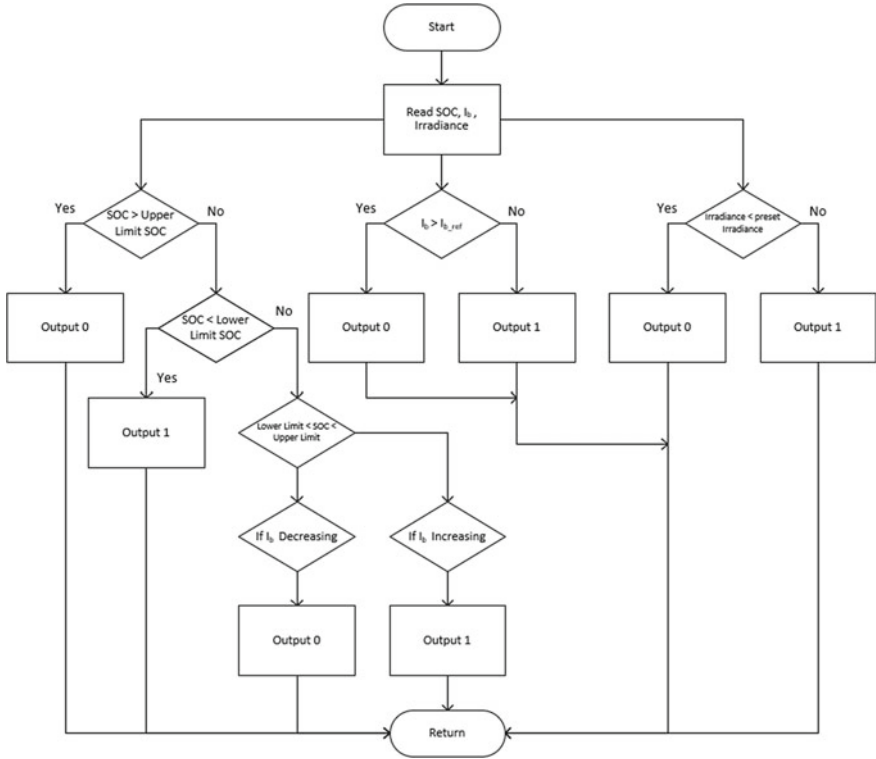


Fig. 11 Modified controller switching logic

the PV power generation will fall to zero, i.e., the PV system won't generate any power (Fig. 12) [8]. To prevent this, the controller measures the irradiance, and if the irradiance falls below a specified reference, the controller switches to MPPT mode. This way, even if power generation is low, the remaining power is supplied by the battery. Hence, we learn that this control operation is a crucial part in maintaining a stable autonomous operation of a standalone system. Figure 13 shows the controller diagram of an overall MPPT controller.

It is to be noted that a reset signal is required for proper functioning of the controller. A change detector is used to detect change in state of the switch, which is then given to the PI controller and MPPT algorithm. The reset signal sends the PI and MPPT algorithm to initial state, and it prevents any malfunctioning of the controller when the PV array shifts from MPPT to Off-MPPT mode or vice versa.

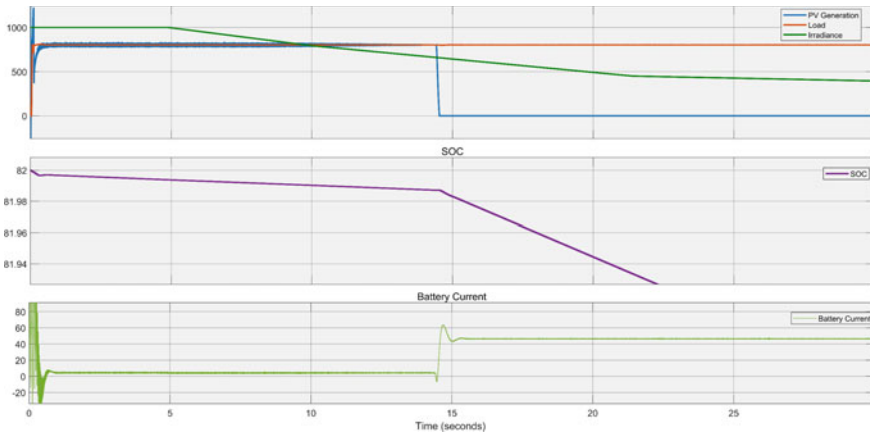


Fig. 12 Effect of falling irradiance on power generation and battery current in modified controller

4 Results and Discussions

The results are obtained so as to verify the logical operation of the controller. First, it is verified that the SOC-based operation of controller is working, i.e., the controller remains in MPPT mode when battery is charging and switches to Off-MPPT mode when the battery reaches a certain max charge. To verify this, a max SOC of 80 and min SOC of 79.99 are taken into account. Figure 14 shows the operation of controller when battery charges and discharges. It is seen that battery stays well within the range of 80 and 79.99% SOC, while the PV generation is max when battery is charging, and it is equal to load demand when battery reaches max charge and stays in this mode until battery loses some charge. Hence, the SOC control of MPPT controller is verified.

Next logic which needs to be verified is the impact of irradiance on control operation. The controller should switch to MPPT mode if irradiance drops below a certain preset. This is important as it prevents overloading of the batteries. Figure 15 shows that controller switches to MPPT mode when irradiance drops below 700, the load line in orange remains constant throughout the operation which shows system is able to adequately supply the load. It is also seen that battery current increases which signifies that battery is providing the lost power due to fall in irradiance. Hence, we can say that controller performs as per the logic.

The last operation of controller which needs to be verified is switching of controller to Off-MPPT mode when the battery charging current increases past a maximum threshold due to a sudden fall in loading. To verify this, the load is allowed to fall from 1 kW to 100 W. From Fig. 16, it is seen that as battery charging current exceeds 32A, the controller switches to Off-MPPT mode to prevent further rise in battery current and hence, protecting the battery.

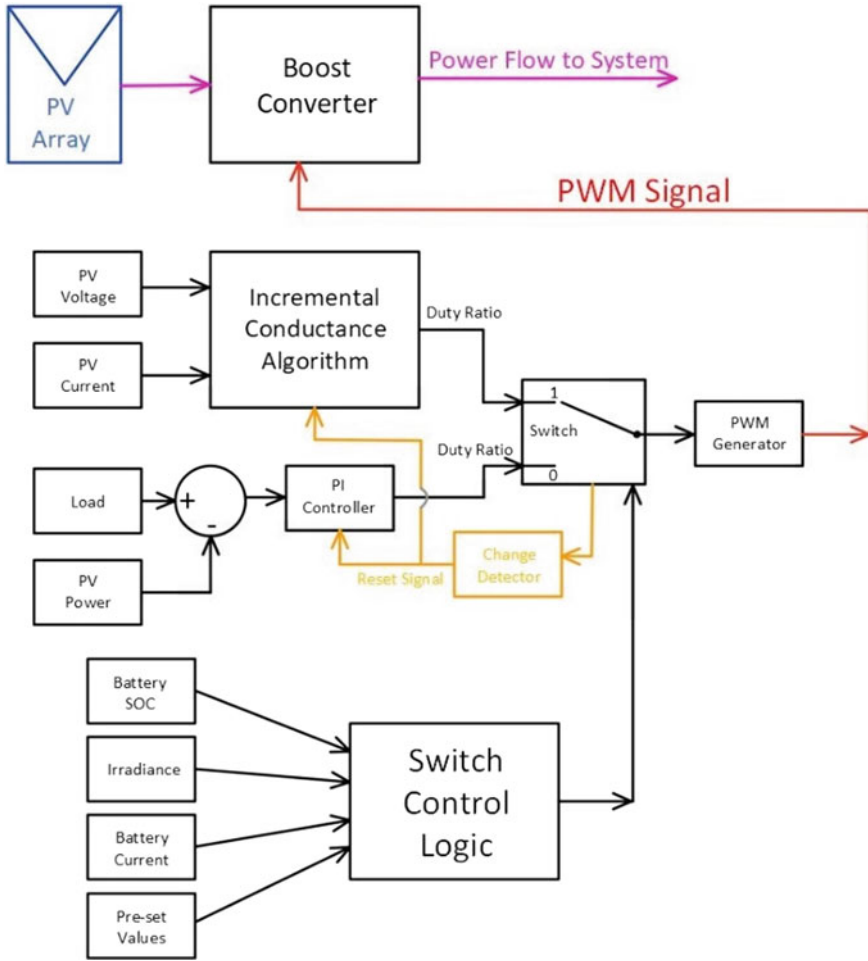


Fig. 13 Modified MPPT controller

5 Conclusion

In this work, a controller which can operate a PV panel in both On- and Off-MPPT mode is proposed, modeled, and verified. It is seen that operating PV panel in continuous MPPT mode can create issues in standalone PV systems, with most common problem being that of overcharging of batteries in the system. Operating PV arrays such that they only deliver power required by the load in some situations can lead to better system stability and healthy battery operation. These situations are as follows, when the battery is at its maximum charge, and when there is sudden disconnection of load. Not only the controller should switch to Off-MPPT mode, it should also be able to go back to MPPT mode, in cases where there is power deficiency in system,

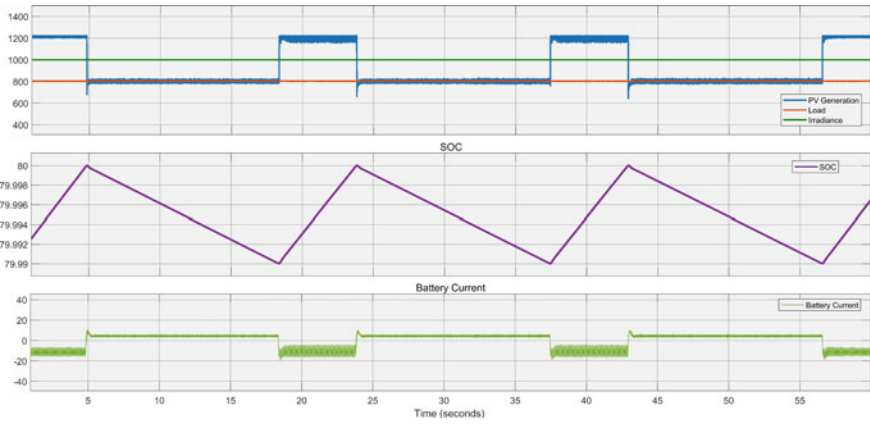


Fig. 14 SOC-based controller operation

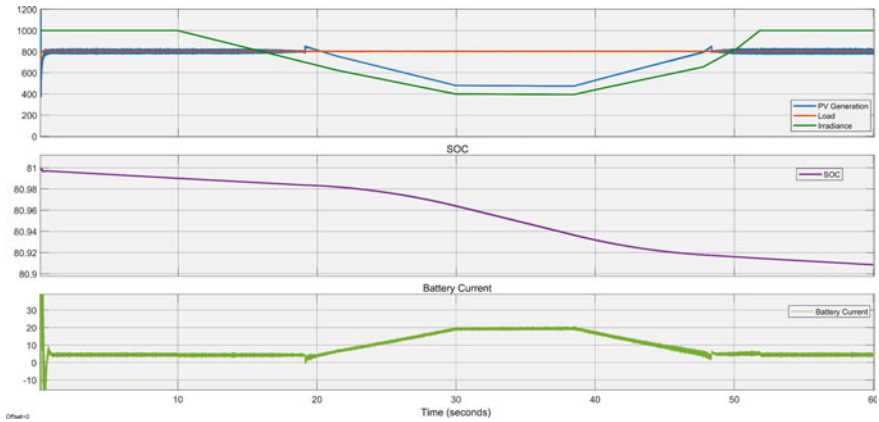


Fig. 15 Irradiance-based controller operation

such as when irradiance drops due to cloud cover. These operations are verified from Figs. 14, 15 and 16, and hence, the concept of an Off-MPPT controller is successfully realized.

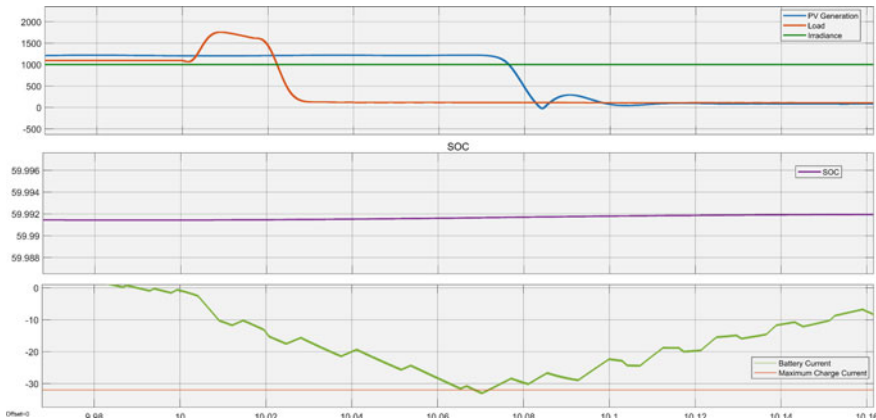


Fig. 16 Charging current-based controller operation

References

1. Sukhatme, S.P., Nayak, J.K.: *Solar Energy*, 4th edn. McGraw-Hill Education (2017)
2. Hu, J., et al.: A model predictive control strategy of PV-battery microgrid under variable power generations and load conditions. *Appl. Energy* **221**, 195–203 (2018)
3. Hill, C.A., Such, M.C., Chen, D., Gonzalez, J., Grady, W.M.: Battery energy storage for enabling integration of distributed solar power generation. *IEEE Trans. Smart Grid* **3**(2), 850–857 (2012). <https://doi.org/10.1109/TSG.2012.2190113>
4. Sovacool, B.K.: The intermittency of wind, solar, and renewable electricity generators: technical barrier or rhetorical excuse? *Utilities Policy* **17**(3–4), 288–296 (2009)
5. Li, F., Alshareef, M., Lin, Z., Jiang, W.: A modified MPPT algorithm with integrated active power control for PV-battery systems. In: *IEEE International Conference on Renewable Energy Research and Applications (ICRERA)* (2016)
6. Zakzouk, N.E., Lotfi, R.A.: Power flow control of a hybrid battery/supercapacitor standalone PV system under irradiance and load variations. In: *10th International Conference on Power and Energy Systems (ICPES)*. IEEE (2020)
7. Kim, M., Bae, S.: Decentralized control of a scalable photovoltaic (PV)-battery hybrid power system. *Appl. Energy* **188**, 444–455 (2017)
8. Alassi, A., Ellabban, O.: Design of an intelligent energy management system for standalone PV/battery DC microgrids. In: *2nd International Conference on Smart Grid and Renewable Energy (SGRE)* pp. 1–7 (2019). <https://doi.org/10.1109/SGRE46976.2019.9020679>
9. Bhattacharjee, A.K., et al.: An efficient ramp rate and state of charge control for PV-battery system capacity firming. In: *IEEE Energy Conversion Congress and Exposition (ECCE)*. IEEE, (2017)
10. Marcos, J., et al.: Storage requirements for PV power ramp-rate control. *Sol. Energy* **99**, 28–35 (2014)
11. Martins, J., et al.: Comparative study of ramp-rate control algorithms for PV with energy storage systems. *Energies* **12**(7), 1342 (2019)
12. De la Parra, I., Marcos, J., García, M., Marroyo, L.: Control strategies to use the minimum energy storage requirement for PV power ramp-rate control. *Sol. Energy* **111**, 332–343 (2015)
13. Khatib, T., Ibrahim, I.A., Mohamed, A.: A review on sizing methodologies of photovoltaic array and storage battery in a standalone photovoltaic system. *Energy Convers. Manage.* **120**, 430–444 (2016)

14. Ding, F., et al.: Modeling and simulation of grid-connected hybrid photovoltaic/battery distributed generation system. In: CICED 2010 Proceedings. IEEE (2010)
15. Eghtedarpour, N., Farjah, E.: Control strategy for distributed integration of photovoltaic and energy storage systems in DC micro-grids. *Renewable Energy* **45**, 96–110 (2012)
16. De Brito, M.A.G., et al.: Evaluation of the main MPPT techniques for photovoltaic applications. *IEEE Trans. Ind. Electron.* **60**(3), 1156–1167 (2012)
17. Tremblay, O., Dessaint, L.-A., Dekkiche, A.-I.: A generic battery model for the dynamic simulation of hybrid electric vehicles. In: IEEE Vehicle Power and Propulsion Conference. IEEE (2007)

Designing and Simulation of Double Stage Grid-Linked PV System Using MATLAB/Simulink



Shamik Kumar Das, M. K. Sinha, and A. K. Prasad

1 Introduction

It has been seen that the production and consumption rates of fossil fuels have increased exponentially in the last decade worldwide. It has been predicted that the coal reserves of India will last for 200 years only, and crude oil will run out in the next 25 years at the current consumption rate. Importing conventional sources of energy is not a healthy option to sustain the energy security of a country. So, we have to invest, promote, and utilize renewable sources as an alternative to conventional sources to meet the energy demand with fewer environmental hazards and to decrease the import dependency as well as the alignment toward fossil fuels.

Among the non-conventional energy applications, photovoltaic technology is one of the important applications to generate electricity using solar energy due to its fastest-growing PV technology, no fuel cost, less installation space, lack of noise, and low maintenance cost. Overall, solar energy is an inexhaustible, pollution-free, and clean source of energy. However, due to variable solar irradiance, it cannot produce constant power throughout the day.

There are mainly two kinds of photovoltaic systems: on-grid and standalone. In a standalone PV system, solar energy is converted into DC through PV array and stored in batteries. The stored energy in batteries is used to run the appliances. While in an on-grid system, DC power produced by PV is not used to charge the batteries; rather, it is converted into AC by the inverter and fed to the grid. Nowadays, grid-tied PV systems are gaining more attention than standalone systems as they can be integrated

S. K. Das (✉) · M. K. Sinha · A. K. Prasad
Mechanical Engineering Department, NIT Jamshedpur, Jamshedpur, Jharkhand, India
e-mail: shamikdeep96@gmail.com

M. K. Sinha
e-mail: mksinha.me@nitjsr.ac.in

A. K. Prasad
e-mail: akprasad.me@nitjsr.ac.in

with thermal and hydropower plants into hybrid power systems. The simplest on-grid system consists of a solar panel and an inverter unit [1] but we have introduced a boost converter in between the PV array and the inverter to level up the voltage output from the PV array, and an LCL filter is attached at the end of the inverter to die out the harmonics.

Due to the lower conversion efficiency (from solar energy to electrical energy) of PV, i.e., 9–15%, and variable solar irradiance, MPPT is a major portion of a grid-linked PV system to ensure that the highest power is always drawn out from the PV panel [2–5]. Various MPPT algorithms have been introduced in the literature. Among them, the most popular is the “P & O” method and the “Incremental Conductance” method [6–9]. A three-phase inverter is required for DC to AC power conversion. One-cycle control and conventional PWM are some of the strategies to control 3-phase inverters [10]. To adjust active and reactive power in single-stage photovoltaic structures, vector control and voltage and current double closed-loop controls can be used [11, 12]. To synchronize the grid voltage, we need to implement a Phase Lock Loop (PLL) using the Synchronous Reference Frame theory, which also shows the necessity of Clark and Park Transformation [13]. To die out the harmonics, the LCL filter is favored over the L-filter and LC-filter as it can come up with a lesser THD and improved decoupling between the filter and grid impedance [14]. We can tune the controller using classical Ziegler–Nichols, but only in a limited area [15]. In our study, the P&O algorithm has been implemented in MPPT control. In this paper, the dynamic performance of a two-stage, three-phase, grid-linked PV system under variable solar irradiance has been simulated in MATLAB/Simulink software. This study also shows the parameter calculations of the Boost converter and the LCL filter.

2 Schematic Layout of the Model

Figure 1 shows the schematic layout of the system.

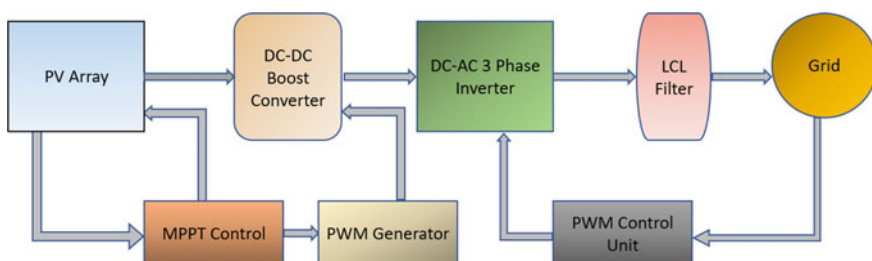
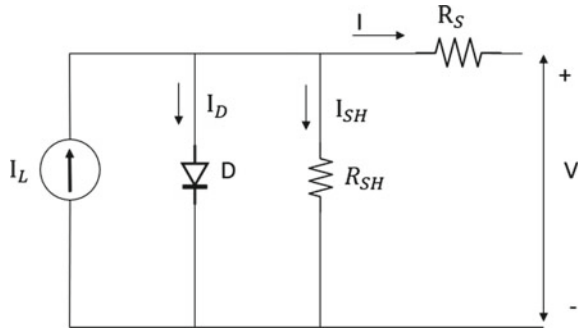


Fig. 1 Schematic figure of grid-linked PV system

Fig. 2 Equivalent circuit figure of a PV Cell



3 System Components

The proposed model contains of the below units.

(a) PV Array, (b) Boost Converter, (c) MPPT Control, (d) 3-Phase Inverter, (e) LCL Filter, and (f) Power Grid.

4 PV Array

4.1 Working Principle

The conversion of light energy into electrical energy is known as the Photovoltaic Effect. A PV cell is made of semiconductor material. When Silicon is doped with Boron (pentavalent atom), it creates an n -type semiconductor and when it is doped with Phosphorus (trivalent atom), it forms a p -type semiconductor. These two types of semiconductors are sandwiched together to make a PV cell. When a photovoltaic cell is brought to sunlight and photon energy is higher than the bandgap energy of the p - n junction, generation of electron-hole pair takes place. The excited electrons flow to the n -side due to an electric field and holes sweep to the p -side. The free charges are collected from the electrical joints applied to either edge before passing to the outer circuit in the form of electricity. It gives rise to the direct current. The equivalent circuit figure of a solar cell has been shown in Figs. 2 and 3 represents the I - V characteristic of a PV cell. The OCC, SCC, and MPP have also been pointed to the below figure.

4.2 Equivalent Circuit and Current Equation

The output current from solar cell is given by Eq. (1)

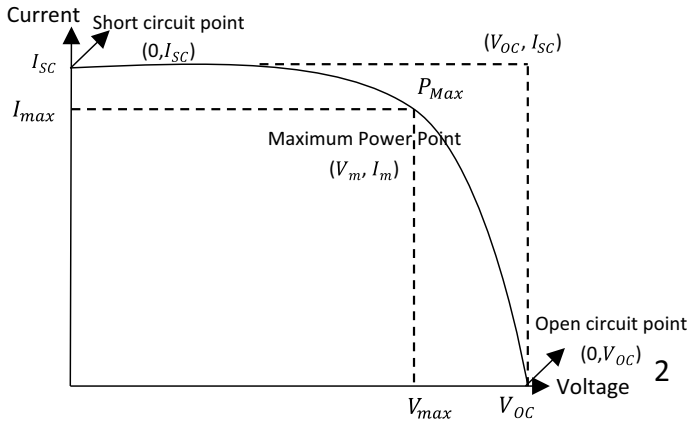


Fig. 3 I-V characteristics of solar cell

$$I = I_L - I_D \left(e^{\frac{q(V+IR_S)}{kT}} - 1 \right) - \frac{V + IR_S}{R_{SH}} \tag{1}$$

- I Cell output current (Amp)
- I_L Photon generated current (Amp)
- I_D Diode saturation current
- q Charge of an electron = 1.6×10^{-19} Coulombs
- k Boltzmann constant
- T Cell temperature (K)
- R_{SH} Shunt resistance
- R_S Series resistance
- V Cell output voltage (Volt)

A PV array is several individual PV panels electrically connected whereas a PV panel is a collection of a single PV cells. We have taken 47 strings consisting of 10 PV modules connected in series with maximum power output from a single PV cell 213.15 W to produce 100 kW power ($47 \times 10 \times 213.15 = 100.18$ kW). We have shown the solar cell parameters value in Table 1 for the proposed model.

The P - V & I - V characteristics of the PV cell used in the proposed model is depicted in Fig. 4. For solar irradiance of 1 kW/sq-m, the maximum power generation by the PV Array is 100 kW.

5 Boost Converter

A fixed DC input voltage can be directly converted into a variable DC output voltage by using a chopper. In this model, we have used an IGBT as a power semiconductor

Table 1 Specification of solar cell

Solar cell data	Ratings
Maximum power (Watt)	213.152
Cells per module (N_{cell})	60
O/C voltage V_{oc} (Volt)	36.2
S/C current I_{sc} (Amp)	7.83
Voltage at MPP, V_{mpp} (Volt)	29.0
Current at MPP, I_{mpp} (Amp)	7.34
Temperature coefficient of $V_{oc}(\%/^{\circ}C)$	-0.36099
Temperature coefficient of $I_{sc}(\%/^{\circ}C)$	0.102

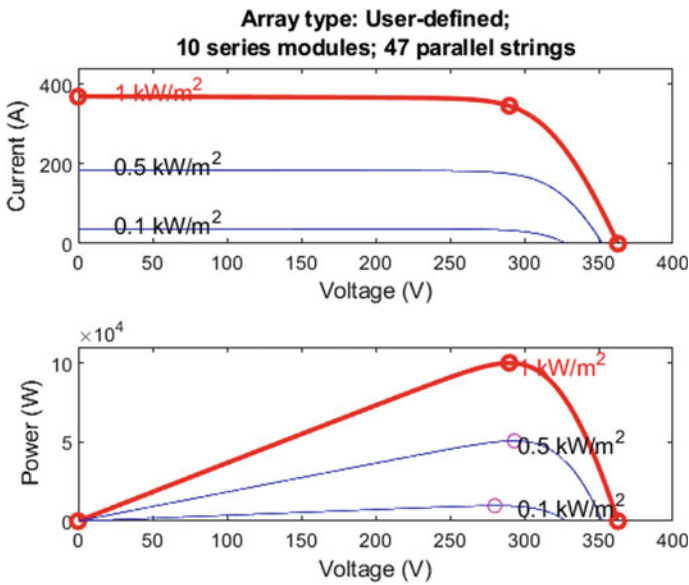


Fig. 4 I - V and P - V characteristic of the solar cell used in the proposed system

device for making the boost chopper circuit. The schematic circuit diagram of a Boost Chopper is shown in Fig. 5.

If we equate stored energy in the inductor for T_{on} and energy released by the inductor to the load during T_{off} , we will get the average output voltage as

Average output voltage, $V_{output} = \frac{V_{input}}{1-D}$, where $D =$ duty ratio

Average output current, $I_{output} = I_{input}(1 - D)$

$$D = \frac{T_{on}}{T_{on} + T_{off}}$$

T_{on} On time duration of IGBT

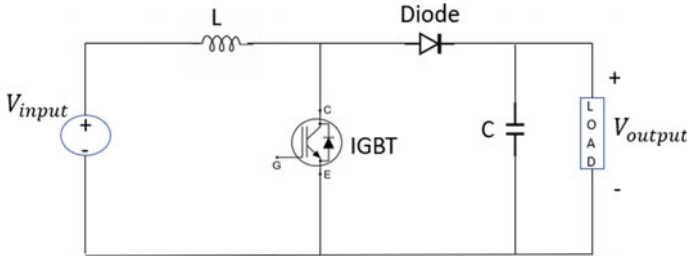


Fig. 5 Schematic figure of a boost chopper

T_{off} Off time of duration IGBT device

$$T_{sw} = T_{on} + T_{off}$$

Switching frequency, $f_{sw} = \frac{1}{T_{sw}}$.

6 MPPT Design

As a solar cell is a non-linear device, it is not able to produce constant power throughout the day due to its dependency on two important parameters, solar irradiance, and temperature. Temperature and solar irradiance depend on the atmospheric conditions and many other factors due to which they vary throughout the day and because of that the output power from the solar cells is not constant either. In the grid-linked PV model, we have to draw out the highest power from the solar cells for which we need an MPPT algorithm. The 'Perturb & Observe' algorithm is one of the best-suited methods which gives accurate results in maximum power point tracking. The flow chart of the Perturb & Observe algorithm is shown in Fig. 6 and the P - V characteristic of solar cells with MPP conditions has been shown in Fig. 7.

6.1 P&O Algorithm Flow Chart

As shown in Fig. 6, in the beginning, output voltage and current at any instance from PV are read. The Power $P = V * I$ is then calculated. After that the difference between the previous and present value of voltage and power is determined. Now observe whether the power has increased or reduced, i.e., $dP > 0$ or not. If YES, that means power has increased. Next check the condition $dV > 0$. If it is YES, that means we are moving in the correct direction. In the next step, increase the voltage

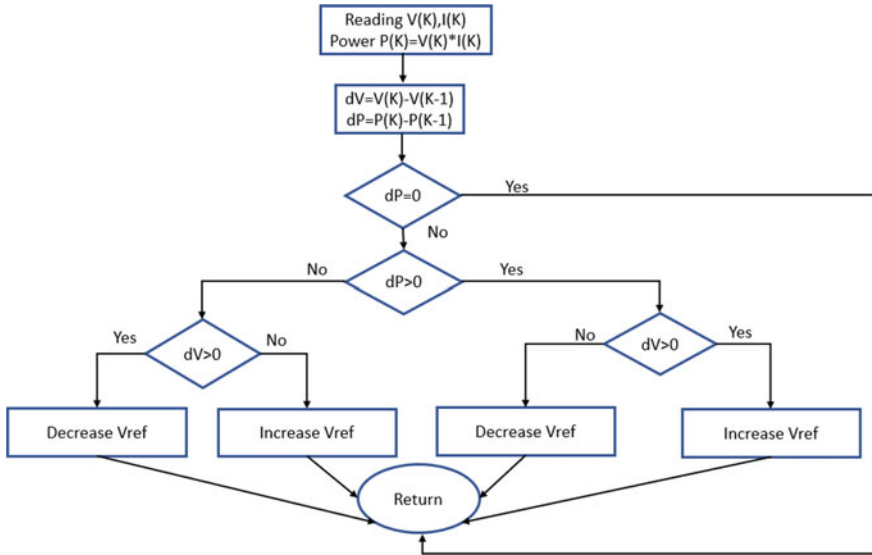
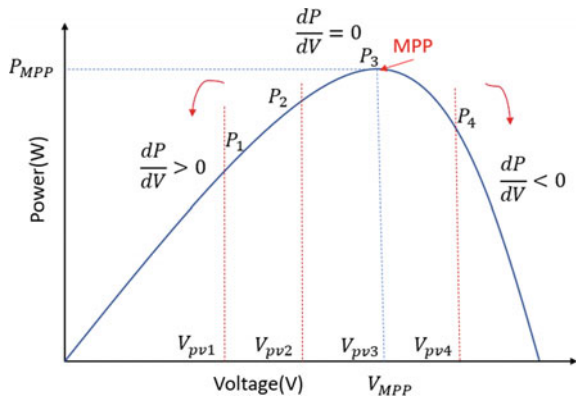


Fig. 6 Flow chart of P&O method for highest power point tracing

Fig. 7 P-V characteristic of a solar cell



and if the condition becomes false, decrease the voltage to obtain maximum power. In addition, if $dP < 0$ and $dV > 0$, lower the reference voltage to obtain MPP.

6.2 Maximum Power Point Tracking Using Boost Chopper

In Fig. 8 we have shown the schematic block diagram and control operation of the highest power point tracing using a boost chopper. The following steps show the control procedure.

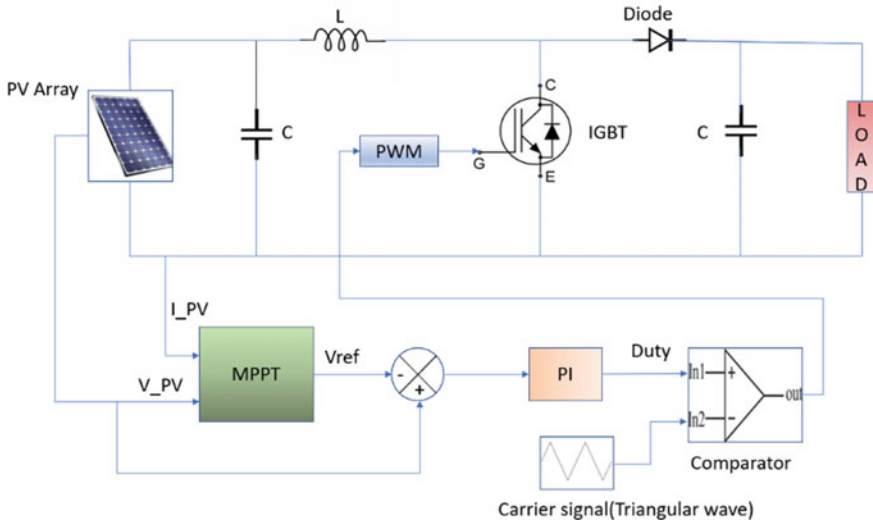


Fig. 8 Block diagram of highest power point tracing using boost chopper

- Sense the current I_{PV} voltage and V_{PV} from the solar panel.
- We get V_{ref} as output from the MPPT block.
- Actual PV voltage V_{PV} is tallied with MPPT output V_{ref} and the error value is applied to the PI controller.
- Triangular wave as a carrier signal is fed to the comparator and compared with PI controller output and the PWM is applied to Gate terminal of IGBT.

The MPPT MATLAB figure is shown in Fig. 9. The Boost converter has been connected to the output of the PV array. The voltage and current from the PV array are measured and the P&O algorithm is implemented in MATLAB Function. The generated PWM is then fed to IGBT to boost up the output voltage at the required level.

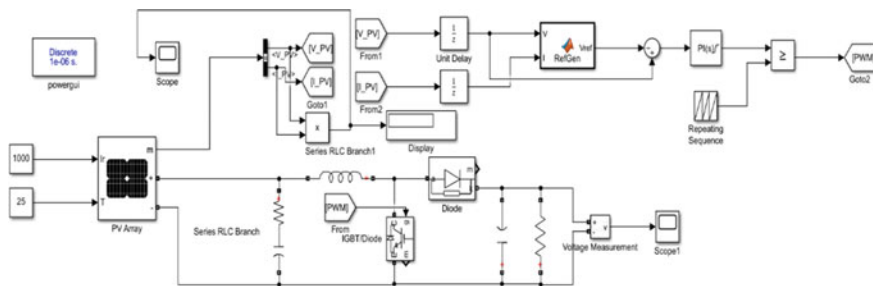


Fig. 9 MPPT implementation in MATLAB

7 Three-Phase Inverter

MATLAB implementation of a three-phase inverter has been shown in Fig. 10. PWM has been used as an internal control method for the inverter. By controlling the ON time and OFF time of IGBTs, we can obtain a controlled output voltage from a fixed DC voltage.

7.1 Synchronous Reference Frame Theory (SRF)

The SRF Theory has been incorporated to implement the control mechanism of a three-phase inverter. First, the three-phase voltage V_{abc} is measured by the 3-phase $V-I$ Measurement block. Then V_{abc} is converted into a 2-Phase frame, i.e., an alpha-beta frame by using Clark's Transformation as shown in Eq. (2). V_α and V_β come as output after Park's Transformation as shown in Eq. (3). These two voltages are used to implement the Phase Lock Loop (PLL) from which we get ωt as output. V_α and V_β are then transformed into $d-q$ frame voltages V_d and V_q with the help of Park's Transformation. The phasor diagram of $a-b-c$ and alpha-beta frames has been shown in Fig. 11.

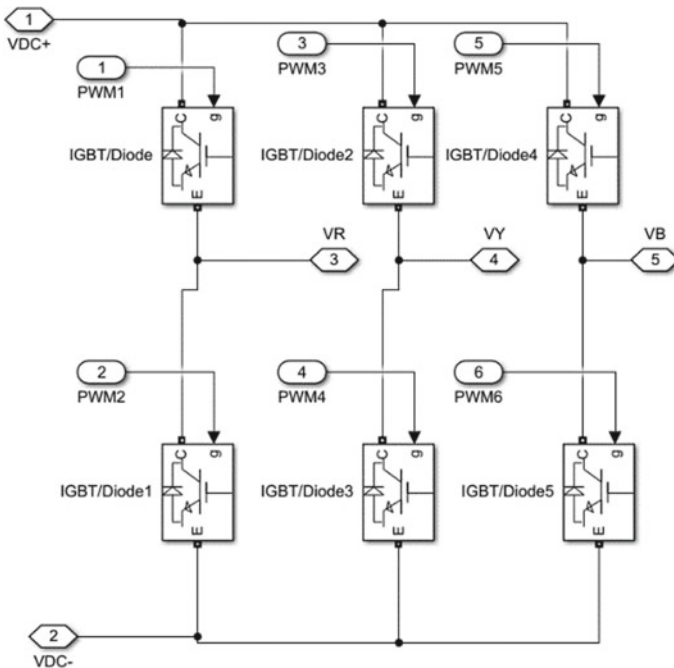
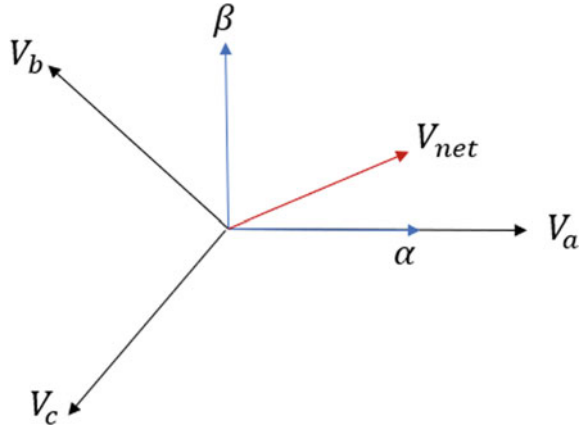


Fig. 10 Circuit design of a three-phase bridge inverter

Fig. 11 Phasor diagram of a - b - c and alpha-beta frame



Clark's Transformation Matrix

$$\begin{bmatrix} x_\alpha \\ x_\beta \\ x_0 \end{bmatrix} = \frac{2}{3} \begin{bmatrix} 1 & -1/2 & -1/2 \\ 0 & \sqrt{3}/2 & -\sqrt{3}/2 \\ 1/2 & 1/2 & 1/2 \end{bmatrix} \begin{bmatrix} x_a \\ x_b \\ x_c \end{bmatrix} \quad (2)$$

Park's Transformation Matrix

$$\begin{bmatrix} x_d \\ x_q \\ x_0 \end{bmatrix} = \begin{bmatrix} \cos \theta & \sin \theta & 0 \\ -\sin \theta & \cos \theta & 0 \\ 0 & 0 & 1 \end{bmatrix} \begin{bmatrix} x_\alpha \\ x_\beta \\ x_0 \end{bmatrix} \quad (3)$$

As shown in Fig. 12, next, 3-phase inverter current I_{abc} is sensed and transformed into d - q frame current I_d and I_q after sequentially passing through Clark's Transformation and Park's Transformation. I_d and I_q are then compared with the reference current along the d -axis and q -axis and the differential value is applied to the PI controller, which causes the voltage signal in the d - q frame. These voltage signals are added with some gain and transformed into an a - b - c frame from a d - q frame by using Inverse Park's Transformation and Inverse Clark's Transformation. As a result, we get V_{abc_ref} which will be used to generate PWM for 3-phase Inverter.

Figure 13 shows the voltage and current transformation block which converts three-phase voltage and current into the d - q frame by performing Clark and Park transformation simultaneously.

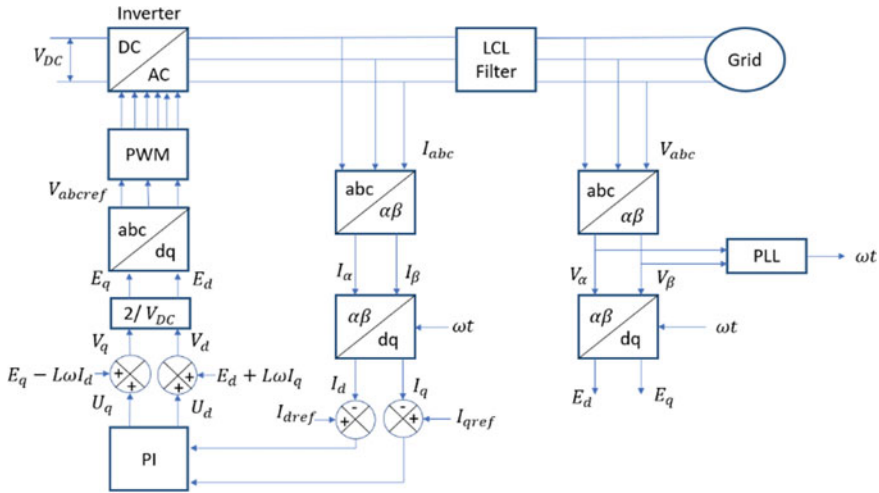


Fig. 12 Controller block diagram for the 3-phase grid-tied inverter

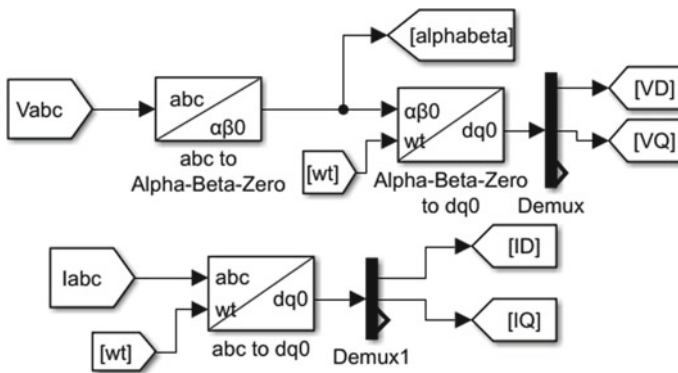


Fig. 13 Voltage and current transformation block

7.2 Phase Lock Loop (PLL)

The d - q frame is a rotating frame whose speed of rotation may or may not be equal to the speed of rotation of the grid voltage. To simplify the controller, we have to make the d - q frame stationary with respect to the grid voltage. Our aim is to lock or align the grid voltage vector along the d -axis and make the q -component of grid voltage zero. Suppose, we have a positive value of V_q and V_d . The net grid voltage V_{grid} is now not aligned with the d -axis. That means, the speed of the d - q frame is slower and we have to accelerate it so that the d -axis get aligned with the grid voltage. Figure 14 shows the alpha-beta and d - q frame where the V_{grid} is not aligned with the d -axis due to the presence of a voltage component along the q -axis. But grid voltage gets

Fig. 14 Net grid voltage

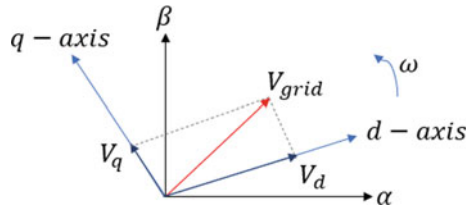
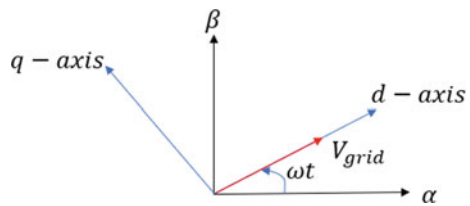


Fig. 15 Alignment of grid voltage with d -axis



aligned with d -axis when we apply PLL to modify the ωt value which is shown in Fig. 15.

Figure 16 shows the schematic diagram of the PLL controller. Three-phase voltages V_a , V_b and V_c are converted into V_d and V_q by using the transformation techniques shown above. The V_q component is compared with $V_{qref} = 0$. Next, the error value is fed to the PI controller which produces angular frequency ω . The ω is integrated to find out $\theta = \omega t$ and ωt is used as feedback to modify the voltage V_q .

Figure 17 shows the actual implementation of PLL in the Simulink environment.

The schematic diagram of the controller for grid-connected three-phase inverter in Fig. 12 has been constructed and executed in MATLAB/Simulink as depicted in Fig. 18. The controller has been developed to generate PWM pulses for the required operation of the inverter. The layout of the subsystem ‘PWM’ is depicted in Fig. 19.

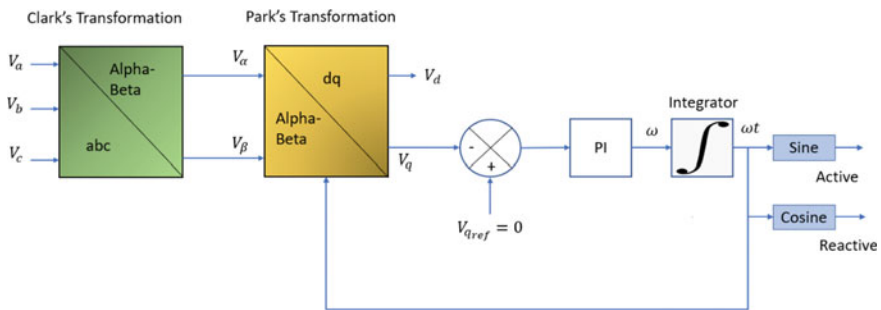


Fig. 16 The phase lock loop (PLL) controller block diagram

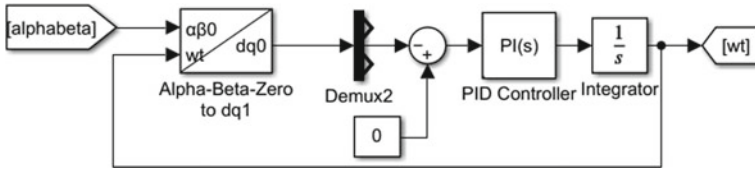


Fig. 17 Phase lock loop (PLL) implementation in MATLAB

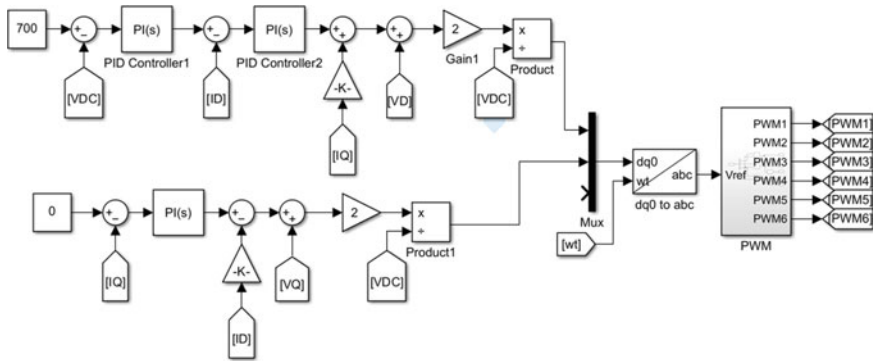


Fig. 18 Controller implementation of three-phase inverter in MATLAB/Simulink

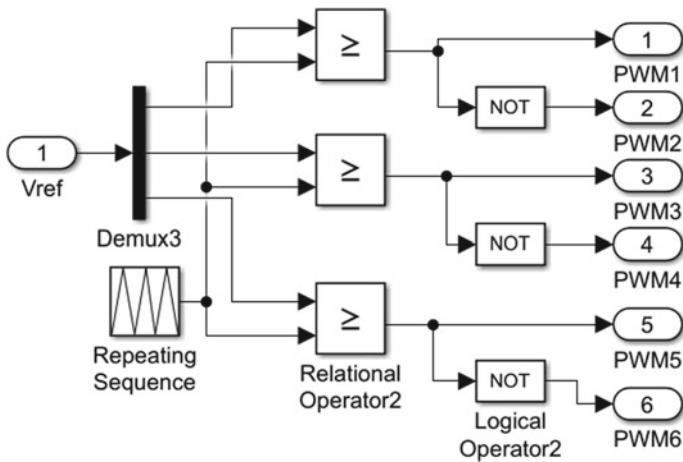


Fig. 19 PWM generation circuit diagram

8 LCL Filter

The output current from 3-phase inverter contains harmonics. Injection of this current into the grid may deteriorate voltage as well as power quality. To avoid these problems, we always connect a filter at the end of the inverter so that we can generate a smooth sinusoidal current before feeding into the grid. LCL filter is favored over L-filter and LC-filter as it can come up with a lesser THD and improved decoupling between the filter and grid impedance. That's why grid-linked employments mostly prefer LCL filters.

9 Power Grid

A Power grid is an electrically interconnected network among multiple generating stations to loads that supplies electricity to the consumers. An electrical grid consists of generating station to produce 3-phase AC power, an electrical substation to step up the voltage before feeding to a transmission line to reduce losses and transmission costs, transmission lines to transmit the power over long distances, and lastly the distribution system to distribute the 3-phase or single-phase AC power to commercial places and houses at required voltage level. Here we have considered Phase-to-Phase RMS voltage of grid is 400 V and frequency is 50 Hz.

10 Results and Discussion

10.1 Boost Converter Design

Specifications

Grid voltage = 400 V (RMS)

For the PV module, $V_{mpp} = 29$ V, as 10 modules are connected in series, the maximum output voltage from PV Array is $29 * 10 = 290$ V

The minimum input voltage for inverter = $400 * \sqrt{2} * 1.2 = 678.82$ V

The voltage output of Boost Chopper should be greater than the Inverter input voltage. Hence, we have considered $V_{output} = 700$ V for the Boost converter.

Specifications

$V_{input} = 290$ V, $V_{output} = 700$ V, Rated Power = 100 kW, Switching Frequency, $f_{sw} = 5$ kHz.

Calculation

Current Ripple, $\Delta I = 5\%$ of Input Current

Voltage Ripple, $\Delta V = 1\%$ of Output voltage

Input Current = $100 \text{ kW}/290 \text{ V} = 344.82 \text{ A}$

Current Ripple, $\Delta I = 5\%$ of $344.82 \text{ A} = 17.24 \text{ A}$

Voltage Ripple, $\Delta V = 1\%$ of $700 \text{ V} = 7 \text{ V}$

Output Current = $100 \text{ kW}/700 = 142.85 \text{ A}$

In Boost Converter, $V_{\text{output}} = \frac{V_{\text{input}}}{1-D}$, where $D =$ duty ratio

$$V_{\text{output}} = \frac{V_{\text{input}}}{1-D} \Rightarrow 700 = 290/(1-D) \Rightarrow D = 0.586$$

The peak-to-peak ripple current across the inductor is given by Eq. (4),

$$\Delta I = \frac{V_{\text{input}} D}{f_{\text{sw}} L} \quad (4)$$

From Eq. (4),

$$\begin{aligned} L &= \frac{V_{\text{input}} D}{f_{\text{sw}} \Delta I} \\ \Rightarrow L &= \frac{290 * 0.586}{5 * 10^3 * 17.24} \\ \Rightarrow L &= 1.97 \text{ mH} \end{aligned} \quad (5)$$

The peak-to-peak ripple voltage across the capacitor is given by Eq. (6),

$$\Delta V = \frac{I_{\text{output}} D}{f_{\text{sw}} C} \quad (6)$$

From Eq. (6),

$$\begin{aligned} C &= \frac{I_{\text{output}} D}{f_{\text{sw}} \Delta V} \\ \Rightarrow C &= \frac{142.85 * 0.586}{5 * 10^3 * 7} \Rightarrow C = 2391.71 \mu\text{F} \end{aligned} \quad (7)$$

10.2 LCL Filter Design

Switching Frequency, $f_{sw} = 10$ kHz

Resonant Frequency, $f_{res} = f_{sw}/10 = 10$ kHz/10 = 1000 Hz

Capacitance value depend on the reactive power required by the capacitor

Reactive Power, $Q = 5\%$ of Rated Power (S)

$$\begin{aligned}
 Q &= \frac{V_{ph}^2}{\frac{1}{2\pi f C}} = 5\% \text{ of } S \\
 \Rightarrow V_{ph}^2 * 2\pi f C &= 0.05 * S \\
 \Rightarrow C &= \frac{0.05 * S}{V_{ph}^2 * 2\pi f} \quad (8)
 \end{aligned}$$

For 100 KVA, 230 V_{p-p} , 50 Hz system, we calculate the capacitor value from Eq. (8)

$$C = \frac{0.05 * (100 * 10^3)/3}{230^2 * 2\pi * 50} = 100.28 \mu F$$

The value of inductor L can be estimated by using Eq. (9),

$$L = \left| \frac{1}{w_{sw} * \frac{I_g(sw)}{V_i(sw)} * \left(1 - \frac{w_{sw}^2}{w_{res}^2}\right)} \right| \quad (9)$$

where

$$w_{sw} = 2\pi f_{sw}$$

$$w_{res} = 2\pi f_{res}$$

V_g = Phase-to-phase Grid voltage

$I_g(sw)$ = Grid current at switching frequency

$V_i(sw)$ = Input voltage of LCL filter at grid frequency

For 100 KVA, 230 V_{p-p} , 50 Hz system

Grid Current, $I_g = (100 \text{ KVA}/3)/230 \text{ V} = 144.92 \text{ A}$

$I_g(sw) = 0.3\%$ of $I_g = 0.003 * 144.92 = 0.434 \text{ A}$

The minimum value of V_i at switching frequency is, $V_i(sw) = 0.9$ times $V_g = 0.9 * 230 = 207 \text{ V}$

Table 2 Design parameters of boost converter and LCL filter

Parameters	Designed values
Boost converter switching frequency	5 kHz
Boost converter input voltage	290 V
Boost converter output voltage	700 V
Inductor (boost converter)	1.97 mH
Capacitor (boost converter)	2391.71 μ F
Filter switching frequency	10 kHz
L(min)	76.68 μ H
L(max) inverter side	500 μ H
L(max) grid side	500 μ H
Capacitor of LCL filter	100.28 μ F
Rated power	100 kW

$$L = \left| \frac{1}{2\pi * 10000 * \frac{0.434}{207} * \left(1 - \frac{(2\pi * 10000)^2}{(2\pi * 1000)^2} \right)} \right| = 76.68 \mu H$$

$L_1 = L_2 = L/2 = 38.84 \mu H$, is the minimum value of inductor.

The maximum value of the inductor is estimated based on the voltage drop across it.

Voltage drops across the inductor, $V_L = 20\%$ of V_g .

The maximum value of the inductor can be calculated by using Eq. (10)

$$L_{max} = \frac{0.2 * V_g}{2\pi f I_g}$$

$$\Rightarrow L_{max} = \frac{0.2 * 230}{2\pi * 50 * 144.92} = 1 \text{ mH} \tag{10}$$

$$L_1 = L_2 = L_{max}/2 = 500 \mu H$$

The design parameters of Boost Converter and LCL Filter are shown in Table 2.

10.3 Power Circuit Diagram

Figure 20 shows the power circuit model of the double stage Grid-Linked PV system which is designed in the MATLAB/Simulink environment.

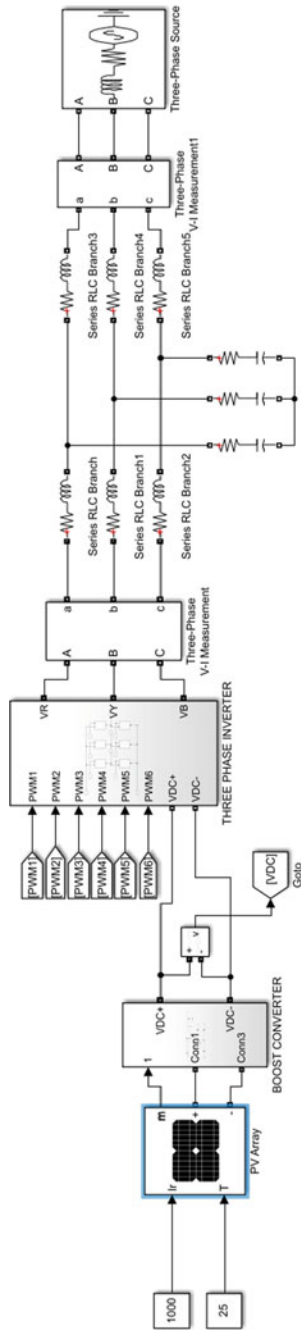


Fig. 20 Circuit diagram of double stage grid-linked PV model in MATLAB/Simulink

11 Simulation Results

11.1 The Output Power Graph from PV Panel

The Power output graph from PV Array at 1000 W/sq-m and 25 °C is 100 kW as shown in Fig. 21. The run time of the simulation is $t = 1$ s.

To visualize the dynamic behavior of grid-tied PV system we have varied the solar irradiance from 1000 W/sq-m to 100 W/sq-m the again increased it to 1000 W/sq-m for the time interval 0 to 1 s at 25 °C. As solar irradiance decreases gradually the output power from the PV array also reduce, but for a reduced irradiance also it will provide maximum power at that instance. Figure 22 shows the output power variation of the PV array due to varied irradiance. Figure 23 shows the output power variation of the PV array due to variation of temperature from 25 to 45 °C at constant solar irradiance of 1000 W/sq-m.

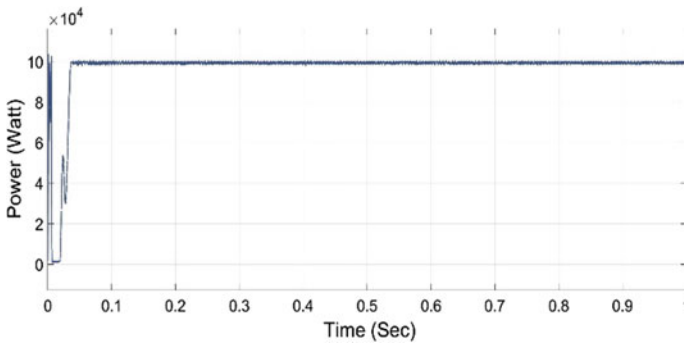


Fig. 21 Plot of power output from PV array

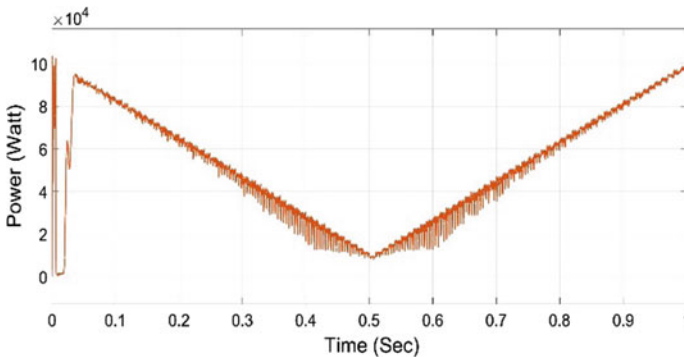


Fig. 22 Output power variation of PV for irradiance

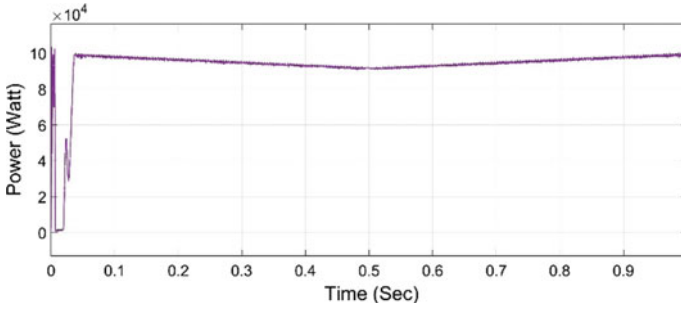


Fig. 23 Output power variation of PV array at variable temperature

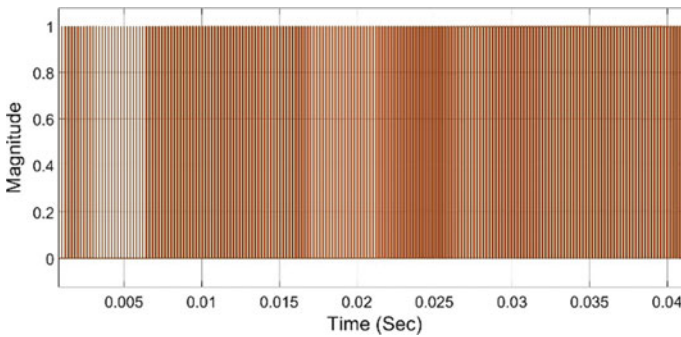


Fig. 24 PWM fed to IGBT in boost converter

11.2 Simulation Result from Boost Converter

Figure 24 shows the PWM pulses fed to IGBT in Boost Converter. A voltage measurement block has been connected at the end of Boost Chopper to read the DC output from the converter. Figure 25 shows the plot of DC output voltage V_{dc} from the converter. We are getting 700 V DC output which is fed to the inverter as an input voltage of the inverter.

11.3 Output Simulation Result

Figure 26 shows the PWM pulses which have been fed to the IGBT in three-phase inverter circuit. Here we have shown only four PWM pulses out of six.

Figures 27 and 28 show the plot of three-phase grid voltage and grid current. The phase-to-phase grid voltage is 400 V, 50 Hz. Phase to ground voltage can be calculated as $400 * \frac{\sqrt{2}}{\sqrt{3}} = 326.6$ V. The three-phase grid current decreases gradually

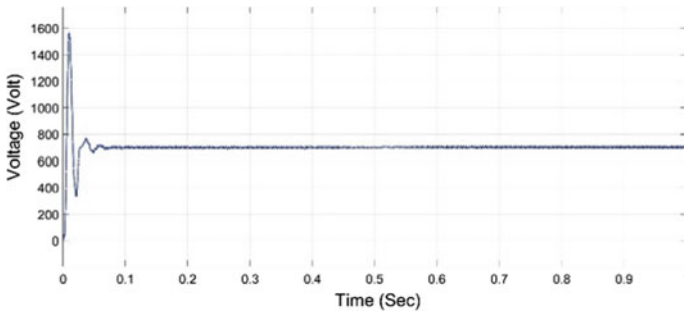


Fig. 25 DC output voltage from boost converter

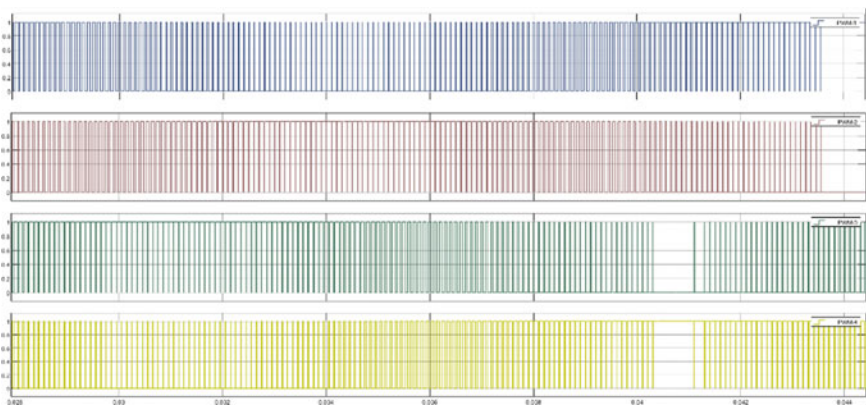


Fig. 26 PWM pulses for IGBT in three-phase inverter

from 0 to 0.5 s as the solar radiation varies from 1000 W/sq-m to 100 W/sq-m. Output current at $t = 1$ s is 200 A.

Figures 29 and 30 show the plot of grid voltage and grid current due to variation of temperature from 25 to 45 °C at constant solar radiation.

11.4 Simulation Result of Grid Power and Solar Radiation

Figures 31 and 32 show the variation of the grid power as the solar irradianc is varying continuously. The output power is 100 kW at solar irradianc of 1000 W/sq-m. At $t = 0.5$ s the irradianc reduced to 100 W/sq-m and the corresponding output power also decreased to 1 kW. The first one is the plot of solar irradianc with time and the second one is the plot of output power.

The temperature has been varied from 25 to 45 °C at constant solar irradianc which has been shown in Fig. 33 and the corresponding output power variation has

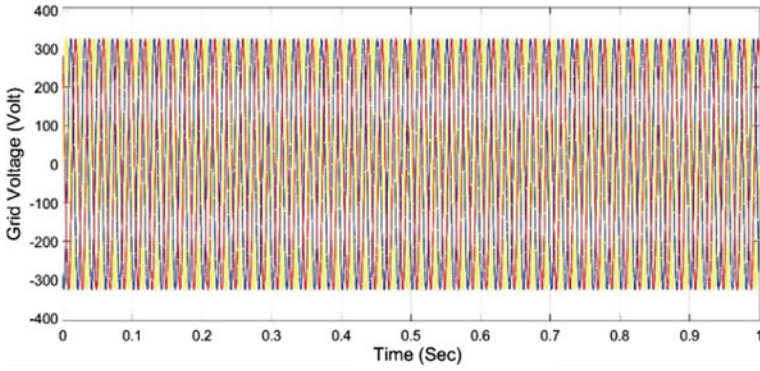


Fig. 27 Plot of grid voltage for variable irradiance

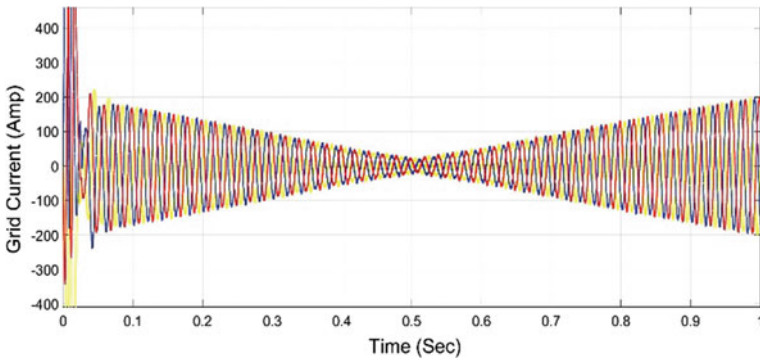


Fig. 28 Plot of grid current for variable irradiance

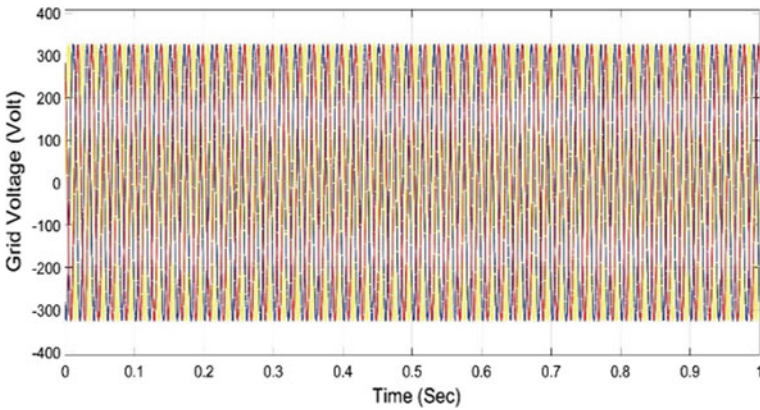


Fig. 29 Plot of grid voltage for variable temperature

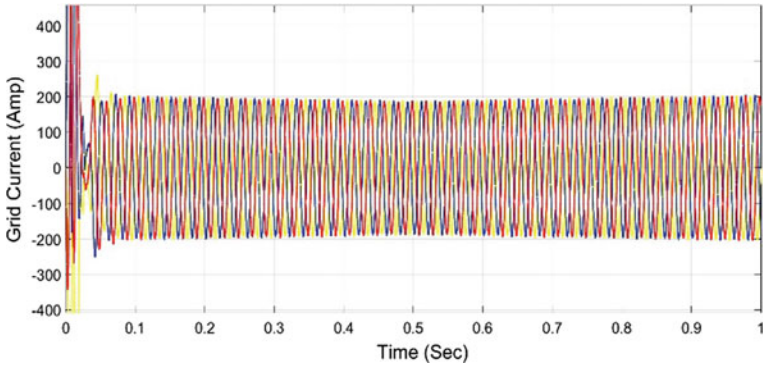


Fig. 30 Plot of grid current for variable temperature

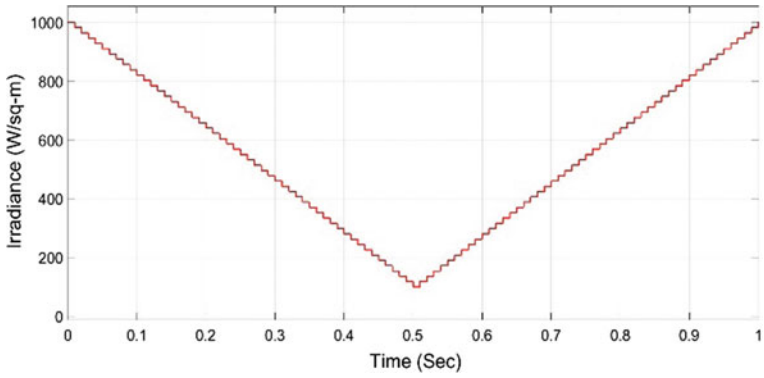


Fig. 31 Plot of solar irradiance versus time

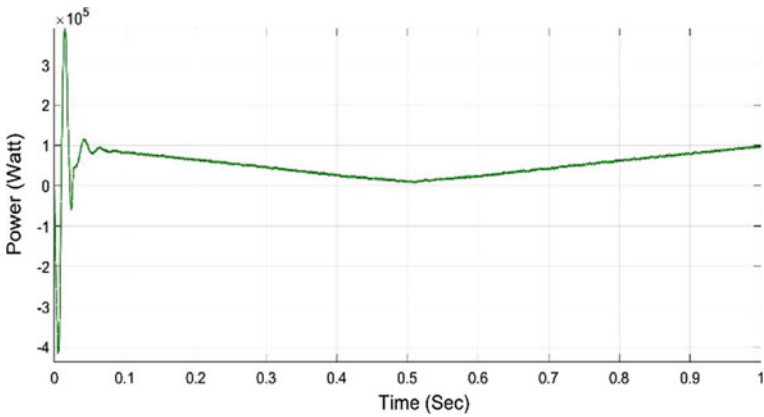


Fig. 32 Plot of output power versus time for irradiance

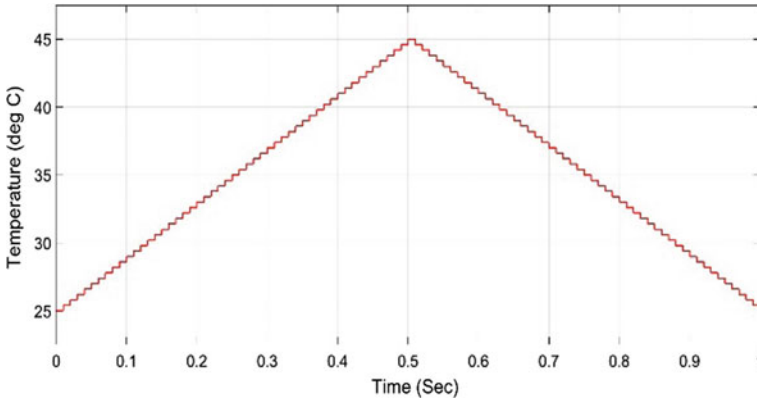


Fig. 33 Plot of temperature versus time

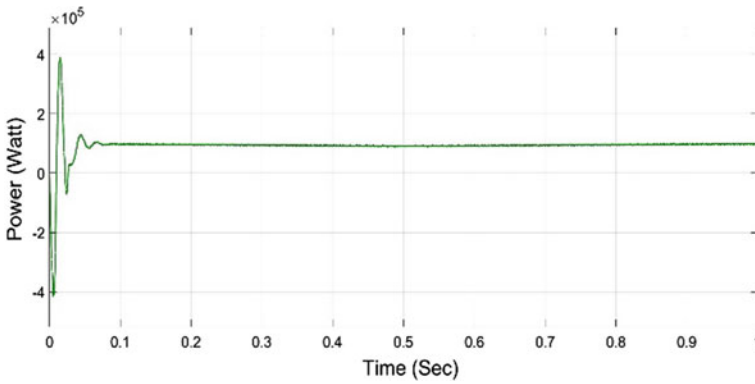


Fig. 34 Plot of output power versus time for temperature

been depicted in Fig. 34. MATLAB modeling of variable temperature and irradiance has been shown in Figs. 35 and 36. Real and reactive power has been displayed in Fig. 37.

12 Conclusion

In this paper, a Double Stage Grid-Linked PV System has been designed and simulated using MATLAB/Simulink version R2021a. The proposed system is able to generate 100 kW of power and feed it to the utility grid. The P&O method has been used in MPPT to draw out the highest power under variable circumstances. Inductance and capacitance values of boost converter have been calculated as 1.97 mH and 2391.71 μ F, respectively. The DC output from the PV array is 290 V which is

Fig. 35 Variable temperature at constant irradiance

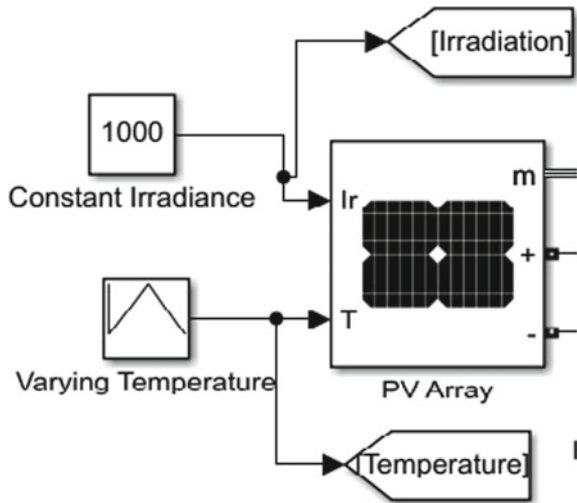
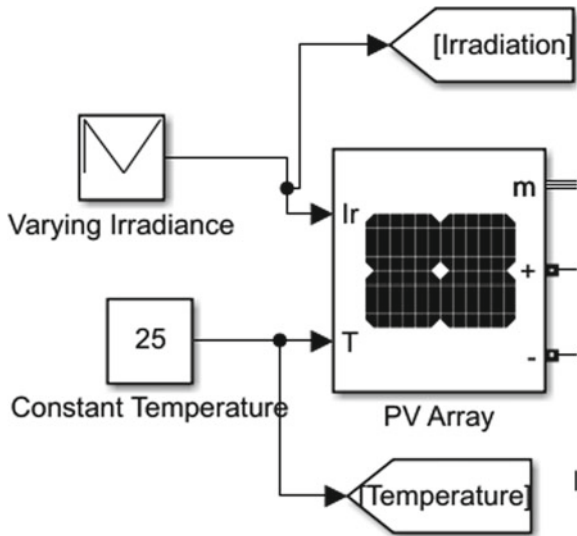


Fig. 36 Variable irradiance at constant temperature



boosted up to 700 V by the Boost converter and converted into AC by the 3-phase bridge inverter. Synchronous reference frame theory has been introduced to achieve PLL control. In LCL Filter the inductance value of 500 μ H on the grid side as well as inverter side and the capacitance value of 100.28 μ F have been estimated for particular specifications. The output of the inverter is passed through the LCL filter to remove the harmonic and maintain improved power quality of the grid. The solar irradiance has been varied from 1000 to 100 W/sq-m at a constant temperature of 25 $^{\circ}$ C and the plot of solar irradiance and real power output has been shown. A dip in

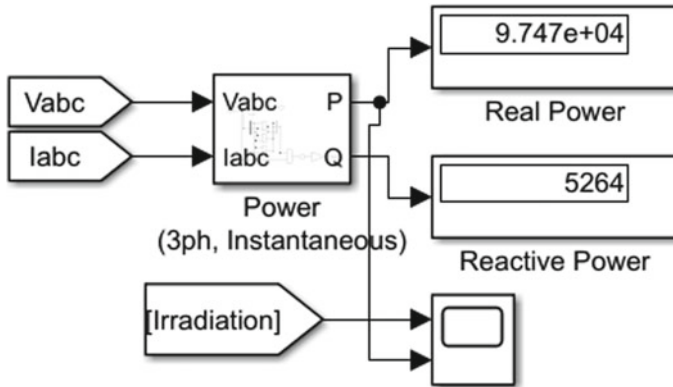


Fig. 37 Display of active and reactive power

real power is noticed due to a decrease in irradiance. The grid current drops drastically at 100 W/sq-m irradiance. Also, a slight dip in real power has been observed due to a change in temperature from 25 to 45 °C at constant solar radiation of 1000 W/sq-m. It has also been shown that the grid current remains almost constant with the temperature variation.

References

1. Jayaram, K.: Simulation based three phase single stage grid connected inverter using solar photovoltaics. *J. Univ. Shanghai Sci. Technol.* **23**(5) (2021)
2. Benaissa, O.M., Hadjeri, S., Zidi, S.A.: Modeling and simulation of grid connected PV generation system using Matlab/Simulink. *Int. J. Power Electron. Drive Syst. (IJPEDS)* **8**(1), 392–401 (2017)
3. Molina, M.G., Espejo, E.J.: Modeling and simulation of grid-connected photovoltaic energy conversion systems. *Int. J. Hydrogen Energy* (2013)
4. Sarath Chandrareddy, E., Chengaiah, Ch., Bullarao, D.: A 100 kw single stage grid-connected PV system with controlled DC-link voltage. *Mater. Today Proc.* (2020)
5. Ravalika, G., Suriyaprakash, M., Srinivas, D.: Grid related PV system with D-Statcom modelling and simulation. *J. Resour. Manag. Technol.* **11**(4), 374–381 (2020)
6. Kothari, D.P., et al.: Perturb and observe MPPT algorithm for solar PV systems-modeling and simulation. *IEEE India Conference*, 16–18 Dec 2011
7. El Hichami, N.: Maximum power point tracker method for grid connected photovoltaic system based on hill climbing technique. *Turkish J. Comput. Math. Educ.* **12**(11) (2021)
8. Shafeek, M.A., et al.: Modelling and simulation of DC-DC boost converter and inverter for PV system. *Malays. J. Sci. Adv. Technol.* (2021)
9. Kasera, J., Kumar, V., Joshi, R.R., Maherchandani, J.K.: Modelling and simulation of grid connected photovoltaic system employing Pertub and observe MPPT algorithm. In: *International Conference on Recent Trends of Computer Technology in Academia* (2012)
10. Chen, Y., Smedley, K.: Three-phase boost-type grid-connected inverter. *IEEE Trans. Power Electron.* **23**(5) (2008)
11. Fethi, A.: Power control of three phase single stage grid connected photovoltaic system. *IEEE Trans* (2016)

12. Wu, X., Xu, F.: Control and simulation on three-phase single-stage photovoltaic (PV) system as connecting with power grids. In: IEEE Workshop on Electronics, Computer and Applications (2014)
13. Aillane, A., Chouder, A., Dahech, K.: P/Q control of grid-connected inverters. In: 18th International Multi-Conference on Systems, Signals & Devices (SSD'21) (2021)
14. Lettl, J., Bauer, J., Linhart, L.: Comparison of different filter types for grid connected inverter. In: PIERS Proceedings, Marrakesh, MOROCCO, 20–23 March 2011
15. Deželak, K., et al.: Proportional-integral controllers performance of a grid-connected solar PV system with particle swarm optimization and Ziegler–Nichols tuning method. *Energies*2021 (2021)

A Review of Sensor-Based Solar Trackers



Ashish Dixit, Suresh Kumar Gawre, and Shailendra Kumar

1 Introduction

Currently, all of earth's energy demands are taken care by conventional sources or non-renewable sources of energy such as oil, natural gas, coal, uranium. But, these energy sources are exhaustive in nature meaning sooner or later, they will end up depleted, and on top of that they are major contributors in overall pollution of environment. One of the most daunting tasks that the society is facing is to find sources of energy that are non-polluting as well as abundant in quantity. Renewable such as solar, hydro, wind seem to be the answer to these challenges. These energy sources will neither pollute the environment nor will end up getting depleted by mankind. Of all the aforementioned renewable sources solar energy seems to be more promising due to the fact that it finds applications ranging from charging an electric vehicle to powering an entire house.

Solar energy is harnessed by using PV cells to convert sunlight directly into electrical energy. A country like India can take advantage of the fact that it has abundant sunshine throughout the year in most parts of the country [1, 2]. China, United States of America, and India have acquired the top 3 spots in terms of installing highest number of PV systems from between 2016–2020 [3]. But, the problem with a static PV system is that the position of sun keeps changing throughout the day [4]. This means that the PV system will be generating power at its maximum capacity only when the position of sun is such that the PV cells are capturing maximum sunlight. Although this might fulfill energy demands of a smaller system say a solar-powered streetlight, but in order to justify the installation costs of a large-scale PV system, we need to make sure that the PV cells capture maximum sunlight among other things.

This is where the solar tracker comes in and positions the PV modules such that they, are perpendicular to the beam of sunlight that falls on them [5]. Studies show that an increase of up to 50% can be achieved in the energy yield of a PV system in

A. Dixit (✉) · S. K. Gawre · S. Kumar
Maulana Azad National Institute of Technology, Bhopal 462003, India

a year by simply installing a solar tracker with a static PV system [6]. Solar trackers are classified in terms of degrees of freedom and type of control system employed to control the tracker. On the basis of degree of freedoms, solar trackers are classified as single-axis solar tracker and dual-axis solar tracker. Sensor-coupled control systems and control systems based on astronomical parameters are the two most used control systems as far as controlling of solar trackers is concerned.

2 Sun-Earth Geometry

The sunlight falling on the PV panels isn't just a single entity because it consists of three components. The three components of sunlight are direct beam, diffuse sunlight, and reflected radiation [7]. Direct beam is the component of sunlight which contains 90% of solar energy, and rest of the solar energy is contained in the other two components [8]. Tracking the sun means, we have to align the PV panels in such a way that PV panels absorb the direct beam component of sunlight as much as possible.

Latitude and longitude are used to express the position of sun on earth. Equator is the imaginary line that runs through the middle of our planet earth. Earth is divided into two halves known as northern hemisphere and southern hemisphere by the imaginary line known as equator. The position of a region between the North Pole and South Pole is determined by latitude, while the longitude is used to express the position of a region on earth with respect to east–west direction.

The one thing that we know for certain about sun is that the sun rises in east and sets in west. But, this fact alone isn't enough to get the position of sun. In order to determine the position of sun, we need to familiarize ourselves with three angles which are azimuth angle, zenith angle, and elevation angle [1] (Fig. 1).

1. Zenith angle is the angle between the line joining the sun and the region on earth and the line perpendicular to that region on earth.
2. Azimuth angle is the angle between the line along North Pole and the line that acts as projection of the sun on earth. Azimuth angle is measured in clockwise direction.
3. Lastly, we have the third angle known as elevation angle which is used to denote the angular height of the sun throughout the day. Solar elevation angle is 90° when the sun is directly above our head. Elevation angle is given by Eq. (2), and the azimuth angle is given by Eq. (3) (Fig. 2).

We need to factor in the tilt that our planet earth has got on its rotational axis. To take into account the tilt of earth on its rotational axis, we use another angle known as declination angle denoted by ' d '. There is a seasonal variation in the value of declination angle owing to the tilt earth has on its axis of rotation. The value of declination angle would be 0° if the tilt of earth was absent, but since the earth has a tilt of 23.45° , the declination angle lies between $\pm 23.45^\circ$.

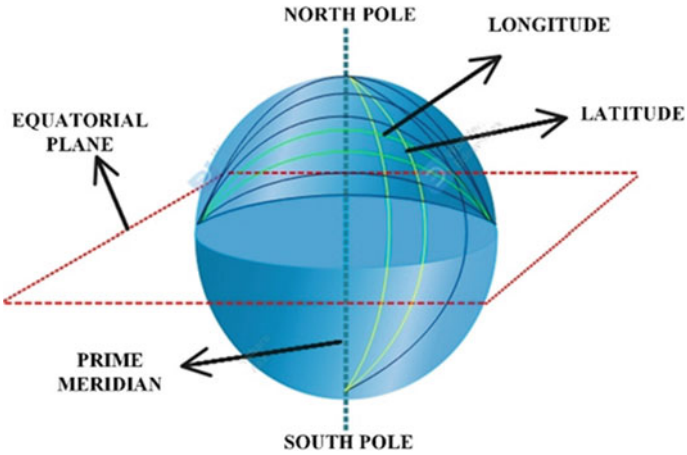
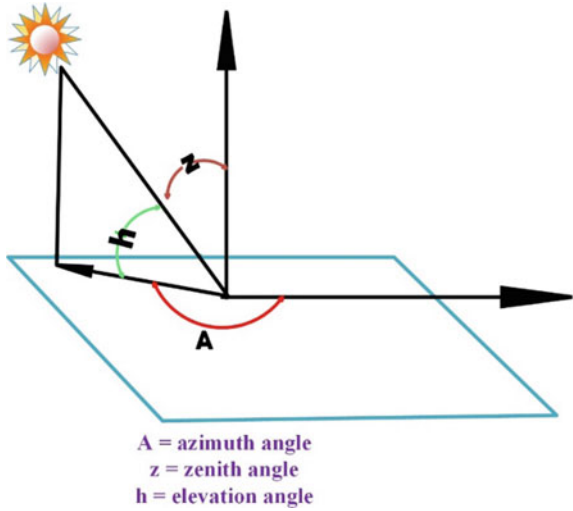


Fig. 1 Latitude, longitude, and equator

Fig. 2 Elevation angle, zenith angle, and azimuth angle



$$d = -23.45^\circ \times \cosine\left(\frac{360}{365} \times (D + 10)\right) \tag{1}$$

where D denotes the day of a particular year

$$h = 90 + \varnothing - d \tag{2}$$

where d is the declination angle in degrees and \varnothing is the latitude angle of the region of interest in degrees

$$A = \cos^{-1} \left(\frac{\sin d \cos \emptyset - \cos d \sin \emptyset \cos(\text{hour angle})}{\cos h} \right) \quad (3)$$

The zenith angle is given by Eq. (4)

$$z = (90 - h) \quad (4)$$

where h is the elevation angle in degrees.

3 Classification of Solar Trackers

Generally speaking, the solar trackers are classified into two categories in terms of the axis of rotation.

1. **Single-axis solar tracker:** As the name suggests, this type of PV tracker can rotate the PV cell along only one axis. This axis could either be the vertical axis or the horizontal axis. Horizontal solar tracker is mainly employed for regions that lie in tropics as the sun is very high during afternoon period [9]. Vertical PV trackers are used for regions that are located near latitudes or for regions that are mountainous because in these regions sun doesn't tend to get very high meaning the sunlight doesn't fall directly onto the surface of PV modules, and hence, they do the east–west tracking of sun [10].
2. **Dual-axis PV tracker:** Unlike the single-axis PV trackers, dual-axis solar trackers are capable of providing full tracking of sun because these trackers possess two axes of rotation. One is known as the declination axis, and the other is known as the polar axis. Polar axis points toward the North Pole and is parallel to the earth's axis of rotation. The declination axis on the other hand is perpendicular to the polar axis. In this way, the dual-axis takes care of both the east–west movement and north–south movement of the sun. Basically, these trackers are not only able to track the daily east–west movement of the sun but are also capable of tracking seasonal angular variations in the height of sun during different seasons thus maximizing the amount of sunlight captured by the PV cell in an entire year. The surface of the receiving PV module is rotated around the polar axis [11] (Figs. 3 and 4).

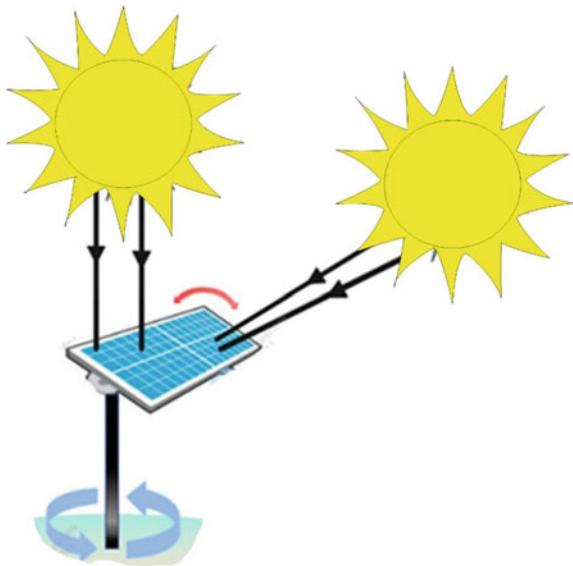
Solar irradiance can be tracked in two ways, namely active PV tracker and passive Sun tracker.

1. **Active PV trackers** are those solar trackers that employ microcontrollers and sensors to track the trajectory of sun. Sensors are used to locate the sun more accurately by decreasing the pointing errors caused while locating the sun in the absence of external sensors.
2. **Passive Sun Trackers:** These trackers don't rely on microcontrollers or external sensors. Instead, these trackers use statistical calculations and astronomical data

Fig. 3 Horizontal axis solar tracker



Fig. 4 Dual-axis PV tracker



to locate the sun in the sky and use mechanical means to reorient the PV panel. In order for these kinds of trackers to work, knowledge about the longitude and latitude of different surrounding regions is crucial.

4 Control System for Solar Trackers

The main purpose of a PV tracker is to carry out the tracking of sun automatically and accurately with minimum pointing errors. Automation in PV trackers is achieved through various control circuits, feedbacks. Broadly speaking, there are three types of control modes available in the current models of solar trackers.

1. Open-Loop Control: As the name suggests, this mode doesn't have any feedback element to reduce positional errors. Stepper motors are generally used as drives in open-loop control mode. Since there is no feedback, there is no way to reduce the error that might creep in case stepper motor loses its step due to overshoot or changes in load.
2. Closed-Loop control mode: Unlike open-loop control, here, the PV tracker will have feedback. This feedback will be responsible for eliminating errors in the steps of the stepper motor drive. Elimination of error is achieved through sensors that are used to determine the deviation between the sunlight that falls on PV module surface and the normal of PV panel. Sun's position can be determined at any given time of a particular day through closed-loop control. In closed-loop control strategy, the sensors used are basically light sensors, and these sensors are placed on the solar panel surface. The difference in the intensity of light falling on light-triggered sensors is used to reorient the PV panel in a direction perpendicular to the incident sunlight (Fig. 5).

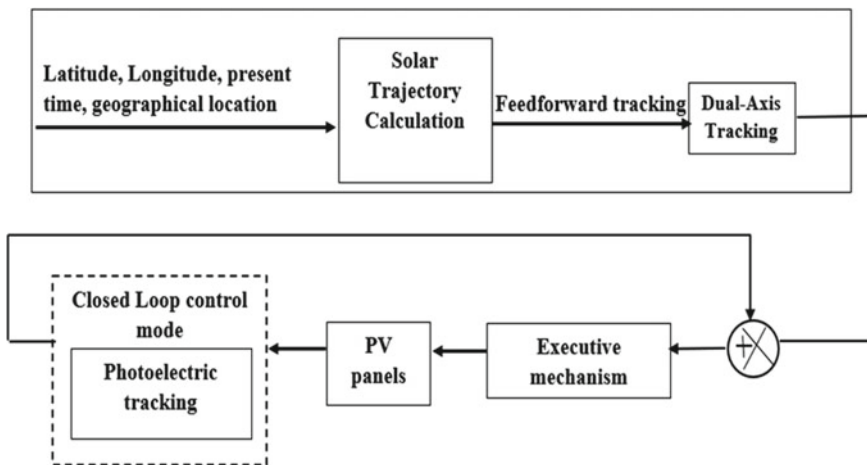


Fig. 5 Photovoltaic tracker in with closed-loop control mode

5 Hardware Required for Active Solar Trackers

As discussed above, the active PV trackers generally use microcontrollers, external sensors to get rid of pointing sensors, stepper motors as drives, storage devices to record azimuth and elevation angle of sun, motor driver circuits, different types of converters such as analog-to-digital converters. We will discuss all these components one by one and their alternatives as well.

1. Microcontroller

It basically acts as the brains behind the operation of a solar tracker. Microcontroller is programmed to generate control commands for the actuator. Basically, the data received by sensors are in terms of resistance/voltage which is fed to the microcontrollers as analog signal. The built-in analog-to-digital converter (ADC) or an external ADC converts this analog signal into digital signal for the microcontroller to interpret, and then, the microcontroller feeds this data to the actuator motor drive via a motor driver. Microcontrollers employed in solar trackers come with built-in pulse width modulation (PWM) pins [12]. These PWM pins are used to control the actuator motor i.e., servomotor. Position of the shaft of servomotor is determined by the help of PWM signals generated by these PWM pins of the microcontroller, and the determined position makes the servomotor reorient the PV panel in the required direction. Additionally, the microcontroller has a built-in micro-SD card to record all the data related to positioning, time of the day, sun trajectories [13, 14].

2. Sensors

Sensors are used to operate the solar trackers in closed-loop control mode. Sensors used are basically light sensors such as light-dependent resistors (LDRs), photodiodes, phototransistors, and silicon photo-triodes. All of these light sensors perform one job which is to convert light signal into electrical signals [15], e.g., LDRs convert light signal into resistance which is nothing but an electrical quantity.

3. Drives used in solar PV trackers

Drives are nothing but electric motors here that perform the task of rotating the PV panel about an axis depending on the type of solar tracker being used. In case of single-axis trackers, a single motor will suffice, but in case of a dual-axis PV tracker, two motors are required. The drive chosen for any kind of solar tracker must be such that it is able to withstand extremes in temperature, wind conditions, humidity. Various types of motors are being used nowadays in solar trackers such as stepper motors, geared servomotors, and brushless DC motors (BLDC).

3.1. Stepper motor

A stepper motor is nothing but a brushless DC motor (BLDC). As the name suggests, a stepper motor divides a normal rotation (360°) into steps of equal size [15]. Although stepper motors provide great economic benefits due to them being quite inexpensive, but when more components are added

in a closed-loop control mode, stepper motors no longer remain the top choice for drives in a PV tracker.

3.2. Servomotor

Servomotors are the kind of actuators that provide rotational or translational motion. In other words, servomotors are employed to get precise control over linear position or angular position. Servomotors possess sensor circuits as position feedback elements to provide position control. Servomotors are fed with pulse width modulation (PWM) signals coming from PWM pins of the microcontroller [16].

3.3. Gear motor

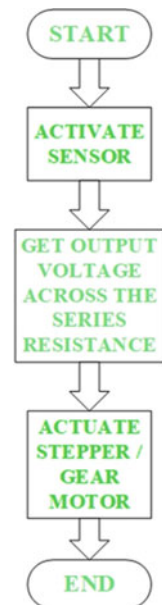
These motors possess the ability to develop large torque at smaller values of acceleration. These motors can be powered by both an AC supply and DC supply. Gearbox is also required with these electrical machines in order to reduce the shaft acceleration to achieve different values of torques.

4. Motor driver

Motors used in simple and inexpensive microcontroller-based solar trackers can't be directly connected to the microcontroller as the microcontrollers used in these solar trackers won't be able to provide the necessary current for the motor to operate. Therefore, we use a motor driver which acts as a current amplifying circuit (Figs. 6 and 7).

To prevent reverse flow of current while the battery discharges, the circuit has been equipped with two one-way diodes [17].

Fig. 6 Block diagram of an active PV tracker possessing external sensors



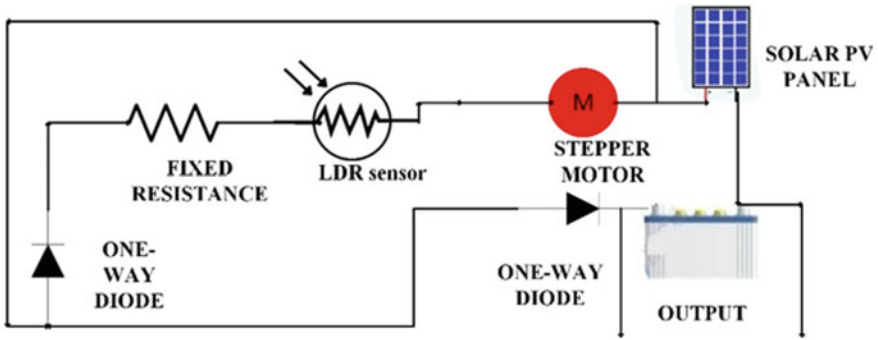


Fig. 7 Line diagram of an active PV tracker with LDR sensor

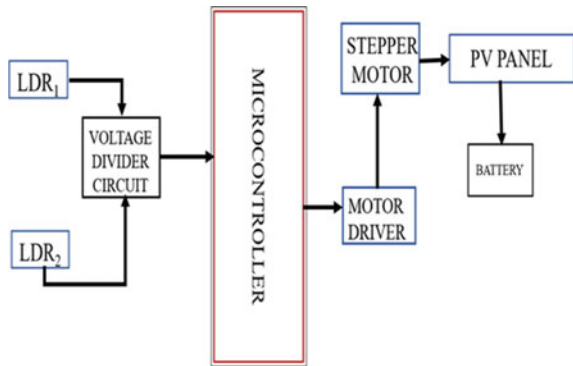
6 Construction

The LDRs are placed on the periphery of the surface of PV panel from where these LDRs capture some of the incident light falling on the solar PV panel. A stepper motor is connected to the microcontroller via a motor driver which basically acts as a current amplifying circuit for the motor to operate.

6.1 Single-Axis Solar PV Tracker

See Fig. 8.

Fig. 8 Block diagram of an active single-axis solar PV tracker



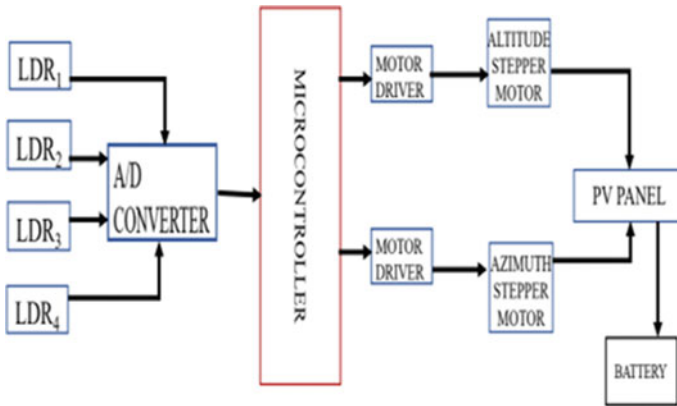


Fig. 9 Block diagram of an active dual-axis solar PV tracker

6.2 Dual-Axis Solar PV Tracker

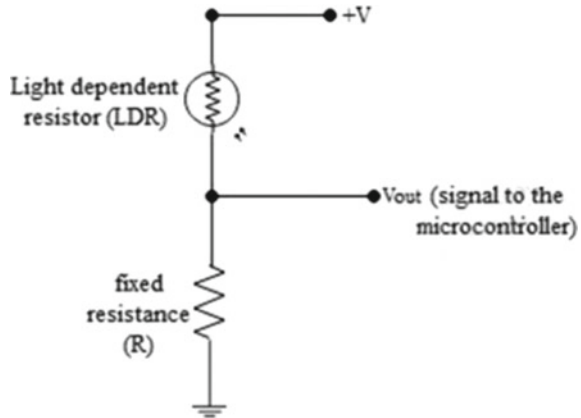
Here, instead of two LDRs, four LDRs are placed on the surface of solar PV panel and two stepper motors as opposed to single stepper motor in a single-axis tracker. This is because of the fact that a dual-axis solar tracker possesses two degrees of freedom, while the single-axis PV tracker has just one degree of freedom (Fig. 9).

6.3 LDR Circuit and Its Sensitivity

We already know that there exists an inverse relationship between the resistance offered by the LDR and the intensity of light falling on it [18, 19]. Also, LDR isn't present alone as there is going to be a fixed resistance in series with LDR as well. Long story short, the overall LDR circuit behaves as a voltage divider. The voltage divider circuit is shown in Fig. 10. The analog reading of the voltage (V_{out}) across the fixed resistance is fed to the microcontroller as the output of LDR is resistance which can't be read by microcontroller. Therefore, we use the analog voltage across the fixed resistance as input to the microcontroller where the analog output voltage (V_{out}) itself is the function of resistance offered by LDR and the resistance offered by LDR is the function of the intensity of light falling on LDR. In other words, when intensity of light decreases, resistance offered by LDR increases, and thus, the analog output voltage across the fixed resistance decreases [20].

$$V_{out} = V \times \frac{R}{(R + \text{LDR})} \quad (5)$$

Fig. 10 Voltage divider of LDR in series with fixed resistance



In order for the sun tracker to track the sun in all conditions, the value of analog output voltage across fixed resistance mustn't be too small. To ensure proper sensitivity of LDR circuit, we need to select the optimum value of fixed resistance ' R ' [21]. This optimum value of R will ensure that the equivalent resistance of voltage divider doesn't reduce analog output voltage (V_{out}) to the point where it becomes unusable as an input to the microcontroller.

6.4 Placement of LDR Sensors on a Dual-Axis Active Tracker

There are three main configurations in which the LDR sensors can be placed on the surface of the LDR as shown in Figs. 11, 12 and 13. Of all the three possible configurations, the four-corner configuration is the best one as it allows the coverage of the entire surface of the target PV panel [22].

7 Operating Mechanism

The working principle will remain same whether it is a single-axis solar PV tracker or a dual-axis tracker with some minor changes such as the dual-axis tracker will have four light sensors. But, the basic principle of operation is the difference between the outputs of LDRs is sent to the microcontroller via an analog-to-digital converter so that the microcontroller can send signal to the motor driver circuit.

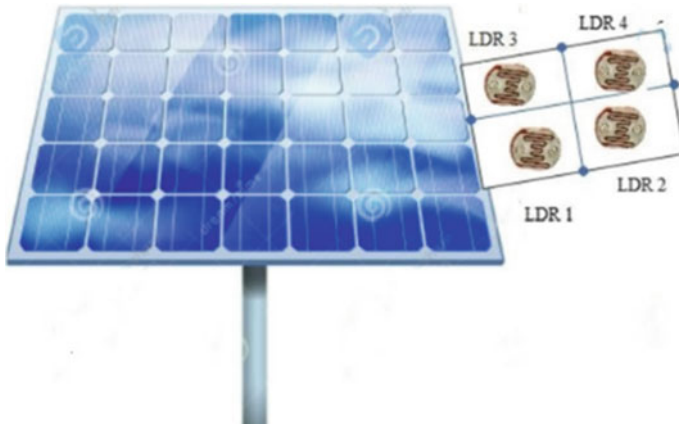
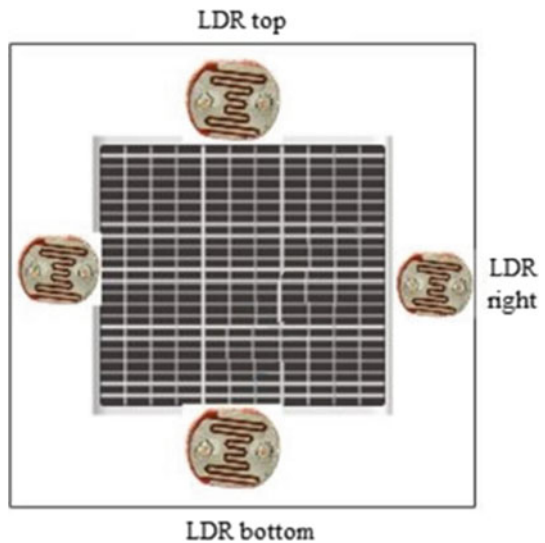


Fig. 11 Four-quadrant configuration

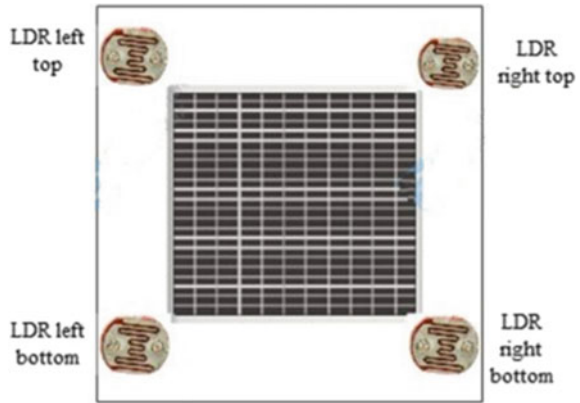
Fig. 12 Center of each side configuration



7.1 Single-Axis Tracker Mechanism

The two LDRs will be placed either along east–west direction or north–south direction. Depending on which LDR has the highest intensity of light on it, analog output voltage is generated across the fixed resistance which acts as input for the microcontroller to send command to the motor driver circuit. The difference between the analog output voltage due to both LDRs acts as the feedback for the closed-loop control mode [23]. There are only two possible states in this type of solar PV tracker. One of the states is that in which intensity of light is same for both LDRs which means

Fig. 13 Four-corner configuration



the difference in the analog output voltage across fixed resistance will be zero, and thus, the PV panel will remain in standstill position [24]. This state also implies that the incident sunlight is exactly perpendicular to the to the PV panel surface. The other state is the one in which the difference isn't zero meaning intensity of light falling on one of the LDR sensors is more than the other sensor. Thus, in this state, there will be a command sent to the motor driver circuit by the microcontroller to reorient the PV panel in the direction of the LDR that has the highest intensity of sunlight on it.

7.2 Dual-Axis Tracker Mechanism

Here, there will be four LDRs placed in four-corner configuration and two stepper motors for north–south and east–west tracking. Here, there are four possible states or scenarios in which the four LDRs can participate during the tracking of the sun.

1. Only one LDR receives the sunlight
 Out of the four LDRs, only one LDR will only receive the sunlight, and the value of this LDR output will be matched with the output of remaining three LDRs. Therefore, in this state, PV panel will undergo rotation continuously about both axes back and forth. Truth table for this scenario is given in Table 1 (Fig. 14).

Similarly, the other three scenarios are self-explanatory.

2. Any two sensors receive sunlight (Table 2)
3. Any three sensors receive sunlight (Table 3)
4. All four sensors receive sunlight (Table 4).

Table 1 Truth table for state-1

Input to LDR sensor				Axis-I		Axis-II	
LDR 1	LDR 2	LDR 3	LDR 4	E-W	W-E	N-S	S-N
1	0	0	0	0	0	0	1
0	1	0	0	0	0	1	0
0	0	1	0	1	1	0	1
0	0	0	1	1	1	1	0

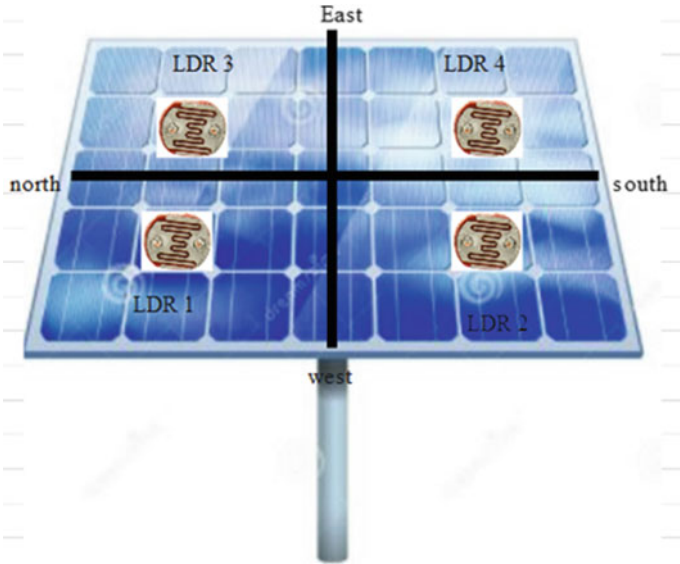


Fig. 14 Sensor placement for dual-axis tracking scheme

Table 2 Truth table for state-2

Input to LDR sensor				Axis-I		Axis-II	
LDR 1	LDR 2	LDR 3	LDR 4	E-W	W-E	N-S	S-N
0	1	0	1	0	0	1	0
1	1	0	0	1	0	0	0
0	0	1	1	0	1	0	0
0	0	0	1	1	1	1	0

Table 3 Truth table for state-3

Input to LDR sensor				Axis-I		Axis-II	
LDR 1	LDR 2	LDR 3	LDR 4	E-W	W-E	N-S	S-N
1	1	1	0	1	0	0	1
0	1	1	1	0	1	1	0
1	1	0	1	1	0	1	0
1	0	1	1	0	1	0	0

Table 4 Truth table for state-4

Input to LDR sensor				Axis-I		Axis-II	
LDR 1	LDR 2	LDR 3	LDR 4	E-W	W-E	N-S	S-N
1	1	1	1	0	0	0	0

8 Major Findings and Key Challenges

8.1 Performance Review

The total amount of sunlight that falls on the surface of a PV panel is measured in terms of solar irradiance. The unit of solar irradiance is watt/metre² (W/m²). Solar irradiance is one of the many performance parameters helps us to determine the efficiency of a solar PV panel. Here, we are concerned with the performance of a fixed PV system versus the performance of a PV system equipped with a sun tracker.

In order to shed light on the performance of a sun tracker-equipped PV array, we need to find out the output current and voltage for such a system. Only, then will we be able to estimate the operational cost of such a system. Output current and voltage will give us the total energy generated by the sun tracker-equipped PV system which will then be compared with the energy generated by a fixed PV system [25].

Studies show that there is an increase of about 30.79% in the amount of produced electricity when the PV system is coupled with a dual-axis PV solar tracker [26–29].

As far as the total electrical energy produced goes, experiments conducted with dual-axis trackers in Indonesian region of Kupang show an increase of 40–50% in the amount of electrical energy produced by a fixed PV system [30].

8.2 Findings

1. LDRs take a longer time to respond, i.e., LDR’s don’t undergo change in their conductivity simultaneously right after they are exposed to incident light. This is because LDRs are basically photoresistors. To address this issue, we can replace LDRs with other types such as photodiodes and phototransistors [31].

2. Photodiodes have a response time of a few nanoseconds (ns). But, for a low cost and inexpensive solar tracker such as the one discussed in this review paper, replacing LDRs with photodiodes isn't such a good idea because photodiodes along with their advantages over photoresistors have their downsides as well and so does phototransistors. Being unidirectional and the requirement of an extra OPAMP circuit makes the assembling of circuit involving photodiodes look daunting and not to mention the additional cost incurred due to OPAMP circuits [31]. On the other and LDRs don't require OPAMPs and are bidirectional which is why LDRs are cheap and their circuits are straightforward. Therefore, selection of the type of opto-sensors to be used must be done wisely.
3. The other issue with the LDR and microcontroller-based setup is that the tracking error might not be zero even when the difference between the outputs of all photosensors is zero. This could be ignored. This happens because we assume that all LDRs coming from the same manufacturer must be identical, but in actuality, this isn't the case. Since these photosensors aren't identical to each other in all respects, different weather conditions will affect each photosensor differently. This shortcoming is unavoidable in photosensor-based sun trackers, and it can't be ignored in applications such as a concentrated PV panels [32].
4. We can use additional components along with sensors such as GPS module, magnetometer, accelerometer, gyroscope, to design an autonomous solar PV tracker. Data from GPS module can be used to determine latitude, length of the day and latitude. Magnetometer will be employed to determine the sunrise and sunset time [33]. In order to determine the inclination of solar PV panel in vertical position, gyroscope will be employed, and to get the inclination angle in horizontal position, accelerometer can be used in conjunction with the magnetometer.
5. To enhance LDR-based solar PV trackers, we can use various techniques such as tracking algorithm, image processing techniques along with fuzzy logic-based algorithm to get rid of non-zero tracking error [34].
6. Fuzzy logic-based solar PV trackers are far more superior than other types of trackers as these trackers don't depend on where the sun is located geographically. Fuzzy logic first came to the notice in the year 1965, the year in which the term "fuzzy logic" was coined by Zadeh. Boolean logic is based on 0 and 1, while fuzzy logic can have values between 0 and 1. Fuzzification of measured data such as inclination angle, time of rise and sunset, azimuth and elevation angles, intensity of sunlight is done in fuzzy logic-based solar PV trackers [35]. Fuzzification is done by assigning values to the variables (recorded data) of membership functions. Membership functions can have any trapezoidal shape.
7. There are five components in a typical fuzzy logic controller, namely fuzzifier, rule base, inference mechanism, data base, and lastly a defuzzifier. Fuzzy variables created by rule base of fuzzy logic controller are converted back to the real values by defuzzifier (Fig. 15).

Fig. 15 Triangular shape of membership plot of solar intensity



9 Future Scope

Besides the externally powered solar tracker system which we saw in previous section, a solar tracker which is self-powered can also be built. In such a self-powered solar photovoltaic tracker, solar panels will perform two jobs of supplying energy to the setup (DC motor along with gear) as well as collect sunlight. Auxiliary solar PV panels for providing supply power besides the main panel will also be required. For such a self-powered tracker, we will require rectifying diodes as well along with DC gear motor and PV panels. The rectifying diodes here will protect the sensing unit as well as PV panels from each other's discharge currents [4, 36]. A microcontroller-free solar PV tracker can also be built with the help of differential amplifier, comparator, and reference PV panels besides the main PV panel [37].

10 Conclusion

This paper discussed the implementation, design, and construction of light-dependent resistor (LDR) sensor-based photovoltaic solar tracker. From the study of different types of photovoltaic solar trackers, one thing is very clear that a dual-axis PV tracker has got an edge over the conventional single-axis PV. To increase the output power even more, a DSP can be used to implement a tracking algorithm. This tracking algorithm will ensure that maximum efficiency is achieved in all types of conditions. Since LDR sensor isn't an end-all be all device, so alternatives such as photodiodes, OPAMP-based opto-sensors were also reviewed in this paper. Fuzzy logic controllers can be employed along with image processing techniques to get the most of photovoltaic trackers in commercial setup so as to justify the huge installation cost.

References

1. Jovanovic, V.M., Ayala, O., Seek, M., Marsillac, S.: Single axis solar tracker actuator location analysis. SoutheastCon 2016, Norfolk, Virginia, pp. 1–5 (2016)

2. Khare Saxena, A., Saxena, S., Sudhakar, K.: Solar energy policy of India: an overview. In: CSEE J. Power Energy Syst. (2020)
3. Masih, A., Odinaev, I.: Performance comparison of dual axis solar tracker with static solar system in Ural region of Russia. In: Ural Symposium on Biomedical Engineering, Radio electronics and Information Technology (USBREIT), Yekaterinburg, Russia, pp. 375–378 (2019)
4. Kumar, S., Kumar Pal, A., Singh, P., Mittal, S., Kumar, Y.: Solar probe based autonomous solar tracker system—a review. In: International Conference on Advance Computing and Innovative Technologies in Engineering (ICACITE), Greater Noida, India, pp. 589–594 (2021)
5. Mehdi, G., Ali, N., Hussain, S., Zaidi, A.A., Hussain Shah, A., Azeem, M.M.: Design and fabrication of automatic single axis solar tracker for solar panel. In: 2nd International Conference on Computing, Mathematics and Engineering Technologies (iCoMET), Sukkur, Pakistan, pp. 1–4 (2019)
6. Allamehzadeh, H.: Solar energy overview and maximizing power output of a solar array using sun trackers. In: IEEE Conference on Technologies for Sustainability (SusTech), Phoenix, USA, pp. 14–19 (2016)
7. Argatu, F., Tarcau, F., Argatu, V., Grigorescu, S., Enache, B., Constantinescu, L.: Building and designing a dual axis solar tracker for educational purposes. In: 11th International Conference on Electronics, Computers and Artificial Intelligence (ECAI), Pitesti, Romania, pp. 1–4 (2019)
8. Kulkarni, A., Kshirsagar, T., Laturia, A., Ghare, P.H.: An intelligent solar tracker for photovoltaic panels. Texas Instruments India Educators' Conference, Bangalore, India, pp. 390–393 (2013)
9. Moradi, H., Abtahi, A., Messenger, R.: Annual performance comparison between tracking and fixed photovoltaic arrays. IEEE 43rd Photovoltaic Specialists Conference (PVSC), pp. 3179–3183. Portland, USA (2016)
10. Whavale, S., Dhavalikar, M.: A review of adaptive solar tracking for performance enhancement of solar power plant. In: International Conference on Smart City and Emerging Technology, Mumbai, India, pp. 1–8 (2018)
11. Zhengxi, L., et al.: The control method and design of photovoltaic tracking system. In: Sixth International Conference on Intelligent Systems Design and Engineering Applications (ISDEA), Guiyang, China, pp. 838–841 (2015)
12. Rani, P., Singh, O., Pandey, S.: An analysis on Arduino based single axis solar tracker. In: 5th IEEE Uttar Pradesh Section International Conference on Electrical, Electronics and Computer Engineering, Gorakhpur, India, pp. 1–5 (2018)
13. Gutiérrez, S.: Prototype for an off-grid photovoltaic system with low cost solar tracking. In: IEEE Mexican Humanitarian Technology Conference (MHTC), Puebla, Mexico, pp. 7–11 (2017)
14. Pratama, A.Y., Fauzy, A., Effendi, H.: Performance enhancement of solar panel using dual axis solar tracker. In: International Conference on Electrical Engineering and Informatics (ICEEI), Bandung, Indonesia, pp. 444–447 (2019)
15. Wang, H., Li, Z., Luo, J., Xie, S., Li, H.: Design and implementation of a dual-axis sun-tracking system based on microcontroller. In: International Conference on Information Technology and Applications, Chengdu, China, pp. 384–387 (2013)
16. Rosma, I.H., Asmawi, J., Darmawan, S., Anand, B., Ali, N.D., Anto, B.: The implementation and analysis of dual axis sun tracker system to increase energy gain of solar photovoltaic. In: 2018 2nd International Conference on Electrical Engineering and Informatics (ICon EEI), Batam, Indonesia, pp. 187–190 (2018)
17. Sahu, P., Maurya, N.S., Sahu, S.: Automatic sun tracking for the enhancement of efficiency of solar energy system. International Conference and Utility Exhibition on Green Energy for Sustainable Development (ICUE), pp. 1–4. Phuket, Thailand (2018)
18. Neacă, M.I.: Solar tracking system for several groups of solar panels. In: 2021 International Conference on Applied and Theoretical Electricity (ICATE), pp. 1–4 (2021)
19. Mourad, A.-H.I., Shareef, H., Ameen, N., Alhammadi, A.H., Iratni, M., Alkaabi, A.S.: A state-of-the-art review: solar trackers. *Adv. Sci. Eng. Technol. Int. Conf. (ASET)* **2022**, 1–5 (2022)

20. Sawant, A., Bondre, D., Joshi, A., Tambavekar, P., Deshmukh, A.: Design and analysis of automated dual axis solar tracker based on light sensors. In: 2nd International Conference on I-SMAC (IoT in Social, Mobile, Analytics and Cloud) (I-SMAC)I-SMAC (IoT in Social, Mobile, Analytics and Cloud) (I-SMAC), 2018 2nd International Conference on, Palladam, India, pp. 454–459 (2018)
21. Nwyanwu, C.J., Dioha, M.O., Sholanke, O.S.: Design, construction and test of a solar tracking system using photo sensor. In: *Int. J. Eng. Res. Technol. (IJERT)* (2017)
22. El Hammoumi, A., Motahhir, S., El Ghzizal, A., Chalh, A., Derouich, A.: A simple and low-cost active dual-axis solar tracker. *Research article* (2018)
23. Rosma, I.H., Putra, I.M., Sukma, D.Y., Safrianti, E., Zakri, A.A., Abdulkarim, A.: Analysis of single axis sun tracker system to increase solar photovoltaic energy production in the tropics. In: 2nd International Conference on Electrical Engineering and Informatics (ICon EEI), Batam, Indonesia, pp. 183–186 (2018)
24. Huynh, D.C., Nguyen, T.M., Dunnigan, M.W., Mueller, M.A.: Comparison between open- and closed-loop trackers of a solar photovoltaic system. In: *IEEE Conference on Clean Energy and Technology (CEAT)*, Langkawi, Malaysia, pp. 128–133 (2013)
25. Hawibowo, S., Ala, I., Citra Lestari, R.B., Saputri, F.R.: Stepper motor driven solar tracker system for solar panel. In: 4th International Conference on Science and Technology (ICST), Yogyakarta, Indonesia, pp. 1–4 (2018)
26. Masih, A., Safaraliev, M., Mukhmudov, K., Odinaev, I., Ghoziev, B., Toshtemurov, A.: Application of dual axis solar tracking system in Qurghontepa, Tajikistan. In: *IEEE 7th International Conference on Smart Energy Grid Engineering (SEGE)*, Oshawa, Canada, pp. 250–254 (2019)
27. Makhija, S., Khatwani, A., Khan, M.F., Goel, V., Roja, M.M.: Design and implementation of an automated dual-axis solar tracker with data-logging. In: *International Conference on Inventive Systems and Control (ICISC)*, Coimbatore, India, pp. 1–4 (2017)
28. Budiyanto, A., Fardani, M.I.M.: Prototyping of 2 axes solar tracker system for solar panel power optimization. In: *International Symposium on Electronics and Smart Devices (ISESD)*, Bandung, Indonesia, pp. 1–4 (2018)
29. Eke, R., Sentürk, A.: Performance comparison of a double-axis sun tracking versus fixed PV system. *Research Paper* (2012)
30. Beily, M.D.E., Sinaga, R., Syarif, Z., Pae, M.G., Rochani, R.: Design and construction of a low cost of solar tracker two degree of freedom (DOF) based on Arduino. In: *International Conference on Applied Science and Technology (iCAST)*, Padang, Indonesia, pp. 384–388 (2020)
31. Afrin, F., Titirsha, T., Sanjidah, S., Siddique, A.R.M., Rabbani, A.: Installing dual axis solar tracker on rooftop to meet the soaring demand of energy for developing countries. *Annual IEEE India Conference (INDICON)*, pp. 1–5. Mumbai, India (2013)
32. Azizi, K., Ghaffari, A.: Design and manufacturing of a high-precision sun tracking system based on image processing. *Int. J. Photoenergy* (2013)
33. Plachta, K.: Autonomous tracking controller for photovoltaic systems using global positioning system. In: *IEEE International Conference on Environment and Electrical Engineering and 2018 IEEE Industrial and Commercial Power Systems Europe (EEEIC/I&CPS Europe)*, Palermo, Italy, pp. 1–5 (2018)
34. Mustafa, G.E.G., Sidahmed, B.A.M., Nawari, M.O.: The improvement of LDR based solar tracker's action using machine learning. In: *IEEE Conference on Energy Conversion (CENCON)*, Yogyakarta, Indonesia, pp. 230–235 (2019)
35. del Rosario, J.R.B., Dadios, E.: Development of a fuzzy logic-based PV solar tracking system simulated using QT fuzzy engine. In: *International Conference on Humanoid, Nanotechnology, Information Technology, Communication and Control, Environment and Management (HNICEM)*, Palawan, Philippines, pp. 1–8 (2014)
36. Rana, M.S., Prodhan, R.S., Hasan, M.N.: Self powered automatic dual axis tracking and positioning system design. In: *IEEE Region 10 Symposium (TENSYP)*, pp. 166–169 (2020)
37. Mitra, D., Das, D., Brahma, D., Maiti, D., Mondal, T.: Sun Tracking solar panel without microcontroller. *International Conference on Opto-Electronics and Applied Optics (Optronix)* **2019**, 1–3 (2019)

Detection and Classification of Faults in VSC-HVDC System Based on Single End Ground and Pole Differential Current Components



Ravi Shankar Tiwari, Rahul Kumar, and Om Hari Gupta

1 Introduction

High voltage direct current transmission (HVDC) system is one of the best solutions for connection of unsynchronized power system or transmission of bulk power over large distances. Voltage source converter (VSC)-based HVDC system is used for the independent control of active and reactive power by pulse width modulated (PWM) technique. In VSC-based HVDC system, the bipolar structure with metallic return is preferred to meet the characteristics of reliability and operational flexibility [1]. In HVDC, transmission lines are more exposed to shunt faults. The presence of shunt capacitance on each terminal in VSC-HVDC leads high severity and level of fault. Faults occurring along the interconnection of DC cables are most likely to threaten system operation. The protection scheme of HVDC transmission line is more complex than conventional alternating current (AC) transmission. This is due to absence of zero crossing points in pole currents and less impedance of the line. The less overload capability of power electronics used in VSC-HVDC avoids the used of conventional relay [2]. Hence, the detection and isolation of fault are a crucial function for safe operation of transmission system. The positive pole-to-ground ($P-p-g$), negative pole-to-ground ($N-p-g$), and pole-to-pole ($p-p$) are the common faults may occur in the HVDC transmission system [3].

In the literatures, there are different schemes proposed to locate the fault in HVDC line. Roughly, these are classified based on the techniques to detect, classify, or locate

R. S. Tiwari (✉)
GLA University, Mathura, Uttar Pradesh 281406, India
e-mail: ravishankar.tiwari@glu.ac.in

R. Kumar · O. H. Gupta
National Institute of Technology Jamshedpur, Jamshedpur, Jharkhand 831014, India
e-mail: 2020pgeepe12@nitjsr.ac.in

O. H. Gupta
e-mail: omhari.ee@nitjsr.ac.in

faults such as over current, under voltage, current differential scheme, and virtual difference in voltage technique, wavelet transform, methods based on neuro-fuzzy system, natural frequency-based method, and artificial neural networks (ANN).

In rate of change of voltage (ROV) technique, the derivative of voltage at line side of current limiting reactor is measured to detect fault. However, this scheme cannot use without reactor [4]. In current differential technique, current at both the ends (i.e., rectifier and inverter end) of DC line is used to discriminate between internal and external fault. Here, the operating and restraining signals are used to distinguish between external and internal fault [5]. In case of virtual difference in voltage scheme, voltage at both the ends of DC line is calculated based on Bergeron formula, then it is compared with measured voltage at both terminal under internal and external fault [6]. The techniques of wavelet and Fourier transform used to extract the spectral components of a transient fault signal to detect and differentiate between internal and external faults. These are the powerful method of signal processing for tracking the fault transients for non-stationary signals. However, these methods require high sampling frequency [7]. In neuro-fuzzy system, Hilbert-Huang transform method is used to find the current signal during fault. The adaptive neuro-fuzzy interface system uses the current signal obtained from Hilbert-Huang transform for locating faults in HVDC lines [8]. In case of natural frequency-based method, single end transient current signal is used to detect external and internal fault. By using S-transform, the frequency component of AC side and DC side is extracted and compared with the magnitude of high frequency component of fault current in the DC line. Moreover, this scheme is not suitable for time varying transients [9]. Similarly, the ANN is a different form of machine learning technique which is reliable and provides fast control against line faults in HVDC transmission system [10]. Here, the line data of fault distance collected from both the ends and compared with actual fault distance. The Levenberg–Marquardt (LM) and Bayesian Regularization algorithms are used to calculate an absolute error to decide the fault location [11].

In this paper, a simplified protection schemes based on single end measurement with least requirement of communication channels are proposed. The scheme is based on pole and ground mode current measured at one terminal of a bipolar VSC-HVDC transmission system. The differential pole current evaluated by proposed algorithm detects the presence of internal faults. However, the ground mode current classifies the nature of faults. Section 2 covers the configuration of test system configuration. Sections 3 and 4 describe the proposed scheme and simulation results. Section 5 concluded the work.

2 System Configuration and Modeling

The configuration of VSC-HVDC test system is shown in Fig. 1 consists of two AC systems operating at 230 kV, 50 Hz, and 2000 MVA. The HVDC system interconnects two AC grids using overhead transmission line of length 150 km and two levels VSC at each end of transmission line. The operating voltage and power rating of HVDC

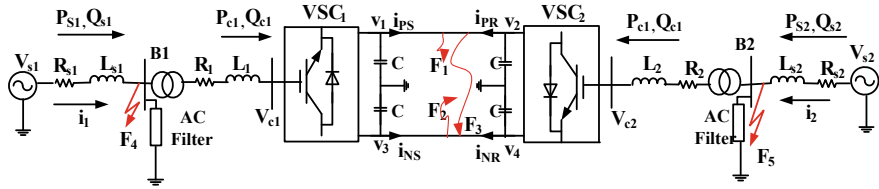


Fig. 1 VSC-HVDC transmission test system

system is ± 100 kV and 200 MVA, respectively. The VSC uses sinusoidal pulse width modulation (PWM) technique of switching frequency 50 times the fundamental for maintaining constant DC link voltage. The system consisting of converter transformer rated at 200 MVA, 230/100 kV, and reactance of 0.15 p.u. in λ -g/ Δ configuration. A 40 MVA AC filter and series converter reactance of 0.15 p.u. are connected on each converter stations.

The voltage and current dynamics during faults are used to model the test system during protection studies are shown in (1), (2), (3), and (4).

Here, (1) and (2) are the per phase dynamic difference in voltage between grid and converter terminal of rectifier and inverter side, respectively.

$$L \frac{di_{1\text{phase}}}{dt} + Ri_{1\text{phase}} = V_{s1\text{phase}} - V_{c1\text{phase}} \tag{1}$$

$$L \frac{di_{2\text{phase}}}{dt} + Ri_{2\text{phase}} = V_{s2\text{phase}} - V_{c2\text{phase}} \tag{2}$$

where L and R are the transfer inductance and resistance connected between AC grid and converter terminals on per phase i_j , V_{s1} , and V_{c1} are the grid terminal voltage on per phase, and converter terminal voltage on per phase, respectively. Similarly, parameters i_2 , V_{s2} , and V_{c2} are defined at inverter terminal.

The relationship between converter output voltage (U_{dc}) and the three phase AC system voltages (V_{abc}) is given by (3) for each end of the HVDC transmission system.

$$V_{abc} = \frac{mU_{dc}}{2} \begin{bmatrix} \sin(\omega t + \delta) \\ \sin(\omega t + \delta - \frac{2\pi}{3}) \\ \sin(\omega t + \delta + \frac{2\pi}{3}) \end{bmatrix} \tag{3}$$

where m denotes modulation index and δ is initial phase angle.

References [12, 13] indicate that the transient DC line current during faults depends on HVDC line parameters as shown in (4). The steady state current during internal line faults depends on the three phases, in the first phase DC link-capacitor discharges into the transmission line. Under such situations, the DC link-capacitor and transmission line parameters create a second order resistive, inductive, and

capacitive (R - L - C) circuit.

$$i_{dc} = I_0 e^{-\frac{R_c}{L_c} t} \quad (4)$$

where i_{dc} is cable current, I_0 is initial value of DC current, and R_c and L_c are cable resistance and inductance of HVDC line, respectively.

In the second phase of operation, the diode freewheels during which capacitor voltage falls below the grid voltage. In this case, voltage across DC link-capacitor drops to zero and IGBT switches should be blocked for protection. In the third phase of operation, the grid supplies the fault and the system reaches a steady state. Thus, the steady state grid side current and voltage are shown in (5) and (6):

$$i_{grid} = I_g \sin(\omega_s t + \theta - \phi) + I_0 e^{-\frac{R_c}{L_c} t} \quad (5)$$

$$e_{grid} = E_g \sin(\omega_s t + \theta) \quad (6)$$

where I_g , E_g , ω_s , and θ are the magnitude of grid current, phase voltage, angular frequency, and grid angle, respectively. However, ϕ is phase angle.

3 Protection Scheme and Proposed Algorithm

The proposed protection includes the detection and classifying the type of internal faults also using numeric or digital relays. The relay should be restrained with the occurrence of any external fault either on the rectifier or inverter side of the AC system.

Differential protection schemes are generally preferred for protection of transformer, generator, or motor instead of transmission lines. However, some authors have proposed the use of current differential protection based on measurement at the sending and receiving end of the transmission lines and wired or wireless communication channels. The reliability of such schemes is directly affected by the reliability of communication channels and the magnitude of differential current varies with line parameters and lengths due to the appearance of distributed capacitance during transients. Thus, the overall sensitivity reduces to avoid any mal-operation due to distributed capacitance by setting a higher value of threshold. However, fault detection and classification using the pole differential current at any one terminal and ground mode of current of the same terminal are a new protection scheme proposed in this section. The difference in current between the two poles of the test systems is calculated using the sampled current data of each pole as given in (7) and (8). The sampling frequency selected is in the order of 135 kHz, and the moving mean of the ground mode current with over the fundamental time period of 20 ms is used to classify the faults. Hence, the criterion for detection and classification of faults is given by (9) and (10), respectively. Figure 2 shows the flow chart for the proposed protection algorithm.

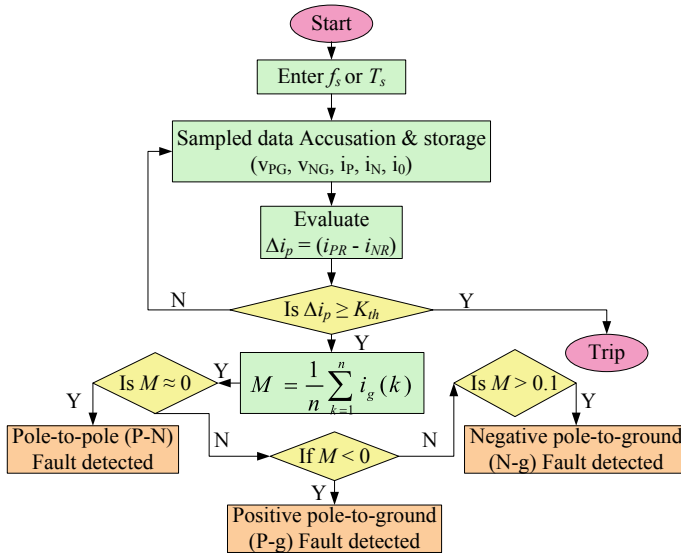


Fig. 2 Proposed fault detection and classification algorithm

A. Detection of Internal faults

The fault detections based on over current are a widely used technique popular for distribution networks or backup protection. The proposed scheme uses the criterion of pole differential over current in comparison with a suitably selected threshold value. The system is allowed to carry an overload current of 20%. The differential pole current on each terminals S and R are given by Δi_S and Δi_R , respectively, as given in (7) and (8) are

$$\Delta i_S(t) = [i_{PS}(t) - i_{NS}(t)] \tag{7}$$

$$\Delta i_R(t) = [i_{PR}(t) - i_{NR}(t)] \tag{8}$$

where $\Delta i_S(t)$ and $\Delta i_R(t)$ are the sending and receiving end instantaneous currents, reconstructed based sampled data obtained from both ends, respectively. As per the proposed scheme, an internal fault is detected in VSC-HVDC transmission system if it satisfies the criterion of (9)

$$|\Delta i_S(t)| \geq k_{th} \text{ or } |\Delta i_R(t)| \geq k_{th} \tag{9}$$

where k_{th} is the set value of threshold available in EPROM of numeric relay for comparison with the differential pole current. The value of threshold k_{th} is selected based on the line length and the minimum differential pole current exists during highest fault resistance of 300 Ω .

B. Classification Criterion

In order to classify the detected internal faults, the moving average of ground mode current in VSC-HVDC system is obtained by (10). The DC line faults in bipolar VSC-HVDC system are classified as pole-to-pole ($P-p$), positive pole-to-ground ($P-p-g$), and negative pole-to-ground ($N-p-g$) faults. Thus, the faults are classified based on the criterion given in (11).

$$M(t_d) = \frac{1}{n} \sum_{k=1}^n i_g(k) \quad (10)$$

where t_d is the instant at which fault is detected, k is the selected sample number, and n is the total number of samples available over a fundamental period of 20 ms. Here, $n = 2700$, for the sampling frequency of 135 kHz.

$$\text{if } \begin{cases} M(t_d) \approx 0 \rightarrow P - p \text{ fault} \\ M(t_d) = -\text{ve} \rightarrow P - p - g \text{ fault} \\ M(t_d) = +\text{ve} \rightarrow N - p - g \text{ fault} \end{cases} \quad (11)$$

In the criterion (11), zero, negative ($-ve$), and positive ($+ve$) magnitudes of $M(t_d)$ refers to the $p-p$, $P-p-g$, and $N-p-g$ faults, respectively.

4 Simulation Results

The test system of Fig. 1 is simulated in MATLAB/Simulink software to obtain the results of proposed protection scheme. Here, the various types of internal DC line fault are simulated at $t = 1.5$ s for a duration of 50 ms. The algorithm proposed the selection of a threshold current (k_{th}) setting at magnitude higher than twice the rated pole current (i.e., k_{th}). The proposed difference in pole current is compared with the k_{th} selected. It is assumed that the test system is working without protection in order to achieve the free response of the system.

The difference in pole current (Δi), DC line voltages (v_{PG} , v_{NG}), sliding average of ground mode current $M(t_d)$, and grid side voltages (v_{abcB1} , v_{abcB2}) are used to represent the simulation results during internal and external fault conditions.

Case I: Internal faults results

The result shown in Fig. 3 is obtained during $P-p-g$ faults at distance of 75 km from sending end. Where the moment Δi greater than threshold (k_{th}) indicates the instant of internal fault detected. However, for fault classification, the negative polarity of $M(t_d)$ shows the existence of $P-p-g$ fault. Figure 3b shows the effect of $P-p-g$ fault on DC voltage. It indicates that after fault detected, voltage across positive pole (V_{PG}) drops to zero while voltage across negative pole (V_{NG}) increases abruptly. Figure 3d shows the grid voltage at rectifier and inverter station overlapped with each other,

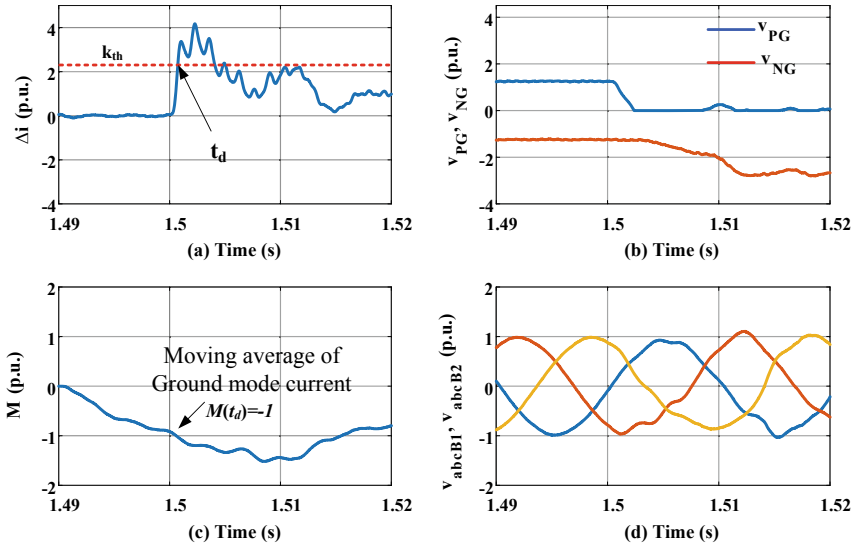


Fig. 3 *P-p-g* fault at the 50% of the line length at F_1

which supplies the grid current to the IGBT switches and transmission line with respect to the fault point.

Similarly, the results of Fig. 4 are obtained during *N-p-g* fault condition at 75 km with fault resistance of 1Ω , considered in each case I and II, respectively. The result of difference in pole current in Fig. 4a indicates that the detection of fault, while the moving average current of ground mode $M(t_d)$ classifies the fault as *N-p-g*, as per the proposed algorithm of Fig. 2 and (11).

Figure 4c shows that moving average of ground mode current is of positive polarity, which shows that the fault is *N-p-g*. In Fig. 4b, the effect of *N-p-g* fault on DC voltage shows that after DC line fault voltage across negative pole (V_{NG}) drops to zero. However, voltage across positive pole (V_{PG}) increases suddenly. Figure 4d shows the grid voltage at rectifier and inverter station overlapping each other. The grid voltage supplies the grid current to the IGBT switches and transmission line with respect to the fault point.

Finally, an internal *p-p* fault results are shown in Fig. 5. Where Fig. 5a shows that difference in pole current during fault. The current crosses the set threshold at instant 1.508 s, referred as fault detection time t_d . Figure 5c shows that $M(t_d)$ is at approximate zero in magnitude. The zero magnitude of $M(t_d)$ shows that the detected fault at time t_d is a type of *p-p* fault. Thus, the scheme classifies the faults instantaneously after fault detection. Figure 5b shows the effect of *p-p* fault on DC line voltage, after which the voltage across negative pole (V_{NG}) and positive pole (V_{PG}) drops to zero. Figure 5d shows the grid voltage at rectifier and inverter station simultaneously, which supplies the grid current via IGBT switches and to the transmission line with respect to the fault point.

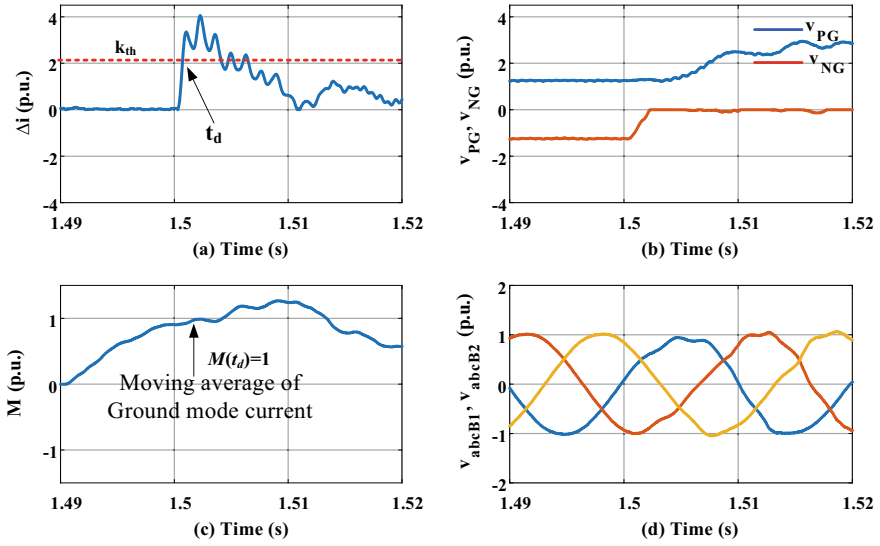


Fig. 4 N - p - g fault at the 50% of the line length at F_2

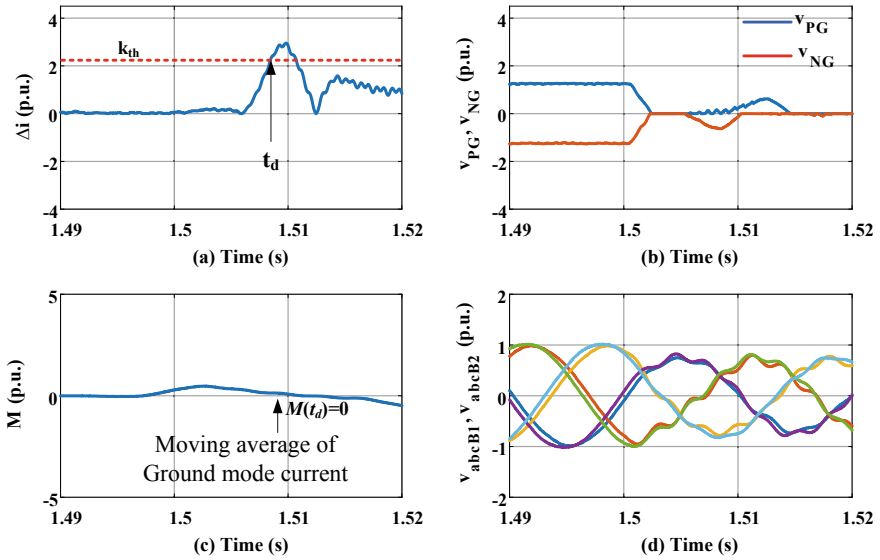


Fig. 5 p - p fault at the 50% of the line length at F_3 .

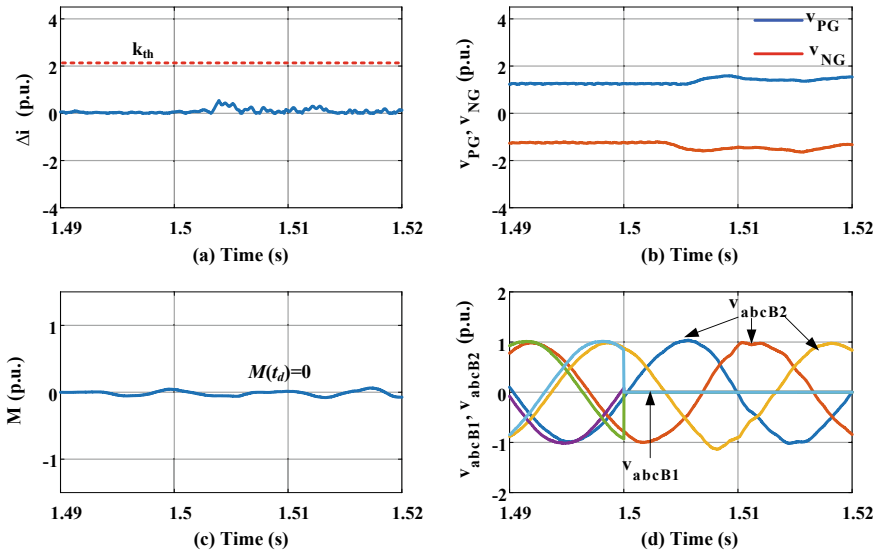


Fig. 6 External three phase shunt fault at location F_4

Case II: External fault results

The results in Fig. 6 are corresponding to external three phase shunt fault on the bus bar B1. Figure 6a shows that difference in pole current during external faults are unable to cross the set threshold by the proposed scheme.

However, the magnitude of $M(t_d)$ is irrelevant because of absence in any internal fault indication for the DC transmission line. Figure 6d simultaneously shows that grid voltage across rectifier station at bus bar B1 reaches to zero and of inverter station bus bar B2, remains sinusoidal. Figure 6b shows the effect of short circuit fault on voltage across positive and negative pole of HVDC line, which is hardly affected. The similar results are obtained for external faults (F_5) at bus bar B2, indicated in Fig. 7.

5 Conclusion

The work proposed a simplified scheme with less computation time, effort, memory storage, and non-complex algorithm for digital relaying of HVDC lines. The scheme included the fault detection and classification of type of fault with minimum possible time without communication delay. The scheme do not required any communication dedicated for measuring data exchange between the two stations of HVDC lines. A VSC-HVDC system of cable/line length 150 km used to implement using MATLAB/Simulink environment. The results indicate that proposed scheme is relevant for detecting and classifying faults with nominal fault resistance of 50 Ω . The

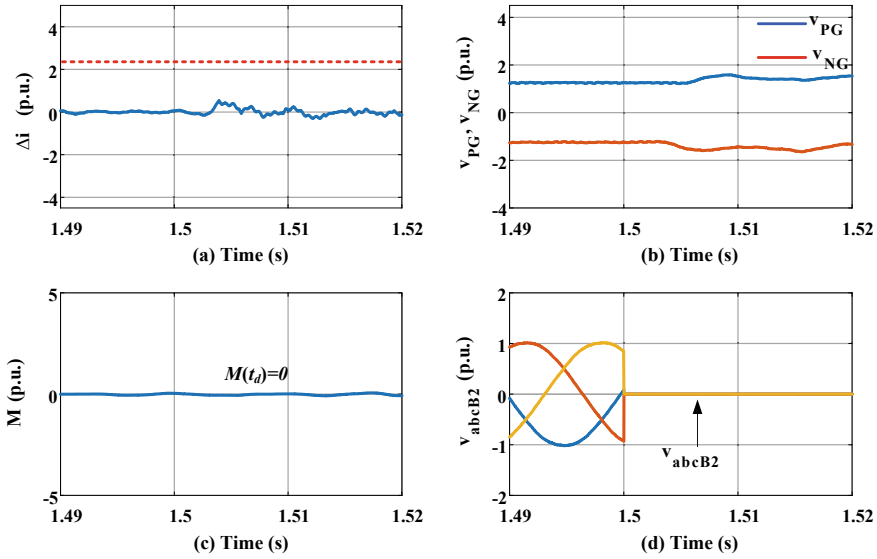


Fig. 7 External three phase shunt faults at location F_5

results indicated that the scheme having less detection time and classify the nature of fault instantaneously after detection. The proposed scheme is equally suitable for both line commutated converter (LCC) and VSC, HVDC systems with monopolar, bipolar, and multi-terminal HVDC configurations.

References

1. Bahrman, M.P.: Overview of HVDC transmission. In: 2006 IEEE PES Power System Conference on Expo. PSCE 2006—Proceedings, pp. 18–23 (2006). <https://doi.org/10.1109/PSCE.2006.296221>
2. Abdou, A.F., Abu-Siada, A., Pota, H.R.: Impact of VSC faults on dynamic performance and low voltage ride through of DFIG. *Int. J. Electr. Power Energy Syst.* **65**, 334–347 (2015). <https://doi.org/10.1016/j.ijepes.2014.10.014>
3. Rafferty, J., Morrow, D.J.: Analysis of VSC-Based HVDC System Under DC Faults, pp. 459–464 (2013)
4. Sneath, J., Rajapakse, A.D.: Fault detection and interruption in an earthed HVDC grid using ROCOV and hybrid DC breakers. *IEEE Trans. Power Deliv.* **31**(3), 973–981 (2016). <https://doi.org/10.1109/TPWRD.2014.2364547>
5. Jahn, I., Johannesson, N., Norrga, S.: Survey of methods for selective DC fault detection in MTDC grids. In: IET Conference Publication, vol. 2017, no. CP709 (2017). <https://doi.org/10.1049/CP.2017.0041>
6. Elgamasy, M.M., Taalab, A.M.I., Kawady, T.A., Izzularab, M.A., Elkalashy, N.I.: Virtual difference voltage scheme for fault detection in VSC-HVDC transmission systems. *J. Mod. Power Syst. Clean Energy* **8**(5), 991–1004 (2020). <https://doi.org/10.35833/MPCE.2019.000172>

7. Suonan, J., Zhang, J., Jiao, Z., Yang, L., Song, G.: Distance protection for HVDC transmission lines considering frequency-dependent parameters. *IEEE Trans. Power Deliv.* **28**(2), 723–732 (2013). <https://doi.org/10.1109/TPWRD.2012.2232312>
8. Rohani, R., Koochaki, A.: A hybrid method based on optimized neuro-fuzzy system and effective features for fault location in VSC-HVDC systems. *IEEE Access* **8**, 70861–70869 (2020). <https://doi.org/10.1109/ACCESS.2020.2986919>
9. Qu, H., et al.: Single-end transient current based protection method for VSC-HVDC cable. In: *Proceedings of 2020 IEEE 3rd International Conference on Information System and Computer Aided Education, ICISCAE 2020*, pp. 408–412. <https://doi.org/10.1109/ICISCAE51034.2020.9236816>
10. Sotirov, S.: A method of accelerating neural network learning. *Neural Process. Lett.* **22**(2), 163–169 (2005). <https://doi.org/10.1007/S11063-005-3094-9>
11. Sourashtriya, A., Tomar, M.: A comparative study for fault location detection in bipolar HVDC transmission systems using wavelet transform and artificial neural networks. In: *2021 3rd International Conference on Signal Processing and Communication, ICSPC 2021*, pp. 161–165 (2021). <https://doi.org/10.1109/ICSPC51351.2021.9451746>
12. Yang, J., Fletcher, J.E., O'Reilly, J.: Short-circuit and ground fault analyses and location in VSC-based DC network cables. *IEEE Trans. Ind. Electron.* **59**(10), 3827–3837 (2012). <https://doi.org/10.1109/TIE.2011.2162712>
13. Li, B., He, J., Li, Y., Li, B.: A review of the protection for the multi-terminal VSC-HVDC grid. *Prot. Control Mod. Power Syst.* **4**(1). <https://doi.org/10.1186/S41601-019-0136-2>
14. Dessouky, S.S., Fawzi, M., Ibrahim, H.A., Ibrahim, N.F.: DC pole to pole short circuit fault analysis in VSC-HVDC transmission system. In: *2018 20th International Middle East Power System Conference, MEPCON 2018—Proceedings*, pp. 900–904 (2019). <https://doi.org/10.1109/MEPCON.2018.8635237>

Investigation of Different Types of Bidirectional Charging Operations of Electric Vehicles



Sneha Mahobiya, Shailendra Kumar, and Suresh Kumar Gawre

1 Introduction

Future transportation is all about electric vehicles, time to time advancement is needed in all the factors related to electric vehicle like advancement of technology, change in the requirements of user, and radical new look at the future of transportation. There are basically 5 types of change which is required that is cost effective, convenient, clever, connected and clean [1]. The paper discusses the designing and modeling, the V2G micro-grid system utilizing fast charging by DC and describes the design of a fast charging station with off-board chargers that connects EVs to the micro-grid. Power is transferred between EVs and the grid using controls designed for power electronic interfaces. Besides control of frequency regulation and reactive power, the V2G system can perform numerous other functions like besides control of frequency regulation and reactive power. Future research should focus on the design of a supervisory controller that provides commands to the individual EV charger controllers [2]. Reference current provided by Active and Reactive power control (PQ) provides that are used to modulate the signal used by the PWM technique and pulses generated for the VSC [3] is used in this review work. Plug-in hybrid EVs (PHEVs) and plug-in EVs (PEVs) are designed to use this multipurpose power electronic interface (MPEI). This integrated multipurpose PEI (IMPEI) meets the new generation major requirements of EVs with its ability to serve multiple functions. PEV and PHEV of almost any kind can be used with IMPEI. The unit supports DC, three-phase, single-phase, and three-phase G2V, drive, and regenerative braking. The IMPEI is available in various configurations and modes including single-phase three-phase, G2V, V2G and PHEV, which incorporates a robust, compact and modifiable reduction of components and cascaded levels of interfaces enables a simplified design [4]. This paper reviews several control strategies for integrating electric vehicles

S. Mahobiya (✉) · S. Kumar · S. K. Gawre
Department of Electrical Engineering, MANIT, Bhopal, India
e-mail: sneha.maho@gmail.com

with the power grid as well as describing with respect to transmission and distribution levels, each has a distinct set of advantages and disadvantages. Akhade et al. [5] explains the differences between their transient stability. There are three new technologies being researched and reviewed for the connection between GEVs and the grid, namely V2H, V2V, and V2G Frameworks, modeling, power electronics, battery technology, optimization strategies, reactive power support, and information and communication technologies are among the methodologies, approaches, and perspectives of these emerging technologies in [6]. The costs of daily energy use were reduced by 57% and 12%, respectively, by V2H and V2G operations for buildings with EVs and solar panels. Energy is charged in the vehicles when it is inexpensive, and sent home when it is expensive IN [7]. A homeowner can use an electric vehicle (EV) as a backup energy source by charging it during off-peak times or by absorbing excess electricity generated by a home renewable energy system, like a wind or solar system. An energy storage device interaction, grid load rebalancing, peak trimming, and lowering the annual energy usage of Smart Buildings (SBs) is explained in [8]. We investigated how power levels are controlled in different scenarios based on the management strategies. A possible improvement might be to provide users with a means of discharging at their own discretion or to manage vehicles individually rather than sharing one profile between the group of users [9]. It also documents how a stable V2G–V2V system can be made possible by addressing both the technical and the engineering challenges that are involved, and how those challenges are solved by the authors [10]. Using EV as a bidirectional load, a new algorithm optimizes Grid/PV/EV hybrid systems within a Smart Building. Maximizing self-consumption and optimal charging of the electric vehicle are the goals of the project. By taking into account the percentage of the building's electrical consumption derived from the PV module in [11], one can calculate the self-consumption rate with consideration to MFGCI and PEV battery capacities, as well as the charging scheme of V2G applications, the configuration which is novel of SSS-MFGCI is applied to a V2G application [12] discusses shunt-connected mode for charging, shunt-connected mode for addressing shallow voltage problems, and series-connected mode for addressing deep voltage problems. Both modes depend on the situation of PEVs and grids, as well as the capacity of MFGCI. So bidirectional charging become an important topic for improving the power quality of the power grid based on the consideration of the performance of electric vehicles and the use of electric vehicles to serve the electric grid [13–21]. In Fig. 1 it is shown how G2V and V2G system actually works.

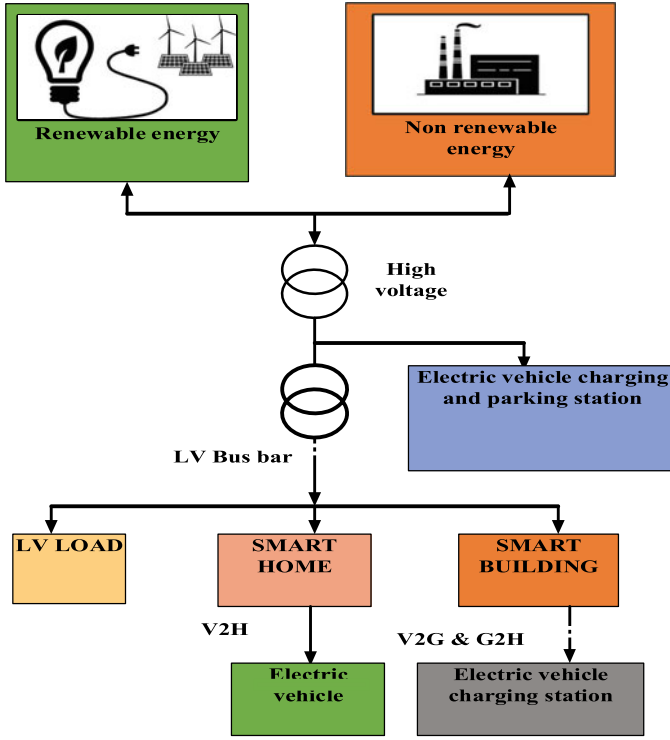


Fig. 1 V2G system frame-work

2 Different Vehicle-to-Grid Bidirectional Charging Methods

2.1 Bidirectional Charger with Vehicle-to-Grid, Grid-to-Vehicle, Vehicle-to-House Technologies

Full bridge AC/DC converter and reversible DC-DC, power converters connected through a dc link were used in this bidirectional charger as shown in Fig. 2. Two power converters are involved in this work: first one which connects to the grid, and another one which connects to the batteries.

As this work only focuses on validating the topology and the control algorithms, the prototype developed to support this work is intentionally oversized in all three experimental modes (V2G, G2V, and H2V) the results are consistent with expected results, which is evidence that the proposed network topology is viable. Future work will be focused on re-designing the power converters so that we can develop prototypes suitable for integration in an EV [22].

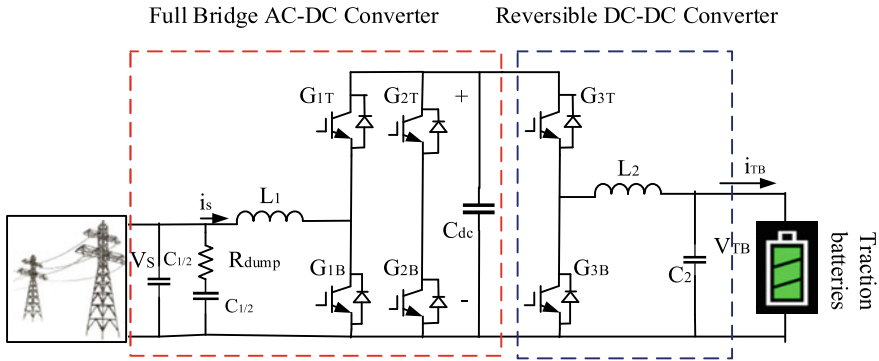


Fig. 2 Bidirectional battery charger made of two power converters: AC-DC full bridge bidirectional converter and DC-DC reversible converter

2.2 *Light Electric Vehicle (LEV) Onboard Charging (OBC) with an Improved Phase Shift Control*

A charging system of this type focuses mostly on e-rickshaws charging electric cars. A 1.1 KW to 500 W power range is taken for this charging method. The circuit made of a PV array connected to a boost converter and DC to DC converter, a DC link capacitor, and a low voltage circuit as visible in Fig. 3. Isolation between low voltage and high voltage sides is accomplished through the use of high frequency transformers for maximum battery utilization, LEV-OBC offers bidirectional power flow. It is possible to operate in two directions simultaneously using a two-stage topology, and to maintain the grid current parameters according to IEEE standards [23, 24].

2.3 *Multi-leg Variable Frequency Converter-Based EV Charging with Improve Adaptive Current Modulation Strategy*

As for high frequency converter legs, the proposed control strategy is more useful toward reducing the requirement for large passive components by controlling the frequency parameter variation G2V or V2G operation [13], using diverged distribution grid connections can be controlled more efficiently using adaptive sliding mode control (ASMC). Combined with the adaptive tracking law, sliding error minimization can add to the dynamic response during load charging while maintaining a unity power factor across distribution grids [25]. The topology of this charger is shown in Fig. 4.

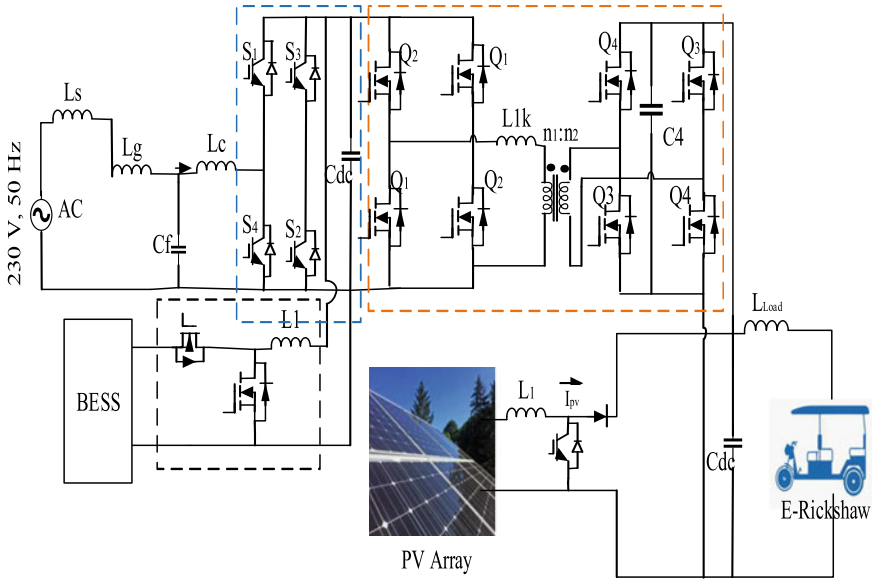


Fig. 3 Multi input isolated bidirectional charger

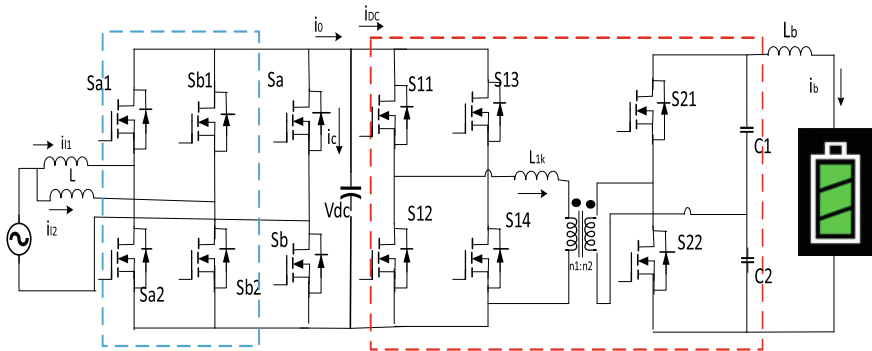


Fig. 4 Multi-leg inverter-based EV charger

2.4 Bidirectional Power Converter and Charger for V2G Capability of Reactive Power Compensation

There are two control converters on this battery charger as shown in Fig. 5. The batteries are controlled by one control converter, while the control organization is controlled by another control. Battery does not affect by the operation of reactive power operation on of the vehicle’s operating modes. PEVs with reactive power support the operation of smart grid applications can be demonstrated

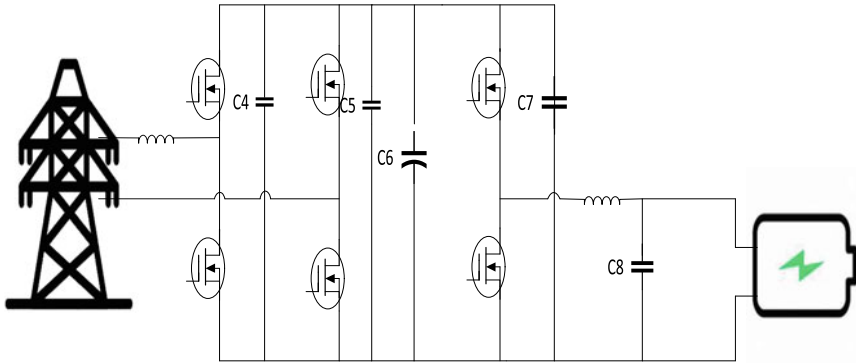


Fig. 5 Schematic of the bidirectional power converter (charger and grid connection)

successfully using the system controller which is unified and a 1.44 kVA charger design which is experimental [26].

2.5 Onboard Bidirectional Charger Using Interleaved ZETA Converter

Bi-ZETA converters are used to control the operations of charging and discharging of light electric vehicles. Bi-ZETA converters reduce the ripple of electric vehicle charging discharging current during G2V/V2G operations. The state-isolated topologies are shown in the diagram below. Onboard chargers of this type provide a 2 kW charging capacity and a 1 kW discharging capacity. The two stages are controlled by separate controllers. The DC link capacitor PQ and voltage can be regulated by the First Stage's controller according to its requirements Controlling overshoot, undershoot, and transient during a charge change is carried out by the controller of the bi-ZETA converter [27] (Fig. 6).

3 V2G, G2V Bidirectional Converter

3.1 System Configuration

A Bidirectional charging system is shown in the figure which get the supply of 415 V, 50 Hz from the grid. LCL filters consist of the inductors L1 and L2 and the capacitor C. Capacitor C which is the filter capacitor, has been included in the circuit topology of the L-type filter, so that the current output of high-frequency harmonic from the main converter circuit will be carried through the filter (Fig. 7).

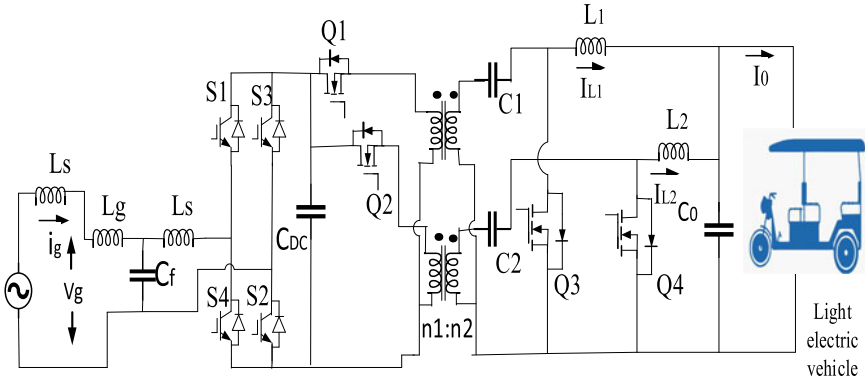


Fig. 6 Bidirectional charger with interleaved BI-ZETA converter

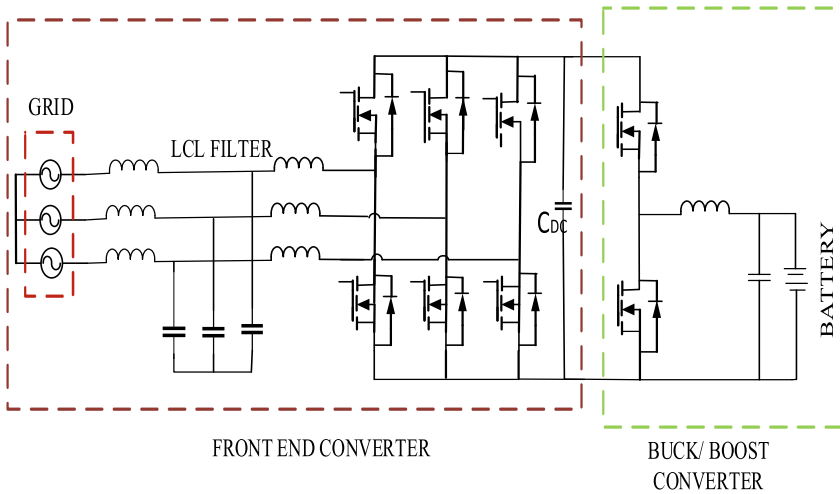


Fig. 7 Topology of system configuration of bidirectional charging system

Other than this front-end converter, which is connected to the LCL filter for the conversion of AC to DC, followed by the DC link capacitor, the high-frequency harmonic current can also travel through the filter. A back-end converter which is used for the charging and discharging of the battery is buck-boost converter.

3.2 Basic Operation

Figure 1 shows the topology of the charging station which is three-phase and the electric vehicles battery is charged by the converter for, two components are used

in the design—(a) three-level DC-DC buck-boost converters (b) three-level AC-DC bidirectional converters [28]. EV batteries are charged and discharged through the integration of these two components.

Front-end converter

Among the multiple applications of AC to DC, they include household electronic devices, battery charging, DC-drive applications, etc. The conversion of AC to DC is continually increasing AC to DC converters have traditionally used uncontrolled rectifiers and line-commutated rectifiers. As a result of the increased firing angle, these converters create low order harmonics in line current and suffer from a decrease in power factor. High power applications will be best served by a three-phase converter using six switches including IGBTs and MOSFETs, the AC-DC converter functions as a rectifier or inverter which is depended on the operation of the six switches. Battery charging applications require the conversion of AC to DC output voltage, which is the rectifier mode. A V2G system uses an inverter which delivers the grid power. For domestic purposes, full bridge converters are generally used for single-phase battery charging applications.

Bidirectional Buck-boost converter

Battery energy is stored by bidirectional DC-DC conversion a wide range of efficient operations are needed for an EV based on the various driving conditions. Three-level DC-DC converters are capable of operating at a wide range of voltages and loads with high efficiency. With the switch (S_1, S_1^*, S_2, S_2^*) and passive elements (L, C) battery is charged during the buck mode, and for the boost mode battery is discharged [29].

3.3 Control Schemes

Front-end converter controller

Voltage regulation is performed by PI controllers by comparing the DC voltage to the reference voltage. Controlling of Front-end VSC controller is shown in the diagram where six pulses are generated and fed to the converter (Fig. 8).

Bidirectional Buck-Boost controller

Current regulation is performed by PI controllers by comparing reference battery current to the battery current. During battery charging mode the difference of both the current i_d fed to the PI controller then limiter, PWM pulses are generated by PWM generator and fed to the converter. During discharging mode difference of Inverter waveform of battery reference current and battery current is fed to the PI controller, then the limiter and the generated PWM pulses are fed to the converter (Fig. 9).

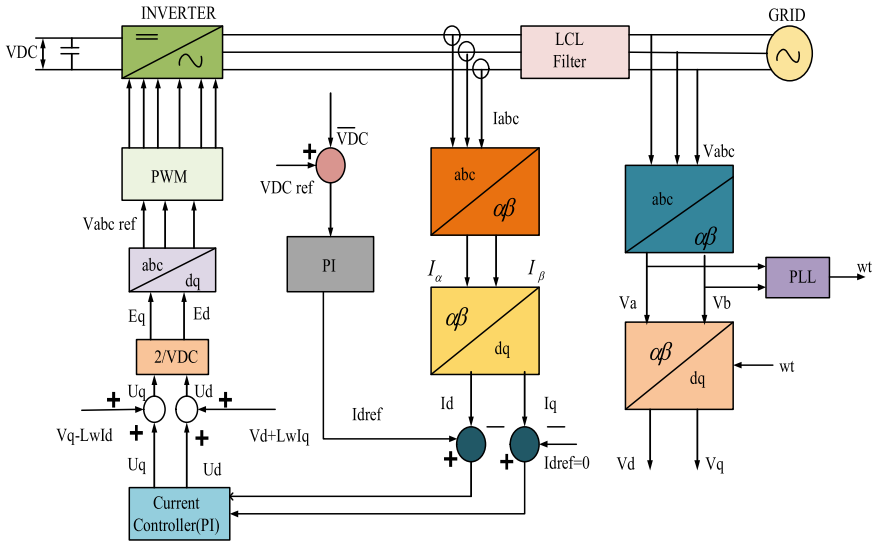


Fig. 8 VSC controller

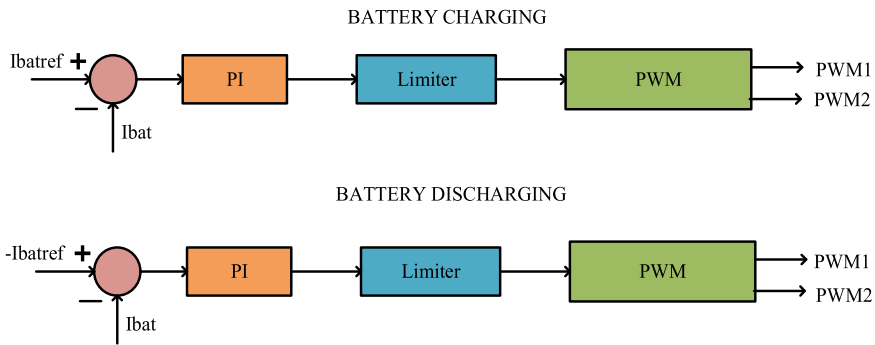


Fig. 9 Bidirectional BUCK-BOOST controller

4 Simulation and Results

Prototypes have been designed for the charging system simulation has been used to implement and verify the charging system (Table 1). Here Table 2 provides the charging station parameters and Table 3 provides specifications for batteries used in electric vehicles.

Table 1 Comparative study of different vehicle-to-grid bidirectional charging methods

S. No.	Method	Advantages	Disadvantages	Special feature of method
1	Bidirectional charger with vehicle-to-grid, grid-to-vehicle, vehicle-to-house technologies	In all the three operation modes the current is sinusoidal with unity power factor	Prototypes supporting this work are oversized	Onboard bidirectional battery charging (EVs) targeting grid-to-vehicle (G2V), vehicle-to-grid (V2G), and vehicle-to-home (V2H) technologies
2	Light electric vehicle (LEV) onboard charging (OBC) with an improved phase shift control	Regulates the power quality within the IEC 61000-3-2 standard	A spike in current occurs when switching modes from discharging to standalone mode for a short time	Improved phase shift control
3	Multi-leg variable frequency converter-based EV charging with improve adaptive current modulation strategy	Reduced switching loss and a significant decrease in passive filter components	Phase-reversal in the presence of grid distortion often adds complexity to achieve zero voltage switching	Adaptive control implantation to take care of the parameter drifts with undesired noise addition
4	Bidirectional power converter and charger for V2G capability of reactive power compensation	Battery does not affect by the operation of reactive power operation on of the vehicle's operating modes	17th harmonic which is only slightly higher than the acceptable limit	Reactive power compensation
5	Onboard bidirectional charger using interleaved ZETA converter	The BI-ZETA converter minimizes ripples from charging or discharging currents because of its interleaving design	Voltage sag and swell are not completely eliminated	The controller is designed so that it controls the charging behavior of the onboard charger (OBC) during transient phases

Table 2 Parameters of EV charging system

S. No.	EV charging station parameters	Rating
1	Supply voltage	415 V
2	System frequency	50 Hz
3	LCL filter specification	5 Mh, 30 μ F
4	Load RC	0.0001 Ω , 0.625 $\times 10^{-6}$ F
5	Load inductance	20 mH

Table 3 Battery parameters of EV

S. No.	Specifications for lithium-ion batteries for electric vehicles	Ratings
1	Battery of Li-ion voltage	360 V
2	Battery of Li-ion capacity	300 Ah

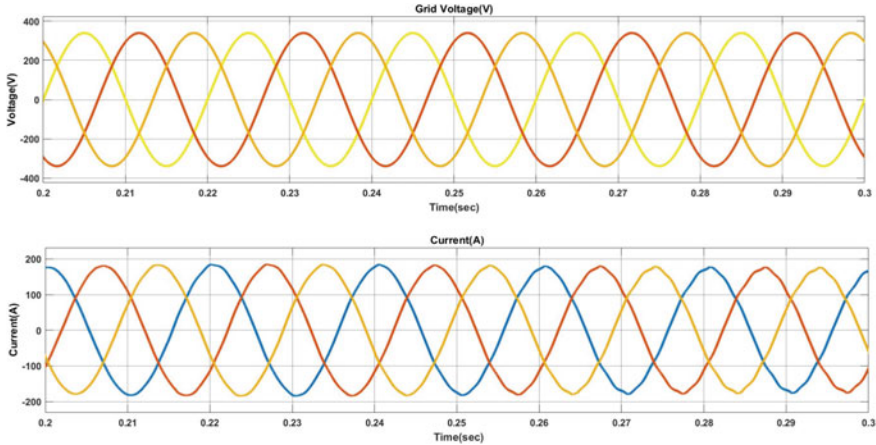


Fig. 10 Grid voltage and current during V2G operation

4.1 Vehicle-to-Grid Operation

The simulation results of grid voltage, grid current and the battery parameters like battery voltage, battery current and SoC during V2G operation are given in Figs. 10 and 11, respectively.

DC link voltage is taken to be 800 V for the reference and the waveform of DC link voltage is shown in Fig. 12.

4.2 Grid-to-Vehicle Operation

The simulation results of grid voltage, grid current and the battery parameters like battery voltage, battery current and SoC during G2V operation are given in Figs. 13 and 14, respectively.

As SoC is increasing the battery is charging during the G2V operation and battery current is also negative because of charging operation as shown in Fig. 14.

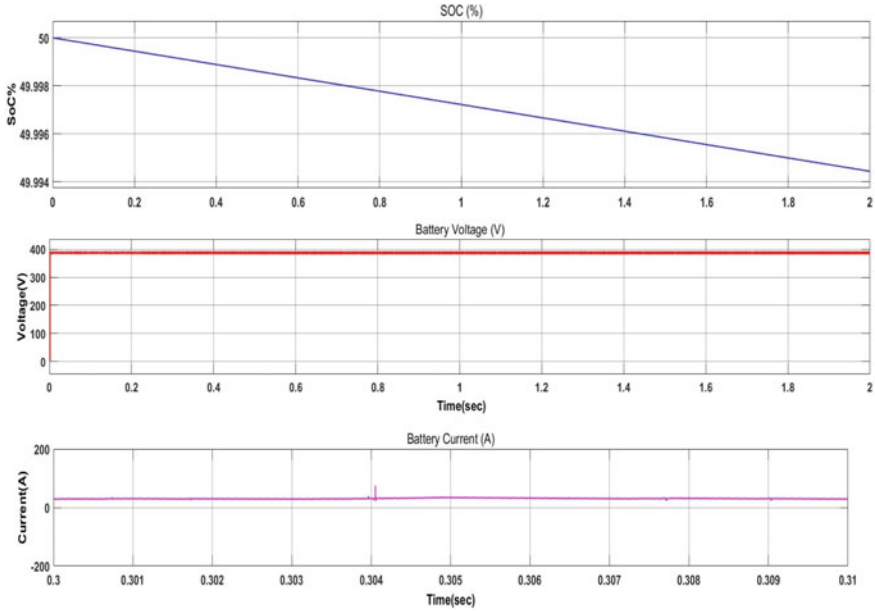


Fig. 11 Battery parameters during discharging

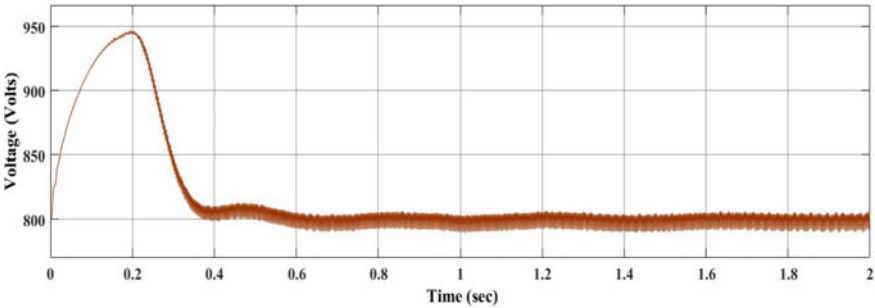


Fig. 12 DC link voltage

5 Conclusion

A review of different types of bidirectional charging topology is done in this work and both bidirectional AC/DC and three-level DC/DC converters are used to characterize chargers. The charging of electrical vehicles has been achieved using a bidirectional AC to DC converter with MOSFETs. It is possible to switch power with PWM in both the rectifier and inverter modes. Approximately 800 V are applied to the DC link and can be controlled in both directions. Charge is provided by a three-level DC to DC converter in Buck mode, which is the indication of rapid battery charging during

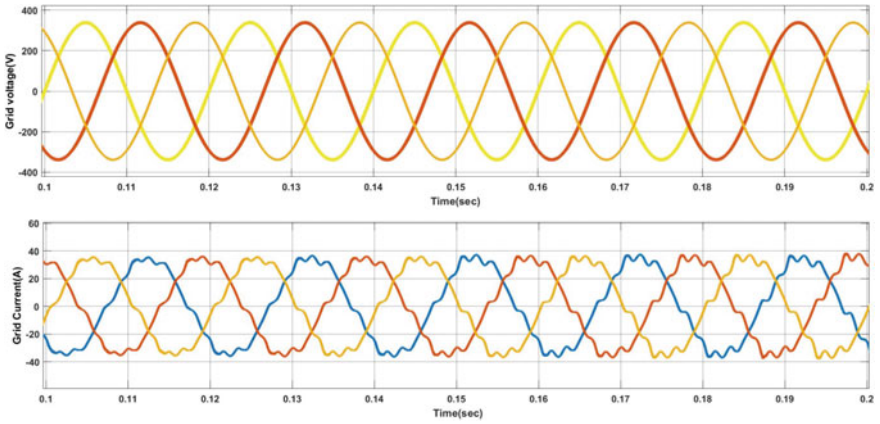


Fig. 13 Grid voltage and current during G2V Operation

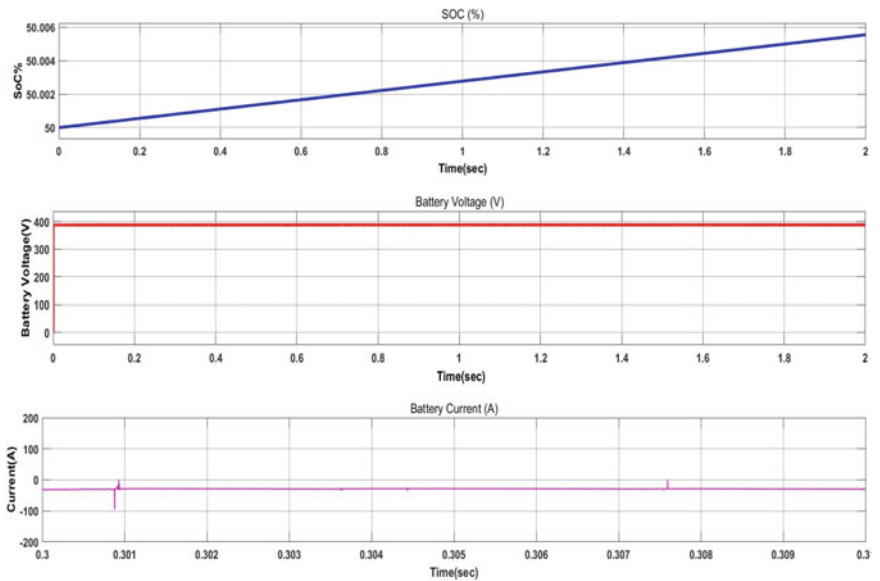


Fig. 14 Battery parameters during G2V operations

G2V operation. In this review work simulated results are discussed and presented and the DC link voltage for charging the vehicle battery is estimated by estimating its interface voltage to the bidirectional power.

References

1. Maini, C., Gopal, K., Prakash, R.: Making of an “all reason” electric vehicle. In: 2013 World Electric Vehicle Symposium and Exhibition, EVS 2014, pp. 20–23. <https://doi.org/10.1109/EVS.2013.6915015>
2. Shakeel, F.M., Malik, O.P.: Vehicle-to-grid technology in a micro-grid using DC fast charging architecture. In: 2019 IEEE Canadian Conference of Electrical and Computer Engineering, CCECE 2019 (2019). <https://doi.org/10.1109/CCECE.2019.8861592>
3. Zafar, S., Amin, M.A., Javaid, B., Khalid, H.A.: On design of DC-link voltage controller and PQ controller for grid connected VSC for microgrid application. In: 4th International Conference on Power Generation Systems and Renewable Energy Technologies, PGSRET 2018, 10–12 September 2019. <https://doi.org/10.1109/PGSRET.2018.8686010>
4. Payarou, T., Pillay, P.: A novel multipurpose V2G G2V power electronics interface for electric vehicles. In: ECCE 2020—IEEE Energy Conversion Congress and Exposition, 4097–4103 (2020). <https://doi.org/10.1109/ECCE44975.2020.9235944>
5. Akhade, P., Moghaddami, M., Moghadasi, A., Sarwat, A.: A review on control strategies for integration of electric vehicles with power systems. In: Proceedings of the IEEE Power Engineering Society Transmission and Distribution Conference, 2018-April (2018). <https://doi.org/10.1109/TDC.2018.8440139>
6. Liu, C., Chau, K.T., Wu, D., Gao, S.: Opportunities and challenges of vehicle-to-home. *Vehicle-to-Grid Technol.* **101**(11), 2409–2427 (2013)
7. Hemmati, R., Mehrjerdi, H., Al-Emadi, N.A., Rakhshani, E.: Mutual vehicle-to-home and vehicle-to-grid operation considering solar-load uncertainty. In: 2nd International Conference on Smart Grid and Renewable Energy, SGRE 2019—Proceedings, pp. 22–25 (2019). <https://doi.org/10.1109/SGRE46976.2019.9020685>
8. Sami, I., Ullah, Z., Salman, K., Hussain, I., Ali, S.M., Khan, B., et al.: A bidirectional interactive electric vehicles operation mode: vehicle-to-grid (V2G) and grid-to-vehicle (G2V) variations within smart grid. In: 2019 International Conference on Engineering and Emerging Technologies, ICEET 2019 (2019). <https://doi.org/10.1109/CEET1.2019.8711822>
9. Chtioui, H., Boukettaya, G.: Vehicle-to-grid management strategy for smart grid power regulation. In: 6th IEEE International Energy Conference, ENERGYCon 2020, pp. 988–993 (2020). <https://doi.org/10.1109/ENERGYCon48941.2020.9236530>
10. Masrur, M.A., Skowronska, A.G., Hancock, J., Kolhoff, S.W., McGrew, D.Z., Vandiver, J.C., Gatherer, J.: Military-based vehicle-to-grid and architecture and implementation. *Ieee Trans. Transp. Electrification* **4**(1), 157–171 (2018)
11. Turker, H., Colak, I.: Multiobjective optimization of grid-photovoltaic-electric vehicle hybrid system in smart building with vehicle-to-grid (V2G) concept. In: 7th International IEEE Conference on Renewable Energy Research and Applications, ICRERA 2018, vol. 5, pp. 1477–1482 (2018). <https://doi.org/10.1109/ICRERA.2018.8567002>
12. Choi, W., Lee, W., Han, D., Sarlioglu, B.: Shunt-series-switched multi-functional grid-connected inverter for voltage regulation in vehicle-to-grid application. In: 2018 IEEE Transportation and Electrification Conference and Expo, ITEC 2018, pp. 668–674 (2018). <https://doi.org/10.1109/ITEC.2018.8450249>
13. Sharma, U., Singh, B.: A generalised double integral sliding mode control for bidirectional charger of light electric vehicle. In: Proceedings—2019 IEEE International Conference on Environment and Electrical Engineering and 2019 IEEE Industrial and Commercial Power Systems Europe, IEEEIC/I and CPS Europe 2019 (2019). <https://doi.org/10.1109/IEEEIC.2019.8783407>
14. Jin, Z., Song, S., Fang, X., Ke, G., Xu, D., Jin, M.: Research on intelligent control model of V2G bidirectional charger considering electricity price constraint. In: 2021 IEEE 2nd International Conference on Big Data, Artificial Intelligence and Internet of Things Engineering, ICBAIE 2021, Icaiba, pp. 718–721 (2021). <https://doi.org/10.1109/ICBAIE52039.2021.9390037>

15. Urcan, D.C., Bica, D.: Integrating and modeling the vehicle to grid concept in micro-grids. In: Proceedings of 2019 International Conference on Energy and Environment, CIEM 2019, pp. 299–303 (2019). <https://doi.org/10.1109/CIEM46456.2019.8937610>
16. Chen, J., Zhang, Y., Su, W.: An anonymous authentication scheme for plug-in electric vehicles joining to charging/discharging station in vehicle-to-grid (V2G) networks. *China Commun.* **12**(3), 9–19 (2015). <https://doi.org/10.1109/CC.2015.7084359>
17. Amamma, S.A., Marco, J.: Vehicle-to-grid aggregator to support power grid and reduce electric vehicle charging cost. *IEEE Access* **7**, 178528–178538 (2019). <https://doi.org/10.1109/ACC.2019.2958664>
18. Das, S., Acharjee, P., Bhattacharya, A.: Charging scheduling of electric vehicle incorporating grid-to-vehicle (G2V) and vehicle-to-grid (V2G) technology in smart-grid. In: 2020 IEEE International Conference on Power Electronics, Smart Grid and Renewable Energy, PESGRE 2020, pp. 1–6 (2020). <https://doi.org/10.1109/PESGRE45664.2020.9070489>
19. Gautam, A., Verma, A.K., Srivastava, M.: A novel algorithm for scheduling of electric vehicle using adaptive load forecasting with vehicle-to-grid integration. In: 2019 8th International Conference on Power Systems: Transition towards Sustainable, Smart and Flexible Grids, ICPS 2019 (2019). <https://doi.org/10.1109/ICPS48983.2019.9067702>
20. Katić, V.A., Stanisavljević, A.M., Dumnić, B.P., Popadić, B.P.: Impact of V2G operation of electric vehicle chargers on distribution grid during voltage dips. In: EUROCON 2019—18th International Conference on Smart Technologies, pp. 2–7 (2019). <https://doi.org/10.1109/EUROCON.2019.8861904>
21. Das, B., Panigrahi, P.K., Samant, C.K.: Impact analysis of plug-in hybrid electric vehicle on integration with micro grid—a review. In: Proceedings—2020 IEEE International Symposium on Sustainable Energy, Signal Processing and Cyber Security, ISSSC 2020, pp. 20–24 (2020). <https://doi.org/10.1109/ISSSC50941.2020.9358824>
22. Pinto, J.G., Monteiro, V., Goncalves, H., Exposto, B., Pedrosa, D., Couto, C., Afonso, J.L.: Bidirectional battery charger with grid-to-vehicle, vehicle-to-grid and vehicle-to-home technologies. In: IECON Proceedings (Industrial Electronics Conference), pp. 5934–5939 (2013). <https://doi.org/10.1109/IECON.2013.6700108>
23. Sharma, U., Singh, B.: A bidirectional onboard charging system for E-Rickshaw using interleaved SEPIC converter. In: 2020 IEEE 17th India Council International Conference, INDICON 2020 (2020). <https://doi.org/10.1109/INDICON49873.2020.9342450>
24. Sharma, U., Singh, B.: Robust control algorithm for light electric vehicle onboard charging system. In: 2020 IEEE 7th Uttar Pradesh Section International Conference on Electrical, Electronics and Computer Engineering (UPCON), pp. 1–6 (2020). <https://doi.org/10.1109/UPCON50219.2020.9376413>
25. Mishra, D., Singh, B., Panigrahi, B.K.: Adaptive current control for a bi-directional interleaved EV charger with disturbance rejection. In: 2020 IEEE International Conference on Power Electronics, Smart Grid and Renewable Energy (PESGRE2020), pp. 1–6 (2020). <https://doi.org/10.1109/PESGRE45664.2020.9070488>
26. Kisacikoglu, M.C., Kesler, M., Tolbert, L.M.: Single-phase on-board bidirectional PEV charger for V2G reactive power operation. *IEEE Trans. Smart Grid* **6**(2), 767–775 (2015). <https://doi.org/10.1109/TSG.2014.2360685>
27. Sharma, U., Singh, B.: An onboard charger for light electric vehicles. In: 9th IEEE International Conference on Power Electronics, Drives and Energy Systems, PEDES 2020, (Dcc), pp. 2–7 (2020). <https://doi.org/10.1109/PEDES49360.2020.9379743>
28. Mehta, C.P., Balamurugan, P.: Buck-boost converter as power factor correction controller for plug-in electric vehicles and battery charging application. In: 2016 IEEE 6th International Conference on Power Systems, ICPS 2016 (2016). <https://doi.org/10.1109/ICPES.2016.7584111>
29. Zhou, L., Liu, Z., Ji, Y., Ma, D., Wang, J., Li, L.: A improved parameter design method of LCL APF interface filter. In: Proceedings of 2020 IEEE International Conference on Artificial Intelligence and Computer Applications, ICAICA 2020, pp. 948–952 (2020). <https://doi.org/10.1109/ICAICA50127.2020.9182457>

Intelligent Fault Location Scheme for HVDC System



Sunil Kumar Singh

1 Introduction

The alternating current (AC) system has been still predominantly applied for power transmission all over the world. However, for transmitting immense power over a longer distance, HVDC system has been preferred as it effectively mitigated major constraints of AC transmission system such as huge losses, charging current issue, and exigency of reactive power compensation. Apart from aforementioned merits, HVDC system also confers asynchronous connection of regional grids which is one of the major needs of present power network. In HVDC system, usually two topologies, i.e., current source converter (CSC) and voltage source converter (VSC), have been widely used. The CSC-based HVDC network is vulnerable toward AC side faults and in addition also requires substantial filter sets, whereas the VSC-based system is more sensitive toward DC faults and significant losses [1–6]. According to reliability statistics reported in [7], it is clear that a significant percentage of forced energy outages occur during fault events in HVDC system. Minimizing the outage time is vital both in terms of reliability and in terms of loss of revenues, since HVDC systems are used to transport large amount of power. Over the past few decades, multifarious articles have been reported for ascertaining the fault events in HVDC system. In [8], a voltage derivative and traveling wave-based protection methodology is explained for HVDC network. However, the efficacy of the reported approach is affected during distant fault events and higher impedance fault events. In [9], a mechanism based on estimation of the time difference between the two reflected waves is reported. But it may get affected in the presence of noise. In [10–12], traveling wave-based methodologies have been reported for ascertaining the fault events in HVDC system. However, reported approach is incompetent of ascertaining close in events, essentially need higher sampling frequency and easily affected by

S. K. Singh (✉)

Shri Ramswaroop Memorial University, Lucknow-Deva Road, Barabanki, Uttar Pradesh, India
e-mail: sksingh.rs.eee13@itbhu.ac.in

noise. In [13], a DWT-based differential relaying mechanism for HVDC network has been discussed. However, it essentially requires both end current measurement and the reported error is 2.992 km. Similarly, [14] also presented a both end current estimation-based methodology for ascertaining the faults in multi-terminal HVDC system. In [15], an intelligent relaying methodology has been reported for HVDC system based on ANN and fast Fourier transform (FFT). However, FFT usually suffers from resolution issues and the maximum error reported is 1.16%. In [16], an unsynchronized measurement-based algorithm has been reported for ascertaining the events in HVDC terminals.

This paper presents an ANN-based method for ascertaining the fault events in the HVDC system. The proposed intelligent computing-based fault ascertaining methodology utilizes the DWT decomposition for input feature selection. The acquired features have been applied as input to the designed intelligent network model, and it predicts the corresponding points of events in the HVDC transmission system as its output. Various events have been simulated in PSCAD test network for ratifying the proficiency of the presented approach. Test results reaffirmed the competency of the proposed methodology is ascertaining the events in HVDC system. The paper is organized as Sect. 2 describes the signal processing aspects. Section 3 presents the detailed of the proposed methodology. The test case simulation has been explained in Sect. 4. Section 5 demonstrates the results and discussion, and lastly, Sect. 6 summarizes the conclusion.

2 Signal Processing Methodology

The unprecedented research and advancement in the area of signal analysis makes it well effectual for examining the characteristics of transient events in the power system. Over the past few decades, multifarious transform mechanism has been effectively utilized for analyzing time-dependent signals. The DWT directly facilitates the exploration of localized characteristics of the transient signals. DWT has been peculiarly proposed for diagnosing the time changing signals with multiple smaller wave components. The DWT for signal $F(t)$ is defined as

$$\text{DWT}_{\psi_s(m,n)} = \int_{-\infty}^{\infty} F(t)\psi_{m,n}^*(t)dt \quad (1)$$

$$\psi_{m,n}(t) = \frac{1}{\sqrt{a_0^m}}\psi\left(\frac{t - nb_0a_0^m}{a_0^m}\right) \quad (2)$$

where a_0 and b_0 are constant; $m, n \in Z$ where Z is set of integers. In the proposed intelligent methodology, apart from multiple mother wavelets like db, Symlets, Morlet, etc., Daubechies (Db2) is opted as it has been positively reported in the literature

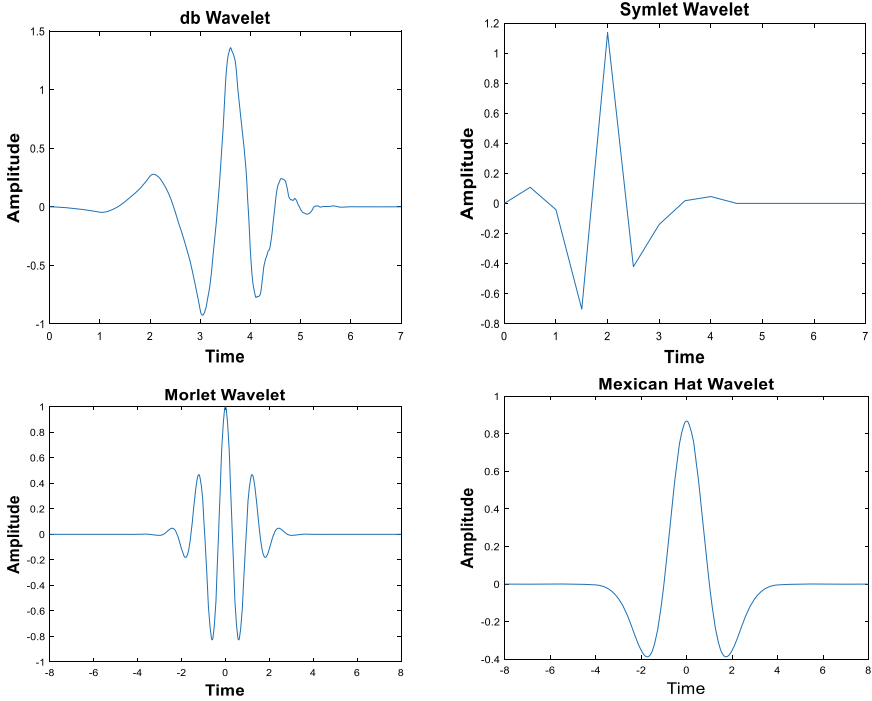


Fig. 1 Different mother wavelets

for examining fault transient signals [17–19]. Figure 1 shows the different available mother wavelets.

3 Proposed Methodology

The proposed fault locating intelligent approach for a HVDC system is demonstrated in Fig. 2 and is fundamentally based on acquiring the critical characteristics of fault signals. The current magnitude samples have been stored at the source side corresponding to multiples events in the simulated HVDC system. Hereinafter, acquired samples have been processed using DWT. Db2 wavelet has been used, and the decomposition count is fixed as six levels. Subsequently, the significant distinctive fault characteristics have been computed in terms of standard deviation (SD) of the 5th and 6th detailed coefficients. At last, the estimated feature samples have been fed to the designed intelligent event locator model and it predicts the distance of the events from relay location as its output.

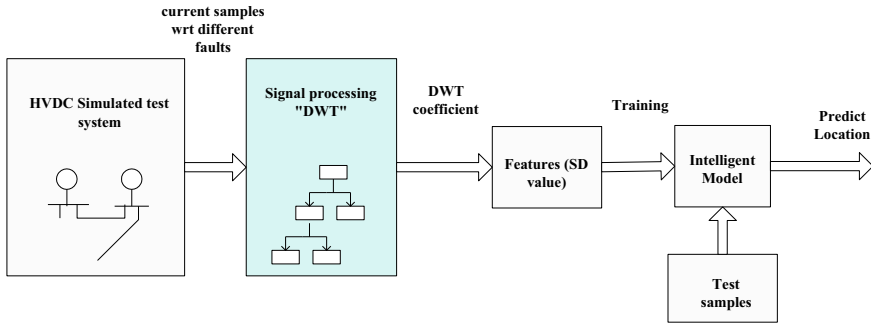


Fig. 2 Proposed mechanism

3.1 ANN-Based Model

ANN-based mathematical models are analogs to highly inter-communicated system which is induced by biological nervous architecture. The ANN algorithm incorporates three layers: input layer to which input vectors has been fed, hidden layer that signifies the core of the model and lastly output layer. Figure 3 depicts the ANN model structure.

The algorithm initiates with arbitrarily opted weights, and based on inputs, linkages hidden layer activation rate has been defined. Subsequently, output activation rate has been identified which depends on linkages in hidden and output nodes. Thereupon, error has been computed, and accordingly, weights have been redesigned till the convergence point obtained. In the proposed methodology, three different training mechanism: Levenberg–Marquardt (LM), Bayesian regularization (BR) and scaled conjugate gradient (SCG) have been used.

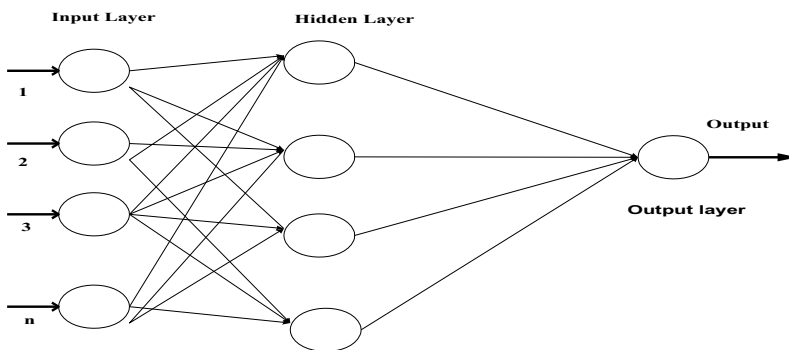


Fig. 3 ANN structure

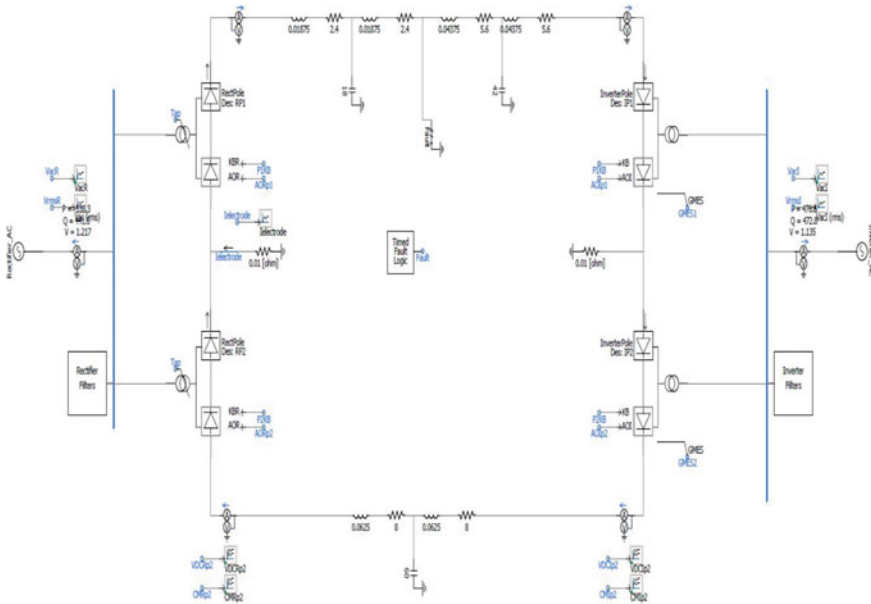


Fig. 4 Simulated HVDC test network

4 Simulated HVDC Test Network

For exploring the competency of the presented scheme, various test cases have been performed. A bipolar HVDC cable model is simulated in PSCAD 4.5 as shown in Fig. 4. The DC voltage is set as 213 kV, and it is designed to deliver 600 MW active power. The cable parameters are decided according to the article reported in [20]. When the fault data has been acquired, the total duration of time for which data was collected was 0.17 s. The LG fault has been initiated at 0.50 ms, and the data was collected between 0.48 to 0.65 s. The current samples have been acquired at the AC side for various fault events ranging from 1 to 199 km at intervals of 1 km, and the plot step was 250 us. The used sampling frequency is 4 kHz.

5 Test Results and Discussion

The realized features, i.e., the SD values of the 5th and 6th detailed coefficients corresponding to various fault sites in the simulated HVDC network have been applied to the designed intelligent ANN model. Eighty-five percentage of the realized dataset has been used for training, 10% is used for validation, and rest 5% has been applied as test dataset. The numbers of neurons on input, hidden, output is 2, 10 and 1, respectively. Figure 5 represents the applied ANN model.

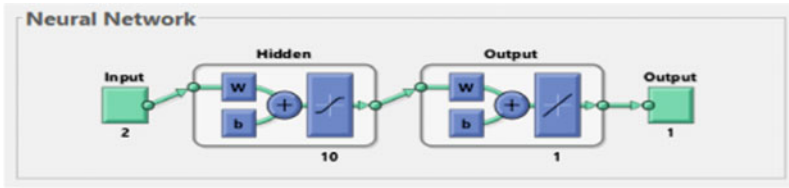


Fig. 5 Applied ANN model

Figure 6 represents regression plots for LM-based training approach; similarly, Fig. 7 represents regression plots for BR-based training and Fig. 8 represents regression plots for SCG-based training mechanism. It has been observed that the result of SCG is superior to LM and BR mechanisms. The SCG training mechanism endows the maximum accuracy level, i.e., 99.84% in ascertaining the point of fault events in the HVDC system. Table 1 represents the result of tracing of fault events in the HVDC network using proposed methodology. It reaffirms the well competency of proposed strategy. In addition, the accuracy level acquired by the proposed strategy is better than that reported in [13, 15].

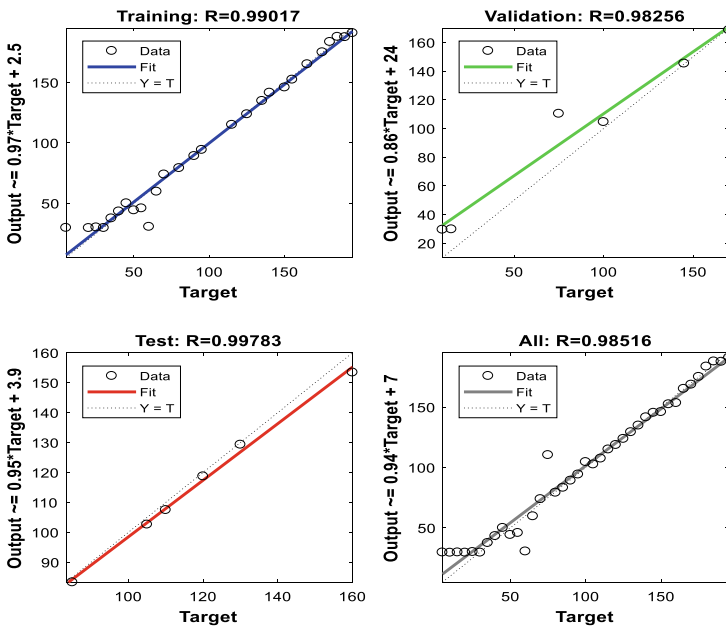


Fig. 6 Regression plots for LM

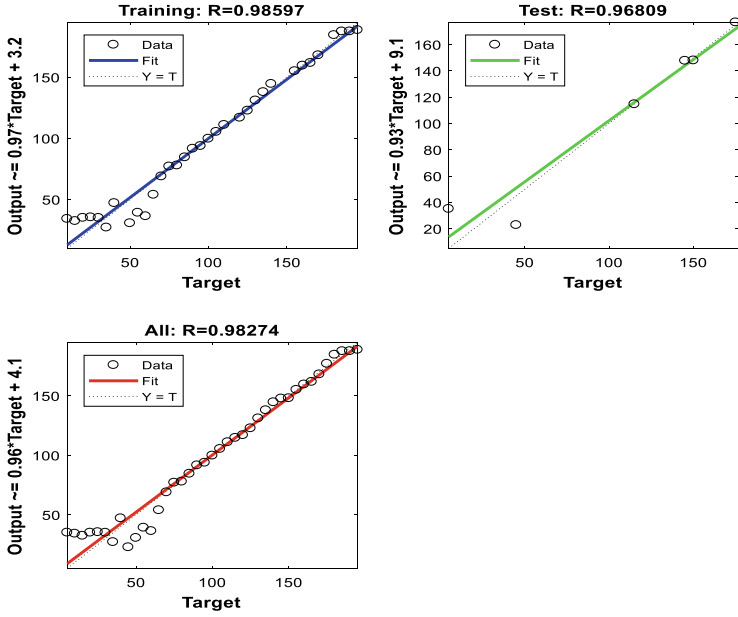


Fig. 7 Regression plot for BR

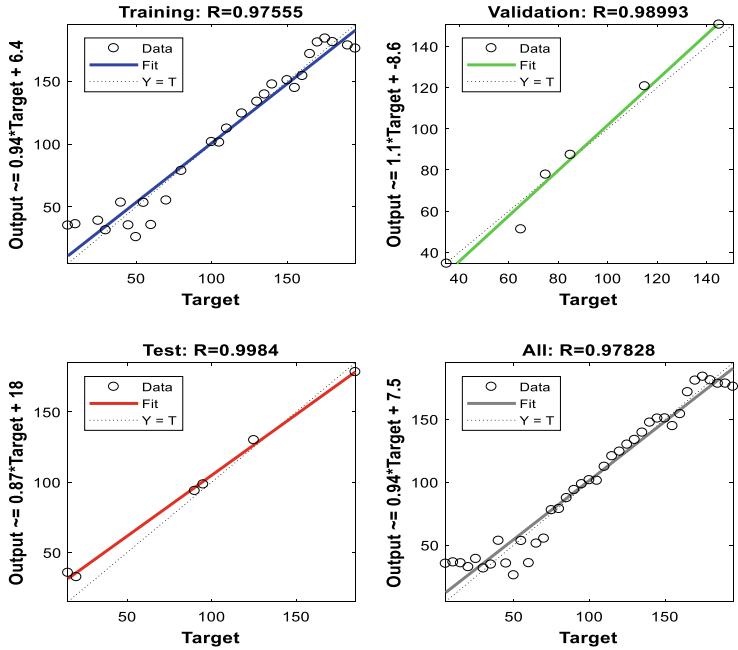


Fig. 8 Regression plots for SCG

Table 1 Tracing of fault events

S. No.	Actual location of faults (km)	Predicted location of faults (km)
1	20	20.125
2	40	39.872
3	60	60.245
4	80	79.885
5	100	100.134
6	120	119.826
7	140	140.159
8	160	159.913
9	180	179.887
10	200	199.843

6 Conclusion

An intelligent feature selection-based fault ascertaining mechanism for a HVDC system is presented in this article. The crucial fault characteristics have been procured in terms of SD values of the detailed coefficients. The feature-based mechanism of the proposed methodology makes it fast with smaller dimensionality. The acquired features are applied as input to the designed intelligent network model, and it predicts the corresponding points of events in the HVDC transmission system as its output. It has been observed that the result of SCG is superior to LM and BR training mechanism. The SCG training mechanism endows the maximum accuracy level, i.e., 99.84% in ascertaining the point of fault events in the HVDC system. The results of all considered test cases show that the proposed approach is well effectual for ascertaining the faults events in HVDC system with very high accuracy.

References

1. Kamakshaiiah, S., Kamaraju, V.: HVDC Transmission. Tata McGraw Hill Education Private Limited, New-Delhi (2013)
2. Rodriguez, J.P.: Dynamic averaged models of VSC-based HVDC systems for electromagnetic transient programs. Ph.D. dissertation, University of Montreal, Canada (2013)
3. Franck, C.M.: HVDC circuit breakers: a review identifying future research needs. *IEEE Trans. Power Deliv.* **26**(2), 998–1006 (2011)
4. Jovcic, D., Ahmed, K.: High voltage direct current transmission: converters, systems and DC grids. Wiley (2015)
5. Xu, L., Yao, L., Sasse, C.: Grid integration of large DFIG-based wind farms using VSC transmission. *IEEE Trans. Power Syst.* **22**(3), 976–984 (2007)
6. Canadelaria, J., Park, J.D.: VSC HVDC system protection: a review of current methods. In: *Proceedings Power Systems Conference and Exposition (PSCE), Phoenix, USA*, pp. 1–7 (2011)
7. Lenden, K., et al.: Reliability Study Methodology for HVDC Grids. CIGRE (2010)

8. Naidoo, D., Ijumba, N.M.: HVDC line protection for the proposed future HVDC systems. In: Proceedings International Conference on Power System Technology—POWERCON, IEEE, Singapore, pp. 1327–1332 (2004)
9. Naidoo, D., Ijumba, N.M.: A protection system for long HVDC transmission lines. In: Proceedings IEEE Power Engineering Society Conference and Exposition, South Africa, pp. 150–155 (2005)
10. Liu, X., Osman, A.H., Malik, O.P.: Hybrid travelling wave/boundary protection for Monopolar HVDC line. *IEEE Trans. Power Deliv.* **24**(2), 569–578 (2009)
11. Li, Y., Gong, Y., Jiang, B.: A novel traveling-wave-based directional protection scheme for MTDC grid with inductive DC terminal. *Electr. Power Syst. Res.* **157**, 83–92 (2018)
12. Hao, W., Mirsaedi, S., Kang, X., Dong, X., Tzelepis, D.: A novel traveling-wave-based protection scheme for LCC-HVDC systems using Teager energy operator. *Int. J. Electr. Power Energy Syst.* **99**, 474–480 (2018)
13. Ahmed, E.B., et al.: A differential protection technique for multi-terminal HVDC. *Electr. Power Syst. Res.* **130**, 68–78 (2016)
14. Azizi, S., Afsharnia, S., Sanaye-Pasand, M.: Fault location on multi-terminal DC systems using synchronized current measurements. *Electr. Power Energy Syst.* **63**, 779–786 (2014)
15. Yang, Q., et al.: New ANN method for multi-terminal HVDC protection relaying. *Electr. Power Syst. Res.* **148**, 192–201 (2017)
16. Yuansheng, L., Gang, W., Haifeng, L.: Time domain fault location method on HVDC transmission lines under unsynchronized two end measurement and uncertain line parameters. *IEEE Trans. Power Deliv.* **30**(3), 1031–1038 (2015)
17. Ekici, S.: Support vector machines for classification and locating faults on transmission lines. *Appl. Soft Comput.* **12**(6), 1650–1658 (2012)
18. Valsan, S.P., Swarup, K.S.: High speed fault classification in power lines: theory and FPFA based implementation. *IEEE Trans. Ind. Electron.* **56**(5), 1793–1800 (2009)
19. Singh, S.K., Vishwakarma, D.N., Saket.: An intelligent scheme for categorizing fault events in compensated power network using K-nearest neighbour technique. *Int. J. Power Energy Convers.* **11**(4), 352–368 (2020)
20. <http://nepsi.com/resources/calculators/calculation-of-cable-data.htm>

Energy-Metrics Analysis of 2 kWp Rooftop PV System Located in Gwalior India



Saurabh Kumar Rajput, Ankit Kumar Tripathi, and Manjaree Pandit

1 Introduction

Green energy is generated from renewable energy resources, and the solar photovoltaic (SPV) has the greatest potential for generating electrical energy of any renewable energy source. The performance and payback period of embodied energy (E_{inPBT}) for SPV plants with balance-of-systems depend on the intensity of solar radiation [1]. In year 2019, an analysis was performed on a 20.4 kWp SPV system under the climatic conditions of Muscat, Oman and observed that the total energy produced is 23,595 KWh (annually), the system efficiency is 10.3%, and the performance ratio and capacity factor were 0.67 and 0.15, respectively. These values may differ on the basis of the temperature. In the summer, an increase in module temperature may lead to higher capture losses and cell temperature losses, which will further cause a reduction in system efficiency [2]. Further, in the same year 2019, similar analysis was performed under the different environmental conditions of Slovenia, and it was found that the behavior of the SPV system primarily depends on the proper inclination, azimuth angle, shading, and snow barrier [3]. The relationship between solar irradiance and ambient temperature along with the performance parameters was developed under the climatic conditions of Jordan [4]. In order to support the growth of SPV plants in the Saharan climate, a similar analysis of a 2.5 kWp SPV system was done in southern Algeria in hot, dry weather [5]. The IEC 61724 standards can be used to investigate the performance of such an SPV system [6], and softwares like PVSOL, PVGIS, SolarGIS, and SISIFO are also used to analyze the performance results [7]. The simulation software-based examination of the climatic conditions in northern India shows that, due to seasonal fluctuations and environmental conditions, the generation is highest in the month of April and lowest in the month of November. They also discovered that after cleaning the panels, the system output increases, and that as the ambient temperature rises, a large quantity of heat is generated in the SPV modules, resulting in increased system losses and reduced system efficiency [8]. An energy and economic analysis were done of a 100

S. K. Rajput (✉) · A. K. Tripathi · M. Pandit
Madhav Institute of Technology and Science, Gwalior, Madhya Pradesh, India
e-mail: saurabh9march@mitsgwalior.in

kW GCPV system having a total effective area of 520.08 m^2 and a total number of 318 modules in series/parallel string combination. The energy analysis for the SPV system was divided into two parts, the first of which is the measurement of total annual energy generated by the plant, and the second is related to the calculation of the embodied energy (E_{in}) of the plant. As the SPV system was installed with a capital investment of 40.00 lakh, the findings were that the total annual energy generated was 113,185.46 kWh, and the EE in the same system was 572,594.78 kWh. With the help of this data, the energy payback time obtained was 5.03 years, and the simple payback time was 9 years. They concluded that the performance of the GRPV system could be upgraded by proper maintenance, washing of panels, and maintaining standard test conditions. Further, it has also been recommended that escalation in the price of electricity be considered for a more accurate forecasting of the payback time of the system [9]. In the year 2019, emissions and energy matrices analysis were done on the Indian rooftop PV market, and the findings were that the total calculated E_{in} of installed PV systems in Delhi was 8493.16 kWh. The E_{in} PBT is estimated to be 8.61 years. They also observed that E_{in} PBT can be improved by the use of MPPT [10]. Similar performance of energy-metrics analysis was done on two co-related PV systems comprising poly-crystalline silicon (p-Si) and copper indium selenium (CIS) arrays having a capacity of 1 kWp and 1.36 kWp, respectively, under the real hot and humid climatic conditions of Tamil Nadu, Southern India with the help of PVsyst software. It was observed that for (p-Si) PV plants and CIS PV systems, the yearly average performance ratio was found to be 78.48% and 86.73%, respectively. It has also been observed that there are higher capture losses in p-Si PV plants than in CIS PV plants. Further, the E_{in} PBT of both the systems has also been computed and is found to be 4.331 years in the case of p-Si technology, whereas for CIS technology, it has been found to be 0.989 years. So, based on these results, they concluded that CIS PV technology is more suitable in the hot climatic conditions of Tamil Nadu, India [11]. Another metric analysis was done on hybrid PV modules under the composite climatic conditions of New Delhi, India. In this analysis, first, the energy consumption in making the components of PV modules has been calculated and then the annual energy available from the PV modules. It has been observed that EPF is higher for hybrid PV/air heating systems without BOS and life-cycle-conversion-efficiency changes marginally from standard test conditions to outdoor conditions [12].

According to the literature study, along with the performance analysis, the energy-metrics of GCPV plants is also important for their acceptance. The need of energy-metrics analysis is more accurately explained through the power flow of a GCPV plant as depicted in Fig. 1. On the one hand, the GCPV plant generates electrical power and provides support to the grid, while on the other hand, it uses grid electricity to build its own components. The comparison of these two power components is important to determine the energy efficiency of the complete system. In this scenario, it becomes necessary to determine the embodied energy-based analysis of the GCPV plant before recommending its adoption and integration with the grid to the consumers. The presented work covers the energy-metrics-based analysis of a 2 kWp PV system in the Gwalior (MP, India) climate condition.

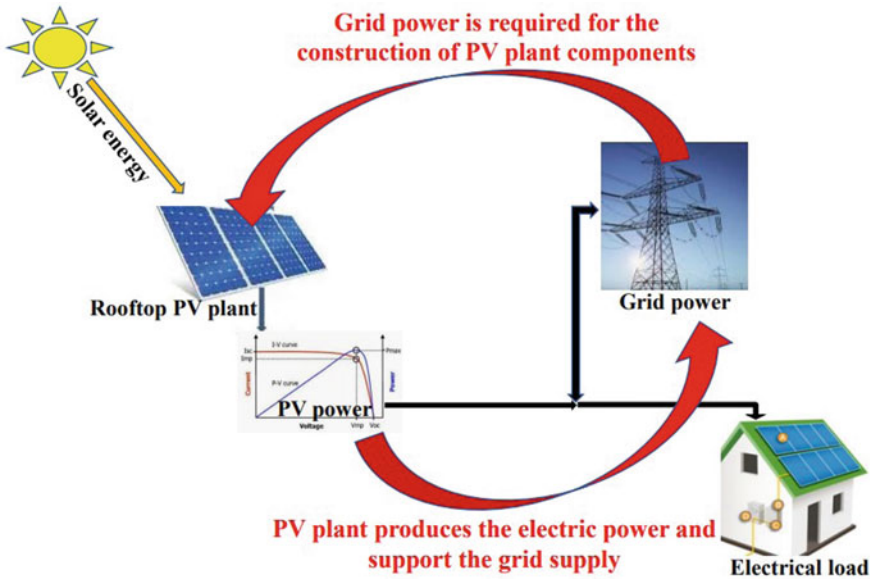


Fig. 1 Power flow diagram of GCPV plant

2 System Description

As shown in Fig. 2, to supply electrical power to an AC load, first, the electricity is generated with the help of the poly-crystalline PV plant having 8 modules whose maximum power rating is 2kWp. The maximum voltage and current rating are 30.62 V and 8.50 A, respectively. Its frame is made of anodized aluminum, and its front glass is 3.2 mm of low-iron textured toughened glass. Now to control the power going to storage battery or to any DC load (if any), system has an solar PV charge controller having a nominal system voltage of 12 V/24 V/48 V with a nominal max. input power of 800 W/1600 W/3200 W, respectively. It has a maximum battery current of 60 A and a maximum solar input voltage of 150 V DC. Now, as we know that we can only get a sufficient amount of electricity from a PV panel in the day time, a battery bank of eight batteries having a capacity of 100 Ah and a rated voltage of 12 V is provided. As most electrical equipment or appliances run only on AC power, so to convert DC power to AC power, system uses a 2kW powerone UPS hybrid inverter. Its input (DC) maximum power is 2000 W with a maximum PV array open circuit voltage of 145 V DC, and 1 MPP tracker is used, having an operating voltage range of 30 VDC-115 VDC. Acceptable input voltage at grid input is 90–280 V AC with a frequency range 50Hz/60Hz (auto-sensing). The battery has a nominal DC voltage of 24 V DC with a maximum charging current (from grid) of 60 A, whereas the maximum charging current (from PV) is 80 A. If we have any DC load to operate, the power can be directly given to the load with the help of a charge controller, as

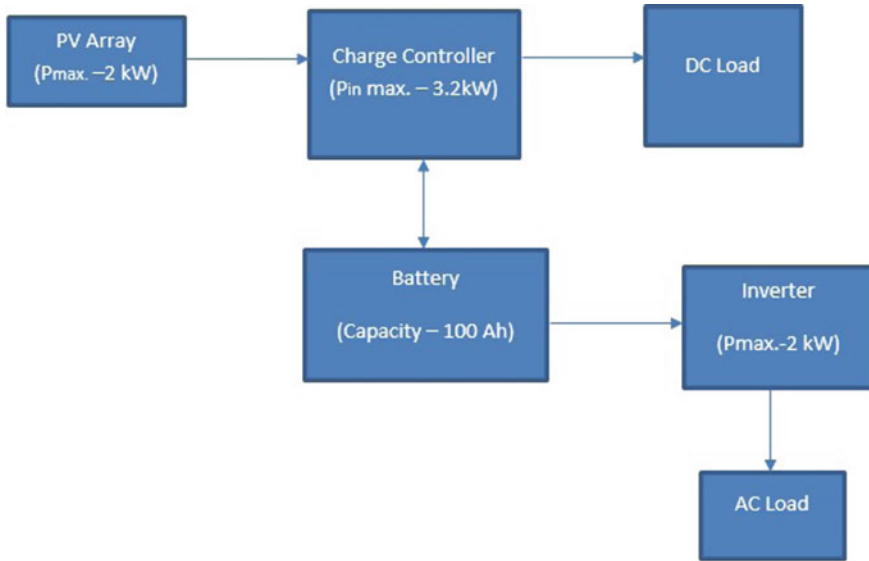


Fig. 2 Block diagram representation of study system

the generated power from the PV will be DC only, so it can be used directly on the DC load.

3 Methodology

In the energy-metrics analysis, basically, we compare the embodied energy with the energy production, and it is divided into these three terms, i.e., energy payback time (EPBT), electricity production factor (EPF), and life cycle conversion efficiency (LCCE) as shown in above Fig. 3.

3.1 EPBT

It is the time period required to recover the embodied energy of SPV plant, i.e., the time period required to recover the total energy used to prepare the SPV plant materials, their transport, installation, and administration.

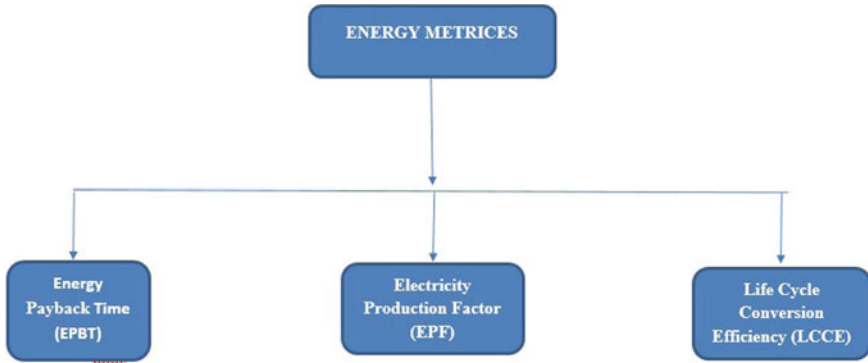


Fig. 3 Energy metrics

3.2 *EPF*

It gives us the information about overall performance of the systems. Thus, it can be defined as the ratio of the output energy to the input energy; hence, it is also a inverse of energy payback time.

3.3 *LCCE*

It is the net energy productivity of the system with respect to the solar radiation over the life time of the system.

For a system to be embodied energy efficient, majorly, three points should be considered which are as follows:

- (a) EPBT should be less than life of a system.
- (b) EPF should be greater than 1.
- (c) LCCE should always be positive.

4 Result and Discussions

The performance analysis of the 2kWp SPV system is done during summer, then winter, and then during the rainy seasons. So the output energy generated on an average daily basis in the months of these three different seasons is measured during the analysis.

The data shown in Fig. 4 is the average daily data in the months of summer. As we know, the solar intensity is much higher in the summer, and it can also be observed that, since the morning at 6:30 AM, the system starts generating electricity to a small

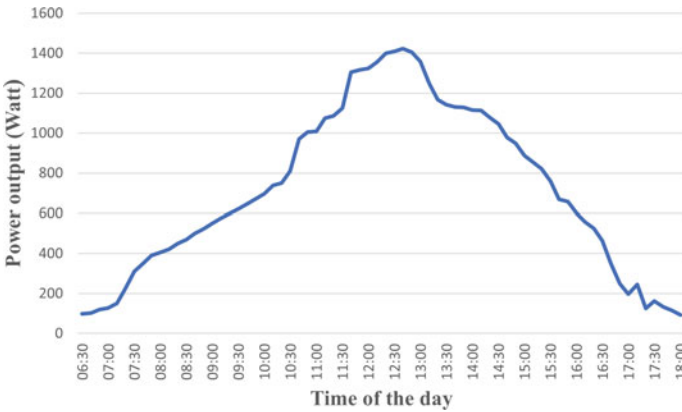


Fig. 4 Average summer day variation of SPV generated power with time

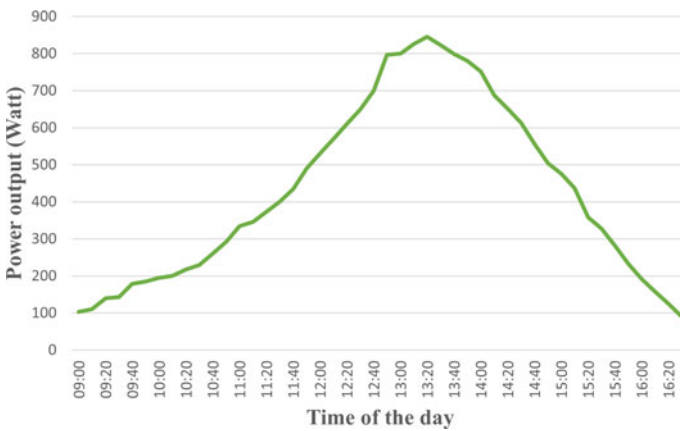


Fig. 5 Average winter day variation of SPV generated power with time

extent, and then after 8 AM, it gradually grows to a considerable amount, as can be clearly seen from the graph. Maximum generation of power occurs at the middle of the day, i.e., between 12:00 PM and 12:30 PM, when the solar intensity is at its peak, and it generates around 1400W during that particular period of time. After that, there is a fall in sun intensity, which results in the generation of power gradually slowing down till 6 PM in the evening, as shown in the graph. The data shown above is average daily data in the months of summer.

During the winter season, as shown in Fig. 5, it was observed that the generation of power starts late in the morning due to late sunrise and fog too. As we can see from the variations that are visible in the above graph, energy generation starts at 9 AM in the morning and gradually grows. This time the solar intensity is at its peak (near to 01:20 PM) with the maximum output power generated being 845 W and then

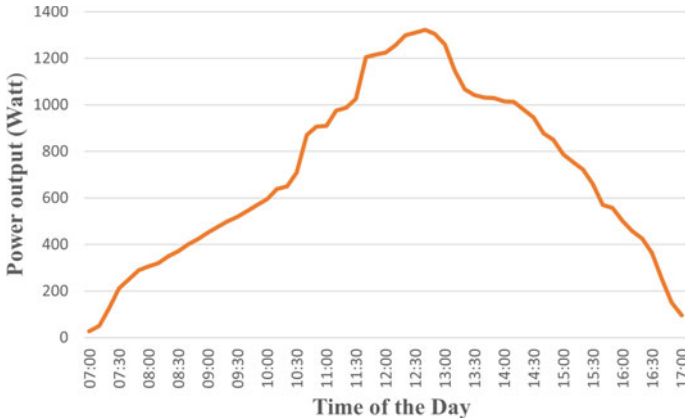


Fig. 6 Average rainy day variation of SPV generated power with time

gradually lowering to 89.8 W at 4:30 PM in the evening. Now if we compare this data with the data obtained during the summer months, we find that there is a fall in energy generation in the winter because of fog, less sunlight intensity, etc. From both of the graphs shown above, it can be verified that at 1 PM, during summer, the average daily power generated is 1400 W, and at the same time during winter, it is about 845 W, so we can clearly see there is a lot of difference in SPV power generation between the two seasons.

During the rainy season, as shown in Fig. 6, the sun’s intensity is quite good, but sometimes due to the sudden occurrence of clouds, the generation of energy falls. So it can be concluded from the above variations of data that during the rainy season, the output energy generated is higher than during the winter season but less than during the summer season for the same time. Here, the maximum energy generated at around 1 PM was about 1305 W, which is less than the energy generated in summer for the same time.

The calculated average energy produced (Wh) in a day of SPV plant is shown in Fig. 7. According to the average daily energy production in all the three seasons (summer, winter, and rain), it is found that in the daytime, solar intensity in the summer season is higher than in the other two seasons, while in the rainy season, the intensity is good but less than in the summer. So it can be concluded that the system performs better when the solar intensity is high during the daytime. The total energy produced by the SPV plant is 6312.217 Wh (per day average). Considering the number of clear days in a year 300 (minimum), the total energy produced by the SPV plant is 1893.6651 kWh (per year). If the life of SPV system is 25 years, the total energy produced by the SPV plant will be 47341.6275 kWh (life time).

As shown in Fig. 8, the embodied energy is measured in four components: material production energy, system installation energy, maintenance energy, and administration energy. From Fig. 8, it can be clearly observed that the major part of energy spent in the production of material. Where the energy is first utilized in silicon purifica-

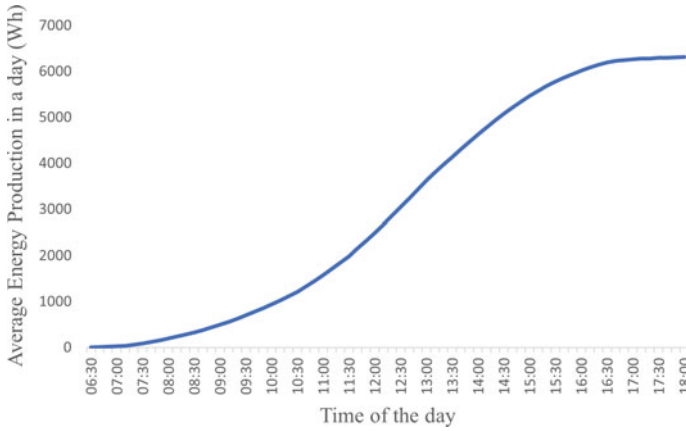


Fig. 7 Average daily energy production of SPV plant

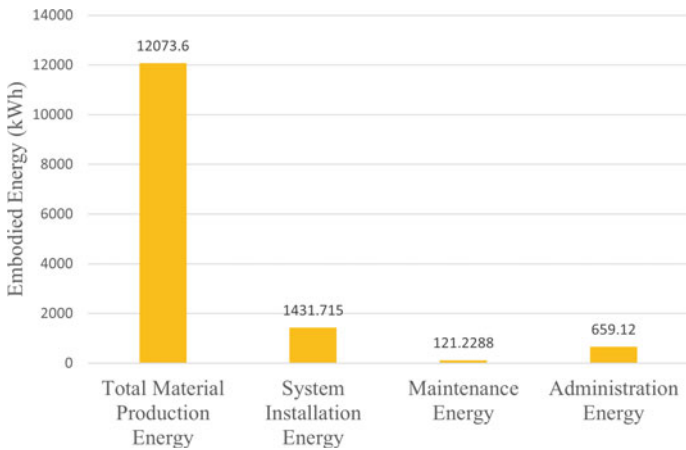


Fig. 8 Embodied energy of SPV plant

tion and processing of about 670 kWh/m^2 and then in the production of solar cell of about 120 kWh/m^2 and then at last, the energy being spent in the lamination of PV module and assembly of about 190 kWh which combinly contributes to a total production energy of material of 980 kWh/m^2 , and if we calculate the total production energy spent in our system of area 12.32 m^2 , then it comes out to be $12,073.6\text{ kWh}$. After this, we have calculated the data of total energy spent in the installation of the system like there were several items needed to install the system like supporting structure (iron stand and screws), charge controller, battery. Inverter, wires, etc., which total contributes to a energy of 485.33 kWh/m^2 and similarly the total installation energy being spent in the system is found to be 1431.715 kWh . To perform all these work manually and to maintain the system in a well manner, of course some

Table 1 Comparison of presented study with earlier research

Year	System	EPBT (years)	EPF	LCCE (%)	References
2022	2kWp PV	6.35	3.93	15.8	Present study
2017	Concentrated PV	5.58	0.17		[13]
2014	BiPV	5.5	9.09	17	[14]
2009	Hybrid solar system	2.25 and 17.21		Increases	[15]
2009	Hybrid PV module	3.00–3.96	Increases		[12]

labor work is also needed which comes under the maintenance, so it has been found to be 9.84 kWh/m^2 . This is the data of 1 m^2 and as our system is of 12.32 m^2 , so the total maintenance energy comes out to be 121.23 kWh . At last, the energy is spent in transportation of material which comes under the administration energy where it has been found that here energy spent was 53.50 kWh/m^2 , therefore administration energy spent for the system is calculated as 659.12 kWh . Table 1 shows the calculated values of energy-metrics parameters for presented study and compare it with the earlier research studies. It is clear from the comparison that the system is well performing in climate condition of Gwalior, India.

5 Conclusion

The EPBT of the RPV plant is 6.35 years when operating under outdoor conditions for a period of one year in Gwalior climate conditions. It demonstrates that the PV plant will recoup its embodied energy within 6.35 years of operation and that, beyond 6.35 years (till the end of its life), the energy generated by the system will be an energy gain. The EPF value of 3.39 indicates that, in comparison with its embodied energy, the system is capable of producing 3.39 times more energy throughout the course of its life. The measured value of LCCE (15.8%) indicates that the system's embedded energy efficiency is likewise quite good. The measured values for these parameters indicate that the system is embodied energy efficient. However, these values can be improved further when operating under conditions of increased insolation, longer sunlight hours, and a greater number of clear days per year, such as those found in India's Leh region. We expect that the outcomes of this study will encourage the expansion of PV energy generation in the smart city of Gwalior (MP, India) and nearby regions.

Acknowledgements The authors are grateful to Department of Science and Technology for providing DST-FIST project (SR/FST/COLLEGE-28412018).

References

1. Nawaz, I., Tiwari, G.N.: Embodied energy analysis of photovoltaic (PV) system based on macro- and micro-level. *Energy Policy* **34**, 3144–3152 (2006)
2. Al-Badi, A.: Performance assessment of 20.4 kW eco-house grid-connected PV plant in Oman. *Int. J. Sustain. Eng.* **13**, 230–241 (2020)
3. Seme, S., Sredenšek, K., Štumberger, B., Hadžiselimović, M.: Analysis of the performance of photovoltaic systems in Slovenia. *Solar Energy* **180**, 550–558 (2019)
4. Alshare, A., Tashtoush, B., Altarazi, S., El-khalil, H.: Energy and economic analysis of a 5 MW photovoltaic system in northern Jordan. *Case Stud. Therm. Eng.* **21** (2020)
5. Necaibia, A., Bouraiou, A., Ziane, A., Sahouane, N., Hassani, S., Mostefaoui, M., Dabou, R., Mouhadjer, S.: Analytical assessment of the outdoor performance and efficiency of grid-tied photovoltaic system under hot dry climate in the south of Algeria. *Energy Convers. Manag.* **171**, 778–786 (2018)
6. Pritam Satsangi, K., Bhagwan Das, D., Sailesh Babu, G.S., Saxena, A.K.: Performance analysis of grid interactive solar photovoltaic plant in India. *Energy Sustain. Dev.* **47**, 9–16 (2018)
7. Dondariya, C., Porwal, D., Awasthi, A., Shukla, A.K., Sudhakar, K., Murali Manohar, S.R., Bhimte, A.: Performance simulation of grid-connected rooftop solar PV system for small households: a case study of Ujjain, India. *Energy Rep.* **4**, 546–553 (2018)
8. Arora, R., Arora, R., Sridhara, S.N.: Performance assessment of 186 kWp grid interactive solar photovoltaic plant in Northern India. *Int. J. Ambient Energy* **43**, 128–141 (2019)
9. Babul, A.K., Rajput, S.K., Singh, H., Yadaw, R.C.: Energy and economic analysis of grid-type roof-top photovoltaic (GRPv) system. In: Singh, A.K., Tripathy M. (eds.) *Control Applications in Modern Power System. Lecture Notes in Electrical Engineering*, vol. 710. Springer (2021)
10. Shukla, C., Pal, N.: Emissions and energy metrics analysis in current Indian roof top photovoltaic market. *Int. J. Ambient Energy* **42**, 1581–1587 (2019)
11. Ramanan, P., Kalidasa Murugavel, K., Karthick, A.: Performance analysis and energy metrics of grid-connected photovoltaic systems. *Energy Sustain. Dev.* **52**, 104–115 (2019)
12. Tiwari, A., Barnwal, P., Sandhu, G.S., Sodha, M.S.: Energy metrics analysis of hybrid-photovoltaic (PV) modules. *Appl. Energy* **86**, 2615–2625 (2009)
13. Tripathi, R., Tiwari, G.N., Dwivedi, V.K.: Energy matrices evaluation and exergoeconomic analysis of series connected N partially covered (glass to glass PV module) concentrated-photovoltaic thermal collector: at constant flow rate mode. *Energy Convers. Manag.* **145**, 353–370 (2017)
14. Sudan, M., Tiwari, G.N.: Energy matrices of the building by incorporating daylight concept for composite climate—an experimental study. *J. Renew. Sustain. Energy* **6**, 053122 (2014). <https://doi.org/10.1063/1.4898364>
15. Prabhakant, Tiwari, G.N.: Energy payback time and life-cycle conversion efficiency of solar energy park in Indian conditions. *Int. J. Low Carbon Technol.* **4**, 182–186 (2009). <https://doi.org/10.1093/ijlct/ctp020>

The Use of Biogas Energy for Electrical Power Generation in Zimbabwe—A Study



Coddell Tanaka Mutate, Artwell Jairos Kanjanda, and Gitanjali Mehta

1 Introduction

Zimbabwe has been facing an energy crisis since the country's independence in 1980. This is mainly due to the fact that the economy of the country has been expanding, but the capacity of the generating power plants has remained almost constant. Zimbabwe relies significantly on hydroelectricity and thermal power. The biggest hydroelectric power station of the country by installed capacity is Kariba which generates a total of 1626 MW located on the perennial river Zambezi. It has been the largest producer of electrical power supply in the landlocked country that relies on importing electricity from neighboring countries. Due to a lot of difficulties that have been faced by these power plants which include lack of service, depletion of water levels, increased cost price of fossil fuels, and poor workmanship, Zimbabwe has faced erratic power supplies and experienced a lot of load shedding over the years [1, 2].

Anaerobic digestion of organic matter produces biogas. The combustible gas is produced when feedstock like manure from animals, sewage, and forestry is fed into the biogas digester in the absence of air [3–16]. In most third world countries, biogas is being used for cooking and lighting because of its efficiency and clean nature, realizing the gas' potential for electricity generation on a large scale could be a huge milestone in Africa. This can minimize the stress on the electrical grid and also provide electricity for the rural population of Zimbabwe where the grid is not extensive. This technology is very promising in Zimbabwe; agriculture is a key component of the country's economy. This is an advantage since a lot of substrates will be available to feed into the digesters. Despite the field being largely untapped, there is not a single biogas plant that generates electricity in the country, which is shocking. Biogas has been regarded as one of the cheapest sources of renewable energy for generating

C. T. Mutate (✉) · A. J. Kanjanda · G. Mehta

Department of Electrical and Electronics Engineering, Galgotias University, Sector 17-A, Yamuna Expressway, Dist. Gautam Budh Nagar, Uttar Pradesh, India

e-mail: tanakacmutate1@gmail.com

electrical power by many research centers and international bodies. When compared with solar energy and wind power, biogas has an advantage over the two because it is not intermittent; therefore, it can generate electrical power at any time be it night or day as long as sufficient substrate is available [4, 5]. Acquiring feedstock does not pose any environmental threats since it can easily be accessed from agricultural residues and even kitchen organic waste. Farmers in the rural areas can make extra money by supplying feedstock to the local biogas plants within the vicinity. There has been little or close to zero experience of implementing these biogas plants to generate electricity in the rural parts of most African countries. Biogas has similar uses to natural gas in engines, for cooking and for lighting [15]. It is a mixture of a few gases with the main gas being methane which is combustible, carbon dioxide, water vapor, and sulfur compounds. The efficiency of biogas depends on the percentage of methane in it. The more methane there is the more the efficiency. Carbon dioxide and water vapor cannot be eliminated entirely, but the content of sulfur should be less. A lot of sulfur content can be damaging to the engine. Approximately, 6kWh of electrical energy is produced by 1 m³ of biogas [17]. Factors affecting the yield of the biogas plants are retention time, type of feedstock, fermentation temperature, and plant design [6, 7]. This paper demonstrates the research methodology used by the researcher, analyzes the results obtained, and finally concludes with a discussion.

1.1 Literature Survey

Studies of this sort have been conducted by few scholars in Zimbabwe. Mukumba et al. (2013) studied the design of a biogas plant at a high school in the outskirts of the country. The biogas produced will be used to generate electricity. The study was conducted to mitigate power cuts due to load-shedding and also reduce the use of fossil fuels like firewood [5]. The school's energy demands were calculated and noted. The feedstock required for the project was identified to be human excreta, cow dung, and poultry manure. The quantity of feedstock to be produced per day was calculated by counting the number of people, cows, and chickens. The total amount of biogas to be produced per day was calculated, and it was observed that this would be sufficient to produce electricity for lighting in periods of load shedding. The technoeconomic analysis of the project was done, and the project was seen to be feasible. This project however was only focused on Nyazura Adventist High School. Garikai and Daniel (2019) studied the status of most biogas digester plants in rural Zimbabwe. Four common types of biogas digester plants were found to be common, and these included Indian type, Chinese type, bio-latrine type, and Carmatec type [3]. 126 biogas digesters were visited, and only, 14 were found to be functional. Most of the biogas digesters did not have proper gas pipes, temperature control and monitoring mechanism, flow meters, heating systems, etc. In Africa, there is only one biogas plant that generates electricity which is grid connected. This biogas plant which was launched in August 2015 is located in Naivasha, Kenya. The Gorge Farm Park has a capacity of producing 2 MW of power. The plant does not only produce

electricity but also produces heat for the farm's greenhouses and fertilizer and as a byproduct. The plant uses Jenbacher gas engines which are of Austrian origin and manufactured in the town Jenbach. The plant was developed by Tropical Power which is incorporated in the United Kingdom and has a subsidiary in Kenya.

2 Research Methodology

2.1 Research Procedure

The researcher conducted a literature survey to get an overview on the operation of biogas digester plants in the country which would help determine the potential of electrical power generation. Detailed information of where these biogas plants are located has been recorded as well as the institutions and individuals responsible for the construction of the plants. To obtain this information, about the current status of the production of biogas in Zimbabwe, four sets of questions were designed and tested to check their feasibility and then applied. Proportional random sampling was used to apply the four sets of questions to the Ministry of Energy and Power Development and head office and provincial offices of Rural Electrification Agency since they are responsible for providing energy as well as monitoring all on-going projects on the generation of energy in the Southern African country. The first category of this set of questions was designed to collect information on the size, design, and number of biogas digesters in Zimbabwe. The next category of questions collected information with respect to the type of feedstock being fed in the biogas plants. The third category focused on the financing of the biogas plant system construction in the country. Next category analyzed the utilization of the biogas and substrate from the biogas plants. The last part collected information regarding the challenges being encountered in operating the plants, ways to improve the production of biogas, and the technology being used. The set of questions were directed to households and institutions in three of the provinces that were randomly selected, i.e., Harare, Mashonaland East, and Mashonaland West. The researcher was able to visit twelve biogas plants in person which were easily accessible to him.

2.2 Aim of the Investigation

The main aim of the survey was to determine the state and condition of biogas digesters in all provinces of Zimbabwe and analyze the feasibility of electricity generation from biogas.

Table 1 Areas of focus for data collection

Operational issues	Technological issues	Ownership issues
Feeding intervals	Size of digester	Year of construction
Quantity of substrate per feeding	Type of digester	Frequency of maintenance
Distance from water source	Type of sensors and valves	Owner's opinion functionality
Distance of digester from user	Material used for construction	

2.3 Data Collection Tool

The tool that was used for this survey focused on the aspects given in Table 1.

3 Results

3.1 Number of Biogas Plants in Zimbabwe

When Zimbabwe realized Biogas can be a good source of clean energy for cooking and lighting unlike firewood which is used by the greater population of rural Zimbabwe, it led to the construction of different biogas plants in the country. According to the researcher, more than 700 biogas digesters had been built in Zimbabwe by 2021. From Fig. 1, it can be seen that there is a steady rise in the number of biogas plants for the period 2013 to 2020.

3.2 Biogas Plant Types

Figure 2 classifies the different types of biogas plants with their quantity expressed in percentages. The largest number of biogas plants in the country is household digesters contributing about 91% of the total number of biogas plants in Zimbabwe. The size of household digesters ranges from 4 to 30 m³. The biogas plants located at schools, hospitals, and prisons are regarded to be institutional digesters. They have a size which ranges from 50 to 200 m³. A few of the biogas plants that are located at local sewage treatment facilities and market areas to process the waste are considered to be municipal digesters. Figure 2 illustrates that 7% of the total number of biogas plants were institutional and municipal biogas plants contributed 2%. It was observed that in Zimbabwe, there is no existence of industrial biogas plants.

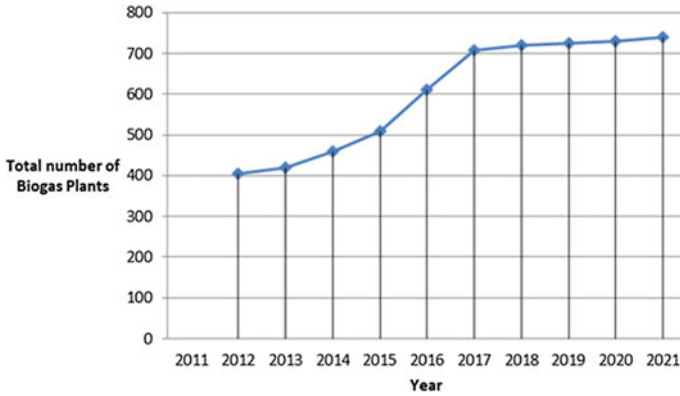


Fig. 1 Gradual increase of biogas plants from 2011 to 2021 in Zimbabwe

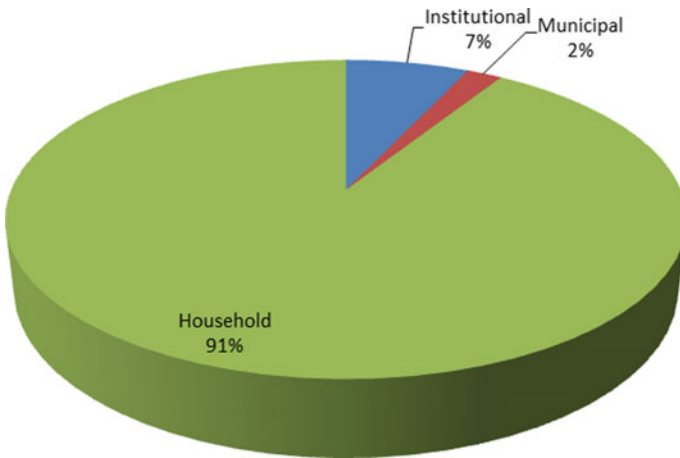


Fig. 2 Classification of biogas plants

3.3 Classification of Institutional Biogas Plants

The size of institutional biogas plants ranges from 50 to 200 m³. Figure 3 shows how these biogas plants are distributed across the different provinces of the country.

Every province has at least one institutional biogas plant except Bulawayo. A total of 48 digesters were recorded to be institutional biogas plants.

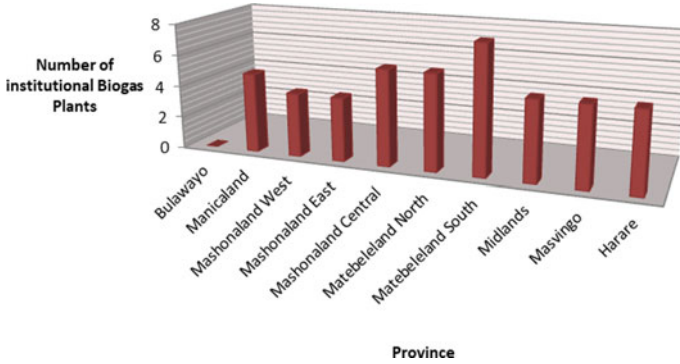


Fig. 3 Classification of institutional biogas plants

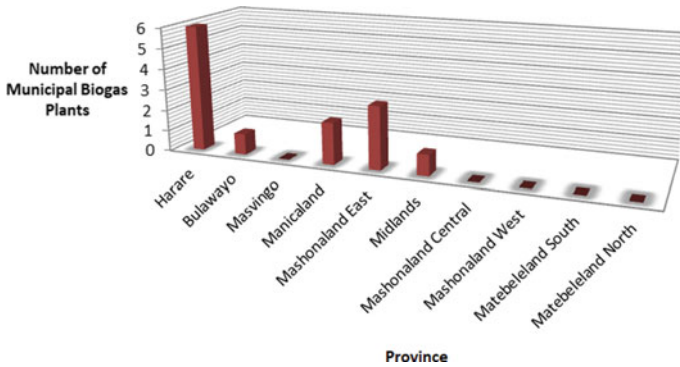


Fig. 4 Classification of municipal biogas plants

3.4 Classification of Municipal Biogas Plants

Biogas plants constructed at local municipal facilities and public market areas were utilized for the treatment of waste. Biogas from these plants can also be used for lighting, heating, and cooking by the local people. Figure 4 shows that only a few provinces have these plants. All municipal facilities across all provinces in the country should adopt this technology for sanitation purposes [14].

3.5 Substrate Used in Biogas Plants

As shown in Fig. 5, more than 90% of biogas digesters use cow dung as a substrate. A small number was using sewage 8%, and only 1% used pig and poultry manure. Kitchen waste was also being used by 1% of the owners. Owners and operators of

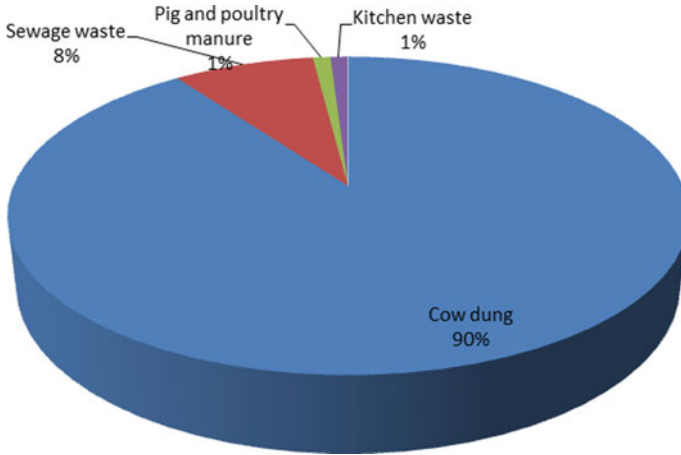


Fig. 5 Substrates for biogas plants

biogas plants should strongly consider using other substrates like forestry and plant residues [12]. The use of pig and poultry manure should also increase because they have a high energy content [13–16, 18]. This will improve the efficiency of the plants and hence increase the biogas production.

3.6 Utilization of Biogas

A large number of biogas owners were using the gas for cooking as shown in Fig. 6. A small percentage used the gas for lighting, space heating, and waste management. This shows that the technology of using biogas energy to generate electricity is still foreign in the country. Biogas can also be used as a fuel to power vehicles the same way compressed natural gas is used in countries like India.

3.7 Challenges Faced in Running Biogas Plants

Operators and owners of biogas plants in Zimbabwe were facing challenges like low gas production, lack of feedstock, and technical maintenance as shown in Fig. 7. All these problems can be solved if adequate knowledge on how to operate and maintain the digesters is provided to the owners [10]. Challenges faced should be minimum to realize full benefits from this technology [11].

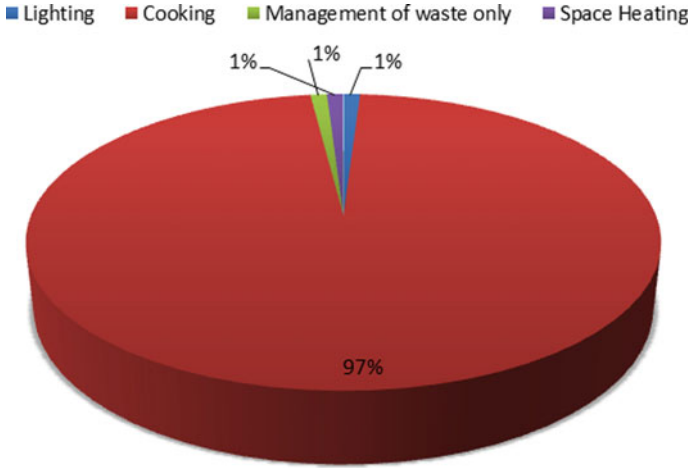


Fig. 6 Utilization of biogas

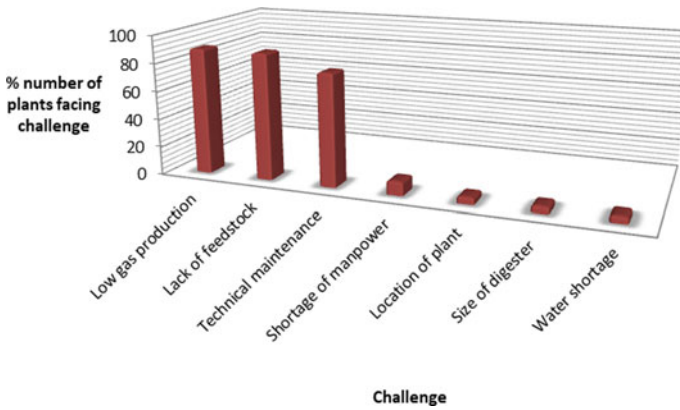


Fig. 7 Challenges faced in running biogas plants

3.8 Proposed Process of Generating Electricity Using Biogas in Zimbabwe

Biogas can be used as a fuel to power different types of internal combustion engines which include gas turbines, diesel engines, and gas engines (Otto motors). It can also be used to drive an external combustion engine like the Stirling motor. In most cases, internal combustion engines are used because of their high efficiency over the external combustion ones. These engines generate mechanical energy which can then be used to drive a suitable generator producing electricity. This technology is well known in industrialized countries like China and Germany. The biogas should

be processed before it is pumped into the combustion engine. This is done to reduce the amount of carbon dioxide, water vapor, and most importantly sulfur compounds in the gas. The presence of sulfur elements in the gas can cause damage to the engine since the sulfur reacts with the metals in the engine. This can shorten the life span of the engine. The suitable generators required for the generation of electricity are present in almost all countries. The electricity generated can be integrated into the national grid or used by independent institutions. Suitable sensors and pumps should be used for this technology to be fully efficient.

4 Discussion

Analyses of all the results obtained by different researchers above show that it is possible to generate electrical power from biogas energy as an alternative energy source in Zimbabwe. The construction of more than 700 biogas plants in 2021 shows that the technology is being adopted in the country quite fairly. It was observed that a lot of biogas digesters were household plants with a few institutional and municipal digesters. This is a major drawback because most of the household digesters are small in terms of size and volume; therefore, the biogas produced will not be able to produce significant electrical energy to power a house. This is not to say household digesters have no use since they also generate sufficient biogas that can be used for cooking, heating, and lighting in homes. The number of municipal biogas digesters should increase because there is a huge amount of sewer that can be anaerobically fermented to produce a significant amount of electrical power that can be used by communities around. The majority of biogas digester owners and operators used cow dung as the substrate, and a few were using pig and poultry manure. A variety of feedstock should be used like plant residues and forestry to maximize the efficiency of biogas production that can be used to generate electrical power. Biogas was mainly used for cooking with a small percentage of people using it for lighting, heating, and in some cases, the biogas was just being released in the air. It is evident that the technology of using biogas to generate electrical power is foreign in Zimbabwe as is the case in most third world countries. A lot of challenges were also being encountered by the biogas owners and operators. These include lack of maintenance, insufficient feedstock to feed into the digesters, poor design of the systems, and lack of water just to mention a few. Most of these challenges can be solved by provision of knowledge to the operators; workshops should be conducted in communities to educate the general public and raise awareness. Biogas production courses should be offered in universities to educate scholars on the technology of using biogas to generate electrical power that is largely untapped in Zimbabwe and Africa as a whole.

5 Conclusion

A literature review was conducted to determine the possible electricity generation from biogas energy in Zimbabwe. At the end of the study, it is concluded that the technology is possible in the landlocked country. It has been observed that there are a decent number of biogas digesters in the country; proper education should be provided to the owners and operators so that they can experience full benefits from this alternative energy source. If proper education is provided and awareness is raised, the owners can be able to generate electrical power for homes and communities at large. The number of biogas digesters should increase in the country, especially in the rural areas since the biogas can also be used for lighting and cooking. If this technology is fully adopted in Zimbabwe, The Rural Electrification Scheme can be realized, and less stress is imposed on the grid. Furthermore, favorable policies should be put in place by the government to make this whole idea come to fruition. The proposed process of electricity generation was illustrated. The biogas generated will fuel a combustion engine coupled to a suitable generator to generate electrical power.

References

1. Dimpl, E.: Small-scale Electricity Generation from Biomass, Part-II Biogas, Experience with Small-scale Technologies for Basic Energy Supply, pp. 2–11 (2010)
2. Kaifa, J., Parawira, W.: A study of the current state of biogas production in Zimbabwe: lessons for Southern Africa. *Adv. Biotech. & 0066 Micro.* **13**(3) (2019)
3. Kajau, G., Madyira, D.: Analysis of the Zimbabwe biodigester status. In: 2nd International Conference on Sustainable Materials Processing and Manufacturing, pp. 561–566 (2019)
4. Vögeli, Y., Lohri, C.R., Gallardo, A., Diener, S., Zurbrügg, C.: Anaerobic Digestion of Biowaste in Developing Countries. Binkert Buag AG, Laufenburg, Switzerland (2014)
5. Mukumba, P., Makaka, G., Mamphweli, S., Misi, S.: A possible design and justification for a biogas plant at Nyazura Adventist High School, Rusape, Zimbabwe. *J. Energy Southern Africa* **24** (2013)
6. Zeng, X., Guo, G., Su, M.K., Danquah, S., Zhang, Y.: Bioprocess considerations for microalgal-based wastewater treatment and biomass production. *Renew. Sustain. Energy Rev.* **42**, 1385–1392 (2015)
7. Rodríguez, R.J., Espada, J., Moreno, G.: Vicente J Dufour, environmental analysis of Spirulina cultivation and biogas production using experimental and simulation approach. *Renew. Energy* **129**, 724–732 (2018)
8. Uddin, W., Khan, B., Shaikat, N., Majid, M., Mujtaba, G., Mehmood, A., Ali, S.M., Younas, U., Anwar, M., Almeshal, A.M.: Biogas potential for electric power generation in Pakistan: a survey. *Renew. Sustain. Energy Rev.* **54**, 25–33 (2016)
9. Pandey, P., Pandey, A., Yan, L., Wang, D., Pandey, V., Meikap, B.C., Huo, J., Zhang, R., Pandey, P.K.: Dairy waste and potential of small-scale biogas digester for rural energy in India. *Appl. Sci.* **11**(22), 10671
10. Abanades, S., Abbaspour, H., Ahmadi, A., Das, B., Ehyaei, M.A., Esmailion, F., El Haj Assad, M., Hajilounezhad, T., Jamali, D.H., Hmida, A., Ozgoli, H.A., Safari, S., AlShabi, M., Bani-Hani, E.H.: A critical review of biogas production and usage with legislations framework across the globe. *Int. J. Environ. Sci. Technol.* 2–20 (2021)

11. Korbag, I., Mohamed Saleh Omer, S., Boghazala, H., Ahmeedah Aboubkr Abusasiyah, M.: Recent Advances of Biogas Production and Future Perspective. Recent Advances and Intergrated Approaches. Laws and guidelines concerning biogas plants, issa.omar@uob.edu.ly, pp. 2–38 (2020)
12. Barragan-Escandon, A., Miguel Olmedo Ruiz, J., David Curillo Tigre, J., Zalamea-Leon, E.F.: Assessment of Power Generation Using Biogas from Landfills in an Equitorial Tropical Context, pp. 2–7 (2020)
13. da S. Antonio, A., Oliveira Filho, D., da Silva, S.C.: Electricity generation from biogas on swine farm considering the regulation of distributed energy generation in Brazil: a case study for Minas Gerais, pp. 2–6 (2018)
14. European Biogas Association: The Role of Biogas Production from Industrial Wastewaters in Reaching Climate Neutrality by 2050, pp. 3–6 (2021)
15. European Biogas Association: The Future Role of Biomethane, pp. 3–19 (2022)
16. European Biogas Association: Biogas Basics, pp. 2–20 (2019)
17. Uddin, W., Khan, B., Shaukat, N., Majid, M., Mujtaba, G., Mehmood, A., Ali, S.M., Younas, U., Anwar, M., Almeshal, A.M.: Biogas potential for electric power generation in Pakistan: a survey. *Renew. Sustain. Energy Rev.* (2015)
18. Esmailion, F., Ahmadi, A., Dashti, R.: Energy-economic-environment optimization of the waste-to-energy power plant using multi-objective particle swarm optimization (MOPSO). *Scientia* (2021)